FABRICATION AND CHARACTERIZATION OF METAL AND INSULATING THIN FILMS FOR SEMICONDUCTOR DEVICES

Thesis

Submitted

In partial fulfillment of the requirement for the

Degree of

DOCTOR OF PHILOSOPY

in

MECHANICAL ENGINEERING

by

SHAILENDRA KUMAR GAUR
(2K20/PHDME/507)
Under the supervision of

Prof. QASIM MURTAZA **Prof. R.S. MISHRA**

Department of Mechanical Engineering
DELHI TECHNOLOGICAL UNIVERSITY
(Formerly Delhi College of Engineering)
Shahbad Daulatpur, Bawana road, Delhi 110042, India

June, 2026

© Delhi Technological University 2026

All rights reserved.

ACKNOWLEDGEMENTS

My research journey has been made possible by the invaluable assistance of numerous individuals. It is an excellent attribute that I have now chance to convey my feelings of appreciation to every one of them in person.

I want to commence by expressing my sincere gratitude, debt, and respect to my supervisors, **Professors Qasim Murtaza** and **R.S. Mishra** of the Mechanical Engineering Department at Delhi Technological University, Delhi, who developed my research skills for an effective professional life in scientific research. Working under outstanding, passionate, and renowned supervisors has been a privilege. I find myself fortunate to have performed pursuant to such outstanding oversight because of their unwavering support, ongoing assiatance, careful monitoring, and positive feedback across my studies for achieving a further accomplishment in my career in academia.

I also enthusiastically appreciative to **Prof. B.B. Arora**, Head, Mechanical Engineering Department, DTU, for his significant support as well as insights. My sincere gratitude to **Prof. Atul Kumar Agrawal**, DRC chairman, and the individuals who are part of my SRC and DRC committee (Prof. **S. Arindan**, IIT Delhi, **Prof. Abid Haleem**, Jamia Millia Islamia University, Delhi, and **Prof. Akhilesh Arora**, DTU, Delhi) for their consistent support and sensible suggestions. I convey my heartfelt admiration particularly to **Prof. M. Rizwan**, Department of Electrical Engineering, DTU and **Prof. Vipin**, Department of Mechanical Engineering, DTU, for their prompt comments and cooperation as SRC representatives.

It honors to extend warm much appreciation for every one of the professors of the Mechanical Engineering Department, DTU for their constant inspiration and contributions throughout my research journey. I am likewise appreciative to technical and non-technical personnel for their swift assistance as well as collaboration regardless of requested.

I would like to thank in particular **Dr.Vanya Srivastav (Scientist'F')** and **Mr. Ajay Kumar Saini (Scientist'E')** of Infrared Device Fabrication Group of Solid State Physics Laboratory (SSPL), DRDO, Delhi for their gracious assistance in the deposition of distinct thin layers/films. Sincere gratitude to **Dr. Akhilesh Kumar Panday (Scientist'F')**, **Mr. Sandeep Dalal (Scientist 'B')**, **Ms. Garima (TO'C)**, **Ms.Monika (TO'A)**, and **Mr. Harsh (STA'B')**, Characterization Group, SSPL; **Ms Nishima Dangwal (Scientist'E')**, IEEE Group, SSPL, for their assistance in assessment and characterization of deposited thin films. I am also grateful to **Mr. Varun (Scientist'E')** of Liquid Phase Epitaxy Group, SSPL, for providing the HgCdTe (MCT) epilayers required for the entire research work.

I take this opportunity to communicate my admiration to my wonderful lab colleagues, both past and current, whose assistance enabled me to complete my task. Along the journey, their

friendship has made for an amazing experience. I also want to express my gratitude to all of the other research scholars at Delhi Technological University's Department of Mechanical Engineering for their assistance and counsel.

Lastly, I praise my entire family for their patience and enthusiasm at every point of my research time frame. I am eternally grateful to all of my cherished friends worldwide for combining my joy and suffering.

I sincerely thank Solid State Physics Laboratory (SSPL) and Delhi Technological University for their resources and invaluable contribution in completing the entire research work. Multiple sections of SSPL, Delhi (Infrared Device Group: HgCdTe (MCT) epilayer accessibility, preparation of specimen, ellipsometer analysis, optical microscope, photolithography as well as vacuum evaporation unit; Characterization and IEEE sections: X-ray diffraction, scanning electron microscopy, atomic force microscopy, EDS, UV vis-spectrophotometer, surface profiler, Multibeam optical stress sensor (MOSS), and current-voltage/capacitance-voltage measurement equipment) offered their immense assistance and resources in executing this research work. I offer heartfelt thanks to DTU professionals in Accounts, administrative dept., Stores and procurement dept., Computer center, and Library for aid and amenities.

I applaud each and every one of you for assisting me in successfully submitting the thesis.

Thank you all!!

Shailendra Kumar Gaur

DELHI TECHNOLOGICAL UNIVERSITY

(Formerly Delhi College of Engineering)
Shahbad Daulatpur, Main Bawana Road, Delhi-42

CANDIDATE'S DECLARATION

I **Shailendra Kumar Gaur** hereby certify that the work which is being presented in the thesis entitled "**Fabrication and characterization of metal and insulating thin films for semiconductor devices,"** in partial fulfillment of the requirements for the award of the Degree of Doctor of Philosophy, submitted in the Department of **Mechanical Engineering,** Delhi Technological University (DTU) is an authentic record of my own work carried out during the period **January 2021** to **December 2025** under the supervision of **Prof. Qasim Murtaza** and **Prof. R.S. Mishra**, Department of Mechanical Engineering, Delhi Technological University, Delhi.

The matter presented in the thesis has not been submitted by me for the award of any other degree of this or any other Institute.

Date:
Place:

Shailendra Kumar Gaur
Research Scholar
(Roll no.2K20/PHDME/507)

DELHI TECHNOLOGICAL UNIVERSITY

(Formerly Delhi College of Engineering)
Shahbad Daulatpur, Main Bawana Road, Delhi-42

CERTIFICATE BY THE SUPERVISOR(s)

Certified that **Shailendra Kumar Gaur (**2K20/PHDME/507) has carried out their search work presented in this thesis entitled **"Fabrication and characterization of metal and insulating thin films for semiconductor devices"** for the award of **Doctor of Philosophy** from Department of Information Technology, Delhi Technological University, Delhi, under our supervision. The thesis embodies results of original work, and studies are carried out by the student himself and the contents of the thesis do not form the basis for the award of any other degree to the candidate or to anybody else from this or any other University/Institution.

Signature

(Dr. Qasim Murtaza)
Professor

Department of Mechanical Engineering
Delhi Technological University,
Bawana road, Delhi 110042

Signature

(Dr. R.S. Mishra)
Professor

Department of Mechanical Engineering
Delhi Technological University,
Bawana road, Delhi 110042

Date:

ABSTRACT

In this thesis the investigation of structural, morphological, and nano-mechanical properties of vacuum evaporated cadmium telluride (CdTe) and Zinc Sulfide (ZnS) stack layers has been done. The films used for the fabrication of optoelectronic sensors in the infrared range. The films had been deposited by vacuum evaporation technique on Si (100) substrate. The X-ray diffractogram had indicated stable polycrystalline cubic structure with (111) preferential orientation for both films. The crystallite size, intrinsic stress, microstrain, and dislocation density values had been evaluated to be 17.5 nm, 0.09 GPa, 9.96, and 3.2×10^{11} lines/cm^2, respectively, for CdTe film. While for ZnS film, the parameters had been estimated to be 15 nm, 0.49 GPa, 9.71, and 4.4×10^{11} lines/cm^2, respectively. The Field Emission Scanning Electron Microscopy (FESEM) study had revealed homogeneous, dense, and defect free structure of the film. Compositional analysis had confirmed that the Te/Cd ratio 1.1 while S/Zn ratio 0.71 in the evaporated films. Atomic Force Microscopy (AFM) measurements had indicated smooth and uniform film with rms surface roughness of ~0.96 nm. Hardness, Young's modulus, strain rate, and creep of the top layer (ZnS) had been evaluated by nanoindentation. The hardness of the ZnS film had evaluated to be 1.80–2.39 GPa, and Young's modulus evaluated to be 181–248 GPa, for a 50–100 μN load. The outcome of the investigations endorsed the fact that the CdTe and ZnS thin films grown by the vacuum evaporation technique are suitable for the fabrication of optoelectronic devices.

In second study, vacuum-sublimated cadmium telluride (CdTe) and zinc sulfide (ZnS) thin films were investigated at 1,5, and 10 Å/s evaporation rates to assess their suitability for mid- to long-wave infrared device applications. X-ray diffraction analysis confirmed the formation of single-phase, polycrystalline films with a face-centered cubic structure and a pronounced preferential orientation along the (111) crystallographic plane. Quantitative diffraction analysis revealed crystallite sizes of 21.4–19.4 nm for CdTe, with dislocation densities of 2.16×10^{11}–2.63×10^{11} lines cm^{-2}, residual stresses of 0.05– 0.19 GPa, microstrain values of 8.18–9.04, and stacking-fault probabilities of 3.80×10^{-3}–4.19×10^{-3}. The corresponding ZnS films exhibited crystallite sizes of 19.4–21.4 nm, dislocation densities of 3.18×10^{11}–12.85×10^{11} lines cm^{-2}, residual stresses of 0.20–0.44 GPa, microstrain values of 8.29–16.58, and stacking-fault probabilities of 4.23×10^{-3}–8.48×10^{-3}. Scanning electron microscopy revealed continuous and compact surface morphologies with high surface coverage and no discernible pinholes, particularly for films deposited under low-temperature sublimation conditions. Energy-dispersive spectroscopic analysis further confirmed near-stoichiometric elemental compositions. Atomic force microscopy measurements showed root-mean-square surface roughness values of 0.84–7.40 nm for CdTe and 0.49–1.27 nm for ZnS. Optical transmission measurements demonstrated appreciable transparency over the 500–4000 nm spectral range, indicating their potential for infrared optical applications. The ex-situ residual stress measured using a multi-beam optical stress sensor (MOSS) was found to be 0.99–1.09 GPa for CdTe and 0.02–1.01 GPa for ZnS films. Nanoindentation measurements yielded hardness values

of 479–753 MPa and Young's moduli of 63–141 GPa for CdTe, whereas ZnS exhibited hardness values of 150–478 MPa and Young's moduli of 60–265 GPa. Furthermore, the creep response and strain-rate behavior of both films were evaluated to assess their mechanical stability. Electrical characterization of metal–insulator–metal (MIM) structures revealed a reduction in background leakage current from 1.5×10^{-6} A at ambient conditions to 1.8×10^{-7} A under liquid-nitrogen cooling, accompanied by an increase in relative permittivity from 6.90 to 7.94. At 77 K, the fabricated component structures exhibited leakage currents of 2.01×10^{-5} and 1.84×10^{-5} A, with stable capacitance values of 38–45 and 30–32 pF, respectively. Collectively, these structural, morphological, optical, mechanical, and electrical characteristics demonstrate the potential of vacuum-sublimated CdTe and ZnS thin films for development of infrared photonic and optoelectronic devices.

In third experimental investigation, CdS nanoscale thin films were deposited on glass substrates at 1, 5 and 10 Å/s deposition rates by thermal evaporation process. XRD diffractogram indicate that the deposited CdS thin films have hexagonal structure with preferred orientation towards (002) plane and nearly stoichiometric composition. From XRD results, the calculated crystal structure parameters such as the crystallite size, microstrain and defect density were in the range of 20.4-14.7 nm, 7.74-10.62 and 2.3-4.52 $\times 10^{11}$ lines/cm^2, at 1, 5 and 10 Å/s deposition rates, respectively. The AFM images indicated that the film's rms surface roughnesses were 2.73 nm, 2.94 nm and 3.18 nm at 1, 5 and 10 Å/s, respectively. The SEM images indicated that the films were uniform, continuous and defect free. The EDX examination revealed that at 1 Å/s deposition rate the film was nearly stoichiometic. The optical band gaps were determined to be in the range of 2.37-2.43 eV. Nanoindentation tests evaluated the hardness, Young's modulus, creep behavior and strain rate of CdS films. Hardness evaluated to be 0.14-1.48 GPa, 0.15-2.46 GPa, and 0.21-2.55 GPa at 1,5 and 10 Å/s deposition rate, respectively for 20-50 μN load. The Young's modulus decreases 1-5 Å/s deposition rate and becomes almost constant 5-10 Å/s deposition rate at 70 μN loads. The characterization of CdS thin film recommends it as a favorable window layer in applications like photovoltaic, optoelectronic, thermoelectric and solar cells.

As the requirement for high-performance, low weight, and efficient Infrared devices continues to rise, the formation of good ohmic is a critical step in fabrication of IR detector arrays. Structural and adhesion properties of tin (Sn) and indium (In) films and their contact formation on the n-HgCdTe substrate are studied using the thermal evaporation technique in the fourth investigation work. The x-ray diffractogram indicated polycrystalline bcc phases with (200) orientation plane and (101) of β-Sn and indium films, respectively. The microstrain and dislocation densities were 4.10 and 9.10 x 10^{10} lines/cm^2 and 3.83 and 9.03 x 10^{10} lines/cm^2 of Sn and In, respectively. SEM examination indicated lumpy deposition of particle sizes from a few nanometers to microns in Sn film and uniform continuous films over the entire HgCdTe substrate with very small numbers of randomly oriented particles of 1-2 μm sizes in In film. EDS compositional analysis confirmed the presence of pure Sn and In films, respectively. Using AFM force microscopy in contact mode, adhesion force and thermodynamic adhesion work were 26.95 nN, 0.42 J/m^2(DMT), and 0.57

J/m^2(JKR) and 50.73 nN, 0.80 J/m^2(DMT), and 1.07 J/m^2 of In and Sn, respectively. Based on the transfer length method (TLM), the Sn/n-HgCdTe interface showed a higher specific contact resistance (ρ_c =2 x 10^{-2} Ωcm^2) with nearly ohmic behavior, but the In/n-HgCdTe specific contact resistance of ρ_c = 3 x 10^{-4} Ωcm^2 indicated that the In/n-HgCdTe interface exhibited ohmic features. Based on the experimental results, it was concluded that indium was the most suitable material to use for forming the ohmic n-contact in HgCdTe-based infrared detectors.

In fifth study, the HgCdTe surface had been grown with small layers of gold using thermal evaporation and an e-beam process. The thermal and e-beam evaporated gold film exhibits a cubic face-centered cubic (fcc) structure along the (111) orientation, possesses favorable The thermally evaporated Au film's crystalline structural parameters such as defect density, residual stress, and microstrain were 1.8 x 10^{15}-2.04 ×10^{15} lines/cm^2, 0.24–0.26 GPa, 4.74–4.99, respectively while e-beam Au film's defect density, residual stress, and microstrain were 1.27 x 10^{11}-1.79 x 10^{11} lines/cm^2, 0.02–0.31 GPa, and 3.94–4.67, respectively. The e-beam evaporated Au film had been the purest thin film with atomic 97.2 %. The e-beam gold film's uniformity, density, and extremely low roughness are confirmed by the AFM. The e-beam gold film's film-forming particles reached the appropriate lower grain size compared to the thermal gold film. The hardness and Young's modulus of the thermal and e-beam gold films were calculated to be 1.02–1.24 GPa & 90.53–102.02 GPa and 0.39–1.94 GPa & 76.31–155.20 GPa, respectively, at a load of 20–50 μN. The transmission line model (TLM) structure with pattern (Au/p-HgCdTe) was fabricated using the optimal gold films that were first established. In comparison to the thermally evaporated gold film (ρ_c =1.1 ×10^{-2} Ωcm^2), the e-beam evaporated TLM structure yielded a more Ohmic gold-contact with a small contact resistivity (ρ_c =7.3 ×10^{-3} Ωcm^2). Therefore, to manufacture HgCdTe infrared detectors, e-beam-evaporated gold thin films might be utilized to provide an attractive and suitable Ohmic p-contact.

Consequently, the enhanced characteristics of these thin films (CdTe, ZnS, CdS, Sn, In, and Cr-Au) establish them as strong potential for incorporation into advanced electro-optic devices, HgCdTe-based infrared detectors, and next-generation photovoltaics.

TABLE OF CONTENTS

Title	Page no.
Title page	i
Acknowledgement	iii
Candidate's declaration certificate	v
Certificate by supervisors	vi
Abstract	vii
Table of contents	x
List of tables	xv
List of figures	xvii
Chapter 1: Introduction	**1-7**
1.1 HgCdTe material/detector, growth, and uses	1
1.2 HgCdTe configuration and processing	2
1.3 Optoelectronic devices	5
1.4 Other semiconductor devices	5
1.5 Overview of the research work	6
Chapter 2: Literature review	**8-18**
2.1 Various methods of thin film deposition techniques	8
2.1.1 Sputtering	9
2.1.2 Pulse laser deposition	9
2.1.3 Thermal deposition	9
2.1.4 E-beam deposition	9
2.1.5 Spin coating deposition	10
2.1.6 Atomic layer deposition	10

2.1.7 Chemical bath deposition	10
2.1.8 Sol-gel deposition	10
2.2 Literature survey/review of CdTe, ZnS, CdS, Sn, In, and Au films	10
2.2.1 Role of CdTe and ZnS as passivant/insulating film	11
2.2.2 Role of CdS thin film as transparent layer	12
2.2.3 Role of Sn and In as n-contact	13
2.2.4 Role of gold film as p-contact	13
2.3 Inspiration and outcome of the research	18
Chapter 3: Experimental set up and characterization procedure	**19-38**
3.1 Preparation of sample	19
3.1.1 HgCdTe (MCT) sample cleaning procedure	19
3.1.2 Silicon sample cleaning procedure	20
3.2.2 Glass sample cleaning procedure	20
3.2 Approaches for thin film evaporation	20
3.2.1. Vacuum evaporation procedure and evaporation mechanism	21
3.2.2 Procedures and prerequisites for thin-film growth	22
3.3 Approaches of characterization for thin films	23
3.3.1 X-ray diffraction	24
3.3.2 Atomic force microscopy	25
3.3.3 FESEM and EDS	27
3.3.4 Nanoindentation analysis	29
3.3.5 Capacitance-voltage (C-V) and current-voltage (I-V) analysis	30
3.3.6 UV vis-spectrophotometer analysis	32
3.3.7 Ellipsometry	33

3.3.8 Multibeam optical stress sensor	35
3.3.9 Surface profiler	36
3.3.10 Microscopy	36
3.3.11 Eddy current method (sheet resistance measurement via. non-contact)	37
Chapter 4: Investigation of structural, morphological, and nano-mechanical properties of vacuum evaporated nanoscale CdTe and ZnS	**39-56**
4.1 Introduction	39
4.2 Materials and method	41
4.3 Results and discussion	43
4.3.1 Structural properties analysis by XRD	43
4.3.2 Morphological and topography analysis	47
4.3.3 Compositional analysis	49
4.3.4 Dektak surface profiler thickness measurement	50
4.3.5 Nano mechanical analysis	51
4.4 Conclusion	55
Chapter 5: Study of evaporated CdTe and ZnS thin film's crystallographic, morphological, nanomechanical, and electrical characteristics for optoelectronic devices	**57-86**
5.1 Introduction	57
5.2 Materials and method	59
5.3 Results and discussion	60
5.3.1 Crystallographic characteristics examination	60
5.3.2 Surface morphological examination	64
5.3.3 Elemental analysis	65
5.3.4 Topography analysis	69
5.3.5 Optical characteristics	74

5.3.6 Thin film stress measurement	75
5.5.7 Nano mechanical analysis	77
5.3.8 Electrical (dielectric) characteristics	80
5.4 Conclusion	86
Chapter 6: Comparative investigation of thermally evaporated nanoscale CdS film's structural, morphological, optical, and nanomechanical properties	**87-112**
6.1 Introduction	87
6.2 Materials and method	89
6.3 Results and discussion	91
6.3.1 Structural analysis	91
6.3.2 Morphological analysis	94
6.3.3 Compositional analysis	97
6.3.4 Thickness measurement	98
6.3.5 Optical properties analysis	99
6.3.6 Nanomechanical properties analysis	102
6.4 Conclusions	111
Chapter 7: Comparison of tin and indium thin film's structural, morphological, adhesion, electrical properties for ohmic contact in HgCdTe-based IR detectors	**113-135**
7.1 Introduction	113
7.2 Materials and method	115
7.3 Results and discussion	116
7.3.1 Crystallinity measurement	116
7.3.2 Surface morphology and compositional analysis	118
7.3.3 Surface topography analysis	120

7.3.4 Calculation of adhesion properties	122
7.3.5 Ellipsometry analysis	124
7.3.6Tin and indium film's adhesion test	124
7.3.7 Surface profiler thickness measurement	125
7.3.8 Electrical properties of tin and indium	125
7.3.8.1 Transfer length method calculation and analysis	127
7.4 Conclusion	132
Chapter 8: Study of nanoscale gold ohmic contact for perspective infrared detectors on a p-type HgCdTe	**136-165**
8.1 Introduction	136
8.2 Materials and method	138
8.3 Results and discussion	140
8.3.1 Crystal structure properties	140
8.3.2 Surface topography analysis	144
8.3.3 Morphology analysis	144
8.3.4 Compositional examination	148
8.3.5 Nanomechanical properties analysis	152
8.3.6 Electrical characteristics of gold film by TLM method	157
8.3.6.1 TLM structure measurement and analysis	158
8.4 Conclusion	165
Chapter 9: Conclusions and recommendations	**166-168**
Chapter 10: Scope of future research work	**169**
References	**170-197**
List of publications	**198**
Brief profile	**199**

LIST OF TABLES

Table No.	Title of table	Page No.
2.1	Use and function of different thin films, such as CdTe, ZnS, CdS, Sn, In, and gold film in the creation of MCT detector, optoelectronic device, and other semiconductor device	14
3.1	Vacuum evaporation parameter optimized for various thin films	23
4.1	Growth parameters of CdTe and ZnS films	42
4.2	Structural parameter examined commencing X-ray results of CdTe and ZnS film and assessment of standard vs experimental parameter	45
4.3	Crystalline parameters of CdTe and ZnS films determined meant for the favored plane (111)	46
4.4	Compositional values of CdTe and ZnS films on silicon substrate	50
5.1	Crystallographic parameters evaluated of cadmium telluride and zinc sulfide films for the dominated (111) plane	62
5.2	Elemental analysis of CdTe and ZnS thin films	69
5.3	AFM surface roughness of CdTe as well as ZnS films evaporation rates of 1, 5, and 10 Å/s	73
5.4	CdTe and ZnS film average stress measurement at 1,5 and 10 Å/s evaporation rate	76
6.1	Crystal structure parameters of CdS films at 1, 5 and 10 Å/s deposition rates	94
6.2	Surface roughness parameters of CdS thin films	96
6.3	Chemical composition of CdS thin film at 1, 5 and 10 Å/s deposition rates	98
7.1	Crystalline structural parameters of Sn and In for (200) and (101) preferred orientation planes	117
7.2	Roughness Table of Sn and In films	122

7.3	Maximum force, pull-off force, and thermodynamic adhesion-work based on DMT and JKR theories	123
7.4	Ellipsometry parameters of Sn and In films	124
7.5	The estimated values of electrical variables for the HgCdTe-based TLM structure made-up (sample D1 and D2; configuration: Sn/n-HgCdTe and In/n-HgCdTe interface)	128
8.1	Computed the gold film's structural properties for the dominating plane (111) using samples A1, A2, B1, and B2	142
8.2	Surface roughness of gold films evaporated by thermal and e-beam process	147
8.3	Compositional analysis of thermal and e-beam evaporated gold films	152
8.4	Electrical characteristics of the SampleA2 and Sample–B2 (transmission line model pattern: Au/p-HgCdTe) and gold layer amid enhanced rate of evaporation -12 Å/s) determined from its transfer line model calculation	154

LIST OF FIGURES

Figure No.	Title of figure	Page No.
1.1	To develop infrared detectors, an assortment of materials, the most common, often used, and mature/developed are employed	2
1.2	Diagram of IRFPA based on HgCdTe (MCT): (a) the detector and readout integrated circuit make up the hybrid structure of IRFPA (b) the single element detector array in cross-section	3
1.3	Process map for the development of an IR phtotodetector array based on HgCdTe	4
2.1	Variants of thin film deposition techniques	8
3.1	Experimental setup and growth mechanism process, which includes (a) mechanism schematic diagram (b) and a picture of the vacuum evaporation unit	22
3.2	Picture of the X-ray diffraction system to determine the crystal structure of films	24
3.3	Atomic force microscope equipment employed for assessing the topographical characteristics of the evaporated small layers/films	26
3.4	FESEM equipment attached with EDS photograph	28
3.5	Nanoindentation(a) schematic diagram (b) Load-displacement curve	29
3.6	Nanoindentation equipment picture	30
3.7	Cryo-prober (Make: Keithly) to evaluate the capacitance-voltage/current-voltage tests of evaporated metal-insulator-metal device (CdTe-ZnS), gold and indium based MIM	32
3.8	Ultra violet-visible spectrophotometer for evaluating the optical characteristics	33
3.9	Ellipsometer photograph to evaluate surface features of the small layer/film as well as HgCdTe (MCT) sample	34

3.10	Photograph of multibeam optical stress sensor (MOSS) to measure ex-situ stress	35
3.11	Surface profiler picture which utilized to measure the size (thickness) of thin films	36
3.12	Image of Nomarski microscope used to examine the sample surface	37
3.13	The conductive capacity and sheet resistance of thin layers/films were assessed using a contact-free sheet resistance evaluation procedure	38
4.1	(a)Schematic diagram of thermal evaporation process (b) schematic diagram of stack structure on silicon substrate (c) image of CdTe and ZnS film on silicon substrate	43
4.2	X-ray diffractogram of CdTe and ZnS film	47
4.3	SEM micrograph of deposited CdTe and ZnS thin films on Si substrate (a) image at 243X magnification (b) image at 138KX magnification (c) Cross-sectional view of deposited CdTe and ZnS thin films on Si substrate	48
4.4	The AFM images of ZnS film (a) 2-dimensional image (b) 3-dimensional image	49
4.5	EDX pattern of CdTe and ZnS thin films deposited on Si substrate (a) image at 1.21 KX (b) EDX spectrum	50
4.6	Dektak surface profiler step height (film thickness) of combined (CdTe and ZnS) thin film deposited on Si substrate	51
4.7	ZnS film's mechanical properties (a) Hardness (b) Young's modulus (c) Maximum depth	53
4.8	Indentation load impression images of ZnS film (a) at load of 50 µN (b) 70 µN (c) at load of 100 µN	54
4.9	Strain rate of ZnS thin film on Si substrate	55
4.10	Creep rate of ZnS thin film on Si substrate	55
5.1	The X-ray diffraction spectra of the cadmium telluride and zinc sulfide films. (a) CdTe film evaporation rate of 1 Å/s (b) CdTe film at 5 Å/s (c) CdTe film at 10 Å/s evaporation rate (d) ZnS film at 1	63

	Å/s evaporation rate (e) ZnS film at 5 Å/s evaporation rate (f) ZnS film at 10 Å/s evaporation rate	
5.2	SEM micrographs of evaporated cadmium telluride films (a) 1Å/s evaporation rate (b) 5 Å/s evaporation rate (c) evaporation rate of 10 Å/s (d) 1 Å/s evaporation rate (e) 5 Å/s evaporation rate (f) 10 Å/s evaporation rate	64
5.3	EDX pattern of CdTe film evaporation rate of 1 Å/s (a) EDX spectrum (b) SEM image with elemental % ; EDX pattern of CdTe thin film at 5 Å/s (c) EDX spectrum (d) SEM image with elemental %; EDX pattern of CdTe thin film at 10 Å/s (e) EDX spectrum (f) SEM image with elemental %; EDX pattern of ZnS thin film at 1 Å/s (g) EDX spectrum (h) SEM image with ZnS elemental %; EDX pattern of ZnS thin film at 5 Å/s (i) EDX spectrum (j) SEM image with ZnS elemental %; EDX pattern of ZnS thin film at 10 Å/s (k) EDX spectrum (l) SEM image with ZnS elemental %	66
5.4	The AFM pictures of CdTe film at 1 Å/s evaporation rate (a) 1D line diagram (b) 2-dimensional picture (c) 3-dimensional picture; The AFM pictures of CdTe film at 5 Å/s evaporation rate (d) 1D line diagram (e) 2-dimensional picture (f) 3-dimensional picture; The AFM pictures of CdTe film at 5 Å/s evaporation rate (g) 1D line diagram (h) 2-dimensional picture (i) 3-dimensional picture; The AFM pictures of ZnS film at 1 Å/s evaporation rate (j) 1D line diagram (k) 2-dimensional picture (l) 3-dimensional picture; The AFM pictures of ZnS film at 5 Å/s evaporation rate (m) 1D line diagram (n) 2-dimensional picture (o) 3-dimensional picture; The AFM pictures of ZnS film at 5 Å/s evaporation rate (m) 1D line diagram (n) 2-dimensional picture (o) 3-dimensional picture	70
5.5	Transmittance plot (a) CdTe film at 1, 5 and 10 Å /s evaporation rate (b) ZnS film at 1,5 and 10 Å/s evaporation rates	75
5.6	Stress measurements at 1, 5 and 10 Å/s evaporation rate (a) CdTe film (b) ZnS film	76
5.7	(a) CdTe film's hardness and Young's modulus at 1,5 and 10 angstrom per second evaporation rate for 80 μN load (b) ZnS film's hardness and Young's modulus at 1,5 and 10 angstrom per second evaporation rate for 90 μN load	78

5.8	Berkovich tip indent image CdTe film at load of 80 μN (a) 2-dimentsional image (b) 3-dimensional image	79
5.9	(a) CdTe film at 1 A/s evaporation rate indentation load : 140 μN , hold time: 5 (b) CdTe film 1, 5, and 10 Å/s evaporation rate indentation load : 80 μN , hold time : 10 s	79
5.10	(a) creep rate of zinc sulfide film evaporation rate of 1, 5, and 10 Å/s evaporation rate, hold time 5 s (b) ZnS film evaporation rate 1 Å/s , strain rate at 100 μN load, hold time: 0 s, 5 s and 10 s	80
5.11	Schematic diagram of plan view and cross-section view of the fabricated CdTe-ZnS MIM capacitors	81
5.12	I-V plot of CdTe-ZnS MIM capacitor (a) at room temperature (300 K) (b) low temperature (77 K)	83
5.13	C-V plot of metal insulator metal (MIM) of CdTe- ZnS film at 1 MHz for all circular capacitors (a) at room temperature (300 K) (capacitors-C01,C02,C03,C04,C05 &C06) (b) at low temperature (77 K) (capacitors-C01,C02,C03,C04,C05 &C06) (c) C-V plot of capacitor C08, C09, C11,C12 at room temperature and low temperature	83
5.14	Schematic diagrams of plan view and cross-section view of the fabricated CdTe /ZnS MIM capacitors	84
5.15	C-V plot (a) CdTe MIM for capacitors-C01,C 03, C04, C05, C06 &C08 for 1 MHz frequency at 77 K (b) ZnS MIM for capacitors-C01, C03, &C04 for 1 MHz frequency at 77 K	84
5.16	I-V plot (a) CdTe MIM at low temperature (77 K) (b) ZnS MIM at room temperature (77 K)	85
6.1	(a) Schematic diagram of thermal evaporation process (b) Schematic diagram of CdS thin film deposition on glass substrate	90
6.2	Photograph of CdS thin film on glass substrate (a) 1 Å/s deposition rate (b) 5 Å/s deposition rate (c) 10 Å/s deposition rate	91
6.3	XRD pattern of the CdS thin film (a) 1 Å/s deposition rate (b) 5 Å/s deposition rate (c) 10 Å/s deposition rate	94
6.4	AFM images of CdS thin film (a) 2D-image image at 1 Å /s deposition rate (b) 3D-image at 1 Å /s deposition rate (c) 2D-image image at 5	95

	Å /s deposition rate (d) 3D-image at 5 Å /s deposition rate (e) 2D-image image at 10 Å /s deposition rate (f) 3D-image image at 10 Å /s deposition rate	
6.5	SEM images of CdS thin film (a) 1 Å/s deposition rate (b) 5 Å/s deposition rate (c) 10 Å/s deposition rate	96
6.6	EDX spectra CdS thin film (a) 1 Å/s deposition rate (b) 5 Å/s deposition rate (c) 10 Å/s deposition rate	97
6.7	Dektak surface profiler CdS step-height (film thickness) measurement (a) 1 Å/s deposition rate (b) 5 Å/s deposition rate (c) 10 Å/s deposition rate	99
6.8	CdS thin films on glass for 1, 5 and 10 Å/s deposition rates (a) Transmittance vs wavelength (b) Absorbance vs wavelength	100
6.9	$(\alpha h\nu)^2$ versus hν graphs of CdS thin film (a) 1 Å/s deposition rate (b) 5 Å/s deposition rate (c) 10 Å/s deposition rate	101
6.10	Mechanical properties of CdS film at 20, 30, 40 and 50 μN load for 1 Å/s deposition rate; (b) Creep of CdS thin on glass at 1 Å/s deposition rate at 30 and 40 μN loads; (c) Strain rate of CdS film at 1 Å/s deposition rate	105
6.11	70 μN indentation load impression image of CdS film at 1 Å/s (a) 2-dimensional image (b) 3-dimensional image	107
6.12	Mechanical properties of CdS film at 20, 30, 40 and 50 μN load for 5 Å/s deposition rate; Creep of CdS thin on glass at 5 Å/s deposition rate at 30 and 40 μN loads; Strain rate of CdS film at 5 Å/s deposition rate	107
6.13	(a) Mechanical properties of CdS film at 20, 30, 40 and 50 μN load for 10 Å/s deposition rate; (b) Creep of CdS film at 10 Å/s deposition rate at 30 and 40 μN loads; (c) Strain rate of CdS film at 10 Å/s deposition rate	108
6.14	Comparison of mechanical properties of CdS films at 1,5 and 10 Å/s deposition rates	111
7.1	XRD pattern (a) tin film (b) indium film	118

7.2	SEM images of tin (a) SEM image at 4 KX magnification (b) Close view at 15KX magnification (c) EDS spectrum graph of tin	119
7.3	SEM images of indium (a) SEM image at 3.48 KX magnification (b) SEM image at 5.11 KX magnification (c) EDS spectrum graph of indium	123
7.4	AFM topography images of Sn and In film	125
7.5	AFM f-d curve of Sn on HgCdTe substrate	145
7.6	AFM f-d curve of In on HgCdTe substrate	126
7.7	Surface profiler thickness measurement graphs (a)Sn film thickness (step-height) (b) In film thickness (step-height)	128
7.8	Schematic representation of HgCdTe based TLM test structure. (a) two TLM structures (Configuration : Sn/n/p-HgCdTe & In/n/p-HgCdTe) of same dimensions are fabricated with eight pads each and each pad has same width and same length. The interpad spacings are 50, 100, 150, 200, 250, 300, 350, and 400 μm. (b) the cross-section of a part of the test structure	129
7.9	(a) The total resistance vs. interpad spacing curve of Tin-HgCdTe based on TLM structure (b) The total resistance vs. interpad spacing curve of indium-HgCdTe based on TLM structure	131
7.10	(a) I-V characteristics of tin TLM structure (b) I-V characteristics of indium TLM structure	131
8.1	Schematic diagram (a) thermal evaporation (b) e-beam evaporation (c) stack layer of chromium-gold on HgCdTe, CdZnTe surface	139
8.2	X-ray diffractogram of gold film (a) Sample A-1: 6 Å/s deposition rate by thermal (b) Sample A-2: 12 Å/s deposition rate by thermal (c) Sample B-1: 6 Å/s deposition rate by e-beam method (d) B-2: 12 Å/s deposition rate by e-beam method	141
8.3	Surface roughness image of gold film (a) thermal evaporation process sample A-1line diagram (b) thermal evaporation process sample A-1 2D image (c) thermal evaporation process sample A-1 3D image; Surface roughness image of gold film (d) thermal evaporation process sample A-2line diagram (e) thermal evaporation process sample A-2 2D image (f) thermal evaporation process sample A-2 3D image;	145

	Surface roughness image of gold film (g) e-beam evaporation process sample B-1line diagram (h) e-beam evaporation process sample B-1 2D image (i) e-beam evaporation process sample B-1 3D image; Surface roughness image of gold film (j) e-beam evaporation process sample B-1line diagram (k) e-beam evaporation process sample B-1 2D image (l) e-beam evaporation process sample B-1 3D image	
8.4	SEM micrograph of gold film (a) thermal evaporation Sample A-1 at 50 KX magnification (b) e-beam process Sample B-1 at 50 KX magnifications; SEM micrograph of gold film (c) thermal evaporation Sample A-1 at 75 KX magnification (d) e-beam process Sample B-1 at 75 KX magnifications; SEM micrograph of gold film (e) thermal evaporation Sample A-2 at 50 KX magnification (f) e-beam process Sample B-2 at 75 KX magnifications; SEM micrograph of gold film (g) thermal evaporation Sample A-2 at 100 KX magnification(h) e-beam process Sample B-2 at 100 KX magnifications	149
8.5	EDX spectrum graph of (a) thermally evaporated gold film Sample A-1 and (b) e-beam evaporated gold film Sample B-1 (c) thermally evaporated gold film Sample A-2 and (d) e-beam evaporated gold film Sample B-2	151
8.6	(a) Hardness plot of gold film e-beam evaporation and thermal evaporation (b) nanoindentation indent image of e-beam gold film at 40 μN load (c) nanoindentation indent image of thermal gold film at 40 μN load (d) Young's modulus plot of gold film e-beam evaporation and thermal evaporation (e) Maximum depth plot of gold films e-beam evaporation and thermal evaporation	153
8.7	Creep at maximum loads of 30, 40 and 50 μN load (a) thermal evaporation process (b) E-beam evaporation process	157
8.8	Effects of varying strain rate at a maximum load of 50 N for loading-unloading periods of 5 s and 20 s (a) thermal evaporation process (b) e-beam evaporation process	161
8.9	Layout of the transmission line model for the estimation of contact resistance. (a) Plan view: the structure has eight pads of same length and width. (b) Front view: the cross-section of one part of the test pattern is shown.	162

8.10	Total resistance vs spacing between pads graph for contact pads of gold film (transmission line model pattern: Au/p-HgCdTe) (a) thermally evaporated gold (b) e-beam evaporated gold.	163
8.11	I-V assessment for the e-beam as well as thermally evaporated contacts of the gold-based transfer line model (pattern: Au/p-HgCdTe)	164

CHAPTER 1

INTRODUCTION

A thin film is a small layer of material that ranges in thickness from a fraction of a nanometer to a few micrometers, runs infinitely in any two directions, but is limited in the third. A substance is said to form a thin film when evaporated on a solid surface by optimizing the condensation of elementary molecules or ions via physical evaporation technique or strong chemical interactions. While physical evaporation methods entail the heat evaporation of solid films through the vaporization or sputtering of materials from a source, chemical evaporation methods evaporate thin films on solid substrates through the reaction of chemical ingredients. The basic ideas of infrared materials and detectors, the history and current advancements of HgCdTe (MCT) infrared detector manufacturing technology, optoelectronic devices, and other semiconductor devices are all briefly included in this chapter. The uses as well as functions of several thin films, including CdTe, ZnS, CdS, tin, Indium, and Cr-Au, in the fabrication of semiconductor devices, and HgCdTe-based infrared detectors. It also discusses motivation, study outcomes, and a brief literature review and discussion of earlier experimental results.

1.1. HgCdTe material/detector, growth, and uses:

The environment provides strong transmissions at those wavelengths with negligible losses, making small wavelength infrared, midwavelength infrared, and long wavelength infrared the majority functional areas of infrared spectrum. Surveillance (movement alarms, invasion identification), industry monitoring (heating, flames identification), healthcare (thermography, medication inspection), and electronic goods (handheld switches, mechanized gates) are only handful of the numerous applications for infrared detectors. They are also crucial for transportation technologies (night time sensing), astrophysics (spotting cosmic entities), and ecological surveillance (chemical recognition, atmospheric condition, and ecosystem analysis) [1-8].

The first infrared detectors were created by Case in 1917 and are capable of converting radiation of infrared radiation (0.75 to1000 micrometer wavelength) towards the region of quantifiable electrical cue. As shown below, Fig. 1.1 shows a wide variety of familiar/admired materials for infrared detector [1-3,5-12].

In terms of material's foundational physical attributes (both semiconductor and optic), infrared sensor as well as focal plane array operating efficiency, and diverse color responsiveness and hyperspectral functionality, no material can surpass mercury cadmium telluride, despite the fact that researchers have investigated a number of proficient materials for infrared detector (illustrated by Fig. 1.1) that may be more cost-effective and manufactured [1, 4].

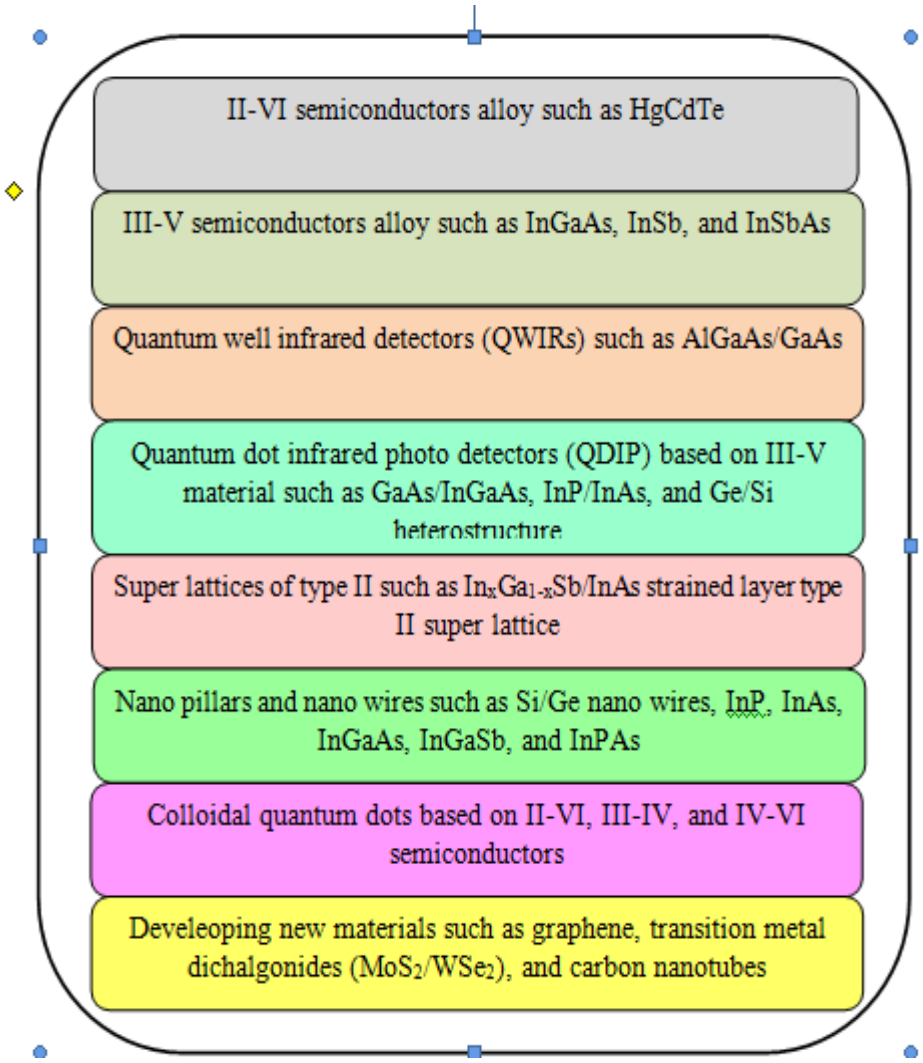

Figure 1.1 To develop infrared detectors, an assortment of materials, the most common, often used, and mature/developed are employed.

1.2. HgCdTe configuration and processing:

Due to their significant impedance along with minimal discharge of power, such light-detecting devices (p-n connection diodes) function under reverse bias conditions, infrared focal plane arrays (with their higher format and 2-dimensional structure) have been very helpful for visioning usages of soaring eminence. In addition to aforementioned benefits, the photosensor or photodetector have a few additional helpful characteristics that are essential for high-performance infrared photo detectors, features such as steady photo responsiveness throughout a broad range of photon-flush, little noise of $\frac{1}{f}$ type, as well as straightforward channelizing (multiplexing) with a readout integreated network (circuit) which rely on silicon [13-15].

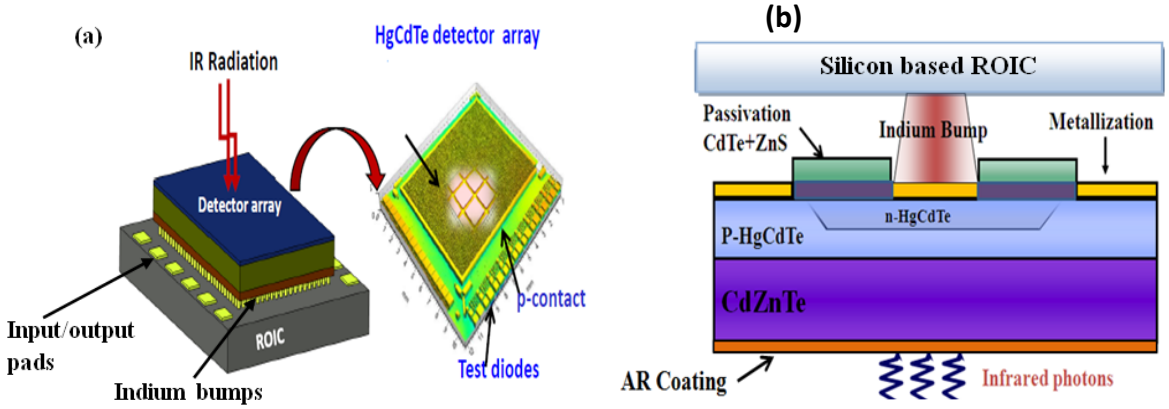

Figure 1.2 Diagram of IRFPA based on HgCdTe (MCT): (a) The detector and readout integrated circuit make up the hybrid structure of IRFPA. (b) The single element detector array in cross section.

The architecture of the infrared focal plane array built on mercury cadmium telluride, a two-dimensional hybrid configuration of the array of detector and readout integrated circuit, illustrated by Fig. 1.2. The flip-chip bonding approach connects the two components via an indium (In) bump array. This array of indium (In) bumps acts as a mechanical, thermal, and electrical interface between them. The incident photon flux with the lowest reflectance in the hybrid IRFPA's operation passes through the CdZnTe (CZT) face and into the detector's rear. After combinations of electrons and holes (electric impulses) are generated along the detector (p-n interface) and propagated to the data selector or multiplexer (readout integrated circuit) by the bump of indium, the resulting signal in terms of video is then received via the readout integrated circuit output driver. The best detector or readout integrated circuits associated with hybridization can be chosen by detectors with a back-illuminated configuration, and the output signal contains all the revelant data within the infrared focal plane array's field of vision of field. The field of view is defined as a solid-angle by a detector recognizes the sight or scene [4-5,14,15].

The low damage threshold of HgCdTe-based backside-illuminated devices makes processing them difficult and can significantly impact the detector's performance, homogeneity, and device yield. Growth of a epilayer of $Hg_{1-x}Cd_xTe$ (x varies from 0.29 to 0.31) of p-type on a analogues lattice structure of cadmium zinc telluride substrate initiates the infrared photodetector array fabrication process. Mercury cadmium telluride surface getting ready (to accomplish the specified size or thickness of 10 micrometer), passivation (to reduce dark current), coating with metal (contact of p-type), formation of p-n junctions (by implanting boron ions), etching of passivation, growth of indium bump (assimilation or integration of readout integrated circuit and array of detector, and formation of n-type contact by means of indium, etc. are some of the unit processing steps that make up this process as illustrated by Fig. 1.3 [2,5,10,15-16]. As a result, the array of infrared

photodetector fabricated on mercury cadmium telluride is essentially a configuration/pattern of multilayers of a substance, contact metal, and photon-absorbing material [2,5,13,15].

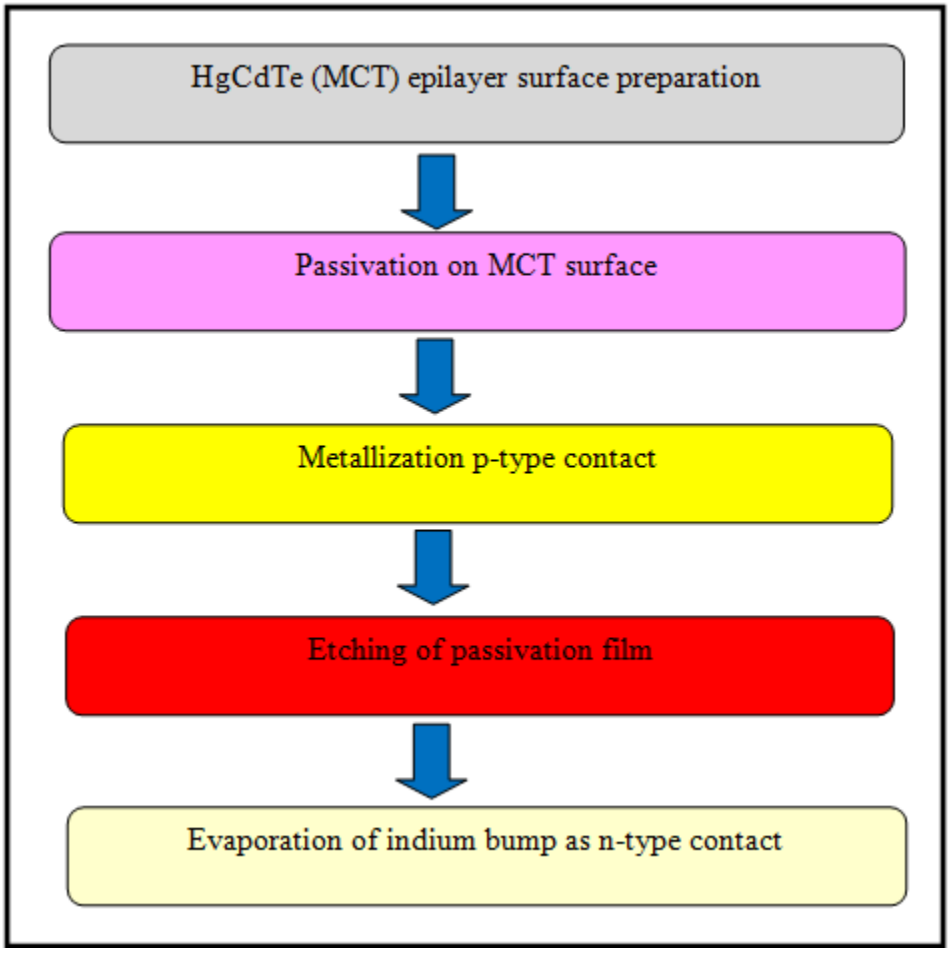

Figure 1.3 Process map for the development of an IR photodetector array based on HgCdTe.

The junction fabrication may be presented in depth because it plays a significant part in the development of the HgCdTe-IR detector. Upon mercury cadmium telluride epilayer, a p-n interface/junction can be created using a variety of techniques, including oxidation by thermal, ion etching of reactive type, milling by ion beam, ion implantation, and diffusion. However, the ion-implantation approach is the most practical and precise way to create a homo-junction (n/p) with the required junction depth because of its exact control over junction formation. Due to the extremely temperature of low degree °C (ambient temperature) as well as incidence-angle during the junction construction procedure, sensitive HgCdTe (MCT) material experiences very little to no heating. Particulate boron ions of precisely the correct energy or dosage are frequently unilaterally implanted into MCT crystal to produce Hg vacancies or defects that function as donor atoms. As a result, the p-type HgCdTe epilayer develops the region of n+/p type in photodetectors

because of its light mass/ slow diffusion, which reduces innate imperfections in lattice of MCT as well as causes nature alteration (the p-section turns hooked on an n+ section), and its capability to create a p-n interface amid a deepness of interface (junction) of one to 1.15 micrometers at the desired energy (35-145 eV/dose (10^{14} atoms/cm^2) [5,16-19].

1.3. Optoelectronic Devices: The inception of the diode of light emitting type and, shortly after, the semiconductor laser marked the beginning of the evolution of optoelectronic devices in the early 1960s. The fundamental concept of optoelectronics is the dimensional mechanical impact of light on electronic components particularly, semiconductors. Optoelectronics is defined as the electronic device that use light as source, identify, and regulate light is known as optoelectronic devices. Various semiconductor alloys deposited on substrates fabricate optoelectronic devices such as LEDs, photodiodes, solar cells, laser diodes, phototransistors, photomultiplier tubes etc. The effect of photovoltaic type, which propagates energy of photon type in energy (electrical type)/ photovoltage, is used by huge photodetectors. Modern photodetectors often rely on the photoconductive effect of the sensing materials, such as a light-dependent resistor whose resistance may be modified by the irradiation light, to quantify various aspects of light, such as wavelength, frequency, intensity, scattering, and polarization. Because of their vast surface area, rapid electron mobility, and distinctive optical characteristics, non-layered 2D materials hold prospects for the engineering of extremely sensitive optical sensors and photodetectors.

Certain II-VI semiconductors are used in optoelectronic devices based on cadmium telluride (CdTe), zinc sulfide (ZnS), and cadmium sulfide (CdS) because of their special optical and electrical characteristics. To improve device performance, the materials can be employed singly or in combination to create heterostructures and quantum dots. The best potential photovoltaic materials for low-cost, high-efficiency are Cd-based compounds like CdTe and CdS because of their appropriate band gaps and substantial absorption coefficients solar cells. Furthermore, Cd-based compounds like CdTe and CdZnTe have been used in radiation detectors due to their high atomic number. Because of these factors, methods for preparing the bulk single crystals and polycrystalline films that these devices require have greatly improved in recent decades, and optoelectronic devices have seen an abundance of beneficial purposes [20-26].

1.4. Other Semiconductor devices: The compact size of semiconductor devices is one of their main benefits. A typical edge-emitting laser, for instance, is roughly 500 x 250 x 100 m^2. A single semiconductor wafer may yield several thousand of these devices. Likewise, by just modifying the makeup of the different layers that make up the structure, semiconductor devices can be customized to satisfy the rigorous needs of an application. MEMS (micro-electromechanical systems) refer to the development of miniature electronics that integrate both electronics and mechanical elements. The fabrication of micro-electromechanical system originated from semiconductor devices fabrication procedures, utilizing fundamental steps such as material layer deposition, photolithographic patterning, and etching to achieve the desired geometries. Prominent semiconductor devices include photocoupler, thyristor, silicon-controlled-rectifier, and MOSFETs (metal-oxide semiconductor field effect transistor), etc.

1.5. Overview of the research work: The entire work, "*Fabrication and characterization of metal and insulating thin films for semiconductor devices*," is structured as follows and has been split up into ten chapters. In ***Chapter 1*** all of the scientific data pertaining to the discovery of infrared radiation, infrared materials and detectors and their uses, the history and current state of HgCdTe-based infrared detector technology (HgCdTe as IR detector/material: unique properties, growth technology, progress, and limitations), as well as the technology's structure, operation, and fabrication are covered. ***Chapter 2*** deals with brief description/literature review of the distinct physical vapor deposition and chemical vapor deposition techniques is explained. The chapter also includes a brief literature overview of all the thin films used in the manufacture of HgCdTe-based infrared detectors and other semiconductor devices, including CdTe, ZnS, CdS, tin, Indium, and Cr-Au film-layer. This chapter also includes the findings and the rationale for the intended study.
An outline of the experimental and characterization methods used to achieve the thesis's stated goals is provided *in* ***Chapter 3***. Sample preparation, various deposition techniques to grow the suggested thin films, and a thorough explanation of the applied thermal evaporation technique (experimental setup and thin film growth mechanism) are all included in the experimental techniques/methodology. X-ray diffraction (XRD) measurement, atomic force microscopy (AFM), scanning electron microscopy (SEM), energy-dispersive X-ray analysis (EDX), nanoindentation, UV-vis spectrophotometer, capacitance-voltage (C-V)/current-voltage (I-V) measurements, surface profiler (Dektak), ellipsometry, multibeam optical stress sensor (MOSS), microscopy, and non-contact sheet resistance measurement are the primary characterization techniques that were used to assess the characteristics of evaporated thin films. This chapter has a detailed designation of each of these characterization approaches.
The crystalline, morphological, and nanomechanical characteristics of vacuum evaporated stack layers of cadmium telluride (CdTe) and zinc sulfide (ZnS) films on silicon has been evaluated in ***chapter 4***. XRD was implemented to evaluate the crystalline characteristics of stack layers of CdTe and ZnS films. The examination using field emission electron microscopy (FESEM) indicated that the film's structure was uniform, compact, and free from defects. AFM studies have indicated homogenous and even layer (top ZnS layer) with surface roughness of 0.96 nm. Hardness, Young's modulus, strain rate, and creep behavior of top layer (ZnS) had been evaluated by nanoindentation. The outcome of the experiments confirmed the fact that the CdTe and ZnS films evaporated by vacuum evaporation approach are optimal for the manufacture of optoelectronic devices in infrared wavelength scale. *Portion of the current investigation has been published in the journal **Optical Materials 154 (2024) 115764**.
In ***chapter 5*** CdTe and ZnS films evaporated at different deposition rates examined for crystallographic, morphological, topographical, nanomechanical, and electrical (dielectic) characteristics. The x-ray diffractogram exhibited a strong multi-crystalline fcc crystal structure along (111) preferential plane for CdTe and ZnS films; the crystalline parameters were evaluated for CdTe and ZnS film; scanning electron microscopy (SEM) assessment revealed a evenly distributed, compact, and defect-free arrangement of the CdTe and ZnS films at low evaporation

rate; elemental analysis evaluated that the CdTe and ZnS films were stoichiometric. Nanoindentation evaluated the creep, strain rate, hardeness and Young's modulus of CdTe and ZnS films. Multibeam optical stress sensor evaluated the ex-situ stress developed in the evaporated CdTe and ZnS films. By fabricating metal-insulator-metal (MIM) structures and using capacitance-voltage as well as current-voltage measurement to assess the capacitance and dielectric constant, the dielectric characteristics of the CdTe and ZnS films were studied. The findings of the assessment of the suggested the compatibility that the CdTe and ZnS films are acceptable for the fabrication of optoelectronic devices.

In ***chapter 6*** the crystalline, morphological, elemental analysis, optical, and nanomechanical characteristics of CdS films at 1,5, and 10 Å/s evaporation rates on glass surface were examined by XRD, AFM, SEM, EDX, UV vis-spectrophotometer, and nanoindentation. Hence comprehensive findings from experiments of crystalline, morphological, optical, and mechanical features promise CdS film at 1 Å/s evaporation rate was having enormous opportunity in the light emitting diodes, photon devices applications and insight layer for solar cells. * Portion of the study has been published in journal of **Molecular structure 1324 (2025) 140850**.

In ***chapter 7*** the internal structure and adhesion characteristics of evaporated tin and indium films along with their interface formation n-type HgCdTe substrate are examined employing utilizing XRD, SEM, EDS, and AFM. The findings reveal that the evaporated indium layer/film that was utilized to develop indium film (in the In/n-type HgCdTe arrangement/configuration) for the transfer length method structure is desirable. The evolved transfer length method structures have been examined with I-V/resistance studies. The obtained electrical characteristics of the In/HgCdTe interface show low contact resistance and ohmic response. This leads us to figure out that indium is the most feasible substance for creating an n-type contact on an infrared photodetector based on HgCdTe through vacuum evaporation. *Part of the investigation has been published in the journal **Materials engineering and performance, 34 (2025) 18502-18515**.

In ***chapter 8*** the crystallographic, elemental analysis, topographical, nanomechanical, and electrical features of the thermally evaporated and e-beam evaporated gold layers/films on p-type HgCdTe have been addressed. The newly formed gold films were evaluated using a variety of characterization procedures such as XRD, AFM, SEM, EDS, and nanoindentation. In order to ascertain the electrical characteristics of the gold films, current-voltage/resistance study was conducted on the constructed transmission line model (TLM) structure to evaluate the contact resistivity of gold-metal contacts (thermally evaporated and e-beam evaporated). Therefore, a comparison analysis is done between thermally evaporated and e-beam evaporated gold films to achieve a compatible and efficient ohmic contact metal for the fabrication of HgCdTe infrared photodetectors. *Part of the study has been published in the journal **Optics communications, 604 (2026) 132846.** Thus, the main conclusions of the thesis are summed up in ***chapter 9***. Thorough comprehension of the features of different thin films, their function in optoelectronic devices, HgCdTe-based infrared detectors and other semiconductor devices technologies, the relationship between device performance and the various thin film properties, and, lastly, the work's potential future directions in ***chapter 10***.

CHAPTER 2

LITERARURE REVIEW

Thin layers/films are a crucial aspect of cutting-edge technology. Thin film coatings may enhance an object's characteristics when they are applied to its surface, such as making it more durable, altering its structural, morphological, electrical conductivity, or enhancing its optical characteristics. The study of distinct thin film deposition techniques is very critical, as deposition techniques control/modify the film's crystallographic structure, morphology, topography, optical, nanomechanical, and electrical characteristics etc., which are essential for the fabrication of various semiconductor devices.

2.1 Various methods of thin film deposition techniques:

Depending on the intended usage and manufacturing specifications, many technologies/techniques are used to deposit thin films. Physical vapor deposition and chemical vapor deposition are the two primary kinds of deposition processes. Physical vapor deposition is appropriate for metals and alloys because it physically transfer materials under vacuum, when vaporized materials condense onto the substrate. On the other hand, chemical vapor deposition, which is appropriate for complex chemicals and polymers, liverages chemical reactions at elevated temperatures to deposit molecules from a vapor phase. While CVD is excellent at producing homogenous layers over complex forms, PVD yields exact control over the thickness and purity. The required material qualities and the particular requirements of the application determine which of the PVD and CVD is optimal. Distinct PVD and CVD thin film deposition techniques are shown in Fig.2.1.

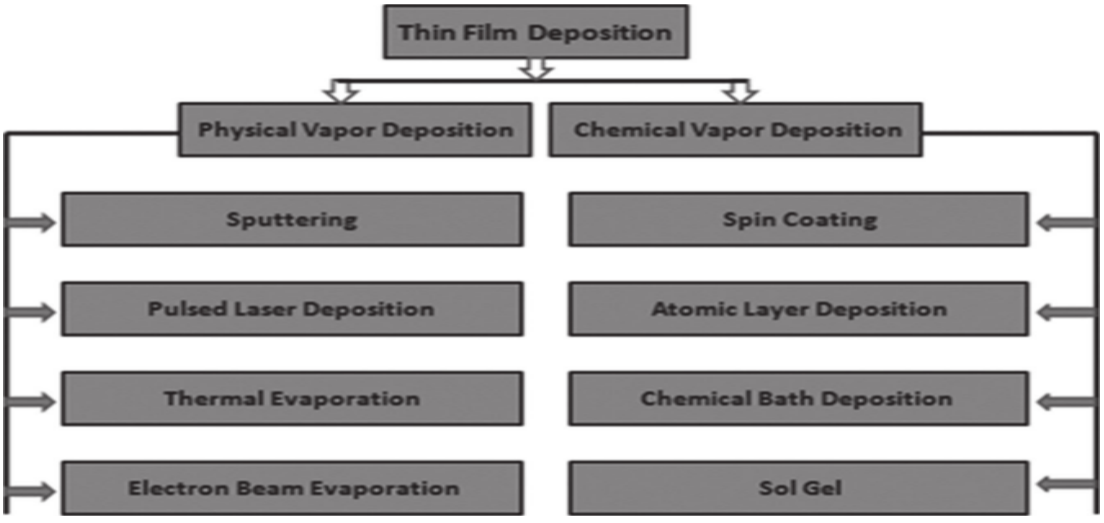

Figure 2.1 Variants of thin film deposition techniques

2.1.1. Sputtering: Thin film deposition uses phenomena called sputtering to eject tiny solid material particles from their surface. By using energetic to attack the solid material, this ejection is accomplished. The thin film layer is subsequently created by depositing the particles in the target materials. Sputtering occurs in a chamber with a vacuum pump continuously operating to evacuate the air, just like other deposition techniques [27].

In magnetron sputtering, the chamber is constantly populated with an inert gas, often argon. Gaseous plasma is produced close to the target's magnetic field by the high voltage. Argon gas atoms, argon ions, and free electrons are all present in the plasma. More positively charged ions are constantly produced as electrons strike argon atoms. The positively charged ions are drawn to the negatively charged sputtering target. A thin layer of the target employed on the magnetron is produced when the expelled atoms land on the substrate's surface.

DC sputtering phenomenon is a relatively simple deposition procedure where the substrate may be at positive, ground or drifiting potential while the target is at high negative voltage. A flash discharge with several sectors such as cathode glow, Crook's dark space, Faraday dark space, negative glow, positive column, anode glow, and anode dark space is created when sufficiently high voltage is put between anode and cathode with gas in it [28].

2.1.2 Pulse laser deposition: One kind of evaporation method that uses laser pulses to evaporate the target material is called pulse laser deposition. As a result, a plasma plume created which deposits onto the substrate to form the thin film. Due to numerous factors involved such as wavelength, ambient gas pressure, energy, and duration of pulse, improving this process can take more time and effort than other approaches. However, its advantages comprise rapid deposition speeds, an intitutive procedure, and no strands for simpler maintenance [29-30].

2.1.3 Thermal/vacuum evaporation: In a vacuum, the source substance evaporates. Vapor particles can move straight to the target item (substrate) thanks to the vacuum, where they condense back into a solid state. In order to obtain the elevated melting temperatures of the corresponding metals, a massive DC current was fed through a resistive filament or boat, where the metal evaporated and reached the substrate under high vacuum conditions. The charge emits vapor when the crucible or heater heats up, which reaches the substrate and adheres to its surface. Evaporated particles can reach the surface of the target immediately under tremendous vacuum (a prolonged mean free pathway) without running into the underlying gas [31].

2.1.4. Electron beam evaporation: The intended substance is evaporated in this procedure by an enormously accelerated electron beam. The thin layer/film is produced by the atoms created when the evaporated substance is transferred onto the substance. This technique uses a filament to create an intense electron beam that is directed through electric and magnetic fields to strike the target and evaporated it in a vacuum. Electron beam evaporated thin layers/films that are homogeneous and of excellent grade [32].

2.1.5. Spin Coating: Usually, a small puddle aqueous resin is deposited in the center of a substrate, and the substrate is then spun at rapid pace. The centripetal force and the liquid's surface tension combine to provide an even coating when a material as well as solvent solution is spun at enormous pace. Spin coating deposits layer with a thickness from nanometers to few micrometers after any leftover solvent has evaporated. The deposition process can be divided into four sections: (a) deposition (b) spin up (c) spin off (d) evaporation. The microscopic manufacturing of functional oxide layers is a common application for the spin coating process [33-34].

2.1.6. Atomic layer deposition: It enables the layer-by-layer deposition of thin layers/films and is based on the self-regulating interactions involving two gaseous precursors. Every gas responds in a fashion that causes the electrically charged surface to become completely filled, which stops the reaction. The outermost layer may interact with the distinct gas in an identical manner. An inert gas, such as nitrogen or argon is used to flush the chamber within the responses of these gases. The nanofabrication procedures for small scale electronic technologies have made great use of it [35-37].

2.1.7. Chemical bath deposition: Despite using an electric field, layers/films can be developed on metallic or non-metallic surfaces by immersing them in suitable metallic salt solvents. Homogenous chemical processes, often the reduction of metal ions in suspension via a reducing agent, can result in deposition. This is referred to as electroless deposition if it takes place on catalyst surface. This approach has provided the most appealing procedure for the manufacture of thin films of metal oxides, metallic spinal type oxides, binary chalcogenides, ternary chalgonides, superconducting oxides etc. because of its high productivity on a wide scale and ease of use [38-39].

2.1.8. Sol-gel deposition: It is a chemical layering technique that produces metal hydroxides through hydrolysis, condensation, and drying process. These hydroxides form a 3D gel that can be dried to generate aerogel or xerogel. This process includes both aqueous and non-aqueous sol-gel procedures, each of which uses a distinct solvent to help metal oxide layers devlop. The interfacial tensions, which seem to be vital, are influenced by the majority of process parameters. The nucleation kinetics are linked to the regulation of the crystal structure [40].

2.2. Literature survey/review of CdTe, ZnS, CdS, Sn, In, and Au films: The HgCdTe based infrared detectors, optoelectric devices, and other semiconductor devices can be developed by utilizing the optimized passivation layers, transparent/ window layer, metallization n-type contact, and metallization p-type contact layer/film; which minimize all the causes of poor and lower performance of above-mentioned devices. The above-mentioned semiconductor devices can be fabricated by utilizing CdTe, ZnS, CdS, Sn, In, and Au films in thickness varying from few nanometers to micrometers depending upon the functionality of the evaporated films which may be evaporated as a single layer or stack of two or more layers. Thin layers/films are double dimensional coatings of liquid or solid substances that are evaporated on the surface of substrate as a result of condensation of microscopic, tiny mass or charged species one at a time. The higher

surface area to volume proportion of thin layers/films as opposed to bulk substances is what gives them their unique characteristics. Substantial surface area to volume proportions, peculiar crystallographic arrangement, distinct imperfect configurations, outer layer and interfacial implications, improved optics propagation, and mechanical rigidity represent a few of the special characteristics of thin layers/films.

2.2.1. CdTe and ZnS as passivant: The high performance HgCdTe (MCT) based infrared detector, optoelectronic device and other semiconductor device can be fabricated by using a suitable passivation film of appropriate thickness. A huge no of fixed charges, charges of oxides, interface state as well as defects can fabricate MCT detector and other semiconductor device with low functioning with regard to huge surface leakage current leakage from surface or unwavering current of dark-current type along with poor electrical insulation of metal-substrate interface, more recombination-generation centers, declined thermal stability, and reasonably challenging chemical passivation of the p-type HgCdTe (MCT) and other semiconductor device. Although MCT detector, optoelectronic device and other semiconductor device have been developed by using a diversity of passivation materials, together with native films for instance sulfides, fluorides as well as oxides etc. and evaporated dielectric films such as cadmium telluride, zinc sulfide, CdTe/ZnS, silicon oxide, polymer, Si_3N_4, along with in-situ evaporated materials of having large band gap (cadmium telluride in addition to cadmium zinc telluride), CdTe and ZnS are commonly used passivant materials for fabrication of semiconductor devices. Both CdTe and ZnS have polycrystalline face centered cubic (fcc) structure (lattice constant 5.40 angstrom (CdTe) & lattice constant 6.40 angstrom (ZnS)), these are excellent passivation materials with almost flawless features such as electric inertness, insulating dielectric material, low surface leakage current and dark current density required for ideal band bending close to the surface, adaptability regarding chemical handling used for fabrication of device, optimal thermodynamic and chemical durability, low stress, sound mechanical characteristics, and well-defined crystalline characteristics. CdTe and ZnS may therefore be a suitable, efficient passivation layer or film for obtaining high performance infrared detector, optoelctronic device and other semiconductor devices [41-46]. The CdTe thin film vacuum evaporated at low evaporation rate such as 1 Å/s possessed the better crystalline structure and morphology compared to film evaporated at higher evaporation rates. The CdTe film possessed the near stoichiometric elemental composition compared to films evaporated at higher evaporation rates [23]. The highest layer thickness evaporated is at the substrate's center, while the minimal layer thickness evaporated is at the substrate's farthest point, according to a time-dependent backward difference formula solver model of a thin film of CdTe created by thermal evaporation. Because of the substrate's huge dimensions, the utmost thickness deviation across the substrate in this instance is fourteen percentages. It is determined that the heat flow and mass transfer rate are, respectively, 1.7 W s and 1.9×10^{-8} kg/s [24].

2.2.2 Role of cadmium sulfide (CdS): The bandgap of CdS is around 2.42 eV, thus rendering it a direct bandgap semiconductor. It has served as a fundamental component in developing the development of photosensitive and photovoltaic devices. In cadmium telluride-based solar cells made up of thin film, cadmium sulfide is typically employed the same as the transparent layer or

window layer, triggering an indispensable p-n heterojunction. CdS devices consistently referred to as photocells or photoresistors, customize their electrical resistance in response to the amount of incident light. For light-sensing applications, such as automated street lights, this makes them worthwhile [47-48].

However, the semiconducting material CdS, which is widely available and falls into the II–VI materials/semiconductors of direct band of 2.4 electron volt (eV), possesses remarkable thermal and chemical stabilities. CdS is a notable material for a variety of optoelectronic applications because of its superior photon absorption [49]. The hexagonal phase of CdS along (002) orientation, which emerged by thermal evaporation, has pleasant mechanical, optical, morphological, and crystallographic characteristics, making it practically adequate for use as a transparent layer in optical semiconductors [50]. Vacuum evaporation at low substrate temperatures can generate CdS layers with low resistivity and high transmittance, which can be implemented strategically numerous usages like LED, solar cell, and semiconductors in inherently [51]. For deployment in the fabrication of optoelectronic devices, thin films of cadmium sulfide (CdS) encapsulating nanostructures of the same composition as the active layer were created and examined. Soft chemistry was used to integrate cadmium sulfide nanoparticles and small layers at temperatures of low degree. The precipitation process was used to create the CdS nanoparticles, while cadmium sulfide thin layer was coated by CBD process. By adding CdS nanoparticles to CdS thin films that were formed using CBD, a homojunction was finished. The cadmium sulfide nanoparticles were prepared by a process called spin coating, and the impact of heat annealing on the films that were coated was assessed [52].

Most specifically, n-type CdS thin films are frequently employed like transparent layer or window layer in the configuration of heterojunction type of CuInSe and solar cells made up of p-type cadmium telluride. To have the capability able to evaporate cadmium sulfide thin layers having appropriate electro-optic qualities for solar usages, numerous investigations have been attempted. Several features of the CdS films are necessary for this purpose :(a) Not large bulky to promote incorporation in cadmium telluride or copper indium selenide layer of absorption, but relatively high transparency. (b) Not excessively thin to prevent short circuiting. (c) Higher photoconductivity to maintain the solar cell's spectrum response and relatively high conductivity to lower electrical solar cell losses [53] Using pure crystal as the evaporated targets, CdS thin films have been grown at three distinct temperatures using vacuum thermal evaporation at 10^{-6} mbar. In order to fabricate optoelectronic devices, the influence temperature of substrate on crystallographic, optical, and electrical characteristics was essential to investigate [54].

2.2.3. Role of tin (Sn) and indium (In) as n-contact: High-performance MCT based detector, optoelectronic, and other semiconductor device require highest connectivity yields of detector-readout integrated circuit (ROIC) and ohmic n-contact cration. Contact formation uses a variety of materials including copper/nickel/tin, titanium/platinum/gold/indium, titanium/platinum/gold/Ep/indium, tin and indium. With their unique properties, including low temperature invariance, suitable mechanical properties, indium is one of particularly compatible

and prevalent interconnection materials for the detector (sensor)-readout integrated circuit interface due to its adhesion, electrical characteristics, high ductility, low melting point (Sn : 135 °C, In : 155 °C), remarkable flexibility amid straightforward cold-pressing, ease of creating minute/compact (dense) interconnection, and ideal TCE (thermal coefficient of expansion) disparity. In the (101) orientation of indium film evaporated by thermal evaporation, the tetragonal bcc phase exhibited a low-surface-roughness, defect-free film. The thermodynamic adhesion-work and pull-off force or surface adhesion force (critical force) of the indium film were both low. The film's coefficient of friction and friction force were both low. Evaporated film is therefore compatible with tribological applications as well. On the detector-ROIC, it has been used to create indium bumps, which are circular columns of approximate height of five to six micrometers. The infrared sensor/detector along with readout integrated circuit are interconnected using binding via flip-chip approach, in which the developed indium pillars on the infrared sensor/detector as well as ROIC serve as contact of mechanical and electrical type. The readout electronics with indium bumps may multiplex the signals, which come from lakhs/millions of pixels, to a finite no of yield lines. Additionally, the indium contacts greatly make straightforward the abridge flanked by system electronics and low temperature bounded by vacuum infrared sensor/detector [55-60]. The optimal and efficiency of the infrared detector/sensing element and other semiconductor devices depend upon the interface or contact of ohmic type, which has resistance of lower grade/power dissipation of smallest, thermal stability and a low noise level. Ohmic electrical contacts are formed on n-HgCdTe (MCT) based infrared photodectors using a variety of solo, binary, and triplicate stacks of metal, including aluminum, titanium, gold, nickel, chromium, indium, molybdenum/gold, molybdenum/indium, mercury telluride/indium/gold, and platinum/titanium/gold. Indium is the widely recognized customary substance that may make an ohmic interface or contact of n-type (using low-temperature evaporation/excellent adhesion stack or layer and noise level of lower range) for particular diodes of the HgCdTe-centered sensor array and other semiconductor devices, to establish connections with the outside environment. Thus, so as to realize high functioning/reliability of mercury cadmium telluride detectors or other semiconductor device, indium metal can produce contact of compact/utmost nexus upon MCT-sensor/silicon-readout integrated circuit, and ohmic contact of n-type to MCT or other semiconductor devices. The tin and indium thin layers evaporated by thermal evaporation method on silicon surface. The thermally evaporated films observed good crystalline structure, uniform grain size, and defect free films after their structural and morphological characteristics examination [55-57, 61]

2.2.4. Role of gold film as p-contact: By developing an ohmic metal-contact/mercury cadmium telluride interface that has reduced resistance against contact, straight current-voltage characteristics and good repeatability, high-performance/reliable infrared photodetectors that can meet present and future technological requirements can be produced. Due to a number of problems, including prolonged thermodynamics suspensibility, 1/f noise, homogeneity, consistency at elevated temperatures of use, as well as contact surface purity, ohmic contact creation on MCT or other semiconductors is quite difficult [8,13,16,20,44, 62]. The sensitive nature of p-type HgCdTe

(MCT) material (weak Hg-Te bond) and the stability of the material with respect to time and temperature make ohmic contact formation-which exhibits non-ohmic behavior- relatively more troublesome. MCT based infrared detectors use a variety of metals, including aluminum, /copper/titanium/silver/platinium/palladium/germanium/tin/mercury telluride/chromium, and gold [9,16,20,62], to create contacts of p-type or usual contacts. Cu/Ag/Pt/Pd/Ge, and Sb all show rectifying behavior but HgTe can form an ohmic contact, which is not very cost-effective because it requires expensive, complex growth equipment, for instance metal-organic chemical vapor deposition (MOCVD) as well as molecular beam epitaxy (MBE) techniques. Additionally, the metals Sn, Au, Cr, and Al have been used to create p-contact that is almost ohmic. Gold is the most distinctive of these metals [2,19,62-63] due to its high electrical conductivity, noble status, anticorrosive properties that prevent oxidation, softness, and strong ductility. These characteristics make gold an excellent choice for establishing an ohmic p-contact on MCT-based detector and other semiconductor devices. The infrared photodetector's and other semiconductor devices exceptional performance is due to created ohmic contact, which provides a low-signal to noise ratio and little power dissipation. The simulation of gold film of nanometer thickness using a backward difference formula solver to determine the dimensions of coating, evaporated mass upon substrate, and rate of mass propagated using a model based upon time dependence. At a temperature of 2000K, Au is vacuum deposited via a resistively heated evaporator source onto a surface that is preset [64].

HgCdTe-type infrared detector, optoelectronic devices, and other semiconductor devices are developed utilizing a variety of thin layers/films, notably CdTe-ZnS (passivation), CdS (optical window layer), Sn/In (as n-type region), and Cr-gold (as p-type region). Experts have implemented the aforementioned thin films in HgCdTe-type infrared detector, optoelectronic devices, and other semiconductor devices manufacturing methodologies during the past few decades. Table 2.1 features a quick overview of the literature of all thin layers/films, including CdTe, ZnS, CdS, Sn, In, and Cr-Au.

Table 2.1 shows the use and function of different thin films, such as CdTe, ZnS, CdS, Sn, In, and gold film, in the creation of MCT detector, optoelectronic device and other semiconductor devices.

Name of the evaporated thin film	Use/goal of the film and the characteristics examined	Characterization technique	Substrate	Method of deposition	References
CdTe	Structural, morphological, optical	XRD, AFM, UV-spectrophotometer	Si, glass	Thermal evaporation	[65]

CdTe	Structural, morphological, optical	XRD, AFM, UV spectrophotometer	Glass	Thermal evaporation	[66]
CdTe	Structural, morphological, optical	XRD, TEM, UV-spectrophotometer	Glass	Thermal evaporation	[67]
CdTe	Structural, morphological, optical	XRD, SEM, EDX, UV-vis spectrophotometer	Glass	Thermal evaporation	[68]
CdTe	Structural, morphological, mechanical, electrical	XRD, SEM, force modulation microscopy-AFM	Glass	Close space sublimation	[69]
CdTe	Structural, morphological, mechanical	XRD, SEM, Nanoindentation	Glass	Thermal evaporation	[70]
CdTe	Structural, morphological, optical, stress	SEM, FTIR, Raman spectroscopy	Si	Close space sublimation	[71]
CdTe	Structural, morphological, optical, passivation	SEM, EDS, FTIR, I-V measurement	HgCdTe	Sputtering	[72]
ZnS	Structural,morphological,(Passivation) electrical	XRD, SEM, I-V measurement	HgCdTe	Thermal evaporation	[73-74]
ZnS	Structural, morphological, (Passivation) electrical	XRD, SEM, I-V measurement	HgCdTe	Thermal evaporation	[20]
ZnS	Structural, morphological, (Passivation) electrical	XRD, SEM, I-V measurement	HgCdTe	Thermal evaporation	[75]
ZnS	Structural, morphological, (Passivation) electrical	XRD, SEM, I-V measurement	HgCdTe	Thermal evaporation	[76]

ZnS	Structural, morphological, (Passivation) electrical	XRD, SEM, I-V measurement	HgCdTe	Thermal evaporation	[77]
ZnS	Structural, morphological, mechanical	AFM, nanoindentation	Si	Pulse laser vaporization	[78]
CdS	Structural, morphological, optical	XRD, SEM, AFM, UV-vis spectrophotometer	Glass	Thermal evaporation	[79]
CdS	Structural, morphological, optical	XRD, SEM, AFM, UV-vis spectrophotometer	Glass	Thermal evaporation	[80]
CdS	Structural, morphological, optical	XRD, SEM, AFM, UV-vis spectrophotometer	Glass	Chemical Bath Deposition	[81]
CdS	Structural, morphological, optical	XRD, SEM, AFM, UV-vis spectrophotometer	Si	Chemical Bath Deposition	[82]
CdS	Structural, morphological, optical	XRD, SEM, AFM, UV-vis spectrophotometer	Glass	Electrochemical	[83]
Sn	Structural, morphological, topographical	XRD, SEM, EDS, AFM,Surface profiler	Si	Thermal evaporation	[84]
Sn	Structural, morphological, topographical, optical	XRD, SEM, EDS, AFM, spectroscopic ellipsometry	Al_2O_3 coated Si	Thermal evaporation	[85]
Sn	Electrical (n-type contact)	I-V measurement	HgCdTe	Thermal evaporation	[86]
In	Indium bump, morphological, microstructural	XRD, SEM, AFM	Sapphire	Thermal evaporation	[87]

In	Indium morphological, compositional	XRD, SEM, EDX	Si	Electroplating	[88]
In	Electrical (n-type contact),morophological, compositional	SEM, EDX, I-V measurement	CdTe	Thermal evaporation	[89]
In	Electrical (n-type contact),morphological, compositional	SEM, EDX, I-V measurement	HgCdTe	Thermal evaporation	[57]
In	Indium bump, microstructural	XRD, I-V measurement	HgCdTe	Thermal evaporation	[58]
molybdenum/gold	Electrical (p-type contact)	I-V measurement	HgCdTe	Thermal evaporation	[90]
Au	Electrical (p-type contact)	I-V measurement	HgCdTe	Thermal evaporation	[62]
Au	Electrical (p-type), compositional	I-V measurement	HgCdTe	Vacuum evaporation	[94]
titanium/platinum/gold	Electrical (p-type contact)	I-V measurement	HgCdTe	Vacuum evaporation	[91]
Au	Electrical (p-type contact), elemental analysis	I-V measurement	HgCdTe	Electroless deposition	[92]
Au	Electrical (p-type contact), elemental analysis	I-V measurement	HgCdTe	Electroless/Thermal deposition	[93]

While every critical characteristic of the aforementioned thin layers/films of materials (CdTe-ZnS passivation, CdS optical window layer, Sn/In n-type ohmic contact, and Cr-Au p-type ohmic contact) have been addressed in the literature (indicated in table 2.1), it would be less detrimental for the ongoing development of MCT based infrared detector, optoelectronic devices, and other semiconductor devices if all the other attributes-crystallographic, morphological, compositional,

topographical, nanomechanical, optical, and electrical- were identifiable within the individual layers/films. The functioning of the semiconductor can be susceptible to an incremental shift in any one of the attributes of thin films because they are all interconnected.

2.3. Inspiration and outcome of the research:

I have been inspired to embark on additional studies on these thin films (CdTe-ZnS: passivation; CdS: optical window layer; Sn/In: as metal (detector-readout integrated circuit interconnection interface)/n-type ohmic contact; and Cr-Au: p-type ohmic contact), owing to the combined advantages of HgCdTe-based infrared detectors, optoelectronic devices, etc., and numerous uses, as mentioned in sections 1.1 and 1.2. The proposal for research is predicated on the removal or enhancement of the flaws (restrictions) in previously published research and the association between the semiconductor devices' performance and the different characteristics of distinct thin layers/films. As a result, this might be tremendously beneficial for the development of extremely difficult, crucial, and stringent HgCdTe-based infrared detectors, optoelectronic devices, and other semiconductor devices.

Vacuum evaporation was implemented in this thesis to evaporate a variety of thin layers/films, including CdTe-ZnS (passivation), CdS (optical window layer), tin/indium (as n-type ohmic contact/detector-readout integrated circuit interconnector), and Cr-Au (p-type ohmic contact). As a consequence, the optimized thin layers were characterized via x-ray diffraction, atomic force microscopy, field emission scanning electron microscopy, energy dispersive spectroscopy, nanoindentation, optical ellipsometer, UV-vis spectrophotometry, microscopy as well as surface profiler. By developing numerous kinds of test patterns/structures and devices, such as CdTe/ZnS/Si, CdS/glass, a metal-insulator-metal (MIM) device with the configuration of Cr-Au/ZnS/CdTe/Cr-Au/Si, a Sn/In/MCT pattern, a transmission length model pattern (setup: Sn/indium/n-MCT), and a transfer length model (Cr-Au/p-HgCdTe), the successful performance and utility of these optimized films were further investigated. The viability developed appliances to MCT infrared sensor, optoelectronic devices, and other semiconductor device development was next established through characterization approaches such as x-ray diffraction, field emission scanning electron microscopy, nanoindentation, current-voltage, capacitance-voltage, and UV-vis spectrophotometry. Thin layers/films with optimal features, such as CdTe-ZnS (passivation layer with sound mechanical properties), CdS (optical window layer amid a band-gap of about 2.4 electron-volt), Sn/indium (n-type ohmic Sn/indium/n-MCT boundary amid short contact-resistivity, Sn/indium film : amid the correct homogeneity, thickness, and stress), and Cr-gold (p-type MCT ohmic boundary amid petite specific contact-resistivity), may be implemented in the development of HgCdTe-based infrared detectors, optoelectronic devices, and other semiconductor devices.

CHAPTER 3

EXPERIMENTAL SET-UP AND CHARACTERIZATION PROCEDURE

An overview of the setup for experiments and characterization methods applied to achieve the thesis's stated goals is provided within this section. The making of HgCdTe samples and the evaporation of different thin films (CdTe, ZnS, CdS, Sn, Indium, and gold film) on these samples are part of the experimental procedures. However, diffraction of x-rays (XRD) examination, field emission scanning electron microscopy (FESEM), energy dispersive spectroscopy (EDS), atomic force microscopy (AFM), nanoindentation, and current-voltage (I-V) or capacitance-voltage (CV) measurements are the primary characterization methods that worked for a while to assess the characteristics of evaporated thin films. Microscopy, ellipsometry, surface profiling (Dektak), UV-vis spectrometer, and multi beam optical stress sensor (MOSS).

The following is a synopsis of the characterization and experimental procedures (sample preparation and thermal evaporation vacuum technique):

3.1 Preparation of sample:

The thin-film competence that is evaporated is largely determined by the sample (HgCdTe, silicon, glass, etc.) surface. Therefore, before thin films were evaporated or deposited over these samples or substrates, the surfaces of all the $Hg_{1-x}Cd_xTe$ epilayer where x varies 0.27-0.29, they were developed using an assortment of normal, sequential procedures (e.g chemical-mechanical or mechanical finishing (polishing)/etching (engraving), sterilization, washing, air-drying, baking etc.) These sample preparation methods employed a variety of electronic grade/semiconductor chemicals (in solid, liquid, and gaseous forms) [95-98].

3.1.1. HgCdTe (MCT) sample cleaning procedure: The above-mentioned procedure and the chemical utilized for HgCdTe (MCT) are as follows:

- The samples or epilayers are mechanically polished (with 0.05 μm alumina powder) to get the appropriate dimensions.
- Chemical polishing was utilized to produce the desired surface morphology and the least quantity of native oxides. The solution used in this process was I_2:KI: $C_2H_6O_2$: (1 gram: 4 grams: ten milliliter) and a small number drops of solution of potassium hydroxide.
- For the purpose of elimination of oil vapors and greasy contaminants from sample surfaces, epilayers are cleaned using a conventional technique that involves heating them for five minutes in each chemical in turn, such as trichloroethylene, acetone, and methanol.
- Depending on the specific thin film development, the sample's surface can be cleaned with DI water, dried with highly pure N2, and baked within nitrogen gas environment for five a period of five minutes at 90-degree Celsius. Alternatively, sample can be chemically etched

for 20 seconds using 0.1% bromine having concentration of 0.10% into solution of methanol to attain native/oxide-free/pure surface.

- Analyzing the samples' or epilayers' surface quality using ellipsometry measurement and microscope observation.
- Lastly, as previously stated, samples and epilayers had been employed to evaporate the requisite thin layers or films.

3.1.2. Silicon sample cleaning procedure: Stuff a glass vessel with the acetone. Set aside the methanol to a different container. To heat it up, place the acetone bottle on a hot skillet (do not raise it above 55 degrees Celsius). For ten minutes, submerge the silicon slice in the preheated acetone bath, retrieve it out and submerge it in methanol for two to five minutes. Take out and rinse with DI water. To dry the surface, propel nitrogen [99].

3.1.3. Glass sample cleaning procedure: To get rid of loose particles, immerse the sample in ethanol, acetone, or deionized water for a few minutes each. Contaminants can be effectively removed with ultrasonic baths. We can employ a mix of solutions, like a series of ethanol, acetone, deionized water, and hydrogen peroxide. To get rid of any remaining cleaning agents, rinse the sample with deionized water. Use a stream of pure nitrogen or argon gas to dry the glass's surface [100].

3.2 Approaches for thin film evaporation

Evaporation techniques such as electron beam, vacuum evaporation, atomic layer deposition, electrochemical deposition, sputtering deposition by ion beam, electroless evaporation, successive ion layer adsorption reaction, and more [92,101-114] can be used to fabricate all of the aforementioned films (CdTe, ZnS, CdS, tin, Indium, and chromium-gold). The cost-effective, classic/traditional, and well-established procedure with numerous advantages [115-119] in film deposition is thermal evaporation. These advantages include precise control over the evaporated layer size or evaporation rate and temperature of substrate, orientation-dependent evaporation, low containment concentration, and more. In addition, thermally produced films provide the electrical/optical (low resistance, reflectance/transmission) and structural (alike consistent, surface roughness of low value, crack-free, smooth, continuous film with no defects) qualities needed for high-performance infrared detectors. Here, we have created a variety of films using the vacuum evaporation process, including CdTe -ZnS (passivation), CdS (optical material), Sn or In (like ohmic contact/interface of n-type readout integrated circuit/detector) (as ohmic n-contact/detector-ROIC connecting link), and chromium-gold (ohmic contact of p-type).

3.2.1 Vacuum evaporation procedure and evaporation mechanism

One of the most widely used, well-known, and straightforward methods for evaporating various materials on a variety of semiconductor substrates and in industrial settings is thermal evaporation. This method involves first placing the solid source material—which can be in the form of chunks or fine particles, small spheres, strand, or coinage—into a molybdenum boat, tungsten filament, or refractory. After that, resistor heating or a current electricity input are applied it heat to appropriate temperature under ideal vacuum conditions, which are accomplished by means of vacuum pump of turbomolecular type accompanied by backing pump or rotary scroll pump. Therefore, a small coating/layer of the intended substance/materials is developed after the produced vapour flux (vapour stream) condenses onto the substrate and is carried straight towards it across the atmosphere in a substantial vacuum with no collision by any additional remnant or incidental gases. The evaporants' collision-free path length is improved by means of the high vacuum; together with resulting vapour atoms follow a straight path or trajectory in the direction of the substrate. Because there is little chance of contamination in the deposited film, this deposition method is known as a line of sight procedure. The gap among the source as well as substrate is also evaluated via the mean free path (evaporated atoms), which is typically set to scale of 15 to 55 centimeter at an ideal vapour-pressure. For this reason, it has been taken to be 30 cm in the proposed research project. Fig. 3.1 displays the experimental setup and growth mechanism/process (together with the graphic illustration of the vacuum evaporation unit).

Here, quartz crystal sensor with automated rate controller installed inside the vacuum evaporation system be able to precisely manage the experimental factors (pace of evaporation and current of evaporation) to grow the layer/film/coating of the intended size/scale upon the substrate.

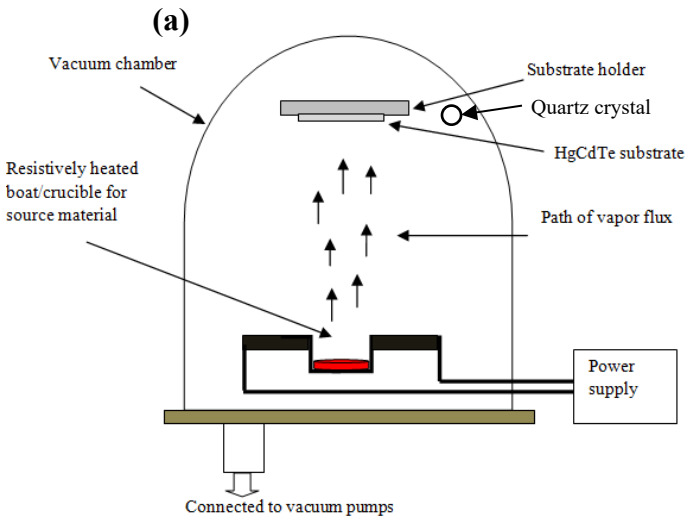

(b)



Figure 3.1 shows the experimental setup and growth mechanism/process, which includes (a) a schematic diagram [100] and (b) a picture of the vacuum evaporation unit

3.2.2 Procedures and prerequisites for thin-film growth

A large number of small layer/films/coating have been evaporated on Si, glass, as well as HgCdTe substrates to achieve the desired research objectives. These are the basic stages in order that are used for evaporating these thin films:

Following sample preparation and a surface quality assessment, siliccon, glass, and HgCdTe epilayers are placed in a coating unit's vacuum chamber:

- The desired source materials are added to the molybdenum boat since different materials might have a variety of shapes, such as lumps, powder, pellets, wire, or coins.
- With the purpose to evaporate a small layer/film of a specific material on the substrate, the bellzar/vessel pressure is reduced so low as to achieve vacuum of high vacuum stage using various pumps of vacuum pump type such as oil-free rotary scroll & turbomolecuar pump/cryogenic. Each material has a different deposition pressure and vacuum.
- The silicon, glass, and HgCdTe-epilayers were coated with films of the necessary thickness (which varies for each film) of CdTe, ZnS, CdS, Sn-In, and Cr-Au.

Each film has its own growth characteristics, and the deposition process is carried out at the ideal conditions (film thickness, evaporation rate, temperature during evaporation, ambient termperaure).

Vacumm evaporation system equipped with an automatic rate controller (quartz crystal sensor/monitor) keeps track of thickness and deposition rate. After the deposition procedure is finished, the samples or epilayers are removed from the vacuum chamber. As a result, as will be discussed later, these deposited samples with different thin films are assessed using a variety of characterization and measurement techniques. Table 3.1 below displays the deposition parameters of several films.

Table 3.1 The vacuum evaporation parameter optimized for various thin films

Evaporated materials/ films	Thickness of film (Å/μm)	Evaporation rate (Å/s)	Evaporation current (A)	Base vacuum (mBar)	Temperature during evaporation (°C)
CdTe	1000 Å	1	40-50	2.0×10^{-6}	Room temperature : 25
ZnS	1500 Å	1	40-90	2.0×10^{-6}	Room temperature : 25
CdS	2000 Å	1	40-90	2.0×10^{-6}	Room temperature : 25
Sn	5 μm	20	160-182	4.0×10^{-7}	Room temperature : 25
In	5μm	20	165-195	4.0×10^{-7}	Room temperature : 25
Cr-Au	2200 Å	12	110-130	7.0×10^{-7}	Room temperature : 25

3.3 Approaches of characterization for thin films

The characteristics of the evaporated layers/films, specifically cadmium telluride, zinc sulfide, tin, indium, and chromium-gold, were assessed using a variety of testing/characterization/quantification methodologies, including x-ray diffraction, atomic force microscopy, field emission scanning electron microscopy, energy dispersive spectroscopy, nanoindentation with scanning probe microscopy, ultra violet visible spectrophotometer, current-voltage/current-capacitance evaluation, surface profiler, optical microscopy, ellipsometry, and multibeam optical stress sensor, many more. Below is a detailed explanation of the aforementioned methods:

3.3.1 X-ray diffraction

One method for examining the extremely small architecture of matter is diffraction by x-rays. Von Laue's 1912 finding out that crystals scatter x-rays and that the way the diffraction reveals the crystal's structure is where this technique got its start. Initially, crystal structure determination was only application of x-ray diffraction. However, numerous additional purposes were subsequently recognized and today the approach is used not only for assessing crystallographic structure but also for a wide range of concerns, including chemical evaluation, stress evaluation, dislocations/defects, phase equilibrium development, particle size assessment, and figuring out the configuration of a single crystal or the ensemble of alignments in a polycrystalline substance [120-123]. The phenomenon known as diffraction of x-ray occurs only when a particular beam (x-ray) strikes a particle/crystal since the x-rays having wavelength range 0.5 to 2.5 angstrom is analogous to space of interatomic or space/region of interplanar of crystalline solids. Each of this crystallographic material has a unique x-ray powder motif that is capable of being utilized to assess its crystalline organization and presence [120-122]. The following Eqn. (3.1) governs the constructive interference/diffraction phenomenon created by this interaction, also known as Bragg's law:

$$n\lambda = 2d \sin\theta \quad (3.1)$$

where d is the interplanar spacing/interatomic distance, θ is the diffraction angle, n is the order of diffraction, and λ is the incident X-ray wavelength.



Figure 3.2 Picture of the X-ray diffraction system to determine the crystal structure of films

The main three sections of a typical XRD diffractometer are generator of x-ray, surface of sample/material, and a sensor. Copper ($CuK\alpha$) is the majority widely used generator of x-ray, and its characteristic wavelength is λ = 1.54 Å. When a sample or specimen is struck by an incoming

X-ray beam, it causes diffraction in all directions and orientations (2θ). The counter, which is attached to a goniometer, gauges the X-ray's intensity while the rotational detector finds the diffracted beam. Using the widely acknowledged Debye Scherrer formula (D= (kλ)/ (βcosθ)), the material's resulting FWHM be able to be used toward assess its average size of grain. The full-width at half maximum of peak of diffraction, diffraction-angle, and value of constant FWHM, angle of diffraction, and constant are depicted by the parameters β, θ, and K, respectively; the constant K often has values between 0.89 and 1.39, but in the majority of cases, it is almost equal to 1 (K=0.94). B.V.-X'Pert PRO MRD-PAN anaytical by Pan analytical unit of diffraction including a copper (CuK_α) generator or source (wavelength 1.542 angstrom, and proportional counter of Xe-type) (Fig. 3.2) was used to perform XRD measurements of the thermally engineered thin films. All of the important and helpful information on the thin films that were created was gathered within the depth of detection at 2-theta = 10° to 90°.

3.3.2 Atomic force microscopy

By perceiving and interacting with material's surface with a mechanical probe, the technique of atomic force microscopy (AFM) collects data. Exact scanning is made attainable by piezoelectric components that permit small but exact motions on (electronic) command. The atomic force microscopy does not employ nuclear force, despite its name. Force estimation, topographic visualization, and manipulation are the three major functions of the AFM. Researchers from international business machine corporation (IBM) founded the AFM in 1985[124]. It belongs among the main methods/instruments for measuring the surface topography/surface morphology, such as the size of grains, surface roughness, and crystallographic density of different substances (such as protein, ceramics, metals, cancer cell identification, and blends of inorganic substances), and is intended for use in visualization (two-dimensional along with three-dimensional images) and material deployment near the nanometer size [125]. The sample/specimen surface is scanned or probed using the AFM instrument's cantilever, which has a sharp made of Si_3N_4 or Si until the very end with curving radii of nanometer order. Signaling electronics and detector assist the cantilever, and sample is fixed to piezoelectric actuator/tube. According to Hooke's law, the cantilever deflects time the specimen region is traversed by the tip due to the force of mechanical interaction betwixt the specimen and tip. Photodiodes attached to the feedback electronics are used to measure the deflection from a stain of laser glanced from the cantilever's top. Because shifting tip-to-sample height can cause damage to the sample, a feedback system is used for governing the specimen to tip height with the object to keep the constant forces among the specimen and tip. AFM incorporates three different image acquision perspectives: contact manner, con-contact manner, and intermittent/tapping manner [125]. Below is a quick comprehension of several imaging modes:

(i) Contact mode: When scanning the specimen, the gap among the specimen or sampe and the tip stays constant, and an image exists using the cantilever deflection because of the force of the tip-specimen/sample interaction. However, the tip may "snap in" to the perimeter of the specimen/sample due to high forces of attraction that exist close to the facade. This manner is

commonly identified as being "contact mode" whilst the force is oftern repulsive near the specimen/sample facade where the cantilever is housed.

(ii)Non-contact mode: In this mode, rather than making contact with the specimen surface, the cantilever tip swings at their frequency at resonance or modulation of frequency otherwise immediately on top of the surface-sample somewhere modulation of amplitude occurs ; amplitude of vibration staying amid a couple of nanometers to a certain picometer. A topographical graphic/micrograph is then produced using the signal that is applied to the mechanics of piezoelectric in order to sustain a consistent resonant frequency. By tweaking the normal space among specimen/sample to tip, and the software used for scanning from topographical visual representation of a sample, the feedback detector/electronics system maintains the oscillation amplitude/frequency constant.

(iii) Intermittent mode: At its resonance frequency, the cantilever first oscillates, nevertheless with larger amplitudes than in non-contact mode. When taken close to the sample, the cantilever-tip makes touch with its surface by decreasing the oscillation amplitude, resulting in the most appropriate imaging mode [125-126].

The surface topological characteristics of thermally produced thin films were measured in present investigation using the equipment of AFM (specifically, from Agilent tech. version-5600LS, AC Model III Module), which is displayed in Fig. 3.3. To improve imaging and reduce the chance of sample surface damage, all samples were scanned and quantified in tapping/intermittent mode.

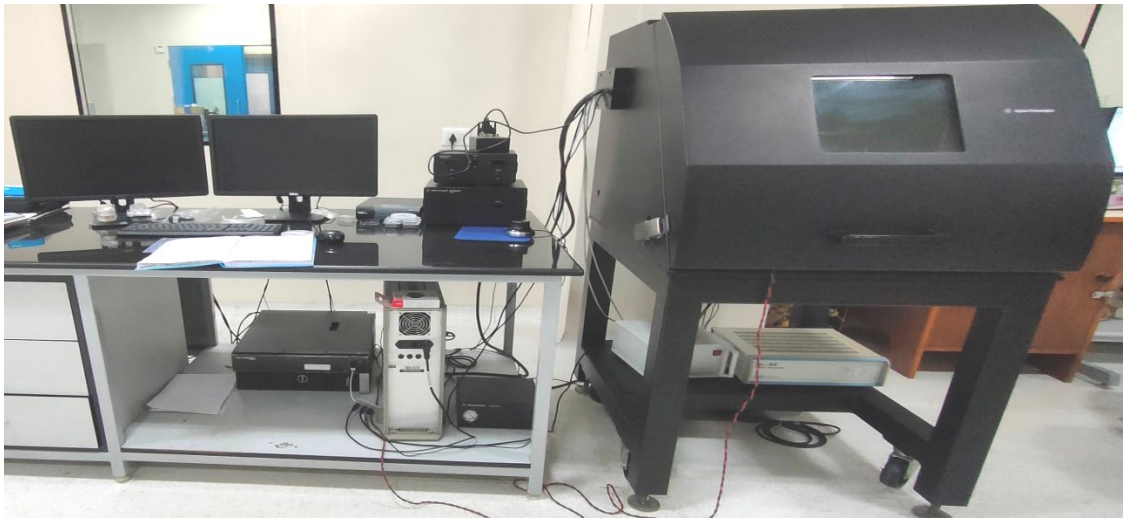

Figure 3.3 Atomic force microscope equipment employed for assessing the topographical characteristics of the evaporated small layers/films

3.3.3 FESEM and EDS

The specimen's as well as the film's compositional parameters, such as percentage elemental analysis, purity, and stoichiometric ratio, along with morphological features, such as coherence, scale size of grains, compactness, distribution, and placement of film-developing particulate characteristics, are assessed using FESEM and EDS characterization techniques. The following is an outline of these methods:

(i) Field emission scanning electron microscope:

The imaging approach known as scanning electron microscopy leverages incoming electrons emanate secondary sample irradiance. When the extremely energetic electron stream (beam) hits a sample's (specimen) surface and associates with its atoms, it produces a range of signals, sucha as secondary electrons, backscattered electrons, and distinctive rays (x-ray type). The surfaces of specimen with a high depth of field and transverse spatial resolutions of about 1-20 nm can then be visualized by examining this. For the majority of the specimens, the scanning electron microscopy that use a thermal emission source (such as tungsten filament) as means as to give rise to the electron beam are usually sufficient and offer good resolution at magnifications up to roughly 10^5 times. Inevitably, a cold field emission gun yields the best scanning electron microscopy resolution for high-resolution and high magnification imaging.The cold field emission gunk uses a powerful electrical field at a very sharp tip to harvest electrons from the field emission cathode. This electron extraction approach produces a smaller beam size and a larger electron yield, resulting in a brighter signal with superior resolution. For FESEM imaging, a useful magnification of up to 500000 times is possible. Having the capability to achieve high-resolution imaging with extremely low boosting voltages is a second benefit of FESEM. Many non-conductive substances can be inspected without using a conductive coating, and very small details are easier to visualize at low voltage. Visualizing nanomaterials, thin films, and polymers is best done with low voltage field emission electron micrscopy. A beam of approaching electrons originates by the FESEM in an electron column situated above the sample chamber. A cold FE source, like a FE cathode, generates the electrons. Depending on the evaluation goals, the incident electrons' energy can range from 100 eV to 30 keV. A set of electromagnetic lenses (condensing optics/lens diminish the size of main stream to an appropriate level and objective optics/lens concentrate the electron stream on the specimen/sample) in the FESEM column focus the electrons into a narrow beam. The focused beam is directed and positioned onto the sample surface by scanning coils toward the end of the column. For imaging, the electron beam is traversed across the surface in a raster pattern. For X-ray analysis, the beam can alternatively be scanned along a line or concentrated at a single location. Because the specimen's (sample) surface, the electron stream (beam) gets angled upward and downward, it may inspect the specified porthole of the specimen, which is its region of rectangular type. Following the refining or converting the various signals/inputs that the sample surface emanated as a result of interacting with the stream (beam) of electron, the electronic devices (backscattered electron detector: chemical and phase

information and secondary electron detector: surface topography) are used to obtain high-resolution images [120, 127].

(ii) Energy dispersive spectroscopy

This approach is implemented in conjunction with SEM, by examining the distinctive x-ray emanating when a specimen/sample is energized by a stream/beam of electron or x-ray provider, energy dispersive x-ray spectroscopy (EDS or EDX) is an analytical method that ascertains the elemental composition or chemical characterization and morphological insights of a sample or film by identifying and quantifying the elements present (at different energy states) and mapping their distribution. X-ray radiation undergoes conversion by a detector into voltage pulses or signals (commands), which undergo transmission to a pulse processor, which evaluates the signals before sending them to an analyzer for data display and analysis. A silicon (lithium) detector conditioned to cryogenic temperatures with liquid nitrogen mostly used detector. It is designed to view samples under specific conditions and has an adaptable minimum working distance (10 mm). The distinctive rays (x-ray) released from the materials surface of the sample/specimen surface when the stream/beam of electron which has a voltage of 10–20 kV, strikes it. Because these x-rays strength is very minimal, it takes many hours to travel the electron beam across the entire specimen in order to obtain an image of every element present in the sample [122, 127].

(iii) FESEM and EDS equipment

The crystallographic as well as elemental characteristics of the evaporated layers/films on the specimen were assessed using the Oxford Instrument X-MAX EDX Spectrometer in conjunction with scanning electron microscope Carl Zeiss SUPRA 55 VP (model), 5 to 20 kilo volt working voltage used, indicated in Fig. 3.4



Figure 3.4 FESEM equipment attached with EDS photograph

3.3.4 Nanoindentation analysis:

A potent technique to figure out the mechanical functions of a variety of materials is nanoindentation. Every aspect of the force-displacement-time response is tracked during a contact mechanics experiment in nanoindentation, a type of depth-sensing indentation (DSI) evaluation that gained popularity for assessing material properties at depths ranging from tens to hundreds of nanometers. Most early research on nanoindentation concentrated on evaluating the characteristics of relatively hard and stiff elastic-plastic engineering materials, including semiconductors, metals, ceramics, and glasses. The indenter is pushed into the sample to create an indent, and then it is taken out of the sample to perform nanoindentation measurements. Throughout the entire test process, the indentation unit logs the load, depth of penetration as well as time data. Viscoelastic parameters, strain rate sensitivity, and elastic modulus and hardness can all be ascertained from the load-displacement plot by means of the Oliver-Pharr procedure [128-131]. The most significant of the technique's many benefits is that it eliminates the requirement to image the hardness imprint and makes it easier to evaluate mechanical parameters at the sub-micron scale through examining the indentation load-displacement data and no-one else. The approach's capacity to execute measurements without removing the film or surface layer from its substrate is another benefit. As is the case with the majority of ion beam modified materials, this makes measurements possible and streamlines specimen preparation in systems that would otherwise be challenging to test.

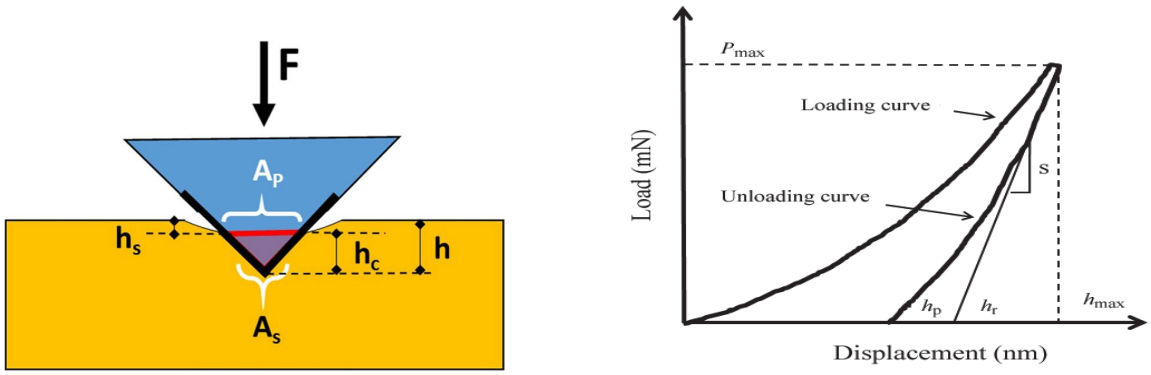

Figure 3.5 (a) Nanoindentation schematic diagram (b) Load-displacement curve

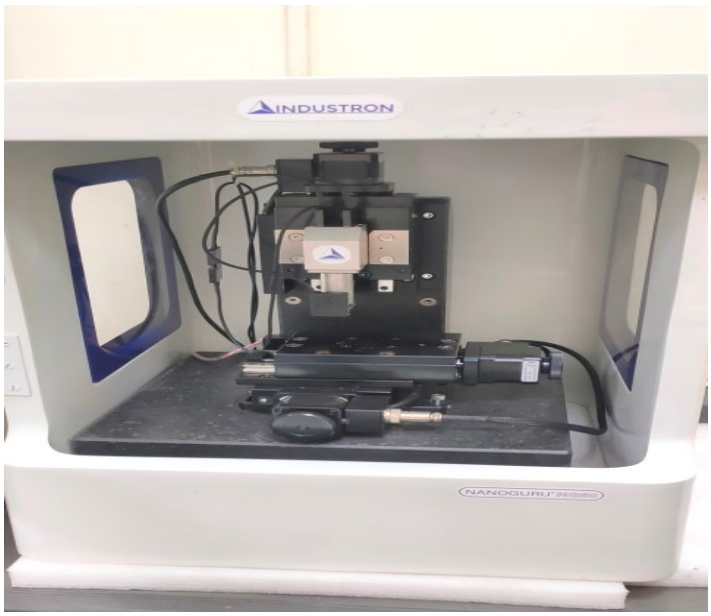

Figure 3.6 Nanoindentation equipment picture

The maximum load (P_{max}), the depth below the specimen surface (h_{max}), the depth of the contact circle (h_c), the depth of the residual inscription (h_r), and the displacement attributable to the elastic recovery during unloading (h_p) are all apparent in Fig. 3.5 (a) [132-135]. The inaugural unloading contact stiffness, $S = \frac{dP}{dh}$, or the slant/slope of the first part of the load removing curvature, can be used to determine the modulus of elasticity of the indented sample shown in Fig. 3.5 (b).

The Nanoguru NG 50 with Berkovitch tip from Industron Ltd is shown in Fig. 3.6.

3.3.5 Capacitance-Voltage as well as Current-Voltage analysis

These evaluations are excellent instruments for assessing the electrical characteristics of dielectric characteristics as well as electrical connections of Ohmic type (contact resistance, ohmicity, and pathway of current), leakage current and thermally evaporated passivation layer in semiconductor devices. A brief explanation of these methods is provided below:

(i) Capacitance-Voltage evaluation

The C-V evaluation approach applies two voltages (AC and DC) to electronic component (that is being tested) concurrently. The AC voltage stays constant in terms of both magnitude and frequency, while the DC voltage varies with time. Since the capacitance of ths device fluctuates with variations in the applied DC voltage, the input preset alternating voltage, which generates a small-signal bias, can be employed to examine the capacitance by the side of a particular deepness of the gadget (this is utilized for sample size of the material/device).

A noteworthy attribute of the MIM device/capacitor is that its capacitance changes in response to the supplied direct current voltage. The capacitance-voltage features for capacitors of distinct type of the developed MIM pattern/device were retrieved at a frequency of 0.5 Megahertz, room temperature (300 kelvin), low temperature (80 kelvin), and 30 millivolts alternating current (root mean square). A DC bias (ranging from 5 to -5 volt) be functional pro punching of every one capacitor of the structure. The current-voltage features of distinctive capacitors be employed to extract a range of aspects (explicitly capacitance, dielectric constant, and leakage current interface states/traps at CdTe-ZnS/Si/HgCdTe interface) using MIM hypothesis, which offers particulars on the efficacy/relevance of vacuum evaporated passivation layers (cadmium telluride and zinc sulfide) in the fabrication of MIM pattern/infrared sensor. [97, 136-137].

(ii) Current-Voltage evaluation

The probes (2 nos.) were placed across various metallic contact pad/patch pairings with the applied voltage range of -2 to 2 volt (gold contact) and -0.5 to 0.5 volt (contact of indium) correspondingly, for current-voltage evaluations of the developed transfer length method pattern (contacts of gold as well as indium) at 80 kelvins. A current-voltage graph for various pairs of contact pads with variable spacing is produced as a result of the corresponding current flowing in the contact pads. This curve is then utilized to determine the resistance of both (two) separate contact pads. Likewise, the consequent I-V graphs were used to extract the resistances for each contact pad. The electrical constraints such as sheet-resistance (R_{sh}), transfer length (L_T), resistance of contact (R_c) as well as specific contact resistance (ρ_c) are then estimated using a graph of total resistance (R_T) vs interspacing (d). Therefore, the voltage-current graphs be utilized to assess the different features of electrical type of the manufactured ohmic contacts of gold-based/indium-based transfer length method pattern as well as to validate the ohmicity of the contacts/current mechanism [92, 99,106, 122,136].

(iii) Capacitance-voltage and current-voltage equipment

To test the capacitance-voltage of the manufactured Cde and ZnS-based metal-insulator-metal device, parametric analyzer made by Keithley low temperature cry-prober equipment) Model-4200 alongside incorporated specific card no. 4200 CUV, was employed. Fig. 3.7 displays the Cryo-prober's picture.



Figure 3.7 Cryo-prober (Make: Keithly) to evaluate the capacitance-voltage/current-voltage tests of evaporated metal-insulator-metal device (CdTe-ZnS), gold and indium based MIM

The current-voltage tests of the indium/HgCdTe-based transfer length method pattern and the gold/p-HgCdTe-based transfer length method pattern were also performed using the same arrangement (system) with the intention of determine the electrical features of the gold/p-HgCdTe (MCT) interface, and indium/n-HgCdTe interface, respectively.

3.3.6 UV-vis spectrophotometer examination

The proportion of ultraviolet as well as visible rays that a surface of a sample absorbs at unique wavelengths is calculated by analytical equipment identified as a UV-vis spectrophotometer. It is commonly used in chemistry, biology, and pharmaceuticals to assess a substance's concentration, identity, and purity by evading a beam/stream of laser via a specimen and detecting the light that emanates/is transmitted. It evaluates how much light a sample absorbs, which raises the energy level of the molecule's electrons. A source of illumination, a sample holder, a diffraction grating or prism acting as a monochromator to separate the various light wavelengths, and a detector are the fundamental components of a spectrophotometer. Prominent sites of radian include filaments composed of tungsten of wavelength 300 to 2500 nanometers, xenon lamp arcs of wavelength 160 to 2000 nanometers, and more recently, light emitting diodes (LED) for the visible spectrum. The sensor that detects light is typically a charge coupled device (CCD), photodiode, photodiode array or photomultiplier tube. Single photodiode detectors and photomultiplier tubes are used with scanning monochromator, to suppress light so that only one wavelength of light assesses the detection mechanism at a time. The instrument’s monochromator switches the diffraction grating to “step-through” each wavelength in order to detect the intensity as a function of wavelength. Fixed monochromator are implemented with CCDs along the photodiode arrays. Because both of these gadgets are composed of many detectors configured into one or two-dimensional arrays, they may simultaneously capture light spanning multiple wavelengths on different pixels or group of pixels [138-140]. Spectrophotomers exist in a couple of forms: single beam and double beam.

Single beam equipment's entire light beam passes through the specimen. This was the original design, and industrial and educational labs persist to utilize it extensively. In double-beam equipment, the light is distributed hooked on 2 streams prior to it approaches specimen. The first stream/beam acts as a benchmark while the second beam navigates the specimen. The assessment indicated is the proportion of the 2-beam intensities; the reference stream intensity is 100% transmission, or zero absorption. Some 2-beam equipments with 2-detectors simultaneously monitor the reference as well as specimen beams. One beam at a time is stopped by a beam chopper in the other equipments once both beams have navigated through it. In addition to the estimated wavelength, parameters of importance include absorbance, reflectance, or transmittance, as well as how they evolve over time [141-142]. UV-vis spectrophotometer from Agilent technologies is shown in Fig. 3.8.



Figure 3.8 Ultra violet-visible spectrophotometer for evaluating the optical characteristics

3.3.7 Ellipsometry

The ellipsometry method is a prominent, versatile, non-contact-in nature, nondetrimental optical approach that applies reflecting light that is usable to assess a sample material's optical features (such as composition, structure, film thickness, and refractive index). It calculates the changes in when light impacts the outermost layer or specimen its polarization mode past it after it has been reflected or transmitted from that surface. It is called "ellipsometry" because, after being reflected from the sample's surface, light with linear polarization that strikes a surface at an inclined angle of incidence between 40 and 90 degrees changes its polarization state to elliptically polarized light. Thin films evaporated on a substrate or samples are frequently examined for thickness using ellipsometry. Because alterations in the material contituents as well as the thickness of the specimen/substance affect its reflecting qualities. If the index of refraction of the underlying material as well as the layer/film is known, ellipsometry can be utilized for figuring out a thin film's dimension. As a result, ellipsometry has been widely utilized to examine substances as well

as surfaces [143]. Eqns. 3.2 and 3.3 can be used to write the well-known ellipsometric expressions as follows:

$$\rho = \frac{r_p}{r_s} = \tan \Psi \; e^{i\Delta} \tag{3.2}$$

$$\Delta = \delta_p - \delta_s \tag{3.3}$$

where the coefficients of parallel and perpendicular reflection, respectively, are symbolized by the symbols r_p and r_s; these are taken with reference to the plane of incidence. In contrast, the proportions of amplitude as well as difference of phase are represented by tan Ψ and Δ. Here, the alterations of phase that correspond to the p as well as s ingredients of light are denoted by δ_p and δ_s [143].

The physical features of the tin/indium film and HgCdTe sample were examined using Gartner LSE-MS Stokes optical ellipsometer (model) featuring a helium neon light (laser type) resource with a λ of 632.8 nanometers (single wavelength) as well as an oblique angle of incidence of 70 degrees to examine the material constituents, impurity layer/oxide (indicated on their façade/outermost surfaces of the specimen/sample), and the surface roughness. Fig.3.9 shows the experimental setup and photograph. A manual XY micrometer, a stream/beam source of laser with a dimension of 15 micrometer diameter, a camera to observe the measurement region on a computer monitor, and a sample table with handheld tilt and height adjustment make up this apparatus. The stability, spectrum precision, and extended lifespan of the laser light source make it extremely advantageous. Therefore, with this sophisticated device that has no moving components or modulators, the ellipsometric measurement may be completed quickly and with extreme precision.

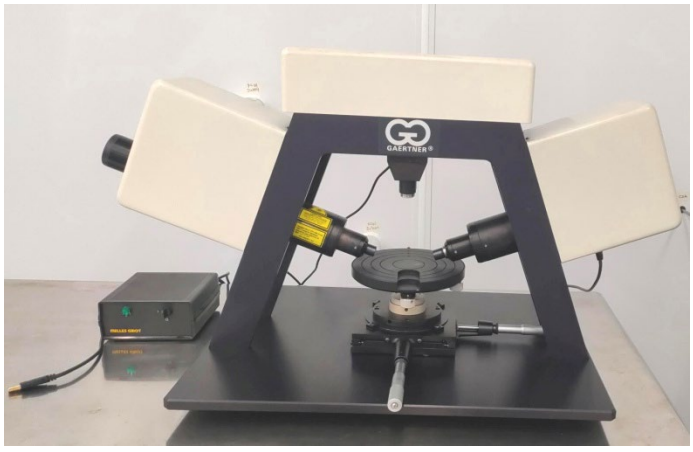

Figure 3.9 Ellipsometer photograph to evaluate surface features of the small layer/film as well as HgCdTe (MCT) sample

3.3.8 Multibeam optical stress sensor

A series of concurrent light beams is utilized by a multi-beam optical stress sensor, a highly sensitive device that measures stress in-situ, ex-situ, and in real time. The sensor can track the curvature of a material in real time by reflecting beams from a surface and using a camera to measure the deflection of those beams. This curvature is directly correlated with the stress within the material. Applications for these systems include the analysis of mechanical stability in devices such as batteries and the monitoring of thin film stress during formation. It develops a two-dimensional laser array of spots using a single laser, which is reflected off the sample surface as well as captured by a high-resolution camera. The variations in sample curvature are influenced by changes in the laser array spot spacing. In contrary to curvature instruments that employ point/line scan with mechanical rastering.



Figure 3.10 Photograph of multibeam optical stress sensor (MOSS) to measure ex-situ stress

MOSS gives two-dimensional curvature data since it simultaneously detects the distance between laser spots in two orthogonal directions. Compared to scanning techniques, simultaneous detection of the laser array also naturally reduces the measurement's sensitivity to sample disturbance. Enhanced curvature resolution capability arises from movement or tilt not being noticed as a change in curvature since the entire laser dots move simultaneously at the same frequency [144-147]. The picture of the multibeam optical stress sensor (MOSS) is shown in Fig. 3.10.

3.3.9 Surface profiler

One tool to evaluate the layer size as well as degree of roughness is a surface profiler. A stylus in the shape of tipped made up of diamond with a radius of 12.5 μm is used in the surface profiler. It is moved vertically when it comes into touching an area of interest and then moving horizontally spanning its surface while the user programs parameters including speed, contact force, and distance/scan length. A linear variable differential transformer (LVDT) is linked to the stylus. The tip is connected to LVDT, which converts the tiny surface variations—the stylus's vertical displacement as a function of height and position—into an analog electrical output. This signal undergoes sequential digitization, storage, presentation, and analysis. Fig. 3.11 depicts the dimensions of the vacuum evaporated small layer/film were examined utilizing the surface profiler Alpha step D500 (model). The size of thickness that the surface profiler can evaluate is 10 nanometers to 65 micrometers [120, 148-149].



Figure 3.11 Surface profiler picture which utilized to measure size (thickness) of thin films

3.3.10 Microscopy

One of the most extensively utilized and practical approaches for assessing HgCdTe epilayers is this one. After completing their surface cleaning procedure, the HgCdTe samples were examined right away using microscope (Nomarski) into opposed imaging approach (it was developed in the mid-1950s by the scientist –Gorges Nomarski and delivers more insight and resolution than classical optical microscopy during the test phase). Through the variation of height and refractive index, this can provide information about the samples under testing or inspection's planarity, contaminations, estimated surface roughness, and 3D features or macro-defects (such as Te precipitates that appear at huge fractures and crystalline formations and are responsible meant to

induce strain in the specimen/sample due to misalignment in the lattice). As a primary approximation, the Nomarski scanning approach is therefore adequate to evaluate the samples' flaws and surface roughness [150]. The microscope's experimental setup and image are displayed in Fig. 3.12.



Figure 3.12 Image of Nomarski microscope used to examine the sample surface

It operates using the polarization principle, which divides a polarized light stream/beam split into two orthogonally polarized rays adhering to their pathway through a polarizer after being formed by a lamp and divided by a Wollaston prism. Through another Wollaston prism, the divided beams /streaks of light rejoin after entering the facade of specimen. An optical trajectory differential between two beams will be formed and the beams will not be able to interfere with one another if the sample's thickness and reflective index are altered. A spatial interference pattern is created when a polarizer is integrated it aligns the beams/steaks into the same plane such that there is no optical path distinction among them (using an unpredictable offset orientation configuration). This contrast is noted with a corresponding intensity or color and recorded as the shear distance [151].

3.3.11 Eddy current method (sheet resistance measurement via. non-contact)

The sheet resistance of metallic small layer/film can be fulfilled with a non-invasive, non-damaging eddy current procedure that be relying upon electromagnetic induction law by Faraday [152]. Therefore, the time-varying magnetic field of an alternating current (AC) coil causes circulation or eddy currents to be induced within the material being inspected or measured. This measurement measures the electrical loss of the material by having the measuring head or sensor move at a constant height above the sample (being measured or tested) without touching or making physical contact with it. Similar to an eddy sensor, an embedded distant sensor quantifies

capacitance, but the signal that is captured is contingent upon the sample's sheet resistance and probe distance. As a consequence, the measured distance and eddy signal values can be used for calculating sheet resistance. This particular information can also be used to continuously show the conductivity and chemical makeup of the test sample. As a result, this non-destructive method is highly beneficial in both science and the metal business for assessing the characteristics of various materials without causing any harm [153].



Figure 3.13 The conductive capacity and sheet resistance of thin layers/films were assessed using a contact-free sheet resistance evaluation procedure

The electrical conductive capacity and sheet resistance of vacuum evaporated metallic layers/films (gold and indium) has been examined using a non-contact sheet resistance measurement instrument (model: EC80), as seen in Fig. 3.13.

CHAPTER 4

INVESTIGATION OF STRUCTURAL, MORPHOLOGICAL AND NANO-MECHANICAL PROPERTIES OF VACUUM EVAPORATED NANOSCALE CdTe AND ZnS FILMS

4.1. Introduction

Polycrystalline thin films are key materials with a tremendous promise for photovoltaic applications and non-conventional energy sources, including nanosystems and nanodevices. Numerous industries, including semiconductors, microelectronics, optoelectronics, and optics, have used nano-thin films for relevant applications [154-160]. However, efforts are still underway to find simple and effective ways to improve the roughness, electrical, and optical characteristics of these nano-thin films.

The growth of good-quality CdTe and ZnS thin films is a promising technology for industrial development, high-performance photovoltaics, and other optoelectronic devices. The technology involves depositing a thin layer on the semiconductor substrate. CdTe's bandgap is optimal for absorption in the infrared and visible regions of the spectrum, with relatively higher quantum efficiency. Typically, scientists grow the ZnS layer above the CdTe layer as a cap layer to stabilize it and enhance its dielectric properties. CdTe is lattice matched to II-VI compound semiconductors like HgCdTe, gives a better interface with low charge density, and is optically transparent to infrared (IR). ZnS has a bandgap of ~3.2–3.6 eV at room temperature, a dielectric constant of ~9 at 1 MHz, and a wide bandpass for 0.4 to 13μm wavelength range, which makes it suitable for optoelectronic sensor applications [161].

An n-type window layer (such as CdS, ZnS, ZnSe, CdSe, etc.) pairs with a p-type CdTe layer in a typical CdTe thin film solar cell to form a heterojunction. The polycrystalline CdTe thin films are relatively less expensive than their single-crystal counterparts. Since a typical thin film layer has a thickness of less than a micron, the material cost per cell is also relatively low. CdTe thin films have grown using a variety of fabrication techniques, such as close-space sublimation, thermal evaporation, electrodeposition, and sputtering [162-166]. According to F.S. Manciu et al., a complete assessment of the spectroscopic as well as microscopic characteristics of CdTe films reveals that a good material with excellent structure is required for the fabrication of photovoltaic devices. SEM micrographs demonstrated that polycrystalline CdTe thin layers were evenly and preferentially deposited on Si (111) as well as Si (211) substrates [167]. The CdTe films deposited by thermal evaporation were studied for structural and topographical characteristics suitable for photovoltaic applications. It was reported that the film had a lower strain value, a low defect density, and low rms surface roughness of about 5.1 nm. The deposited film exhibited an excellent crystalline cubic structure with a crystallite size of roughly 31 nm [168-170]. The structural and nanomechanical characteristics of CdTe films were evaluated on glass substrates. The outcome indicated that the indentation hardness and elastic modulus of CdTe layers were lowered as the size of the grain got larger. The smaller the particle dimension, the stronger the adhesion strength of the coating [167, 171-172].

***Portion of this research has been reported in Optical Materials, 154 (2024) 115764**

V.K. Ashith et al. investigated the fabrication of ZnS/CdTe hetro-junction by conventional vacuum evaporation technique and successive ionic layer adsorption and reaction (SILAR) methods and studied the I-V, C-V, and J-V characteristics [173]. Fabrication of photovoltaic devices with ZnS/ZnSe/CdTe-type double heterojunctions on glass and ITO-coated glass via radio frequency sputtering and thermal evaporation technology was reported by O. Toma. et al. The deposition conditions were optimized to achieve a good photovoltaic response in multilayer double heterojunction structures [174].

The structure and morphology of ZnS thin films play a vital role in the optoelectronic characteristics of thin films. The layers of thin film could be exposed to external factors such as damage and thermal degradation. Therefore, all features of the film were important [160-161, 173-174]. Thin films were frequently subjected to mechanical stress. Thermal mismatch, epitaxial mismatch stress, volume shrinkage or expansion due to crystallization, phase change, and the and the accumulation of other structures were just some of the possible causes of mechanical stresses in films [175].

The ZnS and CdTe films formed using the thermal evaporation process have relatively low packing densities. Water molecules may fill the voids in the film when the device or solar cells are exposed to the atmosphere. As a result, the films' properties were reliant on humidity, which could have an effect on their reliability and robustness [176-177]. The packing density of both films can be significantly increased if the films are deposited at a very low deposition rate or heating the substrate [178]. Z. Zhang et al. investigated the effect of substrate temperature on the humidity resistance as well as the adhesion of ZnS film. The author has reported that the humidity resistance of the film improved significantly after using substrate heating [179]. Due to their excellent mechanical properties, high temperature strength, and other characteristics, alloy parts have become progressively more favorable as a result of the fast advancement of material science and the growing need for high-performance components in contemporary technology [180]. M. Thangaraju et al. prepared the Cu-incorporated CdTe (CdTe:Cu) alloy by mechanical alloying technique and used it for the formation of CdTe:Cu film. Investigation of deposited CdTe:Cu film revealed that surface roughness decreases with increasing Cu concentration on CdTe film. Increasing the Cu concentration in CdTe film also results in an intense XRD peak in the (111) plane [181]. Different Zn-based alloys are synthesized using Mg, Cu, and Al and investigated by several authors, which are extensively used in aerospace, defence and electronic communication [182-183]. V.D. Vankar et al. reported the alloy films of ZnS and MgF_2, prepared by co-evaporation [184].

Doping of ZnS and CdTe films also plays a crucial role in the fabrication of optoelectronic devices, as the doping modifies the mechanical as well as optical characteristics of the films [185-186]. The effect of doping on CdTe film has been investigated by J. Li et al. They described that Te doping improves the conductivity of CdTe film and is also favorable to the crystallite growth of CdTe film [187]. L. Jin also investigated the impact of Sn-doping on the surface morphology, optical characteristics, and microstructure of polycrystalline CdTe films. In this study, they concluded that a strongly preferential orientation of the (111) plane in Sn-doped CdTe films and a larger grain size can be obtained by appropriate Sn-doping [188]. Numerous elements, including Co, Fe, Sn, Cu, Mn, Ni, and Cd, have doped ZnS, resulting in the discovery of various chemical and physical properties. The impact of doping on structural change and phase variation of ZnS film has been

studied by several authors [189]. Studies reported that the diffraction peak position in XRD shifted towards a higher angle after doping due to the change in residual stress, lattice parameters, and defect concentration [190]. Doping of ZnS film with Co, Cu, and Ag increases the stress in the film as the particle size reduces after doping [191].

Residual stress may seriously affect various film properties, including adhesion, the generation of crystalline defects, the perfection of epitaxial deposits, and the formation of film surface growths such as hillocks and whiskers [192-193]. Stress is generated in the film during the growing process due to various factors, such as the difference in the coefficient of thermal expansion of the substrate and the deposited film and the introduction of impurity atoms into the lattice, which is responsible for the observed stress [194]. At low temperatures, surface diffusion is rather small, and hence surface rearrangement occurs much less compared with the films grown at higher temperatures. This also induces stress in the deposited film [195]. Yan. He. et al. studied the atomic stress distribution and surface roughness with molecular dynamics simulation, which is based on the calculation method of Newton's classical mechanics and the basic principles of statistical mechanics [180]. The nature of the interface between two materials in contact is of interest in friction, cold welding, adhesion, residual stress, etc. [196]. The effect of tensile residual stress is investigated by G.A. Webster and A. N. Ezeilo [197-198]. C. Zhang et al. studied the role of surface roughness on interface properties. They reported that surface roughness significantly mitigates interfacial interaction, which reduces the cohesive strength of the interface formed between film and substrate, depending on the film properties and surface roughness [199].

Nanoindentation is a valuable and innovative technique to evaluate the mechanical characteristics of materials, for instance, elastic modulus and hardness. This method was often employed to examine the mechanical characteristics of thin layers [200]. A quantitative evaluation of the material's mechanical properties is vital since contact-induced damage can significantly impact the final electronic properties of the device during the majority of device production procedures [201-204]. Because of its high sensitivity, fine resolution, and ease of use, nano-indentation has been extensively utilized to characterize the mechanical characteristics of a variety of nanomaterials in addition to thin films. Hardness, Young's modulus, and elastic/plastic deformation behavior are among the mechanical parameters of importance that can be easily acquired using nanoindentation testing [205-206].

In this work [207], CdTe and ZnS films grown by vacuum evaporation and their structural, morphological and nano-mechanical characteristics were examined. The ZnS/CdTe films with appropriate thickness play a major role in passivation of II-VI compound semiconductor based IR sensors. In the present work Silicon has been used as a substrate to deposit the CdTe and ZnS film to study the film properties like phase of film, stoichiometry, surface roughness, hardness and elastic modulus etc. The study of morphological and mechanical properties of the films was done using Si as a substrate to establish the deposition process. The results obtained from examination on Si substrate indicated that the CdTe and ZnS films were appropriate or useful in photovoltaic as well as optoelectronic devices.

4.2. Materials and Methods:

Small chunks of CdTe and ZnS compound material were used for growth of CdTe and ZnS films on silicon substrate. The CdTe (99.99 %) and ZnS (99.99%) chunks were placed in a two sequentially arranged molybdenum boat. Researchers have grown different sulfur based film using sulfurization process in tube furnaces [208-211]. In present study single compound ZnS material was used as evaporation material for growth of sulfur based film. The CdTe and ZnS films grown parameters are given in table 4.1.

Table 4.1 Growth parameters of CdTe and ZnS films

Film	**Evaporation rate (Å/s)**	**Film thickness (nm)**	**Vacuum (mbar)**	**Substrate temperature**
CdTe	1	100	$2x\ 10^{-6}$	Room temperature
ZnS	1	150	$2x\ 10^{-6}$	Room temperature

The substrate was placed 30 cm away from the source (evaporant). A pressure of $2x10^{-6}$ was employed for draining the vacuum chamber. The Si substrate was then utilized to deposit CdTe and ZnS films with thicknesses 100 nm and 150 nm, respectively using the fixed process settings (evaporation rate: 1 Å/s, evaporation current: 40-90 A by means of bias voltage of 10 V). The automatic rate controller (incorporated by the quartz crystal) controlled the coating rate and film thickness by controlling the feed current. At room temperature (25°C), the whole deposition of CdTe and ZnS thin films was achieved. The deposited film was used for further structural and nano-mechanical analysis.

The schematic diagram of thermal evaporation process is shown in Figure 4.1(a) **i**ndicating the path of vapor flux leaving from source material and sticking to the Si surface inside closed vacuum chamber. Figure 4.1 (b) shows the schematic diagram of deposition CdTe (thickness: 100 nm) and ZnS (thickness: 150 nm) thin films on Si substrate.The image of deposited CdTe and ZnS film on Si substrate is shown in Figure 4.1(c). A small step height was made by covering the small portion of Si surface before deposition process to reconfirm the total thickness of the film by Dektak surface profiler.

The CdTe and ZnS thin film's crystalline structural properties were determined utilizing a high-resolution X-ray diffraction equipment from PAN analytical B.V. Xper PRO MRD (Material research diffractometer), which had a CuKα (**λ** = 1.542 Å). The X-ray diffraction grazing angle was set to 2° and the scanning range of the second drive axis to 20-70°. The morphology of the film was determined via atomic force microscope (AFM; Model-5600 LS, AC Model III Module, Agilent technologies) and field emission scanning electron microscope (FESEM ; Model : FESEM Carl Zeiss SUPRA55VP with Oxford instrument). With a Berkovich tip indenter, the Industron Nanoguru NG50 executed the nano-indentation. To determine the thickness, a Dektak KLA Alpha step D500 surface profiler was utilized.

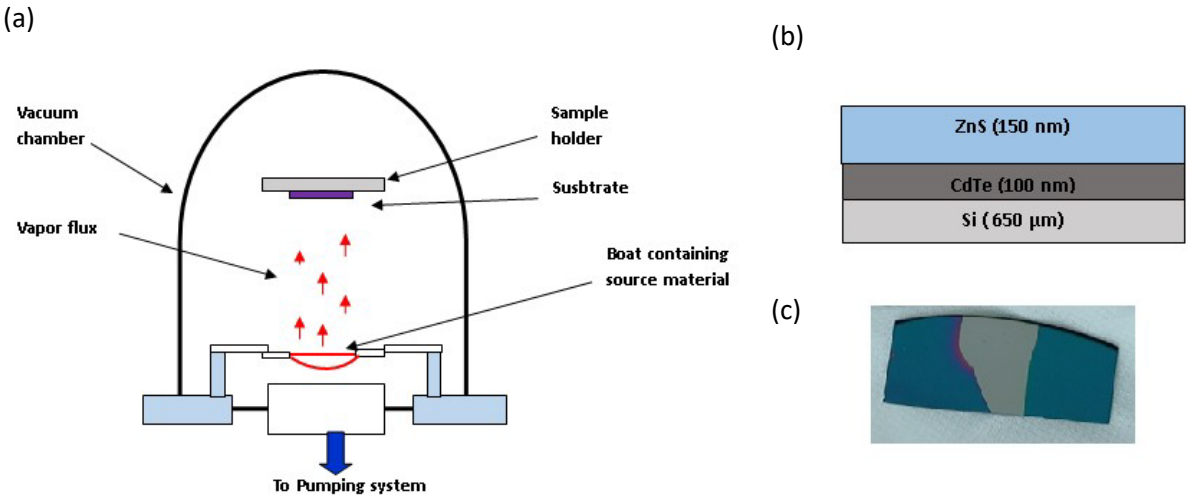

Figure 4.1 (a): Schematic diagram of thermal evaporation process (b) Schematic diagram of stack structure on silicon substrate (c) Image of deposited CdTe & ZnS film on silicon substrate

4.3 Results and discussion

4.3.1 Structural properties analysis by XRD

The crystalline structures of CdTe and ZnS films were characterized by XRD as shown in Fig. 3.2. From the analysis of the XRD peaks, the strong as well as sharp diffraction peaks of the CdTe and ZnS were accredited to the cubic phase at about 23° & 28° of the (111) plane, respectively (CdTe JCPDS no. 89-3053 and ZnS JCPDS no. 65-5476) [164,166,173,212-213]. There were no phase transformations or interdiffusion found at the interface region from XRD examination. The ZnS generally occurs in two different phases: cubic in addition to hexagonal phase, the cubic phase generally forms under 250 °C [214]. Values were reported for cubic ZnS films developed by thermal evaporation process at temperatures between 200 and 300 °C [215].

The CdTe and ZnS thin film's XRD diffractogram examination (peak positions appear in Inset-1 of Fig.4.2) indicated that CdTe and ZnS crystallize in cubic structure with planes being oriented in the CdTe (311) and ZnS (220) directions, respectively. The lattice parameters of CdTe (6.47 Å) and ZnS (5.50 Å) are at diffraction angles of 46.50° and 47.50°, respectively. The X-ray pattern examination of diffraction angle about 56° indicated (peak locations shown in Inset-2 of Fig. 4.2) that ZnS film crystallized in structural phase known as cubic phase with plane being oriented in the (311) and large peak of Si substrate with plane being oriented in the (100) direction.

Using Debye-Scherer's formula, the crystallite size (D) of each of the films was calculated Eqn. (3.1) [164, 216]:

$$D = \frac{0.94\,\lambda}{\beta Cos\theta} \quad (4.1)$$

where **λ**,β and θ represent the wavelength of X-ray, full width half maximum and Bragg diffraction angle, respectively. Additionally, the cubic structure lattice constant (a) of CdTe and ZnS thin films was computed using Eqn. (4.2) [217-218]:

$$a = \frac{\sqrt{h^2+k^2+l^2}}{2sin\theta} \quad (4.2)$$

$$d = \frac{a}{\sqrt{h^2+k^2+l^2}} \quad (4.3)$$

where the interplanar distance was represented by d and h,k and l were Miller indices. The dislocation density (defect density, δ) [219] as well as the strain (ε) were determined for CdTe and ZnS thin films applying the Eqns. (4.4) (4.5) [217,220,221]:

$$\delta = \frac{1}{D^2} \quad (4.4)$$

$$\varepsilon = \frac{\beta}{4tan\theta} \quad (4.5)$$

The stresses (σ_s of CdTe and ZnS film were evaluated by Williamson-Hall expression using Eqn. (4.6) [222]

$$\sigma_s = \frac{Y(a - a_0)}{2a_0\gamma} \quad (4.6)$$

where Y was the Young's modulus of CdTe and ZnS in GPa which were 52 and 75 GPa respectively, a was the calculated lattice constant via X-ray examination, a_0 was the standard value of lattice constants (6.48 and 5.40 Å) for CdTe and ZnS bulk materials and ɣ represents the Poisson's ratio's (0.41 &0.28) for CdTe and ZnS respectively.

The stacking faults (SF) were calculated with using Eqn. (4.7):

$$SF = \frac{2\pi^2\beta}{45\sqrt{3}tan\theta} \quad (4.7)$$

The number of crystallites per unit area (N) of the thin films was calculated with applying following Eqn. (4.8) [223]:

$$N = \frac{t}{D^3} \quad (4.8)$$

where the thickness of the film was represented by t.

Table 4.2 lists the crystal structure parameters such as lattice plane, full width half maximum, experimental lattice constant, standard lattice constant, experimental interplanar space, and standard interplanar space of CdTe and ZnS films. Table 4.3 lists the lattice constant (a), crystallite size (D), defect density (δ), stress (σ_s and strain (ε) of deposited CdTe and ZnS films for the favored plane (111). The X-ray measurements revealed that the lattice constants of the CdTe and ZnS films were comparable to the bulk CdTe and ZnS materials. The structural parameters (crystallite size, defect density, intrinsic stress and strain) of the thin films determined from XRD results are comparable with the best reported results [162,224] which indicated that the attained crystalline parameters are suitable for a good crystalline growth on actual sensor arrays.

It was obvious from experimental data that increased morphology disorder was associated with the formation of thin films. Fine grain size, low intrinsic stress, high strain, large defect density and stacking faults were linked to the generation of thin films. The calculated mechanical characteristics indicated a higher degree of disorder in the thin films than in the bulk. Moreover, the combined passivation film's characteristics were linked to the structural factors.

Table 4.2 : Structural parameter examined commencing X-ray results of CdTe and ZnS thin film and assessment of standard vs. experimental parameters (d: space between planes, a: lattice constant)

	2θ(°)	Lattice plane (hkl)	FWHM (°)	Experimental d (Å)	Standard d (Å)	Experimental a (Å)	Standard a (Å)
CdTe	23.74°	(111)	0.48	3.747	3.741	6.49	6.48
	39.42°	(220)	0.79	2.283	2.291	6.46	6.48
	46.50°	(311)	0.84	1.953	1.954	6.47	6.48
ZnS	28.74°	(111)	0.57	3.106	3.121	5.38	5.40
	47.50°	(220)	1.53	1.944	1.911	5.50	5.40
	56.41°	(311)	0.80	1.631	1.629	5.41	5.40

Table 4.3: Crystalline parameters of CdTe and ZnS films determined meant for the favored plane (111)

	CdTe	**ZnS**
Crystalline parameters	**Evaluated values**	**Evaluated values**
2θ (°)	23.74	28.74
Lattice plane (hkl)	(111)	(111)
FWHM (°)	0.48	0.57
The lattice constant , a (Å)	6.49	5.38
Size of crystallite, D (nm)	17.5	15
Dislocation density, δ (x 10^{11} line/cm^{-2})	3.2	4.4
Stacking Fault (x 10^{-3})	4.62	4.9
Strain, ε (x 10^{-3})	9.96	9.71
Stress, σ_s (GPa)	0.09	0.49
No of crystallite/Area, N (x 10^{12} cm^{-2})	1.86	4.44

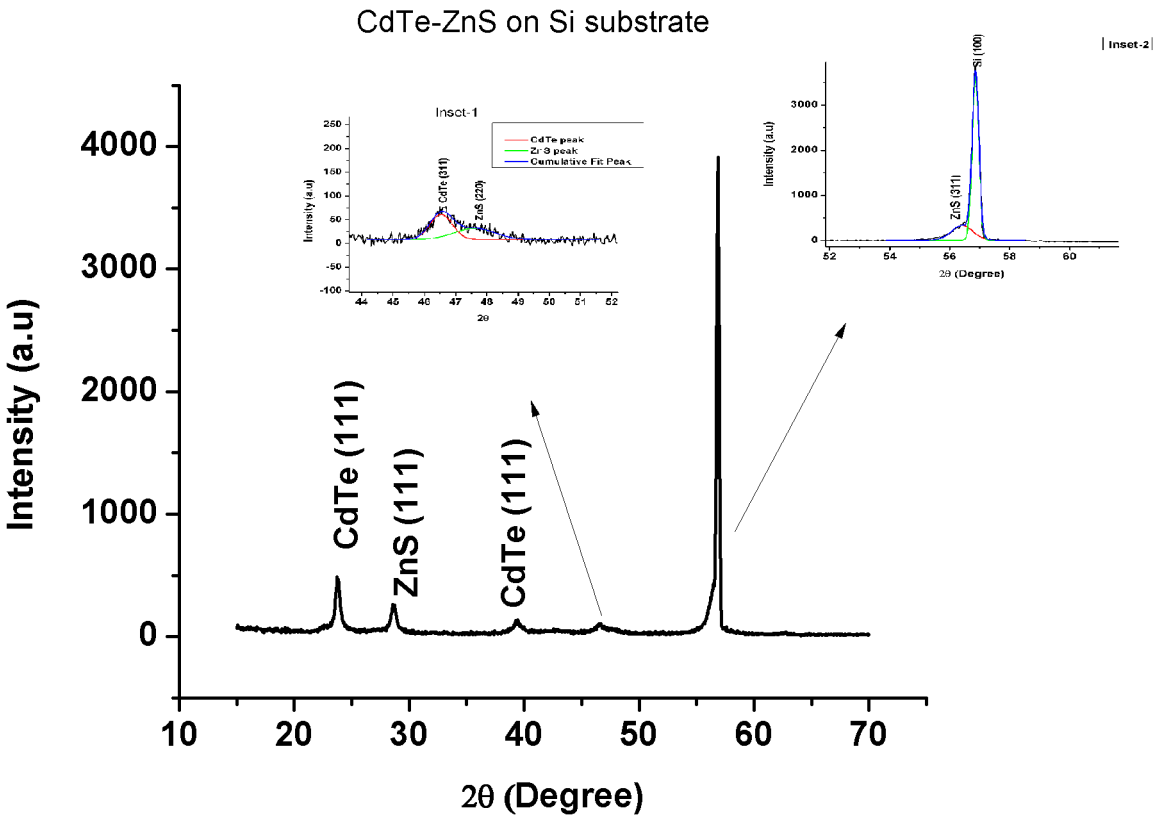

Figure 4.2: The X-ray diffractogram of the CdTe and ZnS films. Peak shown in Inset-1 is magnified to show the overlap peaks of CdTe and ZnS films. magnified peak in inset -2 shows the overlap peaks of ZnS film and silicon substrate.

4.3.2 Morphological and topography analysis

The grain boundaries accumulate the crystallite of the grain [225]. A collection of arranged atoms is incorporated in each crystallite. The configuration of the grain borderlines causes a high number of disordered atoms or trap defects to occur. Uniformity has a significant impact on the reduction of defect states at the interface between CdTe-ZnS and other materials used in electrical and optoelectronic devices, like solar cells [173]. The FESEM planar view images of the ZnS film are shown in Fig. 4.3 (a) & 4.3(b). From FESEM it was observed that the film was smooth, fully covered the Si, compact and free of pinholes [217]. Fig 4.3(a) shown the SEM image of ZnS film at 233 X magnification where film was very smooth but grains of the film were not prominent which implies that deposited film has very fine grain size. To see the grain structure of the film SEM images were taken at 138kX magnification. At this magnification grains of the film are visible and looking uniform as shown in Fig 4.3(b). The FESEM cross-section image was studied to find out the thickness of the CdTe and ZnS films as shown in Fig. 4.3(c) The FESEM cross-sectional image revealed that the CdTe and ZnS films thicknesses were about 100 nm and 150 nm,

respectively. Thus by this method we verified the films thickness values obtained from quartz crystal.

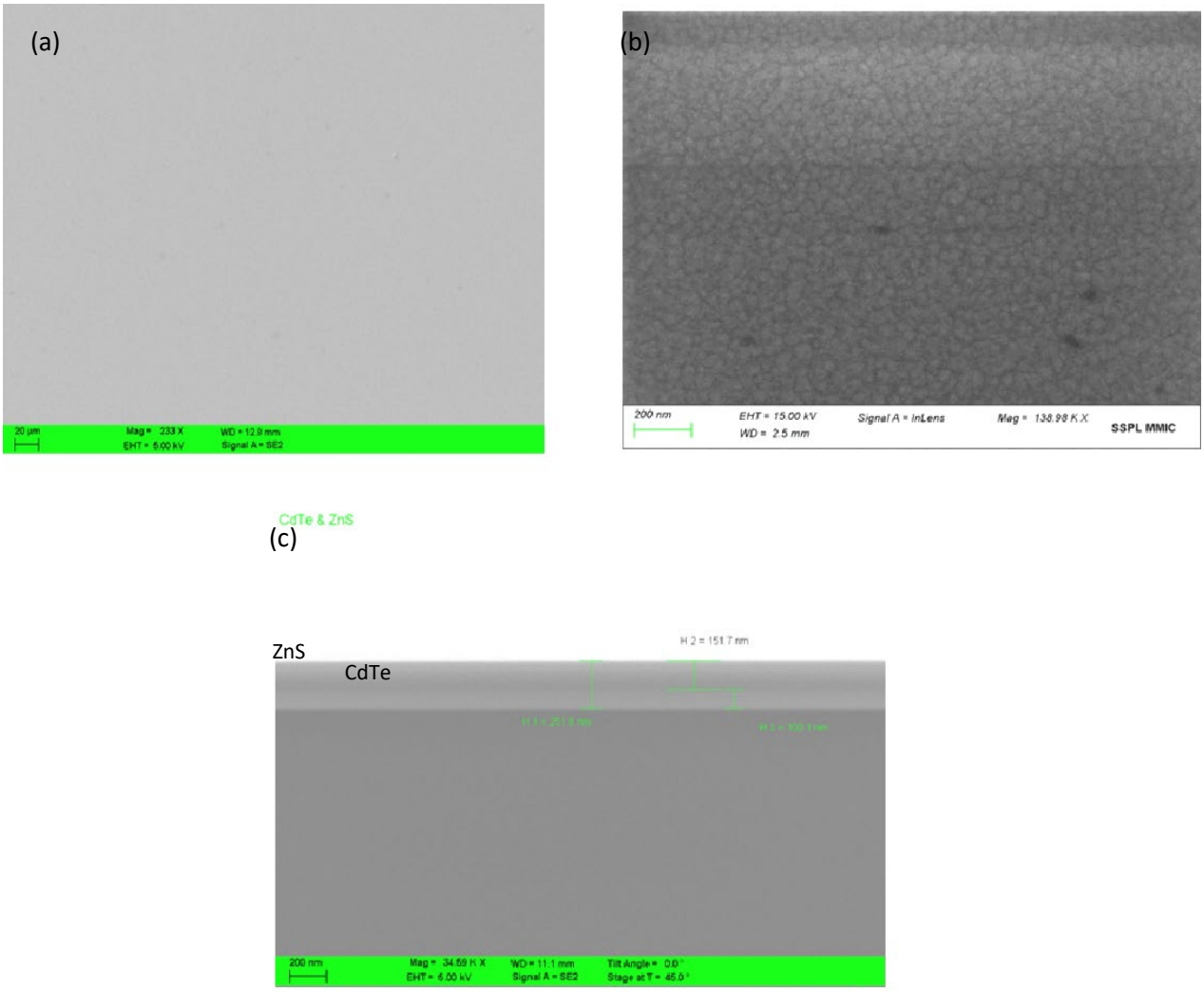

Figure 4.3. SEM micrograph of deposited CdTe and ZnS thin films on Si substrate (a) image at 243X magnification (b) image at 138KX magnification (c)Cross-sectional view of deposited CdTe and ZnS thin films on Si substrate

AFM measurement was done to examine the morphology of the deposited film. We exhibited the AFM pictures in 2-dimensional and 3-dimensional forms in an area of 2 x 2 μm^2 in figs. 4.4(a) and 4.4(b). The root mean square, maximum and average surface roughnesses were found to be 0.69, 9.20 and 0.52 nm, respectively.

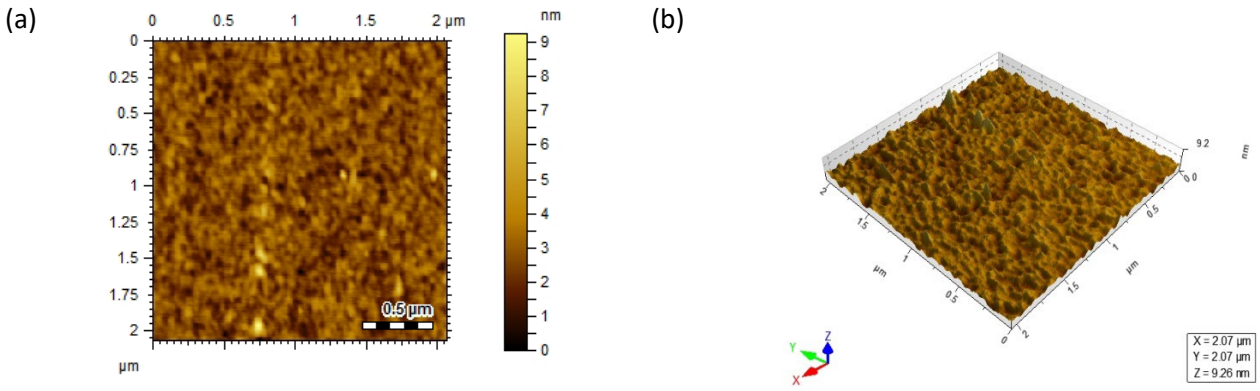

Figure 4.4: The AFM images of ZnS film (a) 2-dimensional image (b) 3-dimensional image

In order to draw vital conclusions, the surface roughness should not exceed 5% of the depth at which outcomes are received, according to the 5% nanoindentation thumb rule (Eqn. 4.9). Large errors in the contact area can be caused by surface roughness, which is promptly used to find out the square root of the Young's modulus (E) and the hardness (H). As a result, H is more significantly impacted by surface roughness than E [226-227].

$$h_{min} = (\text{surface roughness}) / 0.05 \quad (4.9)$$

4.3.3 Compositional analysis

The EDX examination results of CdTe and ZnS thin films are shown in the Fig. 4.5(a) and 4.5(b). The overall elemental analysis of the EDX examination is shown in Table 4.4.It is evident from table 4.4 that constituent elements of the deposited layers are Cd, Te, Zn and S elements and no other element is present. The average atomic ratios of Te/Cd and S/Zn are 1.10 & 0.71 respectively. Zn is abundant on the sample surface, and ZnS film has a ratio that is less than the stoichiometric ratio (S/Zn =1). In CdTe film, the film is rich in Te, and relatively more close to the stoichiometric ratio (Te/Cd=1). The variation in vapor pressure between the Zn and S is responsible for non-stoichiometric compositions of ZnS layer [228]. The difference in vapor pressure of Cd and Te is lower; hence, Te/Cd ratio is stoichiometric [229].

(a)

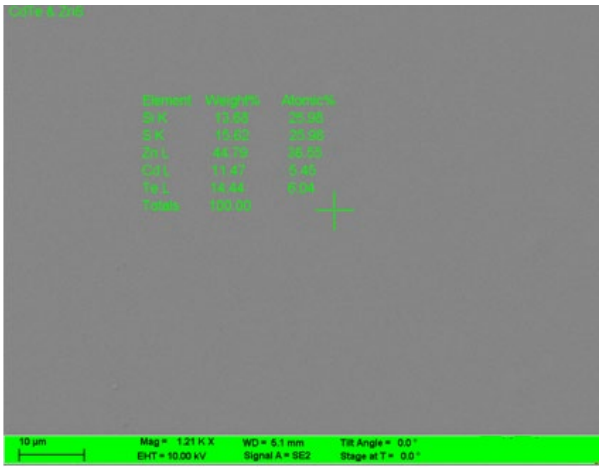

(b)

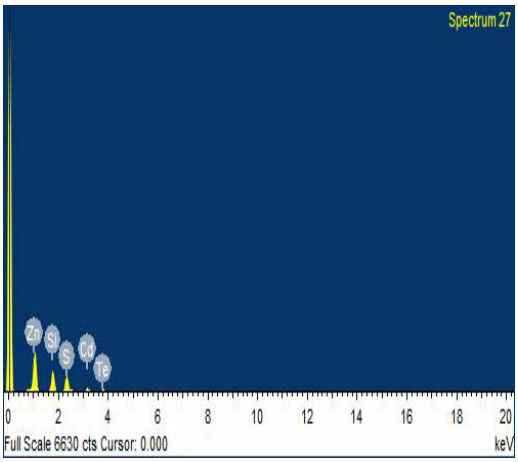

Figure 4.5: EDX pattern of CdTe and ZnS thin films deposited on Si substrate (a) image at 1.21 KX (b) EDX spectrum

Table 4.4: Compositional values of CdTe and ZnS thin films on Si substrate

Atomic %						Weight %					
Te	Cd	Te/Cd ratio	S	Zn	S/Zn ratio	Te	Cd	Te/Cd ratio	S	Zn	S/Zn ratio
6.04	5.45	1.10	25.98	36.55	0.71	14.44	11.47	1.28	15.62	44.79	0.34

4.3.4 Dektak surface profiler film thickness measurement

The deposited combined (CdTe & ZnS) film thickness is shown in Fig. 4.6. The combined film thickness was measured by Dektak surface profiler with diamond tip of 12.5 µm and the thickness (step height) of combined film was found 250 nm. The total thickness measured by the cross-section SEM micrograph of the film was reconfirmed as a result of this method

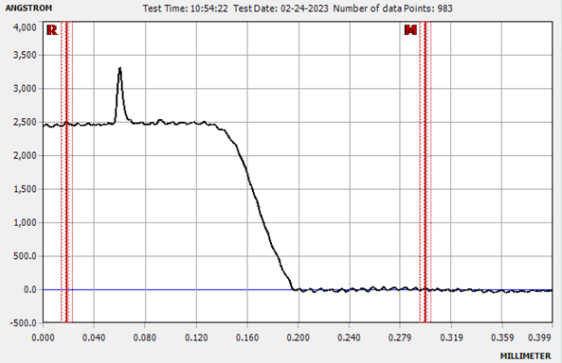

Figure 4.6. Dektak surface profiler step height (film thickness) of combined (CdTe and ZnS) thin film deposited on Si substrate

4.3.5 Nano mechanical analysis

We conducted several indentation runs on the film and applied the techniques reported in [129,131, 230-232], which were based on the Eqns. (4.10) and (4.11) to find out the Young's modulus (E) as well as hardness (H):

$$\frac{1}{E_r} = \left[\frac{(1-\nu_f)}{E_f} + \frac{(1-\nu_i)}{E_i}\right] \tag{4.10}$$

where νf and ν_i were the film and indenter Poission's ratios, respectively. E_f and E_i were the film and indenter elastic moduli, respectively.

$$H = \frac{P}{A} \tag{4.11}$$

where P was the load and A was the contact region.

As shown in Fig.4.7, 4.9 &4.10, ZnS thin film of 150 nm thickness was indentured with a Berkovich tip to test the creep and strain rate behavior and evaluate the mechanical parameters. In Fig.4.8 scanning probe microscopy (SPM) indentation images at loads of 50, 70 and 100 µN are shown.

Fig. 4.7 (a) & (b) show hardness and Young's modulus of ZnS thin film, whereas Fig. 4.7 (c) depicts the maximum depth of indentations under various loads. The ZnS film's hardness and Young's modulus were evaluated at loads of 50, 70 and 100µN. In the ZnS film, the Young's modulus was decreasing with increasing applied load. Due to the microstructure of the film and bulk differing, ZnS film's hardness was lower than that of bulk CdTe (knoop hardness 3.6 GPa) and ZnS (mohr hardenss 3.8). If the depth of penetration is more than 10% [233-234], it is an accepted rule of thumb in nanoindentation that the substrate will be affected by the hardness. Fig. 7 depicts indentation size effect (ISE) with a larger hardness with regard to lesser penetration

depths. The mechanical characteristics are governed by the depth of the indenter's indentation on the test surface [235-238]. Geometrically essential dislocations (GNDs) and statically stored dislocations (SSDs), that arise when there is no strain gradient, obstruct the creation and motion of new dislocations [237, 239-240]. This caused a strengthening result and explains the detected rise in hardness for the CdTe-ZnS thin film at shallower contact depths. The Hall-Petch effect also additionally leads to reduced hardness compared to bulk.

Both the dislocation density process and pile-up mechanism can lead to hardening. The quantities of dislocation stack-up were nonetheless restricted through the nanosized grains in the film's submicron thickness. The greater hardness seems to be principally caused by dislocation density process.

With maximum loads of 50, 70 & 100μN and hold duration of 20 s, creep was shown for typical load-displacement curves in Fig. 4.10. Fig. 4.9 depicts the indentation-displacement curves for various strain rates for maximum load of 100 μN and loading-unloading duration of 0 and 20 s. For the creep data, the displacement throughout the holding period for loads of 50, 70 and 100 μN differ; hence the end points of the unloading curves for all the loads almost coincide. A small displacement of about 5 nm indicated by the unloading curves for 0 s and 20 s hold time from strain rate data. Both tests were carried out at room temperature. Even at ambient temperature, most materials can exhibit creep [241]. Diffusional creep was considered to be the cause of the increased displacements seen in the creep and strain rate [242-243]. The low reaction of the ZnS film to creep and strain rate was applicable in microscopic tribological usages where there was a continuous load or variable load.

It was interesting to know that although we deposited CdTe (100 nm) as first layer and ZnS (150 nm) as second layer both having different hardness and densities (CdTe 5.85 g/cm^3, ZnS 4.09 g/cm^3), the loading and unloading curves of load-displacement curves do not showed sudden change or step (pop-in & pop-out) rather continuous curves were observed. This may be because both the films were of nearly same crystallite sizes. Indentation on top layer (ZnS thin film) does not propagate any cracks or discontinuities on the CdTe thin film on the Si substrate.

(a)

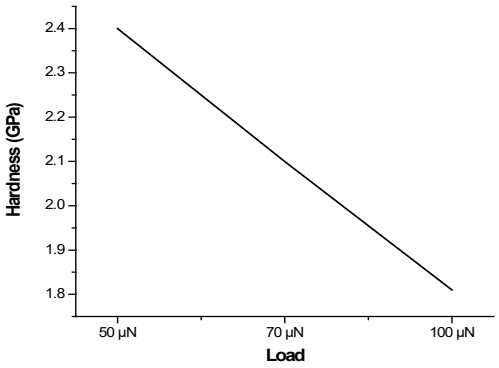

(b)

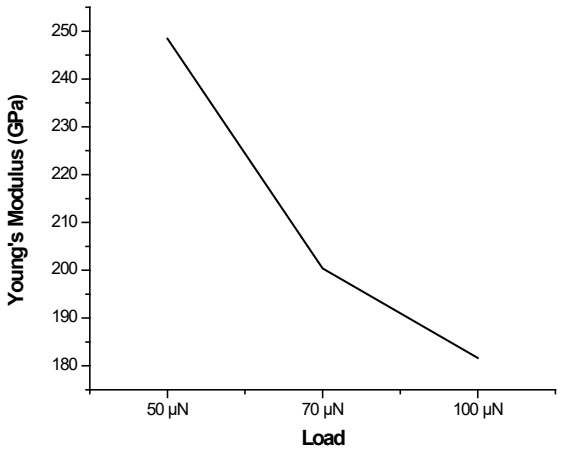

(c)

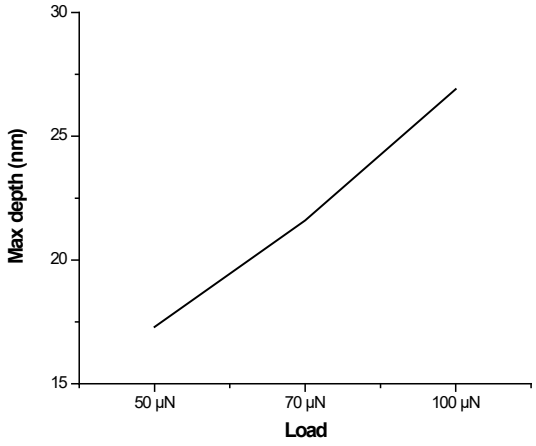

Figure 4.7: ZnS film's mechanical properties (a) Hardness (b) Young's modulus (c) Maximum depth

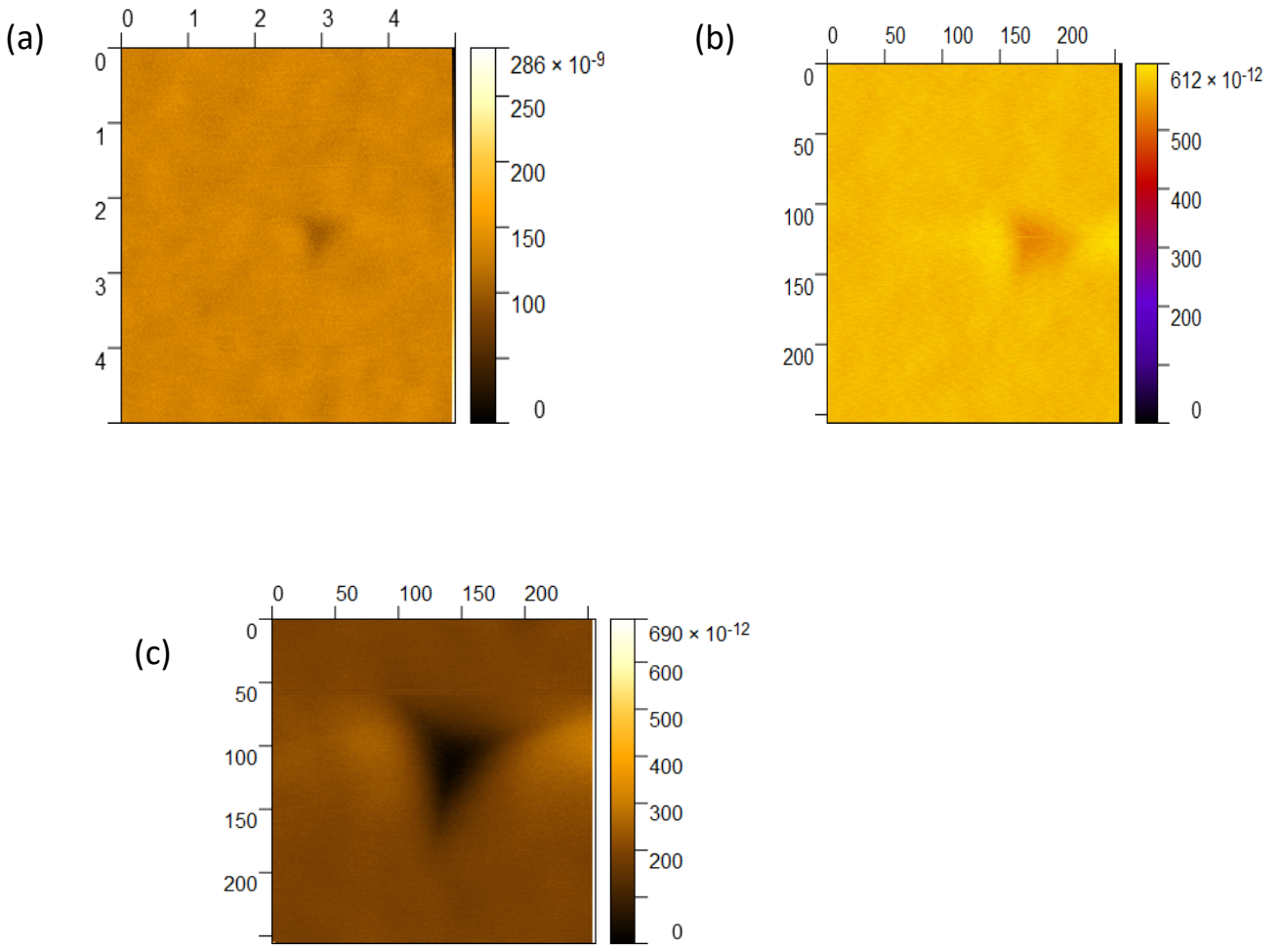

Figure 4.8: Indentation load impression images of ZnS film (a) at load of 50 µN (b) 70 µN (c) at load of 100 µN

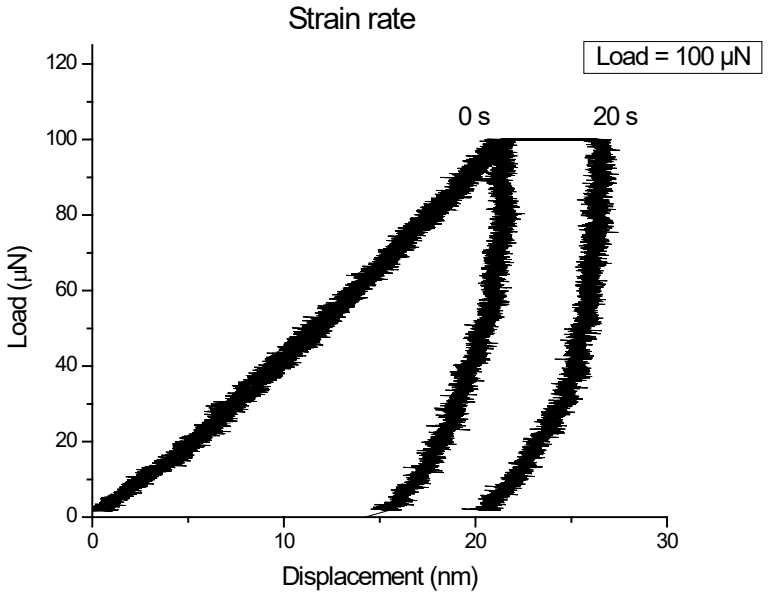

Figure 4.9: Strain rate of ZnS thin film on Si substrate

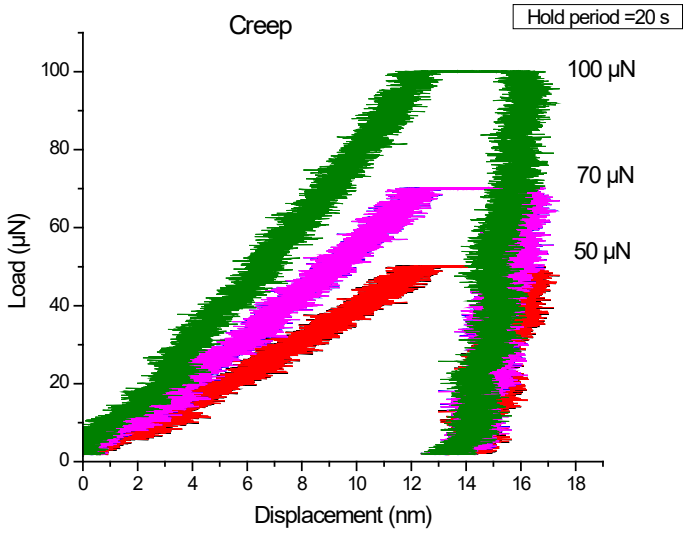

Figure 4.10: Creep rate of ZnS thin film on Si substrate

4.4. Conclusions

In this study, CdTe and ZnS thin films were grown on Si substrate by thermal evaporation process. The XRD examination of both the films confirmed that the films were polycrystalline and exhibited cubic structure with the intense diffraction in the preferred orientation along (111) plane.

Lattice constant, crystallite size, dislocation density, intrinsic stress, strain and stacking faults of both the thin films were found from XRD data. The crystallite size and microstrain of CdTe film were higher than ZnS film but intrinsic stress stacking fault and dislocation density were lower than the ZnS film. SEM images revealed that the ZnS film's coverage on the substrate was uniform with no pinholes or cracks. The compositional analysis by EDX indicated that Te/Cd atomic ratio stoichiometric and S/Zn atomic ratio was less stoichiometric in the grown thin films. The AFM images showed that the film was even and had low surface roughness. Nano-indentation tests revealed that the hardness and Young's modulus decrease with increasing load. Hardness and Young's modulus of ZnS film were greater for shallow depth of indentation. The strain rate of ZnS film was determined at a maximum load of 100 μN and creep was determined at loads of 50, 70, 100 μN loads for 20 s. The absence of pop-in and pop-out during nano-indentation revealed that the film's mechanical properties fairly improved due to enhancement of structural properties like grain boundaries, dislocation density, interstitial atoms, and surface roughness. The combined thin films of CdTe and ZnS on Si substrate was found to be a good engineering approach suitable in photovoltaic and other optoelectronic devices meeting the required structural and mechanical properties. Absence of distortion or cracks due to stress as a consequence of nano-indentation confirms the utilization of vacuum evaporated thins films of ZnS/CdTe for photovoltaic applications.

CHAPTER 5

STUYD OF EVAPORATED CdTe AND ZnS THIN FILM'S CRYSTALLOGRAPHIC, MORPHOLOGICAL, NANOMECHANICAL AND ELECTRICAL CHARACTERISTICS FOR OPTOELECTRONIC DEVICES

5.1. Introduction

Evaporation of high-quality thin films of CdTe and ZnS shows potential for applications in highly rugged photovoltaic, industrial development, and further optoelectronic devices. The process entails applying a thin coating to the semiconductor substrate. A potential material for a variety of optoelectronic uses, including solar cells, field-effect transistors, infrared (IR) detectors, nuclear radiation detectors, etc., is CdTe [244-247]. Passivation for small gap semiconductor devices, like infrared detectors made of $Hg_{1-x}Cd_xTe$, is one example of this use. In addition to being substantially lattice matched and chemically compatible with these small gap semiconductors, CdTe is transparent to infrared light. Surface leakage currents as well as leakage all the way through the passivation typically limit the performance of tiny devices made with premium semiconductor materials. Electrical isolation from the substrate underlayer, optical transparency, high surface morphological quality, low fixed charge density, good adhesion, and chemical stability are all characteristics of a good passivation layer for solar systems. Additionally, the passivation layer must to be appropriate for subsequent device processing stages. When the thickness of the cap-layers is maintained below 3000 Å, the CdTe produced exhibits these characteristics. [248]. Due to breakdown and favored evaporation of the lower vapor pressure constituent atom, stoichiometric compound films of compound insulators are unquestionably difficult to make by evaporation. Surfaces of p-type materials are frequently passivated using native sulfides and evaporated zinc sulfide [248-251].The ZnS/CdTe hetro-junction was fabricated by using the traditional vacuum deposition process and the sequential ionic layer adsorption and reaction (SILAR) method. The current-voltage, current-capacitance, and J-V features were examined [173]. According to O. Toma et al., devices of photovoltaic type with ZnS/ZnSe/CdTe type double hetero junctions upon glass and indium tin oxide-coated glass were fabricated using thermal evaporation and radio frequency sputtering technologies. For multilayer double heterojunction structures to have a strong photovoltaic response, the deposition conditions were improved [174].

Despite not being externally loaded, thin films are continually under stress. Stress in thin films directly affects a wide range of phenomena, including adhesion, the formation of crystallographic defects, the perfection of epitaxial deposits, and the development of film surface growth such hillocks and whiskers. The characteristics of thin films are significantly impacted by stress. It has the ability to alter thin film properties such as mechanical, electrical, and optical. There are numerous instances that demonstrate how mechanical stresses can cause changes in the band gap in semiconductors, the transition temperature for semiconductor films, or the anticipated magnetic anisotropy in thin films [252-254]. Giedrous Laukaitis et al. studied the ZnS thin film's crystalline structure, topography, and stress developed. The stress measured by multi-beam optical laser stress

interferometer and observed to vary from tensile to compressive depending upon film thickness [255].

In terms of mechanical characteristics, nanoindentation has been extensively employed to ascertain thin film hardness and elastic modulus [256-260]. Unlike microindentation, however, the contact area does not need to be measured separately for nanoindentation. Through the use of a calibrated indenter tip, the specimen's penetration depth for the duration of nanoindentation is connected to the actual contact area. This method provides a way to measure the hardness and elastic modulus of ultra-thin films, which is challenging to do with conventional approaches. Since the uppermost layers of thin films may be subject to external mechanical impacts including wear, damage, and heat deterioration, it is crucial to understand their mechanical properties. Techniques for nanoindentation have been used recently in in-depth research on thin-film mechanical characteristics [261-262]. Vacuum evaporated CdTe thin film's hardness and Young's modulus was calculated via nanoindentation. It was established that the CdTe thin film's hardness and Young's modulus increase with decreasing grain size [263]. The mechanical characteristics, such as Young's modulus as well as hardness of zinc sulfide film, were analyzed for grain size, structure, and morphology by nanoindentation [264-265].

Ireneusz Strzalkowski et al. evaluated the dielectric constant of evaporated cadmium telluride, GaAs and ZnSe by fabricating rectangular capacitor plate with the gold. The low frequency capacitance measurement revealed the dielectric constant values at 0 K 10.3, 12.3, and 8.8 for CdTe, GaAs and ZnSe, respectively. The dielectric constant increases with increase in temperature [266]. The study of dielectric properties of the vacuum evaporated Ag/CdTe/Ag revealed that the cracks, microvoids, faults, defect centers, and other simple or complicated flaws that could exist in the film at a high enough concentration cause the emergence of both superficial and profound defect states. These states can have three charge states or be donor or acceptor types. By functioning as traps and recombination locations for carriers, these defects have a significant impact on the materials' transport characteristics. Additionally, some donor or acceptor centers that are near together create dipoles, which are in charge of the dielectric behavior. As a result, when an electric field is applied to the disordered grain size of the film, the electrons move between certain locations. Between these locations, the charge carriers transition between donor and acceptor states. Each pair of sites thus contributes to the widespread dielectric relaxation and produces a dipole [267]. A. Goswami et al. measured the capacitance of ZnS film and found that it varies with temperature though it was constant at low temperature. They studied that the dielectric constant of ZnS film was constant for frequency and thickness [268]. The current–voltage non-ohmic features for as-deposited In/n-ZnS and Au/n-ZnS heterojunctions measured. The conductance of ZnS film with Au and In were found to be 9.14×10^{-10} and 1.49×10^{-9} $(\Omega cm)^{-1}$ respectively [269]. As a result, it is best to first maximize the merit of these films independently as a dielectric material before employing them. In order to provide a factual image of conduction by the insulator, leakage currents are typically examined by creating MIM parallel-plate capacitors.

This study evaluated the crystallographic, morphological, topographical, optical, nano-mechanical, and dielectric characteristics of CdTe and ZnS films produced by vacuum evaporation. To maximize the vacuum sublimation procedure, the films' crystallographic, morphological, topographical, optical, as well as nano-mechanical characteristics were examined. We created three metal-insulator-metal (MIM) capacitors: Cr-Au/CdTe/Cr-Au MIM , Cr-

Au/ZnS/Cr-Au MIM and Cr-Au/CdTe-ZnS/Cr-Au MIM. At room temperature (300 K) and at low temperature (77 K), the capacitance of both capacitors was measured using the four probe method. The examination's findings showed that the cadmium telluride and zinc sulfide films were suitable or helpful for usage in both photovoltaic and optoelectronic devices.

5.2. Materials and Methods:

Cadmium telluride as well as zinc sulfide films were vacuum sublimated on a silicon substrate using tiny pieces of the compound material. Two successively organized molybdenum boats were filled with the CdTe (99.99%) and ZnS (99.99%) pieces. The vacuum chamber has been drained using a pressure of $1x10^{-6}$ mbar. Then, using fixed procedure parameters (rates of evaporation: 1, 5, and 10 angstroms/second; current of evaporation: 20-110 ampere by means of a bias voltage of 20 volts), the silicon substrate was used to develop cadmium telluride and zinc sulfide films with thicknesses of 200 nm and 400 nm, respectively. By regulating the feed current, the quartz crystal's automated rate controller managed the coating rate and film thickness. The complete evaporation of ZnS and CdTe thin films was accomplished at room temperature (25°C). Additional structural, electrical, and nanomechanical analyses were conducted using the deposited film.

For the C–V characterization of CdTe and ZnS film, circular metal–insulator–metal (MIM) capacitors were evaporated at a 1 Å/s optimized evaporation rate on a semi-insulating Si substrate. A thin layer of gold (3000 Å)/chromium (350 Å) was first applied to the silicon via evaporation in that order. The purpose of the thin Cr metal interlayer is to increase Au's adherence to the Si substrate. Vacuum evaporation was then used to evaporate a thin (1000 Å) film of CdTe and ZnS (2000 Å) at an evaporation rate of 1 Å/s at ~10^{-6} mbar vacuum. After that, the film was patterned into 700 µm-diameter circles using conventional photolithography methods in order to deposit the top gate metal electrode. In order to fabricate the final MIM capacitors, a layer of chromium (350 Å) and gold (3500 Å) was evaporated on the motif substrate and removed. A quartz crystal thickness controller installed within the evaporation system was used to track the layer thickness. The gate electrode is made up of the top Au/Cr metals. Figure 11 shows a top view and a sectional view of a part of the manufactured capacitors. To measure the C-V characteristics of ZnS, a Cr-Au/ZnS/Cr-Au MIM capacitor was also fabricated. The ZnS (thickness 4000 Å) was evaporated at an optimized 1 Å/s evaporation rate, and Cr-Au (cromium: 350 Å and gold: 3000 Å) evaporated like the earlier MIM capacitor.

Using a Bragg diffraction (x-ray diffraction) apparatus by Philips- PAN analytical B.V. Xper PRO Material research diffractometer with a copper K- alpha shell with wavelength of 1.542 Å, the crystallographic features of the cadmium telluride as well as zinc sulfide thin films were ascertained. The second drive axis's scanning range was set to 20–70°, and the grazing angle was set at two degree. An atomic force microscope (AFM; 5600 LS-model, AC Model III Module made from Agilent Technologies) and a field emission scanning electron microscope (FESEM; Carl Zeiss SUPRA55VP-model made from Oxford equipment) were used to assess the film's morphology. The optical properties were measured by 640 FTIR spectrometer. The nano-indentation was performed through the Industron Nanoguru NG50 using a Berkovich tip indenter. A surface profiler Alpha step D 500- model was applied to measure the film thickness. A Multibeam optical stress sensor (MOSS) system (k-space associates Inc., Ann Arbor, Michigan)

was utilized to quantify the stress ex-situ deposition. The apparatus was installed into a Flexion AP-1 Cryo test station, and individual capacitors were probed to characterize it at 80 K in total darkness. The probe tip had a diameter of 12 lμm. Silver epoxy was used to create the bottom contact, while the probe tip served as the top contact. A 4200 semiconductor characterization equipment and a Keithley 590 C-V meter were used to perform current-voltage and capacitance-voltage evaluation on huge number of capacitors. C-V measurements can be used to evaluate how the film's dielectric behavior has changed.

5.3. Results and discussion

5.3.1 Crystallographic characteristics examination

Fig. 5.1(a), 5.1(b), and 5.1(c) depict the crystalline structures of CdTe films at 1, 5, and 10 Å/s evaporation rates as evaluated by X-ray diffraction, respectively. The XRD diffractograms showed that the cubic phase at 2θ was approximately 23.78°, 23.75°, and 23.9° of the (111) preferred plane, respectively, with the strong and intense peak of CdTe films at 1, 5, and 10 Å/s evaporation rates (JCPDS no. 651085) [212,270].At an evaporation rate of 1 Å/s, the CdTe film showed further peaks in the (220) and (311) planes of 39.45° and 46.57°, respectively. Likewise, the other peaks in the CdTe film with an evaporation rate of 5 Å/s were 39.88° and 46.54° at (220) and (311), respectively. The CdTe film's other maxima at the (220) and (311) planes were 39.22° and 46.31° at an evaporation rate of 10 Å/s, respectively. Because it had a more intense peak and a lower FWHM value than the CdTe film that evaporated at 5 as well as 10 Å/s rates, we concluded that the CdTe film that evaporated at a rate of 1 Å/s had superior crystallinity. For optoelectronic applications, especially thin-film solar cells, high-quality CdTe with a low FWHM is widely demanded. This is due to the fact that enhanced material qualities such as more uniform crystallites as well as less strained and device performance are directly correlated with high crystallinity [271**]**. X-ray diffraction was used to characterize ZnS films at evaporation rates of 1, 5, and 10 Å/s, as illustrated in Fig. 5.1(d), (e), and (f), respectively. ZnS films displayed a cubic phase at 2θ angle 28.51°, 28.61°, and 28.66° along the preferred plane (111) at evaporation rates of 1, 5, and 10 Å/s (JCPDS no. 651691) [173,213**]**. ZnS film at 1 Å/s evaporation rate other peaks are at 2-theta angle 47.52° and 56.29° along the (220) and (311) planes, respectively. Other peaks in the ZnS film at 5 Å/s evaporation rate were located along the (220) and (311) planes at 2θ angles 47.57° and 56.29°, respectively. Similar to this, the remaining peaks in the zinc sulfide film at 10 Å/s evaporation rate were located at 2-theta angles 47.71 and 56.35 along the (220) and (311) planes, for example. Since the ZnS film had the lowest FWHM value and more intense XRD peaks than the ZnS film that evaporated at 5 and 10 Å/s, we concluded that the ZnS film that evaporated at 1Å/s exhibited superior crystallinity [272]. The XRD analysis revealed no interdiffusion or phase changes at the interface region. In addition to the hexagonal phase, ZnS typically exists in two distinct phases: the cubic phase, which typically develops at temperatures below 250°C [215]. The cubic phase zinc sulfide films evaporated by vacuum evaporation at temperatures ranging from 200-300 C were reported to have values [214]. The size of crystallite (D) of each of the films was estimated by applying Debye-Scherer's Eqn. (5.1) [272, 273]:

$$D = \frac{0.94\lambda}{\beta Cos\theta} \quad (5.1)$$

where beta (β), lambda (λ), and theta (θ) symbolize the full-width half maximum (FWHM), wavelength and angle of Bragg's diffraction, respectively. Furthermore, the face centred cubic phase lattice constant (a) of cadmium telluride and zinc sulfide films was evaluated by applying the Eqn. (5.2) [273]:

$$a = \frac{\sqrt{h^2+k^2+l^2}}{2sin\theta} \quad (5.2)$$

$$d = \frac{a}{\sqrt{h^2+k^2+l^2}} \quad (5.3)$$

where h, k, and l symbolize miller indices and d was interplannar distance. The film's defect density alongwith microstrains were evaluated by applying Eqn. (4.4) and (4.5) [273-274]. By applying the Williamson Hall Eqn. (5.6), we evaluated the stress of the film [222]:

$$\delta = \frac{1}{D^2} \quad (5.4)$$

$$\varepsilon = \frac{\beta}{4tan\theta} \quad (5.5)$$

$$\sigma_s = Y\frac{(a-a_0)}{2\gamma a_0} \quad (5.6)$$

where Y, a_0, and γ symbolize the Young's modulus, standard lattice constant, and poission's ratio of the films. The stacking fault (SF) was evaluated by applying the Eqn. (5.7)

$$SF = \frac{2\pi^2\beta}{45\sqrt{3tan\theta}} \quad (5.7)$$

By applying Eqn. (5.8), the no. of crystallite per unit area (N) of CdTe and ZnS films was evaluated:

$$N = \frac{t}{D^3} \quad (5.8)$$

where t symbolizes the thickness of the thin film.

The crystalline structural properties of the evaporated CdTe and ZnS films evaporation rates of 1, 5, and 10 angstrom per second for the preferred (111) plane are listed in Table 4.1, including the lattice constant, average crystallite size, dislocation density, residual stress, and micro-strain. According to the X-ray analysis, the lattice constants of the ZnS and CdTe films were analogous with those of the bulk materials. Based on X-ray diffraction results, the crystallograhic parameters such as size of crystallite, dislocation density, stress and micro-strain of the ZnS as well as CdTe films at 1 Å/s were comparable to previously published results [162,224], suggesting that the resulting crystalline characteristics were suitable for a superior crystalline development on optoelectronic and photovoltaic devices. The investigational data made it comprehensible that the

fabrication of thin films was linked to increasing morphological disorder. Thin film formation was associated with light grain size, stress of low value, elevated strain, substantial dislocation density, and stacking faults. The computed mechanical properties showed that the thin films had more disorder than the bulk. Furthermore, the structural parameters were associated with the properties of the passivation film.

Table 5.1 Crystallographic parameters evaluated of cadmium telluride and zinc sulfide films for the dominated (111) plane

	CdTe film			**ZnS film**		
Crystallographic parameters	**1 Å/s evaporation rate**	**5 Å/s evaporation rate**	**10 Å/s evaporation rate**	**1 Å/s evaporation rate**	**5 Å/s evaporation rate**	**10 Å/s evaporation rate**
2θ (°)	23.78	23.75	23.69	28.51	28.61	28.66
Lattice plane (111)	(111)	(111)	(111)	(111)	(111)	(111)
FWHM (°)	0.395	0.406	0.435	0.483	0.707	0.971
Crystallite size , D (nm)	21.47	20.90	19.49	17.72	12.11	8.82
Dislocation density, δ (x 10^{11}) (lines/cm^2)	2.16	2.28	2.63	3.18	6.81	12.85
Strain, ε (x 10^{-3})	8.18	8.41	9.04	8.29	12.09	16.58
Stress, σ_s (GPa)	0.050	0.0299	0.195	0.448	0.006	0.203
No of crystallites /area, N (x 10^{12} cm^2)	2.02	2.19	2.70	3.58	2.25	5.82
Stacking fault (x10^{-3})	3.80	3.90	4.19	4.23	6.21	8.48

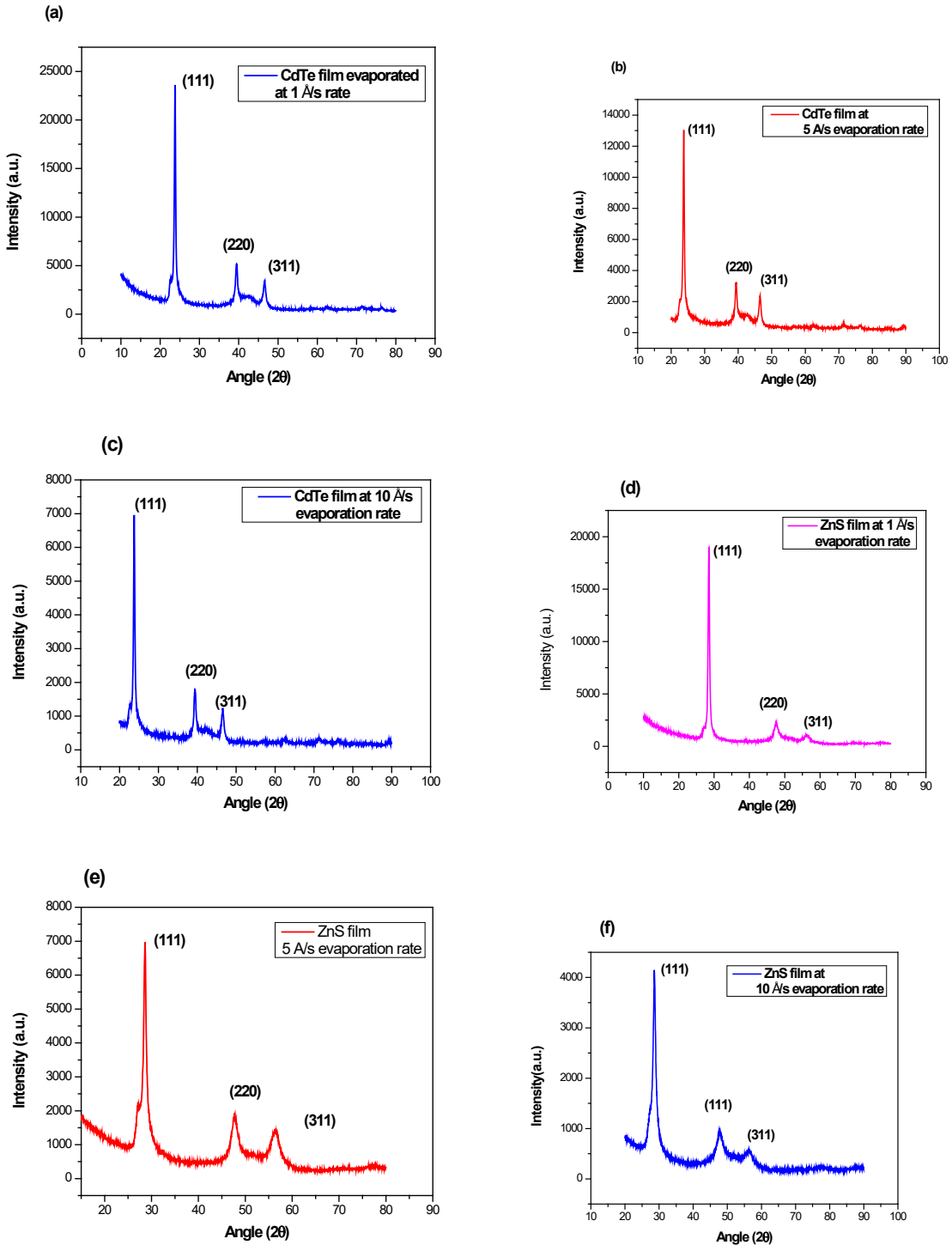

Figure 5.1: The X-ray diffraction spectra of the cadmium telluride and zinc sulfide films. (a) CdTe film evaporation rate of 1 Å/s (b) CdTe film at 5 Å/s (c) CdTe film at 10 Å/s evaporation rate (d) ZnS film at 1 Å/s evaporation rate (e) ZnS film at 5 Å/s evaporation rate (f) ZnS film at 10 Å/s evaporation rate.

5.3.2 Surface morphological examination

The boundaries of grain accrue the grain's crystallite. A compilation of prearranged atoms are built-in in each crystallite. The pattern of the grain outlines causes a high number of messy atoms or entraps defects to occur [275]. Evenness has a noteworthy blow on the decline of defect states at the intersection between CdTe or ZnS film as well as substrate materials used in electrical and optoelectronic devices, like solar cells [173]. CdTe film's SEM images at 1, 5 and 10 Å/s evaporation rates were indicated in Fig. 5.2(a), (b) and (c), respectively. The SEM images of CdTe films indicated that the film evaporation rate of 1 Å/s had dense and smooth morphology with fine grains of different sizes 10 nm to 1 µm sizes with small grain boundaries compared to 5 and 10 A/s evaporation rate where apart from nano scale size grains more no of particles of 1-5 µm sizes present. It appeared that some sort of splashing on the CdTe films at 5 and 10 A/s evaporation rates. CdTe film at 1 Å/s evaporation had visible clear small grains of smaller grain boundaries. Thus, overall CdTe film at 1 Å/s evaporation rate was continuous and had fewer defects such as pinhole, cracks, voids etc. compared to other evaporation rates.

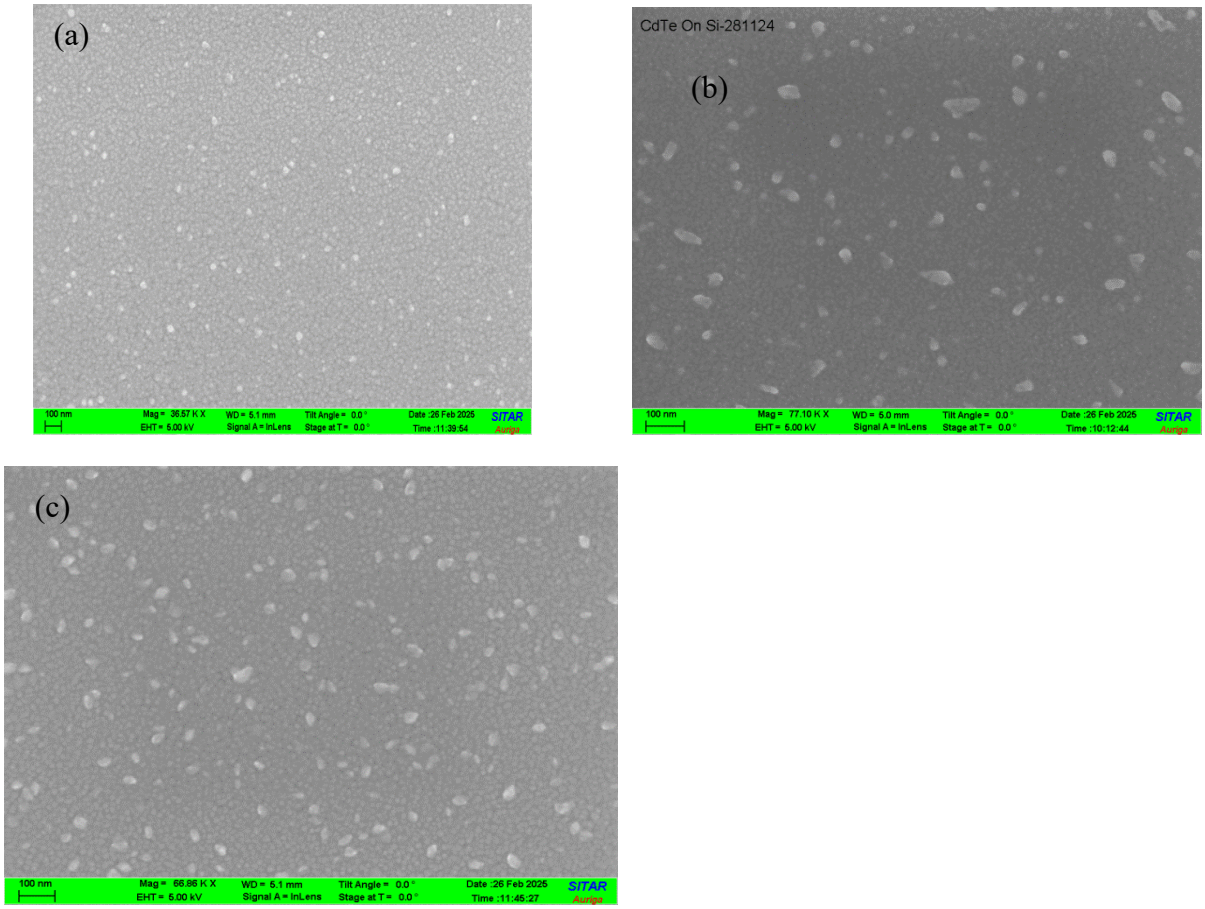

Figure 5.2. SEM micrographs of evaporated cadmium telluride films (a) 1Å/s evaporation rate (b) 5 Å/s evaporation rate (c) evaporation rate of 10 Å/s

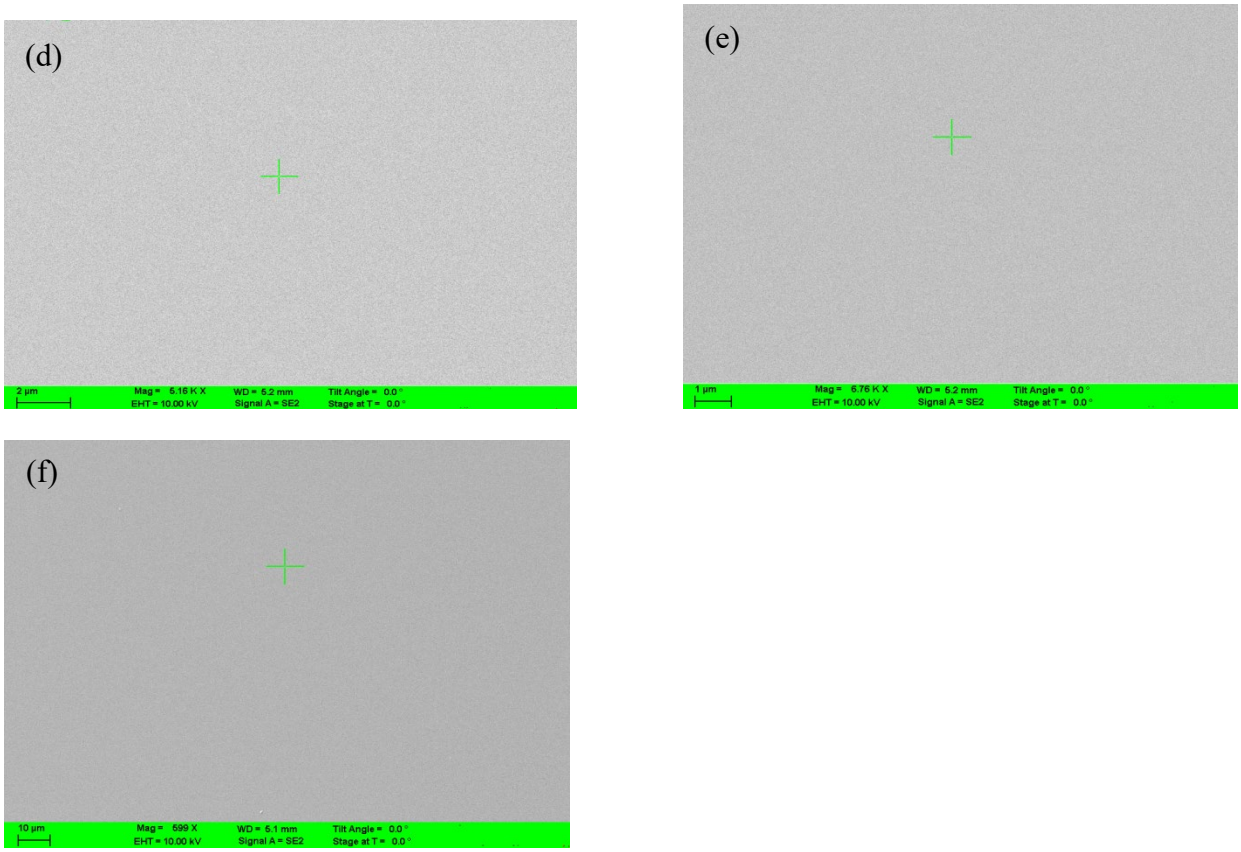

Figure 5.2 SEM micrographs of evaporated ZnS thin films (d) 1 Å/s evaporation rate (e) 5 Å/s evaporation rate (f) 10 Å/s evaporation rate

The SEM micrographs of ZnS film at 1, 5, and 10 Å/s evaporation rates were indicated in Fig. 5.2 (d), (e), and (f), respectively. It was observed that the SEM images of all the ZnS films appeared to be almost even and flat, or the grains were too fine such that the grains were not substantial [273]. The ZnS film SEM images were dense, continuous, and defect-free, such as pinholes, cracks, etc. The grains are composed of crystallites illustrated by X-ray and SEM examination.

5.3.3 Elemental analysis

The EDX inspection outcome of CdTe thin films at 1. 5 and 10 Å/s evaporation rates were revealed in the Fig. 5.3(a),(b),(c),(d),(e) and (f), respectively. Ingredient elements of the evaporated films were Cd, and Te elements no additional element was there. The usual atomic ratio of Te/Cd was nearly stoichiometric ratio at 1 Å/s evaporation rate compared to 5 and 10 A/s evaporation rate. The overall CdTe films were Te rich except at 5 A/s evaporation rates as per the atomic % analysis. The ZnS films EDX inspection at 1, 5 and 10 Å/s evaporation rates were indicated in Fig. 5.3 (h),(i),(j),(k),(l) and(m), respectively. The S/Zn atomic ratio at 1 Å/s evaporation rate was more

stoichiometric ratio compared to the 5 and 10 Å/s evaporation rates. The ZnS film at 10 Å/s evaporation rate had small amount of fluorine elements present which may be due to man handling. The overall ZnS films at 1, 5 and 10 Å/s evaporation rates were rich in sulphur as per the atomic % analysis. Sulphur rich films are advantageous for their high, wide bandgap (about 3.6 eV), which makes them excellent optical windows, transmitting higher energy photons in semiconductor devices like CIGS and solar cells [276]. The distinction in vapor-pressure among Cd and Te present less compared to between Zn and S which was the reason for variation of CdTe and ZnS film stoichiometric composition [229,277]. On the whole compositional analysis (atomic % and weight %) of the CdTe and ZnS films EDX inspection was revealed in Table 5.2.

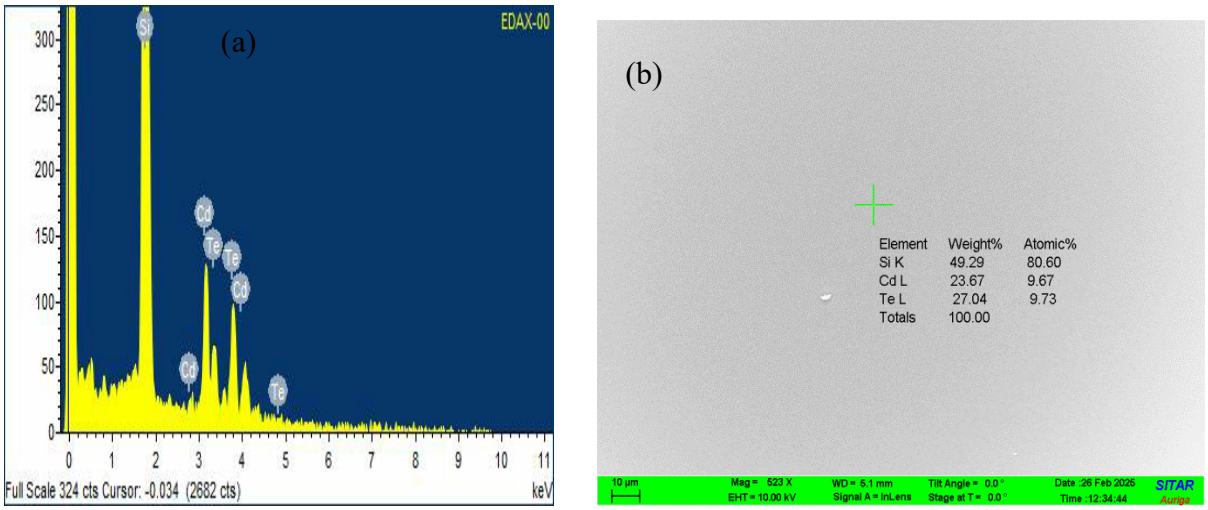

Figure 5.3 EDX pattern of CdTe film evaporation rate of 1 Å/s (a) EDX spectrum (b) SEM image with elemental %

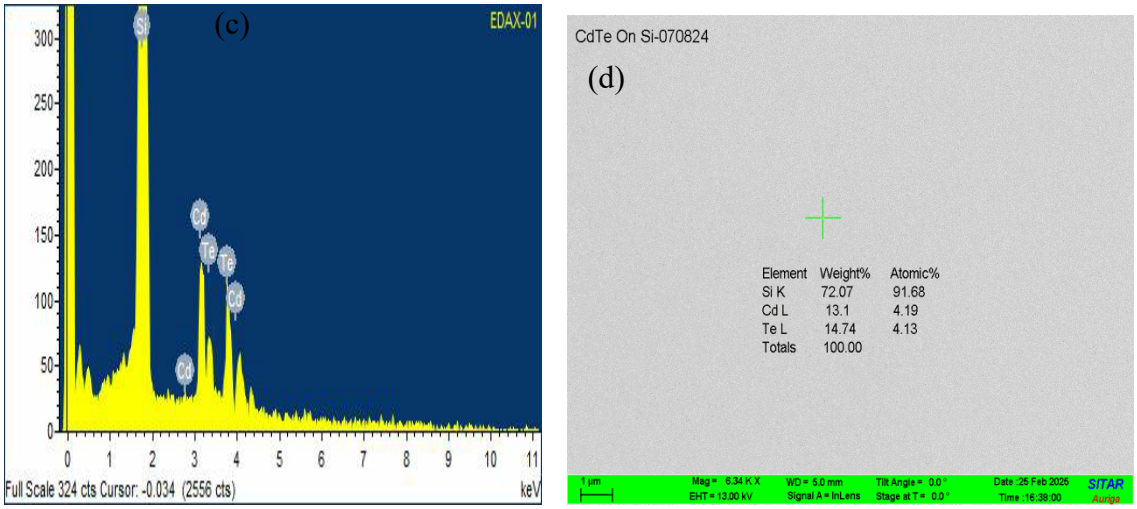

Figure 5.3: EDX pattern of CdTe thin film at 5 Å/s (c) EDX spectrum (d) SEM image with elemental %

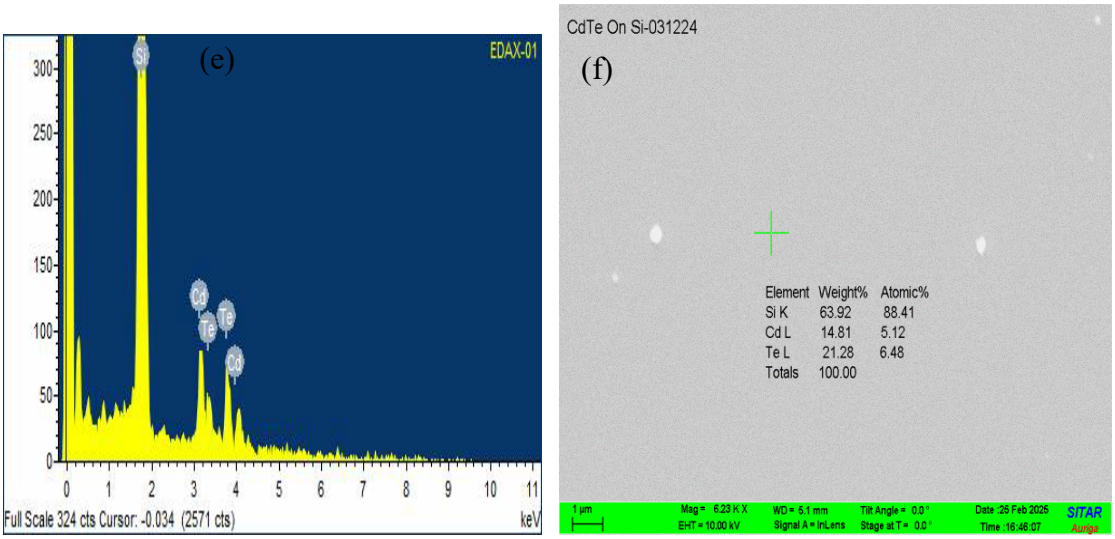

Figure 5.3: EDX pattern of CdTe thin film at 10 Å/s (e) EDX spectrum (f) SEM image with elemental %

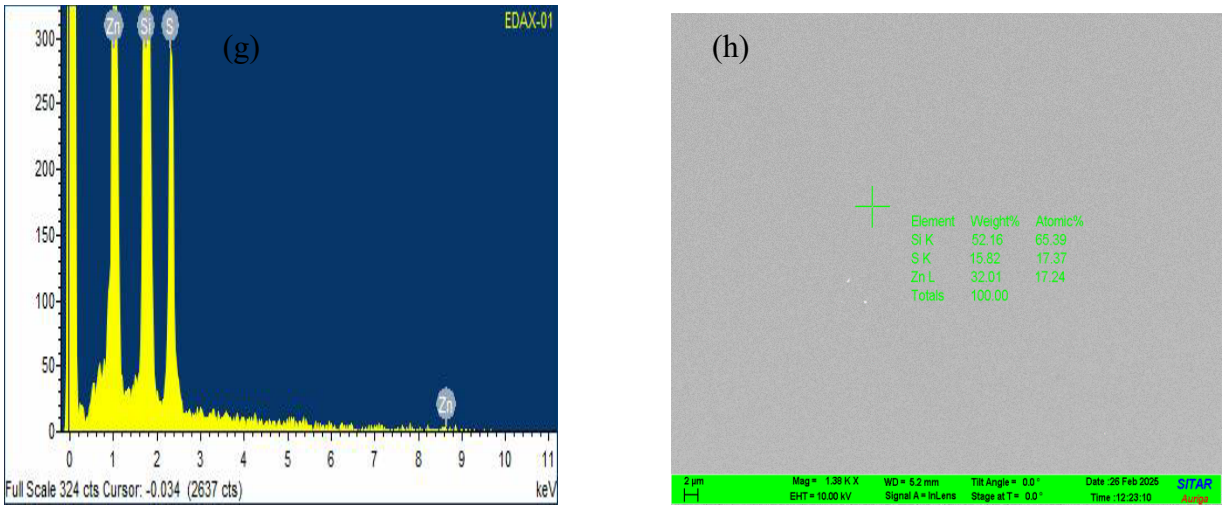

Figure 5.3: EDX pattern of ZnS thin film at 1 Å/s (g) EDX spectrum (h) SEM image with ZnS elemental %

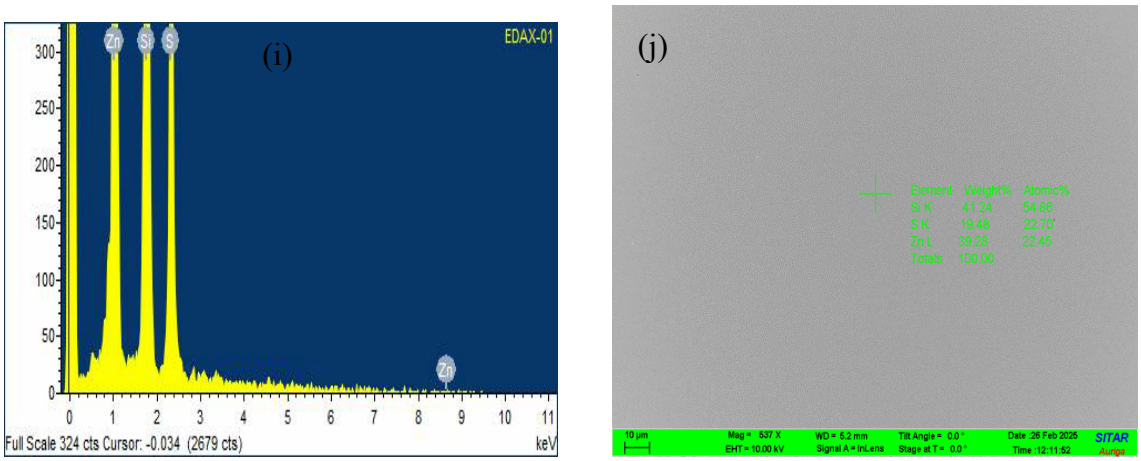

Figure 5.3: EDX pattern of ZnS thin film at 5 Å/s (i) EDX spectrum (j) SEM image with ZnS elemental %

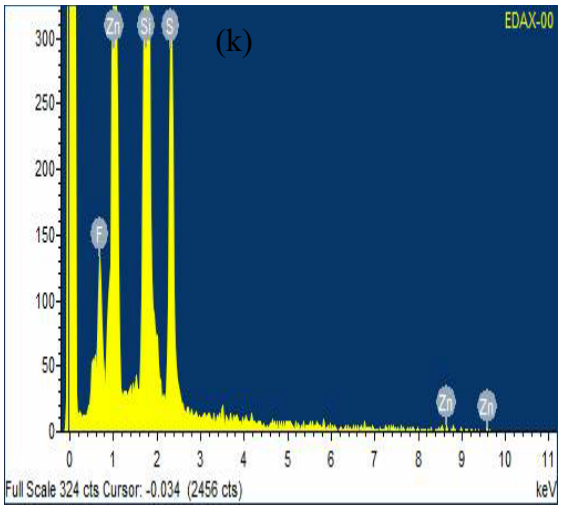

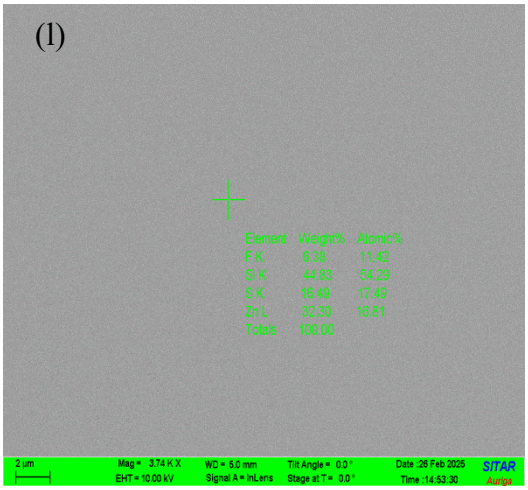

Figure 5.3: EDX pattern of ZnS thin film at 10 Å/s (k) EDX spectrum (l) SEM image with ZnS elemental %

Table 5.2: Elemental analysis of CdTe and ZnS thin films

	Atomic %						Weight %					
Evaporation rate	Te	Cd	Ratio of Te/Cd	S	Zn	Ratio of S/Zn	Te	Cd	Ratio of Te/Cd	S	Zn	Ratio of S/Z
1 Å/s	9.73	9.67	1.0006	17.37	17.24	1.0075	27.04	23.67	1.14	15.82	32.01	0.49
5 Å/s	4.13	4.19	0.9856	22.70	22.45	1.0111	14.74	13.10	1.12	19.48	39.28	0.50
10 Å/s	6.48	5.12	1.2656	17.49	16.81	1.0404	21.28	14.81	1.43	16.49	32.30	0.51

5.3.4 Topography analysis

AFM evaluation was done to study the surface morphology of the evaporated CdTe and ZnS films. We exhibited the CdTe film's AFM micrographs at 1, 5 and 10 Å/s evaporation rates in 1D line diagram, 2-dimensional and 3-dimensional forms in an area of 5 x 5 μm^2 in Fig. 5.4(a), (b),(c),(d), (e),(f), (g), (h),(i), (j), (k), (l), (m), (n),(o),(p),(q), and (r), respectively. The 1D line diagram is cross-section of an AFM height picture, indicating the surface topography along a selected line. It

indicates a thorough 1D view of surface characteristics and their height variations. The 1D line diagram of CdTe film at 1 Å/s evaporation rate was smoother than other evaporation rates. The root mean square surface roughnesses of CdTe film at 1, 5 and 10 Å/s evaporation rates were 0.84, 1.64 and 7.40 nm respectively [278]. Thus, CdTe film at 1 Å/s evaporation rate had lowest surface roughness compared to other evaporation rate and compatible to the earlier reported results. The ZnS film's lD line diagram at 1 Å/s evaporation rate was more even or smooth than the 5 and 10 Å /s evaporation rate as shown in Fig. 5.4 (j), (m) and (p). The ZnS film's surface roughness at 1, 5 and 10 Å/s evaporation rates were 0.49, 0.56, and 1.27 nm, respectively [221,279]. The ZnS film at 1 Å/s evaporation rate had lowest surface roughness among all the evaporation rates.

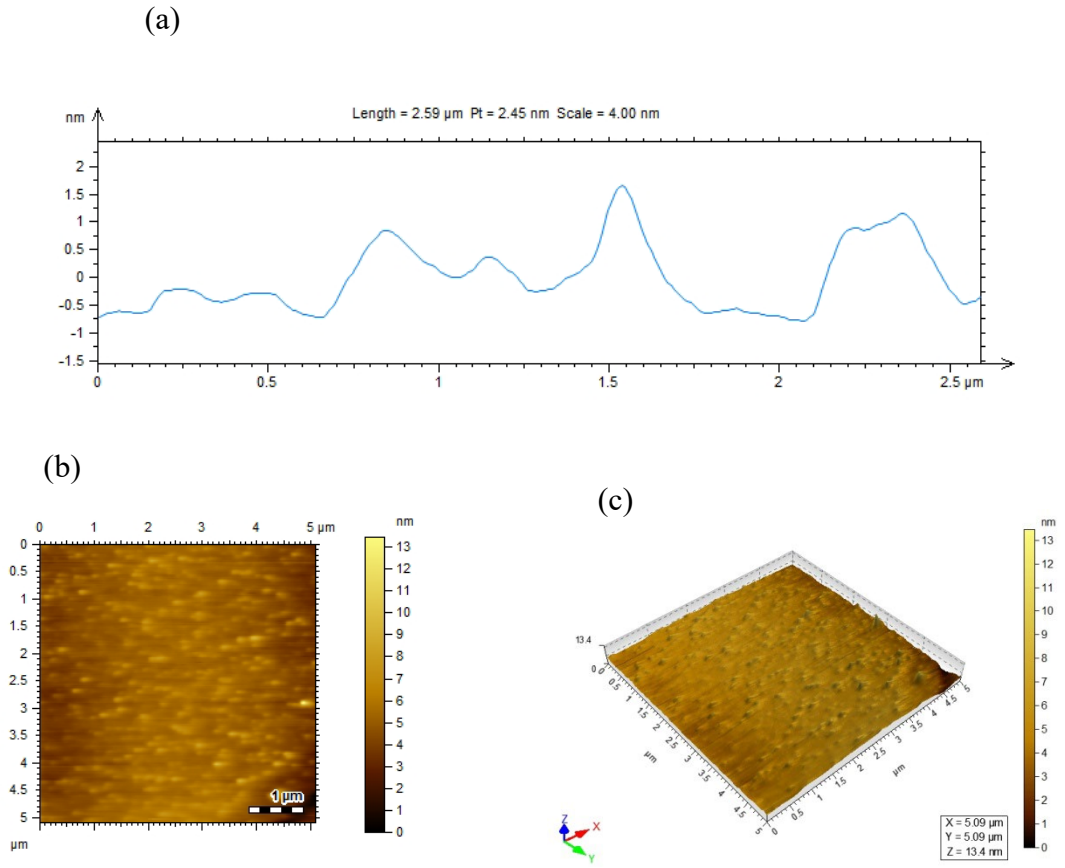

Figure 5.4: The AFM pictures of CdTe film at 1 Å/s evaporation rate (a) 1D line diagram (b) 2-dimensional picture (c) 3-dimensional picture

(d)

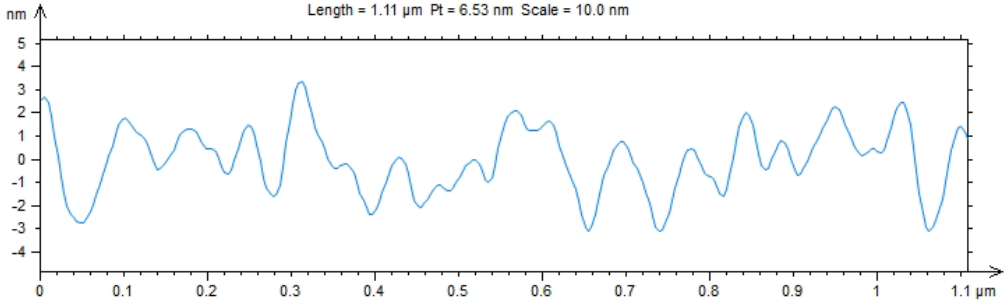

(e)

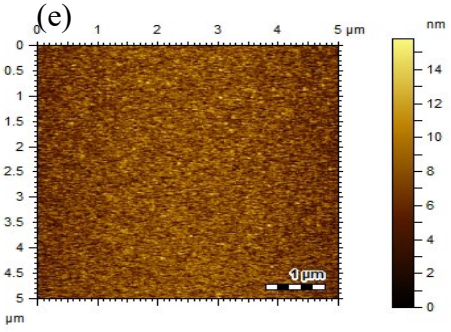

(f)

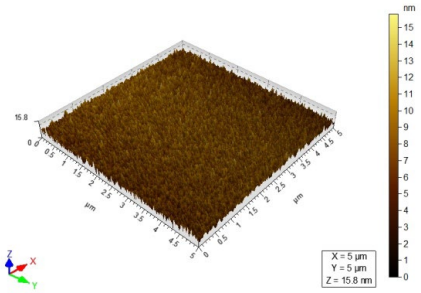

Figure 5.4: The AFM pictures of CdTe film at 5 Å/s evaporation rate (d) 1D line diagram (e) 2-dimensional picture (f) 3-dimensional picture

(g)

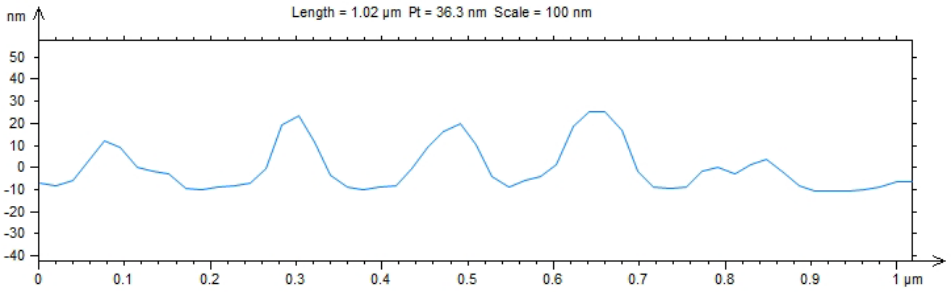

(h)

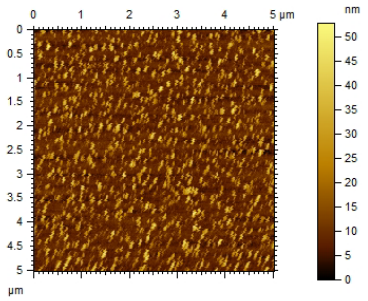

(i)

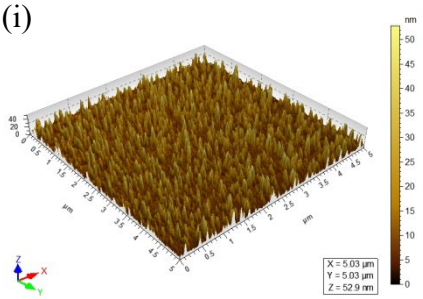

Figure 5.4: The AFM pictures of CdTe film at 5 Å/s evaporation rate (g) 1D line diagram (h) 2-dimensional picture (i) 3-dimensional picture

(j)

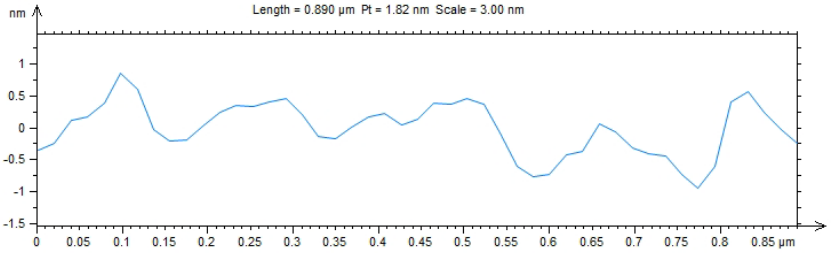

(k)

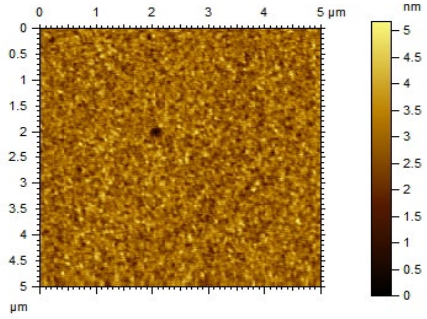

(l)

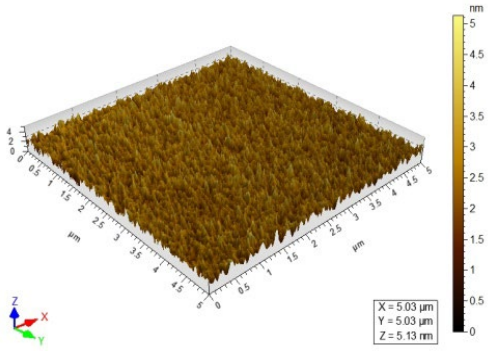

Figure 5.4 The AFM pictures of ZnS film at 1 Å/s evaporation rate (j) 1D line diagram (k) 2-dimensional picture (l) 3-dimensional picture

(m)

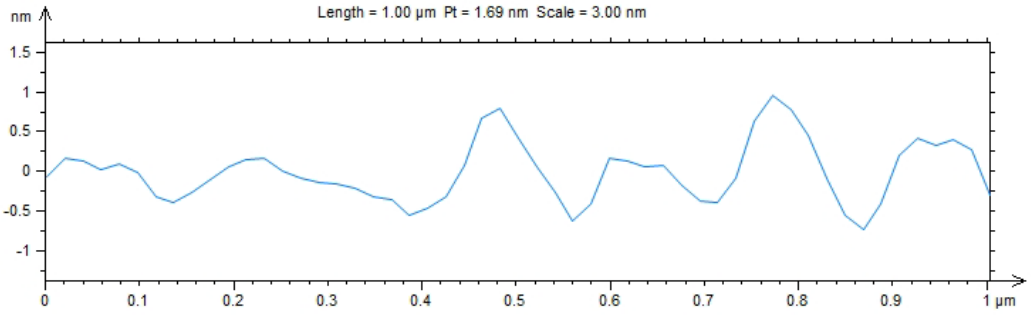

(n)

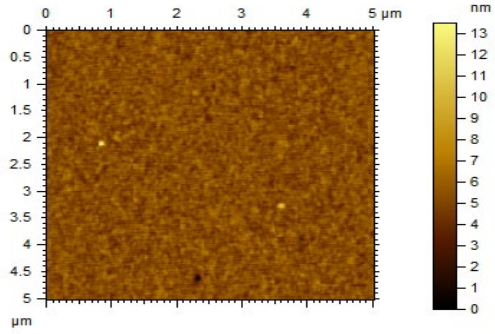

(o)

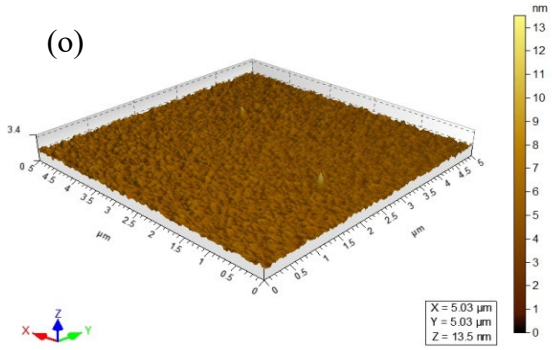

Figure 5.4 The AFM pictures of ZnS film at 5 Å/s evaporation rate (m) 1D line diagram (n) 2-dimensional picture (o) 3-dimensional picture

(p)

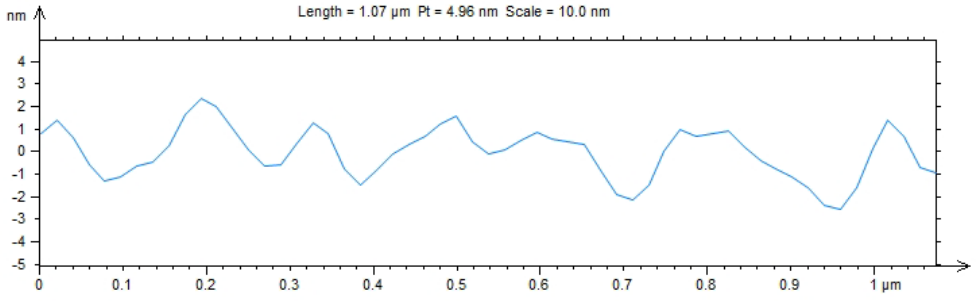

(q) (r)

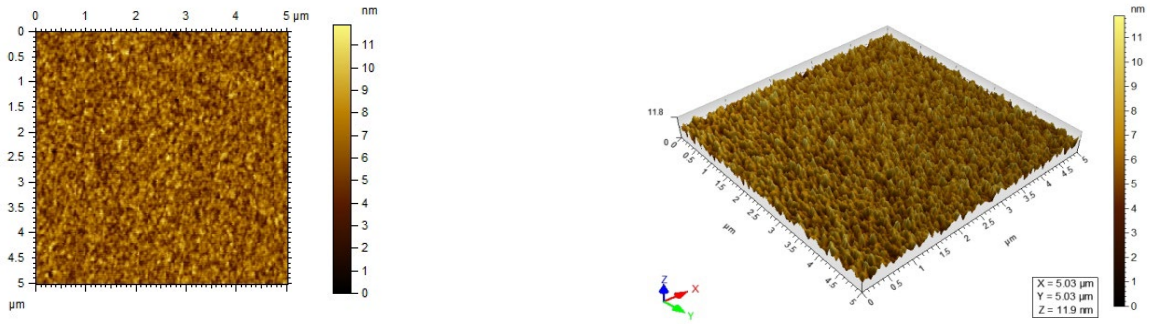

Figure 5.4 The AFM pictures of ZnS film at 10 Å/s evaporation rate (p) 1D line diagram (q) 2-dimensional picture (r) 3-dimensional picture

Table 5.3 AFM surface roughness of CdTe as well as ZnS films evaporation rates of 1, 5, and 10 Å/s

Surface roughness	CdTe film evaporation rate			ZnS film evaporation rate		
	1 Å/s	5 Å/s	10 Å/s	1 Å/s	5 Å/s	10 Å/s
Root mean square S_q , (nm)	0.84	1.64	7.40	0.49	0.56	1.27

One of the most crucial aspects of nanoindentation is surface roughness. The area of contact between the indenter and the specimen is inaccurately determined due to the inherent roughness of real surfaces, as the contact area is estimated indirectly from the depth of penetration. By raising the contact radius, surface roughness often lowers the mean contact pressure. As a result, the depth of penetration and the calculated combined modulus E are both decreased for a given indenter load P. A roughness parameter α can be used to quantify surface roughness Eqn. (5.9) [280]:

$$\alpha = \frac{\sigma_s R}{{a_0}^2} \tag{5.9}$$

, where R is the indenter radius, a_o is the contact radius that would be produced for smooth surfaces under the same stress P, and σ_s is, roughly speaking, equal to the greatest asperity height in Eqn. (5.10). Moreover, in order to depict critical outcomes, the surface roughness of the film should not go beyond 5% of the distance downward at which results are acknowledged, as per the to the 5% nanoindentation thumb law (Eqn. 5.10) [281-282]

$$h_{min} = \text{(surface roughness)} / 0.05 \tag{5.10}$$

Thus the surface roughness achieved at 1 Å/s evaporation of CdTe and ZnS films strongly satisfied the criteria of succeeding nanoindentation study. Though, CdTe and ZnS film evaporated at 5 and 10 Å/s rate also satisfied the criteria of nanoindentaion study.

5.3. 5 Optical characteristics

Optical characteristics of cadmium telluride and zinc sulfide films at 1, 5, and 10 Å/s evaporation rates measured by FTIR spectrometer in the span of 500-4000 nanometer are given in Fig. 5.5 (a) and (b). The CdTe film evaporated at 1 Å/s had the highest transmittance among all the other evaporation rates shown in Fig. 5.5(a). Similarly, the ZnS film evaporated at 1 Å/s also achieved the highest transmittance among the films evaporated at 5 as well as 10 Å/s rates, as indicated in Fig.5.5 (b). The higher transmittance of CdTe and ZnS thin films was due to the presence of lower impurities and low surface roughness at 1 Å/s evaporation rates, as confirmed by the structural and topography studies. Thus, this high transmittance of cadmium telluride and zinc sulfide films, with an evaporation rate of 1 Å/s, makes it suitable for various applications, including use as a window layer in solar cells, in optoelectronic devices, and as a dielectric filter due to its high refractive index.

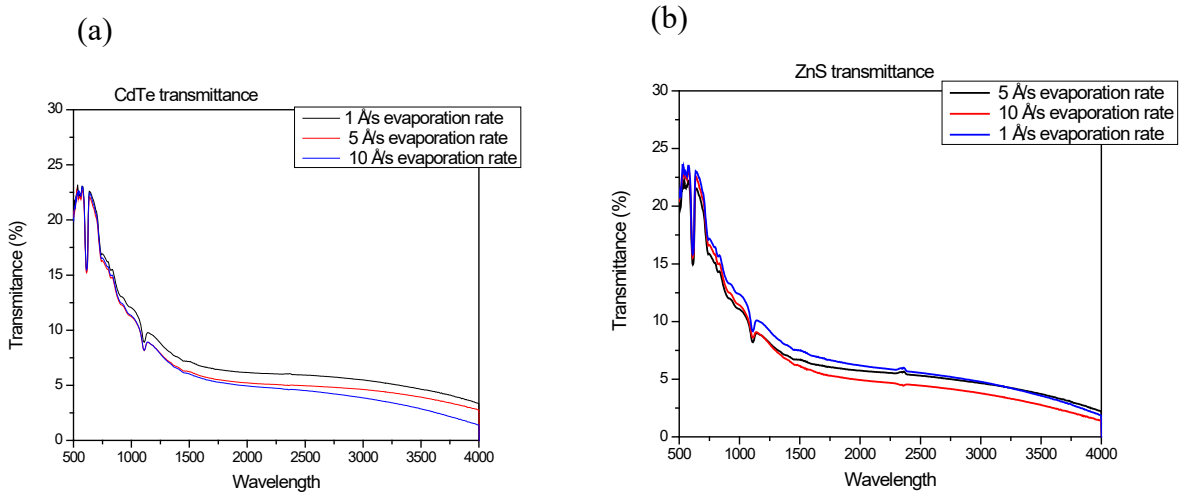

Figure 5.5 (a) Transmittance plot of CdTe film at 1, 5 and 10 Å /s evaporation rate (b) ZnS film at 1,5 and 10 Å/s evaporation rates

5.3.6 Thin film stress measurement

A multibeam optical stress sensor called MOSS, which gauges the curvature a stressed thin film induces in the substrate, was used to track the evolution of film stress ex-situ. A parallel array of beams created by passing a laser through an etalon bounces off the surface of the film. A charge-coupled display (CCD) then images the beam positions. The reflected beam spacing is shifted by the corresponding curvature variation when the film stress varies. The beam spacing (Δd) and substrate curvature (R) are connected by, Eqn. (5.11) [283-285]

$$R = \frac{\Delta d}{d_0}\frac{\cos\alpha}{2L} \qquad (5.11)$$

where L is the distance between the sample and the CCD, $\Delta d/d_0$ is the normalized beam spacing shift, and α is the angle formed by the beam path and the film surface normal. The Stoney formula, which gives an expression for the curvature, can be utilized for transforming the measured curvature into the film stress given the material parameters and geometrical dimensions of a film–substrate system Eqn. (5.12)[283-286]

$$\sigma = \frac{R\, M_s h_s^{\,2}}{6\, h_f} \qquad (5.12)$$

where h_s is the substrate thickness and M_s is the substrate biaxial modulus. As the film develops and relaxes down, h_f and σ both change over time.

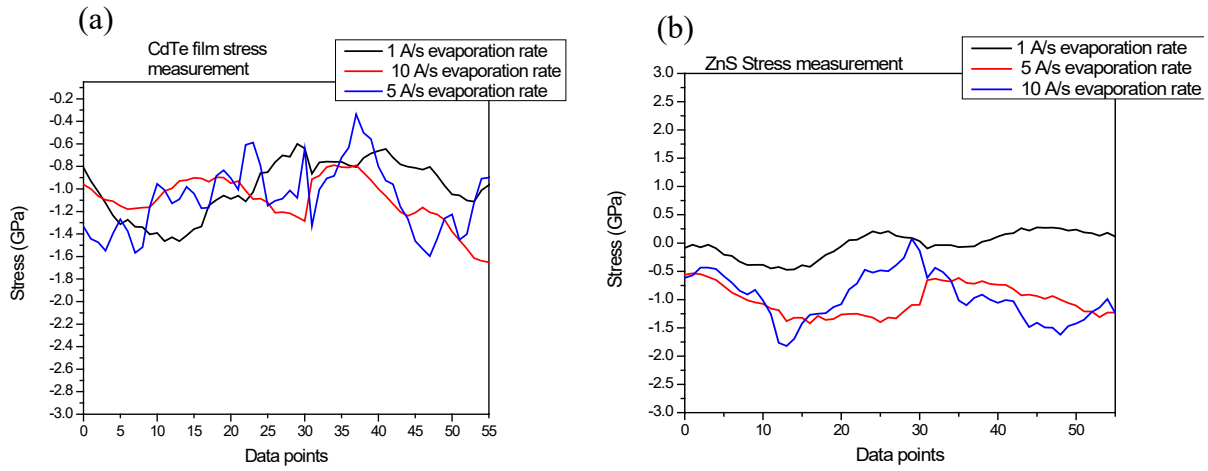

Figure 5.6 Stress measurements at 1, 5 and 10 Å/s evaporation rate (a) CdTe film (b) ZnS film

Table 5.4 CdTe and ZnS film average stress measurement at 1,5 and 10 Å/s evaporation rate

	CdTe film evaporation rate			ZnS film evaporation rate		
	1 Å/s	5 Å/s	10 Å/s	1 Å/s	5 Å/s	10 Å/s
Average Stress (GPa)	-0.9908	-1.0823	-1.0978	-0.0266	-0.9554	-1.0116

Fig. 5.6 (a) and (b) show the stress distinction of CdTe and ZnS film at 1, 5 and 10 Å /s evaporation rates at various points on the film. It was found from Fig. 5.6(a) that the cadmium telluride film the nature of stress produced in the film is entirely compressive at 1, 5 and 10 Å /s evaporation rates. The stress variation of films at different deposition rates are zig-zag and mingle up with each

other. From Table 5.4, we found the CdTe film average stress value is minimum at 1 Å/s evaporation rate and maximum at 10 Å/s evaporation rates which is due to more thermal stress produced at higher deposition rate. Another reason for higher stress at 10 angstrom per second evaporation rate was due to more defect density and more surface roughness generated during film growth. The Fig. 5.6(b) show the ZnS film stress variation at 1, 5 and 10 Å /s evaporation rates at along on the film. It was found from Fig. 5.6 (b) that in ZnS film the nature of stress produced in the film was nearly compressive and variation of stress was less at 1 Å /s evaporation rate. The ZnS films evaporated at 5 and 10 Å /s rate were purely compressive and variation of the stress was more compared to ZnS film evaporated at 1 Å/s. The ZnS film's stress at 1, 5 and 10 Å/s were -0.026, -0.955, and -1.01 GPa (-ve sign due to compressive nature), respectively and compatible to earlier reported results [287]. From Table 5.4, we found that the value of average stress of ZnS film at 1 Å /s evaporation rate had lowest value compared to other evaporation rates. Moreover, the ZnS film evaporated at 1 Å/s evaporation rate had lowest value of average stress than the CdTe film.

5.3.7 Nano mechanical analysis

We performed numerous indentation tests upon CdTe & ZnS films and used the processes studied in [129,131], which were based on the Eqn. (5.13) &(5.14) to evaluate the hardness (H) and Young's modulus (E):

$$\frac{1}{E_r} = \left[\frac{(1- \nu_f)}{E_f} + \frac{(1- \nu_i)}{E_i} \right] \tag{5.13}$$

where E and E_i were the corresponding elastic moduli, and ν and ν_i were the film's and indenter's respective Poission's ratios.

$$H = \frac{P\ (load)}{A(\ contact\ area)} \tag{5.14}$$

The traditional 10% of the thickness rule combined with a sharp indenter seems to be the most widely employed method when there is no strict correlation [241,288-289]. The mechanical properties are run through the deepness of the indent of indenter upon the surface of sample [238,241,290-291]. During plastic deformation, random trapping processes induce statically stored dislocations (SSDs) to assemble. They originate when mobile dislocations, which frequently come from sources including the Frank-Read source, entanglement and multiply. A short-range, local stress field is created by SSDs. They serve as barriers that prevent other mobile dislocations from moving. Isotropic hardening is caused by this process. Geometrically necessary dislocations (GNDs) are generated by strain gradients and are required to keep the crystal lattice compatible when plastic deformation occurs that is not uniform, like bending or indentation. The crystal structure would develop gaps or overlaps in their absence. The size of the damaged region affects the density of GNDs, causing "size effects" in mechanical tests like nano-indentation [239,241,292]. It shows the observed increase in hardness of the cadmium telluride and zinc sulfide

films at superficial contact depths and allowed for an intensification result. In addition, the Hall-Petch results in a lower hardness than bulk. The pile-up mechanism and defect density process can proceed to hardening together. However, the grains of nanoscale in the less than a micron thickness of the film reduced the amount of dislocation stack-up. The flaw density technique appears to be the primary reason of the increased hardness. Creep of diffusional was supposed being origin of the augmented shifts observed in the rate of strain and creep. The little response of the cadmium telluride as well as zinc sulfide film to rate of strain and creep was appropriate within infinitesimal tribological applications wherever nearby an uninterrupted load or unpredictable load. Indentation on the films do not generate any discounties or cracks on the thin films on substrate.

The hardness and Young's modulus of CdTe and ZnS films at 1, 5 and 10 Å/s evaporation rate are shown in Fig. 5.7 (a) and (b). From Fig. 5.7(a) it was found that the highest value of hardness and Young's modulus were 753.51 MPa and 141.90 GPa, respectively at 1 Å /s evaporation rate of CdTe films for 80 µN load. Similarly, from Fig. 5.9(b), it was observed that the highest values of hardness and Young's modulus were 1540 MPa and 265.97 GPa, respectively at 1 Å/s evaporation rate of ZnS films for 90 µN load. The highest values of hardness and Young's modulus of CdTe and ZnS films at 1 Å/s evaporation rate were due to lower crystallite size or grain size (based on Hall-Petch relation), shape, lower surface roughness, low residual stress, low defect density, and crystallographic orientations, all of which had profound effects on the mechanical characteristics of polycrystalline thin films [293-296]. For ZnS we applied higher load (90 µN) while for CdTe lower load (80 µN) due to more film thickness of ZnS film compared to CdTe. As maximum depth can be taken more for nanoindentation load in order to compensate the substrate effect during measurement.

(a)

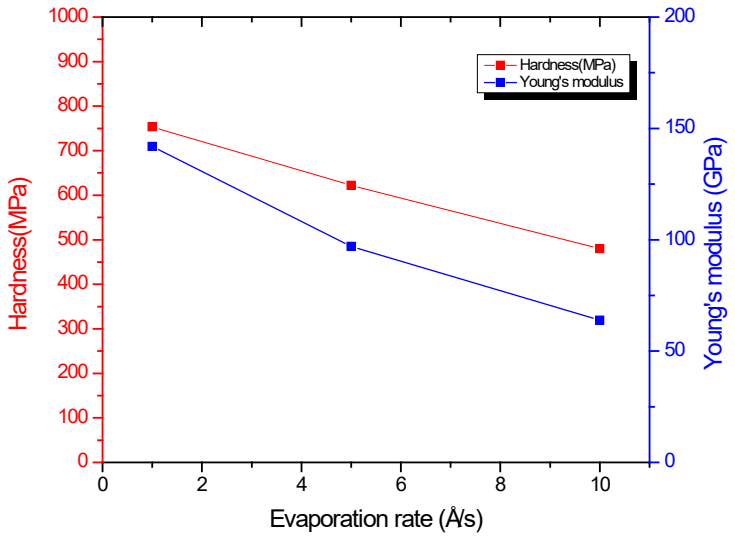

(b)

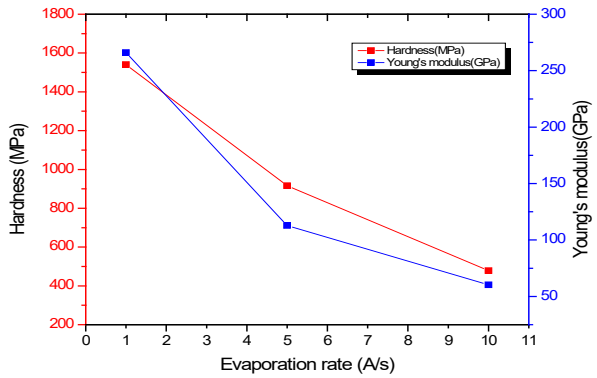

Figure 5.7 (a) CdTe film's hardness and Young's modulus at 1,5 and 10 angstrom per second evaporation rate for 80 µN load (b) ZnS film's hardness and Young's modulus at 1,5 and 10 angstrom per second evaporation rate for 90 µN load

(a)

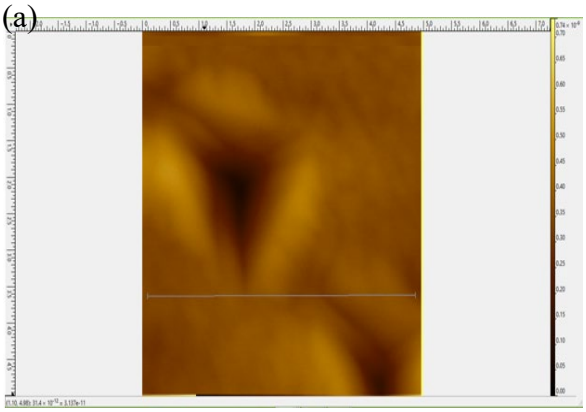

(b)

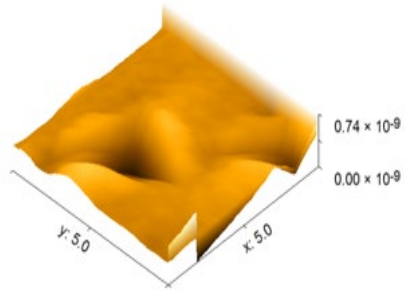

Figure 5.8 Berkovich tip indent image CdTe film at load of 80 µN (a) 2-dimentsional image (b) 3-dimensional image

(a)

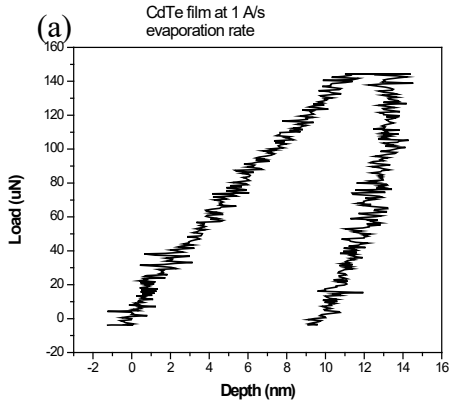

(b)

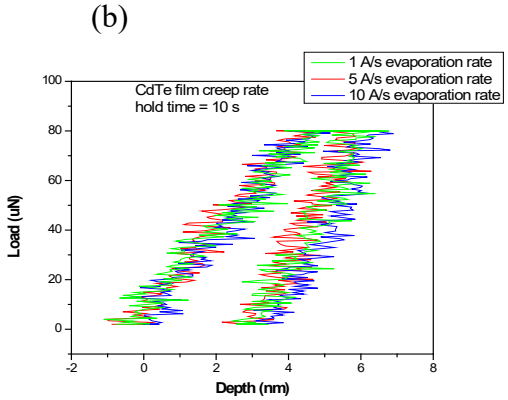

Figure 5.9: (a) CdTe film at 1 A/s evaporation rate indentation load: 140 µN, hold time: 5 (b) CdTe film 1, 5, and 10 Å/s evaporation rate indentation load: 80 µN, hold time: 10 s

The nanoindentation berkovich indent 2D image and 3D image of CdTe film at 80 µN load were shown in Fig. 5.8 (a) and (b), respectively. As seen in Fig. 5.9 (a), CdTe film was incised with a 140 µN load for a hold period of 5 s at an evaporation rate of 1 Å/s in order to further investigate its mechanical capabilities. The CdTe film was found to maintain its mechanical characteristics without cracking or deforming, as shown in Fig. 5.9(a). Despite this, the film had some pop-in and pop-out characteristics during nanoindentation. While pop-ins are abrupt, discontinuous jumps in displacement at a constant load, usually caused by the onset of plastic deformation such as dislocation nucleation or movement, or by a phase transformation, pop-outs in nanoindentation are abrupt expansions on the unloading curve, often caused by a material's expansion as a result of a phase transformation during the unloading phase [297]. The CdTe film at 1, 5, and 10 A/s nanoindented at 80 µN load for a hold period of 10 s is displayed in Fig. 5.9(b). It was discovered from Fig. 5.9(b) that the loading-unloading curves of CdTe films overlapped one another and that the films had specific pop-in and pop-out events. However, careful examination of the curves showed that the CdTe film with an evaporation rate of 1 Å/s was relatively evenly or smoothly dispersed throughout the graph.

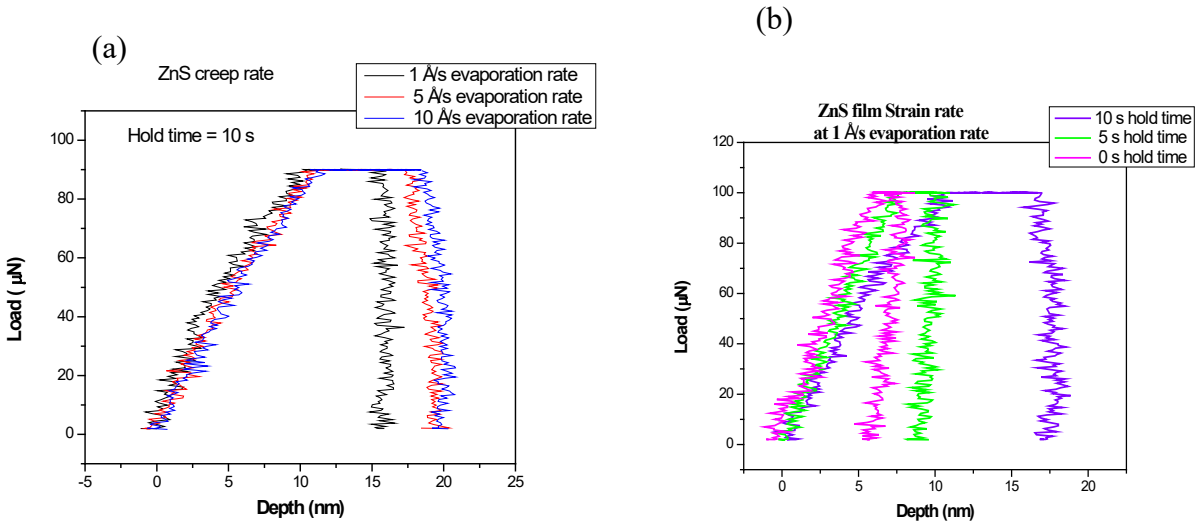

Fig. 5.10 (a) creep rate of zinc sulfide film evaporation rate of 1, 5, and 10 Å/s evaporation rate, hold time 5 s (b) ZnS film evaporation rate 1 Å/s , strain rate at 100 µN load, hold time: 0 s, 5 s and 10 s

The creep behavior of the ZnS films at 1, 5, and 10 Å/s evaporation rates for a hold time of 10 s at a 90 µN load is shown in Fig. 5.10 (a). From Fig. 5.10(a), it was found that the loading-unloading curve at 1 Å/s evaporation rate was more appropriate than the other curves, particularly the unloading curve. Although some pop-in and pop-out events occurred during the nanoindentation experiment. Tsui et al. [298] examined into how residual stresses affected the outcomes of nanoindentation tests. The presence of lower no of pop-in and pop-out at low evaporation rate of CdTe and ZnS films during the nanoindentation indicated the mechanical properties were fairly good enough to be used for MEMS applications.

5.3.8 Electrical (Dielectric) properties

Fig. 5.11 shown the fabricated CdTe-ZnS MIM in which circular capacitors made by stack layer deposition of Cr-Au, CdTe, ZnS and Cr-Au on top. Twelve no of capacitors fabricated and measured only those which were not loose and not punchered during measurement.

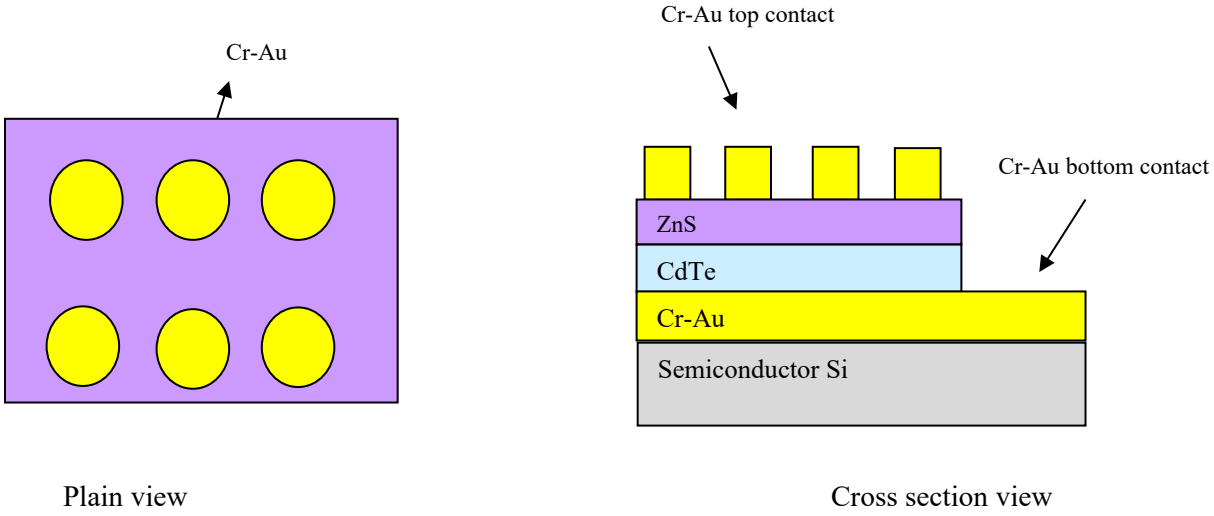

Figure 5.11 Schematic diagram of plan view and cross-section view of the fabricated CdTe-ZnS MIM capacitors

The leakage current and dielectric constant of the CdTe-ZnS MIM structure is calculated by fabricating circular capacitors C01 to C12. The capacitance of all these capacitors is measured at -0.5 V to 0.5 V. Even though a large number of capacitors on the wafer were evaluated, merely individuals that produced consistent and dependable findings were taken into consideration for more research. The calculated current-voltage characteristics of metal-insulator-metal capacitors are displayed in Fig. 5.12 (a) and (b). I–V measurements were performed at 80 K (LT) at room temperature (RT) as shown in Fig. 5.12 (a). The Fig. 5.12 (a) and (b) illustrates that, aside from the anticipated decrease in leakage current, the measured current-voltage features of the capacitors exhibit remarkably analogous behavior at room temperature and low temperature. At room temperature and low temperature, the usual near-zero-bias minimum leakage current is -1.5 x 10^{-6} and -1.8 x 10^{-7} A, respectively.

MIM capacitors' LT C–V characteristics, obtained at 1 mega hertz within the bias range of ±0.5 V at room temperature, low temperature and combined (room temperature and low temperature along with dielectric constant), are displayed in Fig. 5.13 (a), (b) and (c), respectively. Fig. 5.13 (a) shown the low temperature capacitance was about 20-24 pF while Fig. 5.13 (b) shown the room temperature vary from 17-22 pF within the bias range of ±0.5 V. The dielectric constant of CdTe-ZnS MIM calculated 7.94 and 6.90 at low temperature and room temperature, respectively as

shown in Fig. 5.13 (c). From -0.5 to -0.3 V the capacitance varies more sharply than the rest measured voltage. This variation at room temperature may be due to high density of point defect dominated on the film at room temperature. Apart from that the dielectric constant's temperature dependency or the thickness can both cause an alteration in capacitance as a function of temperature or area of the dielectric material. Differentiating the capacitance with respect to temperature (T) and then dividing by C yields a straightforward relation for the temperature dependence of the MIM capacitance [299]:

$$\frac{1}{C}\frac{dC}{dT} = \frac{1}{\epsilon_r}\frac{d\varepsilon_r}{dT} - \frac{1}{t}\frac{dt}{dT} \qquad (5.15)$$

Eqn. (5.15) relates the variation in capacitance as a function of temperature in the form of the temperature coefficient of dielectric constant [$k = (1/\varepsilon_r)\, d\varepsilon_r /dT$] and the thermal expansion coefficient of CdTe and ZnS. The thermal expansion coefficient [$\alpha = (1/t)\, dt/ dT$] of CdTe and ZnS are 5.9 x 10^{-6}/K and 6.6 x 10^{-6} /K, respectively although that of the gold electrode is much lesser (5.1 x 10^{-8}/K), consequently the temperature dependence of the electrode area can be ignored. Amit Goswami et al. studied the ZnS film capacitance, and dielectric characteristics at different temperatures and frequencies. They found that the dielectric characteristics independent of frequency but the capacitance dependent on the temperature and frequency [268]. M. Rapos et al. studied the CdTe MIM at various temperature and low frequency ranges. They studied that the relaxation occurrence with decreasing frequency and increasing temperature [300]. Some of the real capacitors are typically lossy and have dielectric losses. So, they are ignored and not considered in the measurement. The obtained value of dielectric constant is comparable with the earlier reported results [266-268].

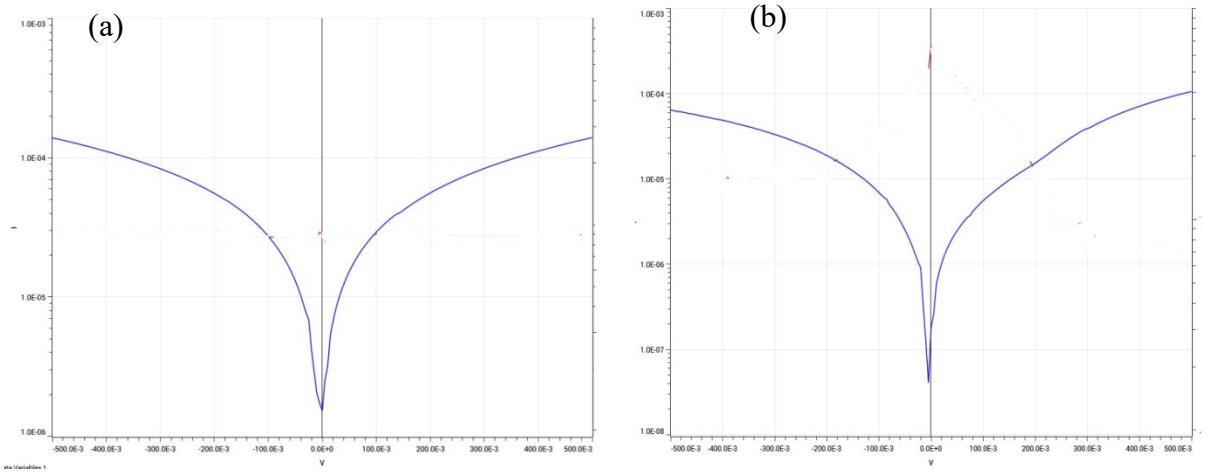

Figure 5.12 I-V plot of CdTe-ZnS MIM capacitor (a) at room temperature (300 K) (b) low temperature (77 K)

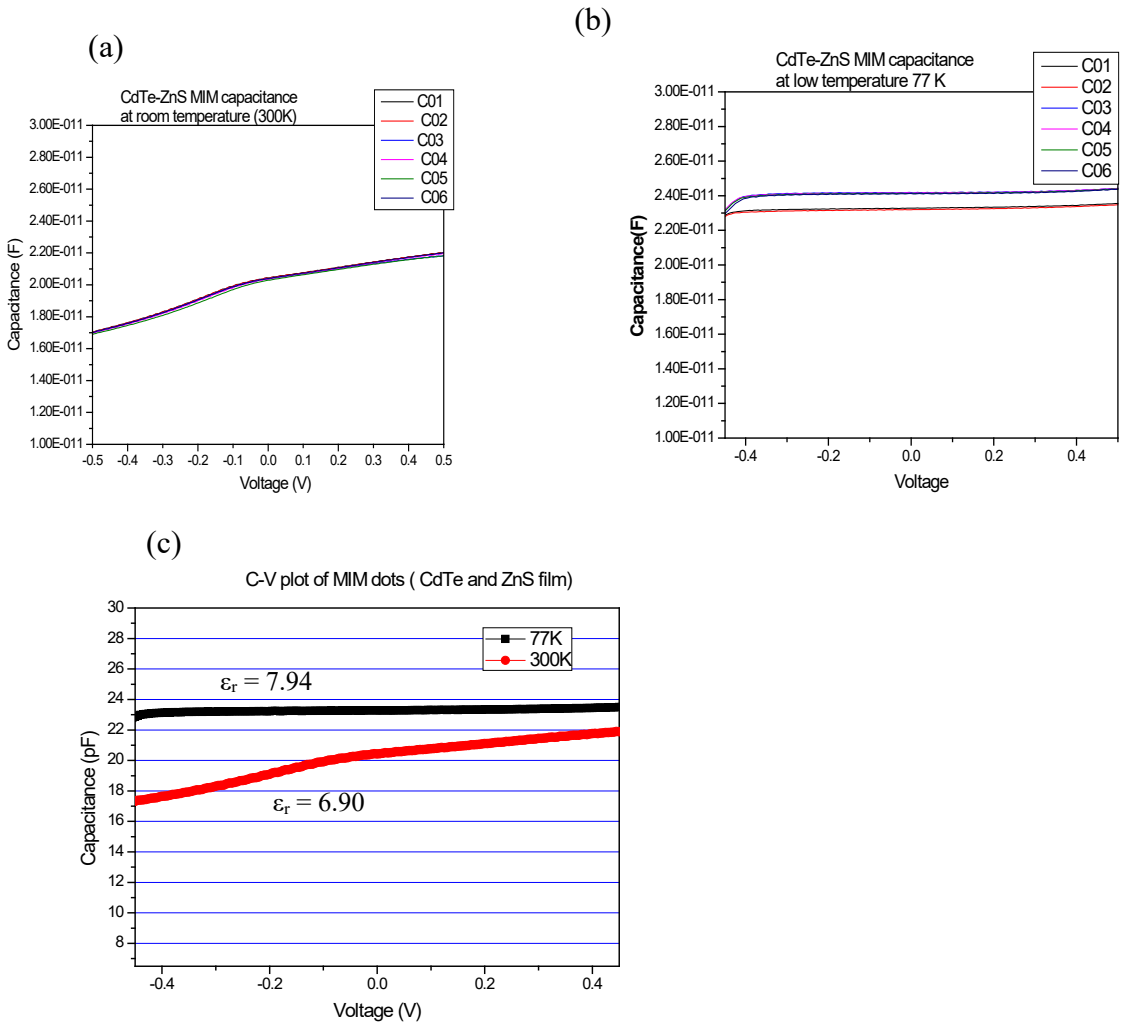

Figure 5.13 C-V plot of metal insulator metal (MIM) of CdTe- ZnS film at 1 MHz for all circular capacitors (a) at room temperature (300 K) (capacitors-C01,C02,C03,C04,C05 &C06) (b) at low temperature (77 K) (capacitors-C01,C02,C03,C04,C05 &C06) (c) C-V plot of capacitor C08, C09, C11,C12 at room temperature and low temperature ; dielectric constant at room temperature ε_r = 7.92 and at low temperature ε_r= 6.95

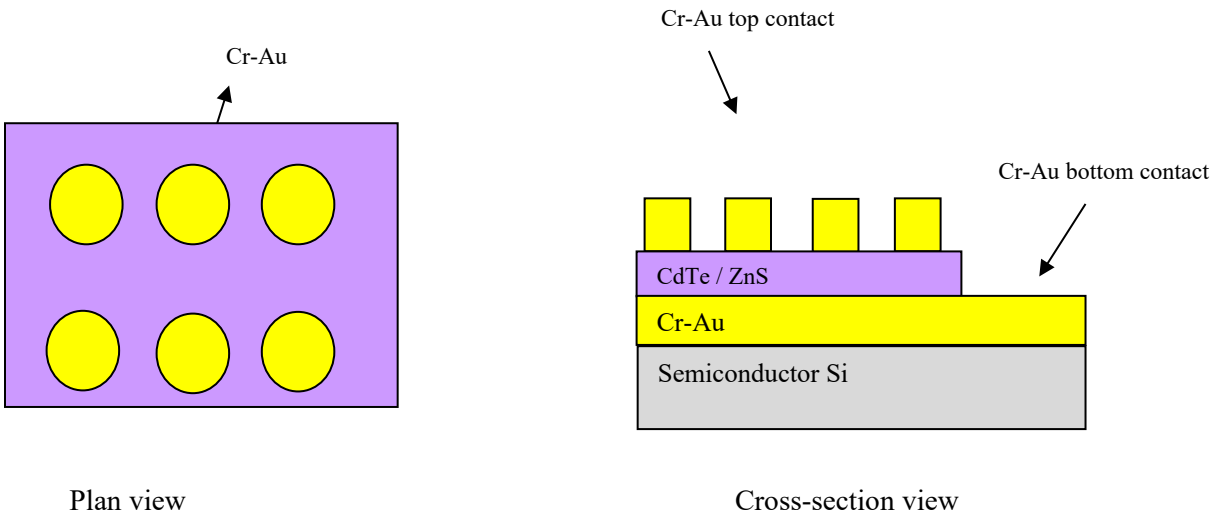

Figure 5.14 Schematic diagrams of plan view and cross-section view of the fabricated CdTe /ZnS MIM capacitors

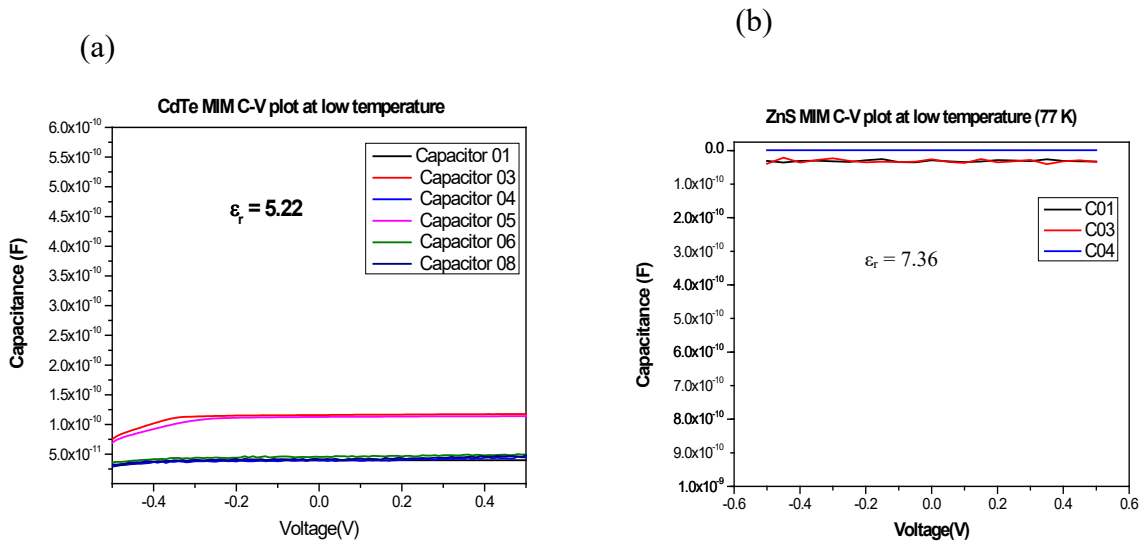

Figure 5.15 C-V plot (a) CdTe MIM for capacitors-C01,C 03, C04, C05, C06 &C08 for 1 MHz frequency at 77 K (b) ZnS MIM for capacitors-C01, C03, &C04 for 1 MHz frequency at 77 K

(a) (b)

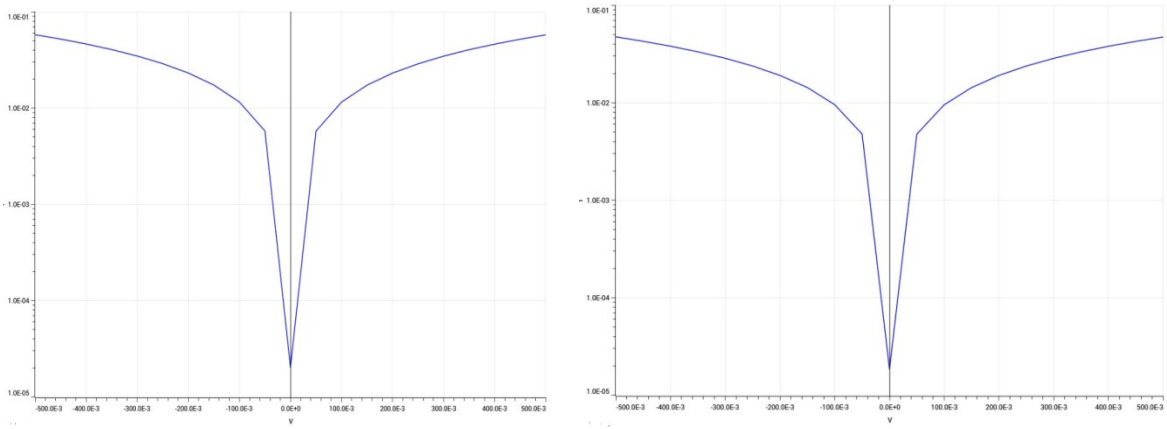

Figure 5.16 I-V plot (a) CdTe MIM at low temperature (77 K) (b) ZnS MIM at room temperature (77 K)

The CdTe/ZnS film based MIM fabricated plan view and cross-section view was shown in Fig. 5.14. The capacitance of the CdTe MIM and ZnS MIM measured at -0.5 V to +0.5 V at 1 MHz frequency at low temperature (77 K) shown in Fig. 5.15 (a) and (b), respectively. From figure 5.15 (a), it was observed that the CdTe MIM capacitance of all the capacitor were about 3.87 to 45.4 x 10^{-11} F for capacitors C01, C03, C04, C05, C06 & C08. The CdTe MIM dielectric constant calculated from the measured data had been about 5.22. Fig. 5.15 (b) shown the ZnS MIM capacitance of capacitors C01, C03 & C04 at low temperature which were from were 3.14 to 3.20 x 10^{-11} F. The low value of dielectric constant compared to bulk CdTe and ZnS was due to since CdTe often has a wide band gap, the states inside the band gap most likely aid in electrical conduction. Traps are extra energy states near the band edge caused by the structural flaws. These traps become the predominant current mechanism by limiting the current flow through a capture and emission process. Because shallow traps occur, Frenkel-Poole emission is an often seen process [301-302]. Another reason for low capacitance of CdTe was due to presence of void etc in the CdTe capacitor film [268]. The low thickness of CdTe compared to ZnS film may also be the reason of low dielectric constant. The I-V plots of CdTe MIM and ZnS MIM at low temperature (77 K) shown in Fig. 5.16 (a) and (b), respectively. The leakage current found at low temperature as 2.01 x 10^{-5} and 1.84 x 10^{-5} A of CdTe MIM and ZnS MIM, respectively. The Eqn. (5.16) for the MIM structure's capacitance is [299]

$$C = \epsilon_0 \epsilon_r A/t, \qquad (5.16)$$

where ϵ_r stands for the relative dielectric constant, ϵ_0 for the vacuum permittivity, and t and A for the dielectric film's thickness and area. Possible structural and morphological changes during the evaporation process or charge trapping into defect states in the film are the causes of the dielectric constant's deviation from the conventional values of bulk CdTe (8.3) and ZnS (10.2). Grain boundaries, impurities like Cd or Zn vacancies, donor (Cl, In) impurities, or complexes of the two are common defects in thermally evaporated CdTe and ZnS films [303-304]. There is typically a significant density of trapping centers along these grain boundaries. Furthermore, during

evaporation, thermal stress and hillock defects may form in the film, which could have a significant and permanent impact on the electrical and optical characteristics of the films.

Thus, on comparing the ZnS based MIM and CdTe-ZnS based MIM, we observed that the CdTe-ZnS based MIM is useful and compatible. The leakage current of CdTe-ZnS based MIM has less leakage current than the ZnS based MIM.

5.4. Conclusions

The evaporation method evaporated the cadmium telluride and zinc sulfide thin films. The X-ray diffraction assessment of the films together established that the film's crystal structure was polycrystalline and found an fcc phase with strong diffraction in the dominated orientation towards the (111) plane. The crystallite size, defect density, residual stress, micro-strain, and stacking faults of CdTe films were 21.4-19.4 nm, 2.16 x 10^{11}-2.63 x 10^{11} lines/cm², 0.05-0.19 GPa, 8.18-9.04, and 3.80 x 10^{-3}-4.19 x 10^{-3}, respectively, evaluated as of X-ray diffraction data. The ZnS film's average size of crystallite, defect density, residual stress, micro-strain, and stacking fault of ZnS films were 21.4-19.4 nm, 3.18 x 10^{11}-12.85 x 10^{11} lines/cm², 0.44-0.20 GPa, 8.29-16.58, and 4.23 x 10^{-3}-8.48 x 10^{-3}, respectively. The SEM images of CdTe films showed that at a 1 Å/s evaporation rate the film was smoother, more uniform, denser, and fully covered on the substrate and had no defects compared to the film at 5 as well as 10 Å/s evaporation rates. The ZnS film SEM micrographs showed an almost flat or too fine structure at all evaporation rates. The ZnS films were continuous and uniform in coverage on the substrate surface with no defects such as cracks or pinholes. The EDX analysis exhibited that the CdTe and ZnS films were nearly stoichiometric at low evaporation rates. The CdTe films were Te-rich at evaporation rates of 1 and 10 Å/s, while the ZnS films were sulfur-rich at all the evaporation rates. The AFM analysis indicated the uniform and low surface roughness of CdTe and ZnS film at low evaporation rates. The higher transmittance was found of CdTe and ZnS films at low evaporation rates. The MOSS ex-situ stress measurement indicated compressive stress of low value at low evaporation rates of CdTe and ZnS films. Nanoindentation experiments indicated that the hardness and Young's modulus of both the CdTe and ZnS films decrease with increasing evaporation rates. The CdTe film creep behavior was evaluated at a load of 80 N for 10 s. The ZnS film's creep behavior was evaluated at a 90 μN load at 10 s and a strain rate at a 10 μN load for 0-10 s. The nonexistence of deformation or cracks owing to stress as an outcome of nanoindentation ensures the deployment of evaporated thin films of ZnS/CdTe for good mechanical characteristics. For CdTe-ZnS MIM, the leakage current and dielectric constant values were lower at low temperature (77 K) than at room temperature (300 K). The CdTe MIM and ZnS MIM dielectric constants were 5.22 and 7.36, respectively. The ZnS MIM had a slightly lower value of leakage current compared to the CdTe MIM. The combined films of CdTe as well as ZnS films were established to be a superior manufacturing step toward appropriate photovoltaic as well as further optoelectronic devices that attained the requisite crystalline, mechanical, and electrical characteristics.

CHAPTER 6

COMPARATIVE INVESTIGATION OF THERMALLY EVAPORATED NANOSCALE CdS THIN FILM'S STRUCTURAL, MORPHOLOGICAL, OPTICAL AND NANOMECHANICAL PROPERTIES

6.1. Introduction

CdS are one of the most extensively used materials in photovoltaic devices. It is a direct band gap material and has been widely used as pigments on plastics and window or buffer layer in solar cells. Beside these applications, research community treats CdS as a promising material in a wide variety of fields like light emitting diode (LED) in flat panel displays, transistors for electronic switches, photoconductive sensors, etc.

Cubic polycrystalline CdS thin films grown by thermal evaporation method and found that grain size increase with substrate temperature. The band gap value calculated were decreasing with annealing temperature while other optical properties like refractive index, absorption coefficient rise with an increase in annealing temperature [306]. Thermally deposited CdS thin film on glass and PET develop transmittance in the range of 71-81%. The band gap value of 2.43 and 2.41 eV for glass and PET substrates, respectively. Glass deposited CdS thin film exhibit excellent feature, thus ensuring applicable for photovoltaic devices [315]. CdS Double-layer thermal deposition technique used to reduce the material consumption without compromising the efficiency. Improved crystalinity of CdS thin film on FTO and AZO/FTO glass rather than glass only. The band gap determined in the range of 2.36-2.38 eV with high absorption coefficient [318]. The polycrystalline n-type CdS thin film of orthorhombic phase along (040) plane developed by vacuum evaporation on amorphous glass. The obtained CdS film contained particle size of 6.88-10.86 nm, Fermi level 0.098-0.006 eV and band gap 2.42 eV which recommend it suitable for electronic device applications [319]. CdS thin film deposited by spin-coating on glass by altering the concentrations (X= 0.5, 0.75, 1.25) M and found that the band gap cease with the molarity. CdS thin film with 1 M with high absorption value assured in optoelectronic applications [305]. The SnS_2 and CdS films deposited by hydrothermal and chemical bath method reveal polycrystalline phase. The absorbance pattern indicated the band gap values were 2.45 eV and 2.20 eV of CdS and SnS_2, respectively. The roughness and grain size were higher of SnS_2 than the CdS film [307]. The substrate temperature effect was studied on CdS nanoscale thin film deposited by vacuum evaporation method. All films reveal hexagonal phase with intense orientation along (002) plane independent of substrate temperature [308]. Chemical bath deposited CdS thin based n-CdS/p-PbSe heterojunction was analyzed to find the mid-infrared

***The portion of this research work has been reported in Journal of Molecular Structure, 1324 (2025) 140850**

spectral photo response applied in Infra-red detector. It revealed peak responsivity R_k and specific directivity 0.055 A/W and 5.482 x 10^8 $Hz1^{/2}$ W at $\boldsymbol{\lambda}$ = 4.7 μm [309]. Chemical bath deposited CdS thin films characterized by altering the NH_4OH concentrations. 0.24 M of ammonium hydroxide revealed best properties for their application as window material: transmittance ~ 70%, band gap 2.37 eV, low defect density and quality crystalinity [310]. A process known as chemical bath deposition (CBD) was used to create CdS nanoparticles and gold quantum dots. Variations in reagent concentration control the Au/CdS density ratio [311]. Thin film of CdS with Co and without Co were fabricated by CBD method. It was observed that as the crystal structure of the CdS thin film decrease with increase in Co concentration. The composition of CdS were rich in Cd and Co takes the position of Cd^{2+}. The surface void density becomes fewer with Co doping. The Band gap graph showed decreasing trend with increased doping [312]. The CdS nano scale thin film deposited by sol-gel spin coating technique shown hexagonal phase and found that larger grain size with higher speed of spin coating. The transmittances were found to be better with higher spin speed. The cluster growth formation was confirmed by the SEM analysis. Thus, enabled the deposited CdS thin film to be suitable for photovoltaic and optoelectronic applications [313]. The photoconductive-sensors fabricated by rf magnetron sputtered CdS thin film. The CdS thin film revealed compact, uniform and continuous surface with polycrystalline structure. The higher employed working pressure decreases the growth rate. The sensitivity of resistance decreases with decrease in dark and photoresistance [314]. Cubic phase CdS film deposited by CBD involving $CdCl_2$, NH_4OH and thiourea. CdS film deposited do not depend upon the growth mechanism in an nearly uniform independent reaction bath [316]. Annealing of thermally deposited CdS thin film with Al doping enhanced the transmittance in near infrared wavelength 500-1100 nm. The other optical properties such as extinction coefficient and refractive index greatly influenced by the annealing temperature [317]. CdS thin film regulated from without NH_4 free solution to achieve same deposition on the entire surface of the substrate. The solution having small pH give greater concentraton of Cd^+ ions that further change the feature of the film. The hexagonal phase achieved at low deposition rate with band gap of 2.4 eV [320]. Different activation period of $KMnO_4$ rising from 5 to 20 minutes smooth the CdS thin film deposited on glass substrate by CBD method. The cubic phase with spherical grain size of improved void space on the surface of film achieved. Activation time of $KMnO_4$ directly related to the transmittance and absorbance of the film [321]. Close space vacuum transport (CSVT), CBD and sputtering deposition methods compared by characterization of CdS thin films on ITO glass substrate. The crystal structure of sputtered film was found to be of better quality and lower grade of CBD method. Annealing improved the crystalinity of CdS films deposited by sputtering and CBD method only while in case of CSVT it decreased. The band gap values were 2.38, 2.42 and 2.44 eV of CBD, sputtering and CSVT, respectively [322]. CdS thin film deposition and decomposition compared by spin coating and CVD with same environment (temperature and time). The n-ethyl replaced with isopropyl xanthate and 3-methyl to 3,5-dimethyl pyridine. The different growth planes (hexagonal structure of CVD method) achieved with different surface morphologies and band gap values were in the range of 2.39-2.48 eV [323]. The hexagonal phase along (001) plane obtained by magnetron sputtering

while cubic phase achieved by CBD method of CdS thin film though both films were of pin hole and void free. The film thickness variation and uniformity were less in sputtering compared to CBD and deposition keeping deposition rate higher of sputtering [324]

Nanoindentation is the reasonably well-established method of testing measures the applied force and the recorded depth of penetration of an indenter into the specimen to determine the area of contact and, consequently, the hardness of the test specimen. The experimental load-displacement curve can also yield several additional mechanical parameters, the most straightforward of which is the elastic modulus. In other words the analysis of the mechanical characteristics of materials at the nanoscale length is done using the versatile and effective method of nanoindentation [330-331]. It involves the controlled application of a load to a material surface using an indenter with a sharp tip, typically in the nanometer range, while simultaneously monitoring the depth of penetration. This method allows for precise characterization of the material's response to localized stress, including hardness, Young's modulus, and various other mechanical properties [325-326]. The development of nanoindentation method has largely contributed to the understanding and design of materials at the nanoscale. It gives the potential to the research community to analysis the mechanical properties of a wide range of materials, from metals and ceramics to polymers and biological tissues. Nanoindentation has become typically priceless in the fields of materials science, mechanical engineering, and nanotechnology [332].

The objective of this study is to analysis the structural, morphological, optical and nanomechanical properties of CdS thin films at 1, 5 and 10 Å/s deposition rates on glass substrate. The CdS thin films were deposited on precleaned glass substrate as film quality greatly depends upon glass surface. The structural and morphological properties were characterized by XRD, AFM, SEM and EDX. The optical and nanomechanical properties were characterized by UV-vis spectrophotometer and nanoindentaton.

6.2. Materials and Methods

Thermal evaporation was used to grow CdS thin films at deposition rates of 1, 5 and 10 Å/s on glass substrates illustrated in Fig. 6.1 (a). The glass substrates were cleaned ultrasonically and then in acetone, methanol and rinsed in distilled water for 6 min and lastly dried in N_2. The resistively heated molybdenum boat was topped with 99.99 % CdS small pieces. A vacuum of 2 x 10^{-6} mbar employed for evacuating the deposition chamber. CdS thin films 200 nm thicknesses on three glass substrates were deposited applying optimized process parameters (deposition rates: 1,5 and 10 Å/s, evaporation current: 40-90 A with bias voltage of 10 V). In order to achieve uniform, compact and stoichiometric films with small roughness, process parameters were optimized. The deposition rates are controlled by controlling the resistively heated boat current through rate controller based on the feedback from the quartz crystal monitor deposition rate data. Life of the quartz crystal monitor plays the crucial role to reproduce the deposition rate. For reproducible deposition rate measurement life of quartz crystal life is not allowed to degrade less than 90% life in any

experiment. Vacuum of the chamber is also kept same (2 x 10^{-6} mbar) in all experiments. The deposition is done at room temperature without substrate heating and cooling. Fig. 6.1 (b) shows the schematic diagram of CdS film of 200 nm deposited by thermal evaporation process on glass substrate. The deposited CdS thin films were used for further structural, morphological, optical and nanomechanical examination.

Dektak KLA Alpha step D500 surface profiler was used to confirm the thickness of CdS films. Crystallography and structural composition were investigated using the X-ray diffraction (XRD; (2 theta mode), PAN analytical B.V. X'Pert PRO MRD (Material research diffractometer)) having a CuKα (**λ**= 1.54 Å) radiation source and Xe-proportional counter with high-precision angle of (±0.001°), through scanning with step size of 0.02° in the 2theta range from 20 to 60°. Energy Dispersive X-ray (EDAX; Model-FESEM Carl Zeiss SUPRA55VP with Oxford Instrument X-MAX EDS Spectrometer, Operating voltage 5-12 kV) Field Emission Scanning Electron Microscopy (FESEM) employed to investigate the surface morphology, grain and compositional analysis. Average roughness and topographical properties were studied using Atomic Force Microscope (AFM; Model- 5600 LS, AC Model III Module, Agilent Technologies). Agilent Technologies UV-Vis spectrophotometer is the wavelength range 200-800 nm was used to study the optical properties. The nanomechanical properties were evaluated by Industron NanoGuru NG50 nanoindenter with berkovich tip.

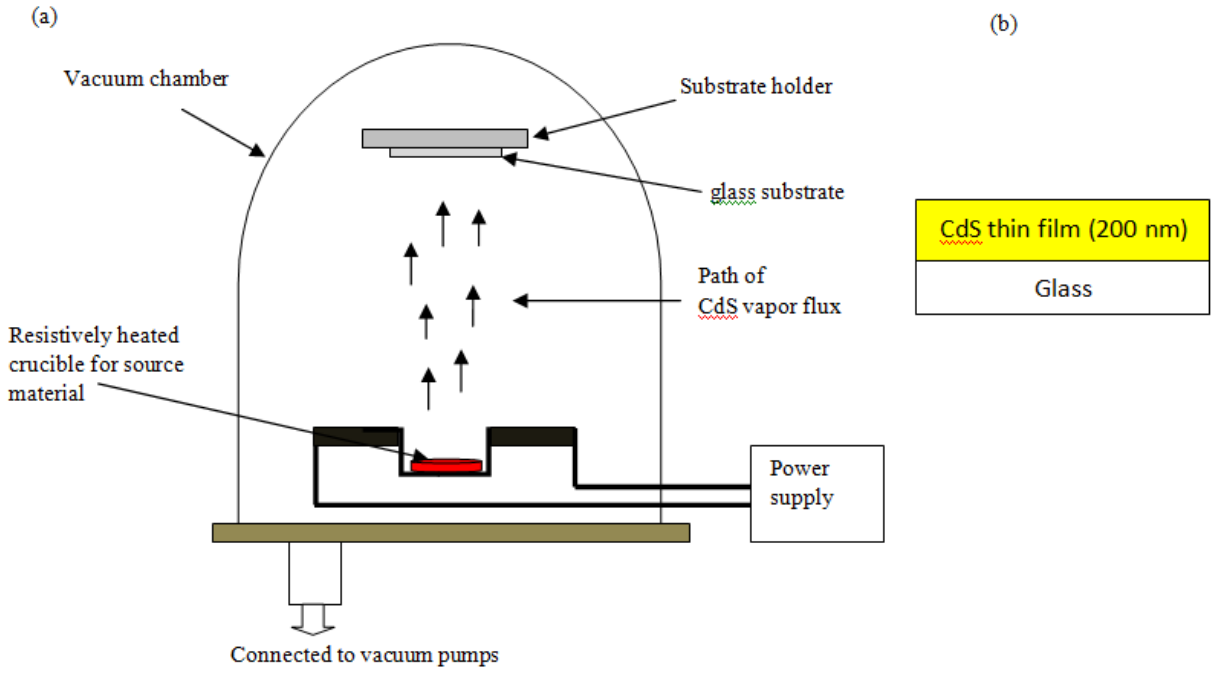

Figure 6.1: (a) Schematic diagram of thermal evaporation process (b) Schematic diagram of CdS thin film deposition on glass substrate

In Fig. 6.2 photographic images of CdS thin films on glass substrate are shown for 1, 5 and 10 Å/s deposition rates. CdS thin films were yellow in color, smooth and covered the whole glass surface. Small steps were made by covering the glass surface to measure the step-height (film thickness) from surface profiler.

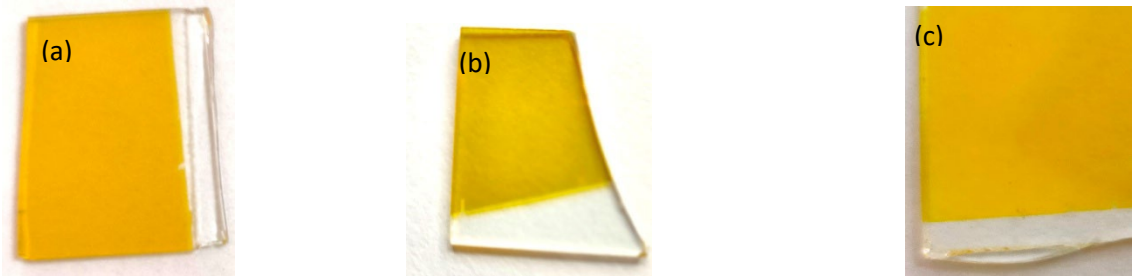

Figure 6.2: Photograph of CdS thin film on glass substrate (a) 1 Å/s deposition rate (b) 5 Å/s deposition rate (c) 10 Å/s deposition rate

6.3. Results and discussion

6.3.1 Structural analysis

Because of CdS thin film's more stable characteristics, increased optical band energy, and advantageous lattice misfit factors, the buffer layer with a hexagonal phase is preferred over one with a cubic phase [333]. CdS is applied as a binary II-IV semiconductor, with hexagonal (wurtzite) phase being the most common. The cubic (zinc blende) phase of CdS is metastable and manifests in nanocrystals and thin films, which are examples of low-dimension applications [334]. The XRD diffratogram of CdS thin films on glass substrate at 1, 5 and 10 Å/s deposition rates is shown in Fig. 6.3. Intense refraction (002) associated with the hexagonal structure is visible in the XRD pattern at approximately $2\theta = 26.46°$, 26.52° and 26.48° at 1,5 and 10 Å/s deposition rates, respectively [337-338]. The CdS film at 1 Å/s deposition rate shows other low intense diffraction peaks at $2\theta = 24.81°$, 28.18°, 43.58°, 47.70°, and 51.62° corresponding to the diffraction planes (100), (101), (220), (103) and (112), respectively (JCPDS no 65-3414). The CdS film at 5 Å/s deposition rate also associated with a hexagonal structure consisting (100), (101), (220), (103) and (112) planes (Fig 6.3(b)). These planes associated to diffraction peaks at $2\theta = 24.74°$, 28.04°, 43.54°, 47.74° and 51.62°, respectively. Similary, the CdS film at 10 Å/s deposition rate recognized diffraction peaks at $2\theta = 24.86°$, 28.06°, 43.82°, 47.66°, and 52.06° analogous to the diffraction planes (100), (101), (220), (103) and (112), respectively. The wide hump in the range of 20-35° is caused by the presence of substrate made of amorphous glass. Implementing the results of the XRD spectra, the crystalinity of the deposited CdS thin films on glass substrate at

various deposition rates is measured. In a cubic structure, the interplanar distance d was determined using Bragg's formula and Vegard's law [322],

$\boldsymbol{\lambda}=2d\sin\theta$ (6.1)

$a_{cubic} = d\,(h^2 + k^2 + l^2)^{1/2}$ (6.2)

where $\boldsymbol{\lambda}$ = 0.15406 nm and θ is the angle of the diffraction position (angle between the adjacent crystal planes). Furthur, lattice constant c (in plane), and a (out plane) correlated to hexagonal unit cell can be calculated using following Eqns. (6.3) and (6.4) [322,340]:

$$a_{hex} = \sqrt{\frac{1}{2}}\, a_{cubic} \quad (6.3)$$

$$c_{hex} = \sqrt{\frac{4}{3}}\, a_{cubic} \quad (6.4)$$

The Scherrer's formula is used to calculate the crystallite size, D [335,341]:

$$D = \frac{0.94\,\lambda}{\beta cos\theta} \quad (6.5)$$

where θ is the Bragg's angle at (hkl) plane and β is the full-width half maximum (FWHM)

The strain (ε) is calculated using the Eqn. (5.6)[307,322,340] :

$$\varepsilon = \frac{\beta cos\theta}{4} \quad (6.6)$$

The Williamson and Smallman's relation is used to calculate the dislocation density (defect density) [321-322,335]

$$\delta = \frac{1}{D^2} \quad (6.7)$$

The X-ray peak broadening due to inhomogeneous local strain in the material is called lattice strain.

The inhomogeneous local strain in the material that causes X-ray peak broadening is called lattice strain. Plastic deformation is attributed by dislocations, and the broadening of the XRD diffractogram lines is applied to calculate the dislocation density. The Eqn. (6.8) is used to calculate the crystallite no per unit surface area, N [333,336]:

$$N = \frac{t}{D^3} \quad (6.8)$$

where t is the thickness. The unit cell volume for the CdS of the films is calculated by Eqn. (6.9) [3]:

$$V = \frac{\sqrt{3}}{2}\, a^2\, c \qquad (6.9)$$

The stacking fault is calculated by Eqn. (6.10)[344]:

$$SF = \frac{2\pi^2\beta}{45\sqrt{3Tan\theta}} \qquad (6.10)$$

The CdS thin film's crystal structure parameters such as lattice constant , crystallite size, strain, defect density, crystallite no per unit surface area, unit cell volume and stacking fault for the preferential (002) plane are summarized in Table 6.1.The X-ray measurements revealed that the lattice constants of the CdS films were comparable to the bulk CdS material. The structural parameters (crystallite size, defect density (dislocation density), intrinsic stress and micro strain) of the CdS thin films calculated from XRD results are compatible with the earlier reported results [340, 343]. Increased internal stress caused by a higher dislocation (defect) density in the film could have a negative impact on the functionality of the device. From table 6.1, it is obvious that the obtained crystalline parameters of the CdS film at 1 Å/s are appropriate for a good crystalline growth on actual optoelectronic device.

(a)

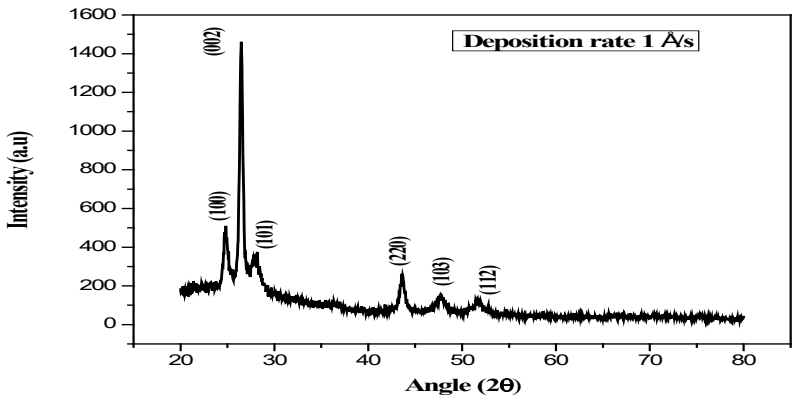

(b)

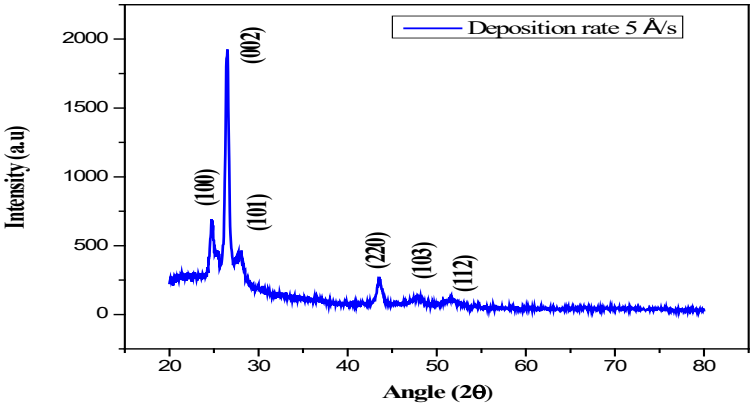

(c)

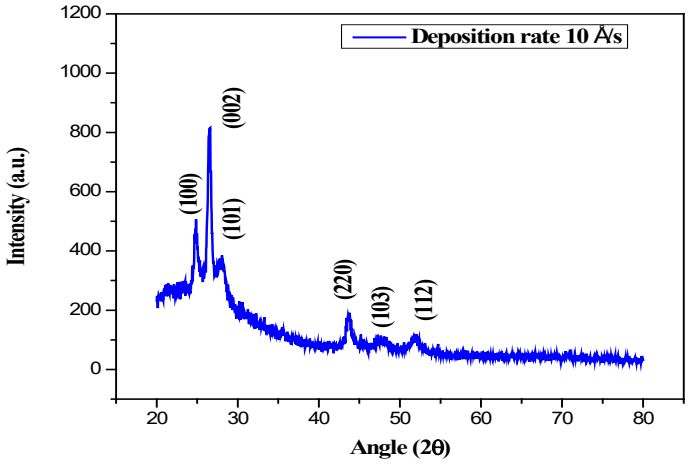

Figure 6.3 : XRD pattern of the CdS thin film (a) 1 Å/s deposition rate (b) 5 Å/s deposition rate (c) 10 Å/s deposition rate

Table 6.1 Crystal structure parameters of CdS films at 1, 5 and 10 Å/s deposition rates

Rate of deposition	hkl	θ (Theta)	β (Beta)	a (Å)	c (Å)	d_{hkl} (Å)	D (nm)	ε (x 10^{-3})	δ (x 10^{11} lines/ cm^2)	N (x 10^{12} cm^{-2})	V $(Å)^3$	S.F. (x 10^{-3})
1 Å/s	(002)	13.23	0.417	4.758	7.770	3.3649	20.43	7.74	2.39	2.34	2.523	3.79
5 Å/s	(002)	13.26	0.466	4.748	7.753	3.3574	18.29	8.62	2.98	3.26	2.517	4.23
10 Å/s	(002)	13.24	0.574	4.755	7.765	3.3624	14.87	10.62	4.52	6.08	2.521	5.21

6.3.2 Morphological analysis

AFM images of CdS thin film on glass substrate with scanning area of 5x5 μm^2, the film surface are plotted in Fig. 6.4. CdS thin films at 1, 5 and 10 Å/s deposition rates were rough, yet the peak-to-valley distance was little compared to the film's overall thickness. This assured the films uniform coverage, smooth and continuous.

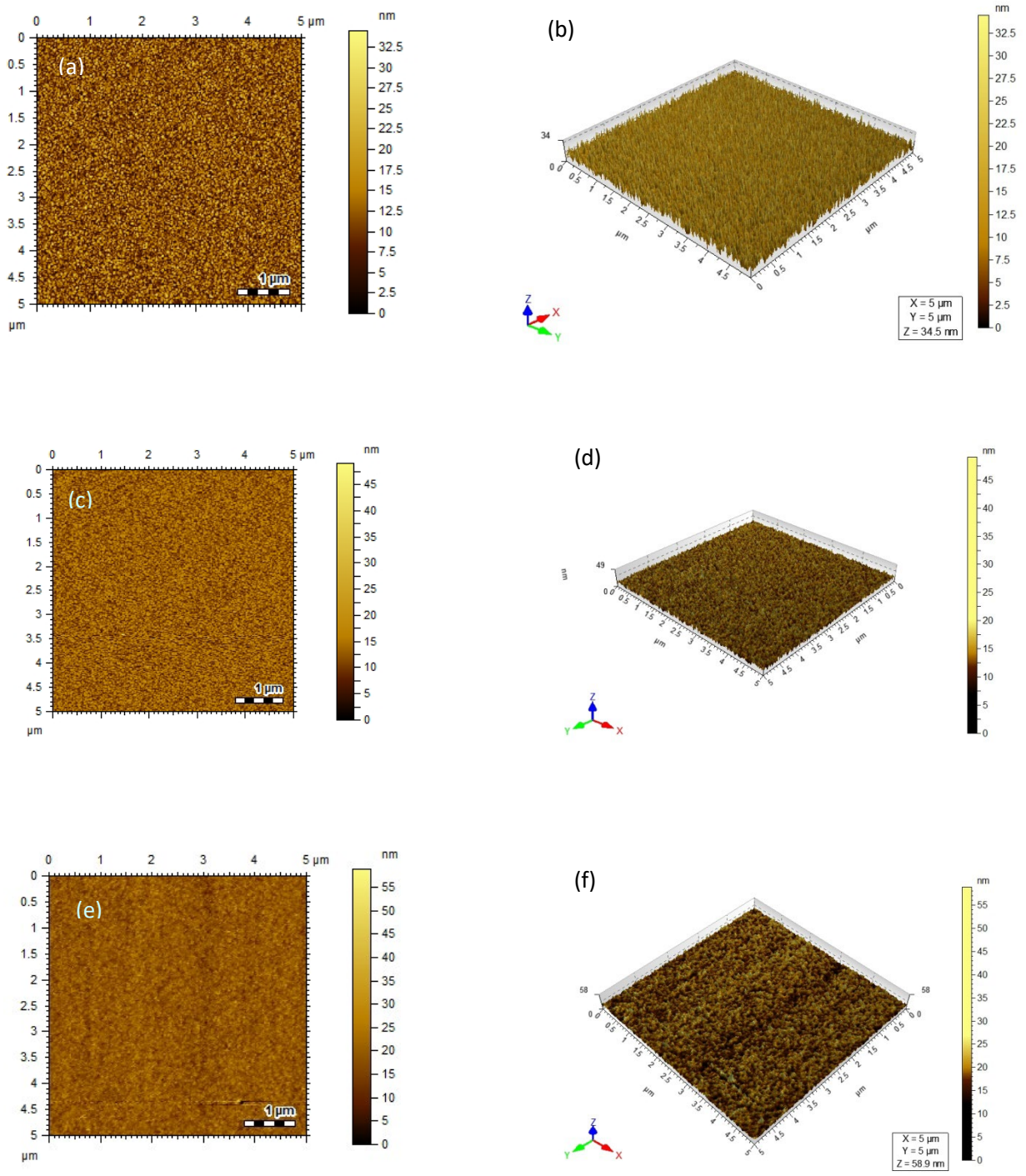

Figure 6.4 : AFM images of CdS thin film (a) 2D-image image at 1 Å /s deposition rate (b) 3D-image at 1 Å /s deposition rate (c) 2D-image image at 5 Å /s deposition rate (d) 3D-image at 5 Å /s deposition rate (e) 2D-image image at 10 Å /s deposition rate (f) 3D-image image at 10 Å /s deposition rate

The roughness parameters of CdS thin films at 1, 5 and 10 Å/s deposition rates are shown in Table 6.2. Roughness is influenced by the deposition rate since the thicknesses of the films were same for all the deposition rates. From Table 6.2, we observed that the roughness average R_a values are 1.20, 1.80 and 2.1 nm for 1, 5 and 10 Å/s, respectively [340]. Thus, CdS film at 1 Å/s deposition rate has least value of surface roughness which indicated a good quality film.

Table 6.2 Surface roughness parameters of CdS thin films

Rate of deposition (Å/s)	R_a (nm)	R_q (nm)	R_z
1	2.18	2.73	34.7
5	2.35	2.94	49.0
10	2.49	3.18	58.9

Fig. 6.5 shows the SEM images of the CdS thin films on glass substrate at 1, 5 and 10 Å/s deposition rates. All the films are free of cracks, voids and pinholes [308]. The compact surface morphology of the CdS thin films that were grown on glass substrates and the irregularly shaped grain distribution were both found. The morphological parameters such as grain size, shapes and thickness of films are very vital since they bear a large no of applications relying on grain size and morphology [344].

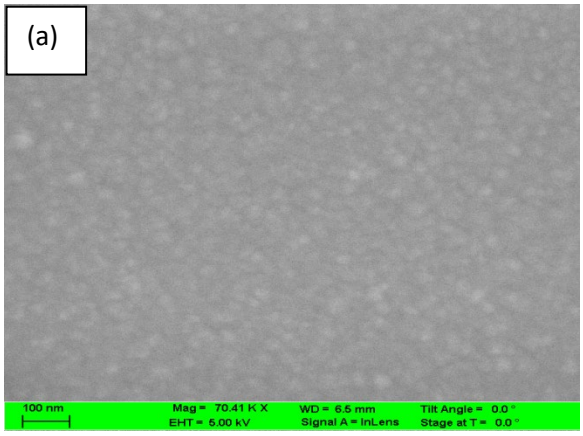

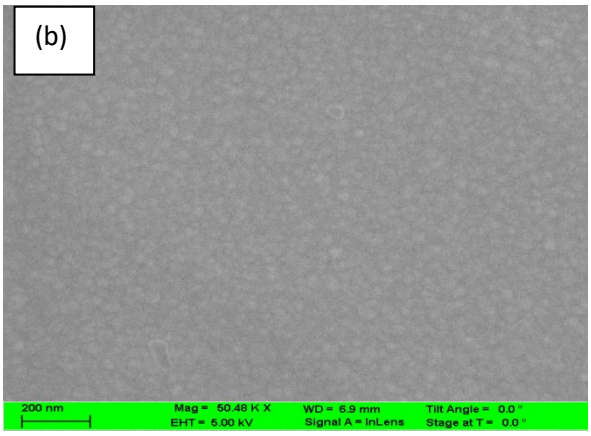

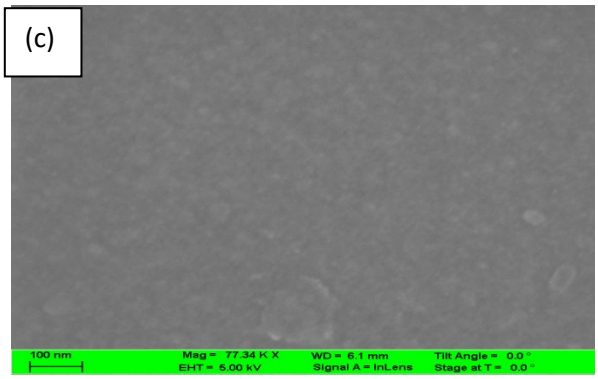

Figure 6.5: SEM images of CdS thin film (a) 1 Å/s deposition rate (b) 5 Å/s deposition rate (c) 10 Å/s deposition rate

6.3.3 Compositional analysis

The EDX examination used for quantitative stoichiometry analysis of CdS thin film on glass at 1,5 and 10 Å/s deposition rates as shown in Fig. 6.6 . The presence of Cd and S elements was assured by the EDX peaks. The CdS thin film elemental examination indicated that the S/Cd ratios were 0.96,0.94 and 0.88 at 1,5 and 10 Å/s deposition rates, the film was having excess Cd with S deficiency which may be due to S great affinity towards oxygen, forming SO_2. Due to nature of glass substrate some more peaks were found excluding Cd and S.

Table 5.3 shows the atomic % of CdS thin film on glass substrate at 1,5 and 10 Å/s deposition rates. The determined compositional values of Cd and S were comparable with the earlier reported values [339]. Thus, it is investigated from EDX experimental results that CdS film at 1 Å/s deposition rate is more stoichiometric than other deposition rates which indicated that film quality is better this deposition rate.

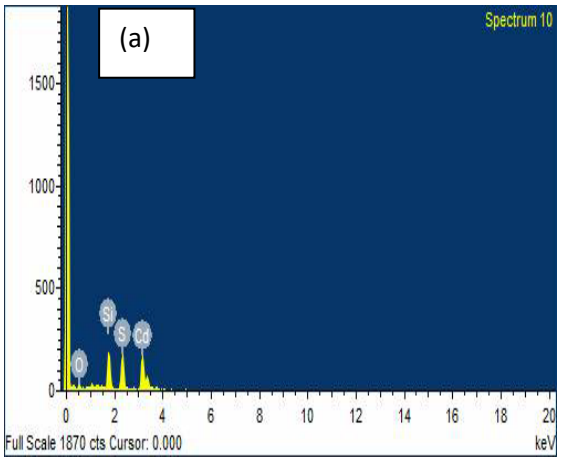

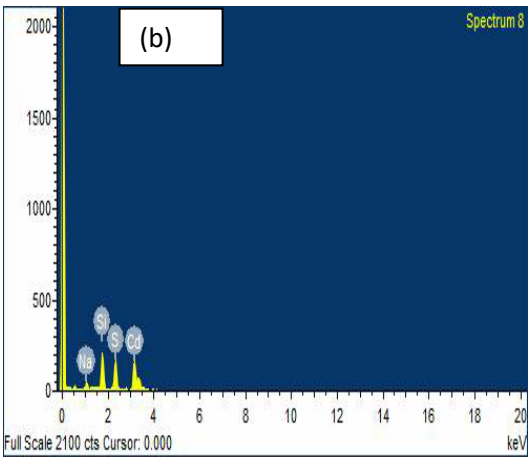

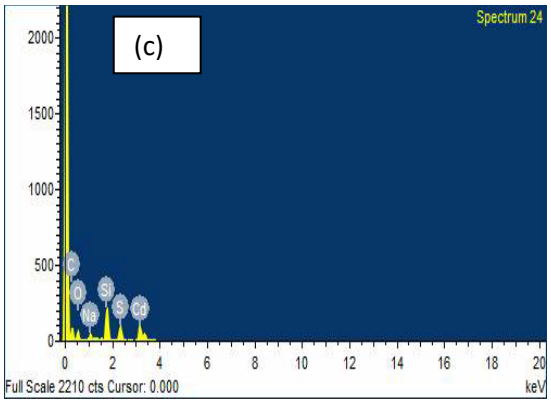

Fig 6.6: EDX spectra CdS thin film (a) 1 Å/s deposition rate (b) 5 Å/s deposition rate (c) 10 Å/s deposition rate

Table 6.3 Chemical composition of CdS thin film at 1, 5 and 10 Å/s deposition rates

Rate of deposition (Å/s)	Cd %	S %	S/Cd ratio
1	50.88	49.11	0.96
5	51.59	48.44	0.94
10	53.14	46.85	0.88

6.3.4 Thickness measurement

The CdS film thickness on glass substrate was measured by Dektak surface profiler having tip of 12.5 µm and the step height of the CdS film was found to be about 200 nm. The deposited CdS film thickness profiles on glass substrate are shown in Fig. 5.7 for 1,5 and 10 Å/s deposition rates

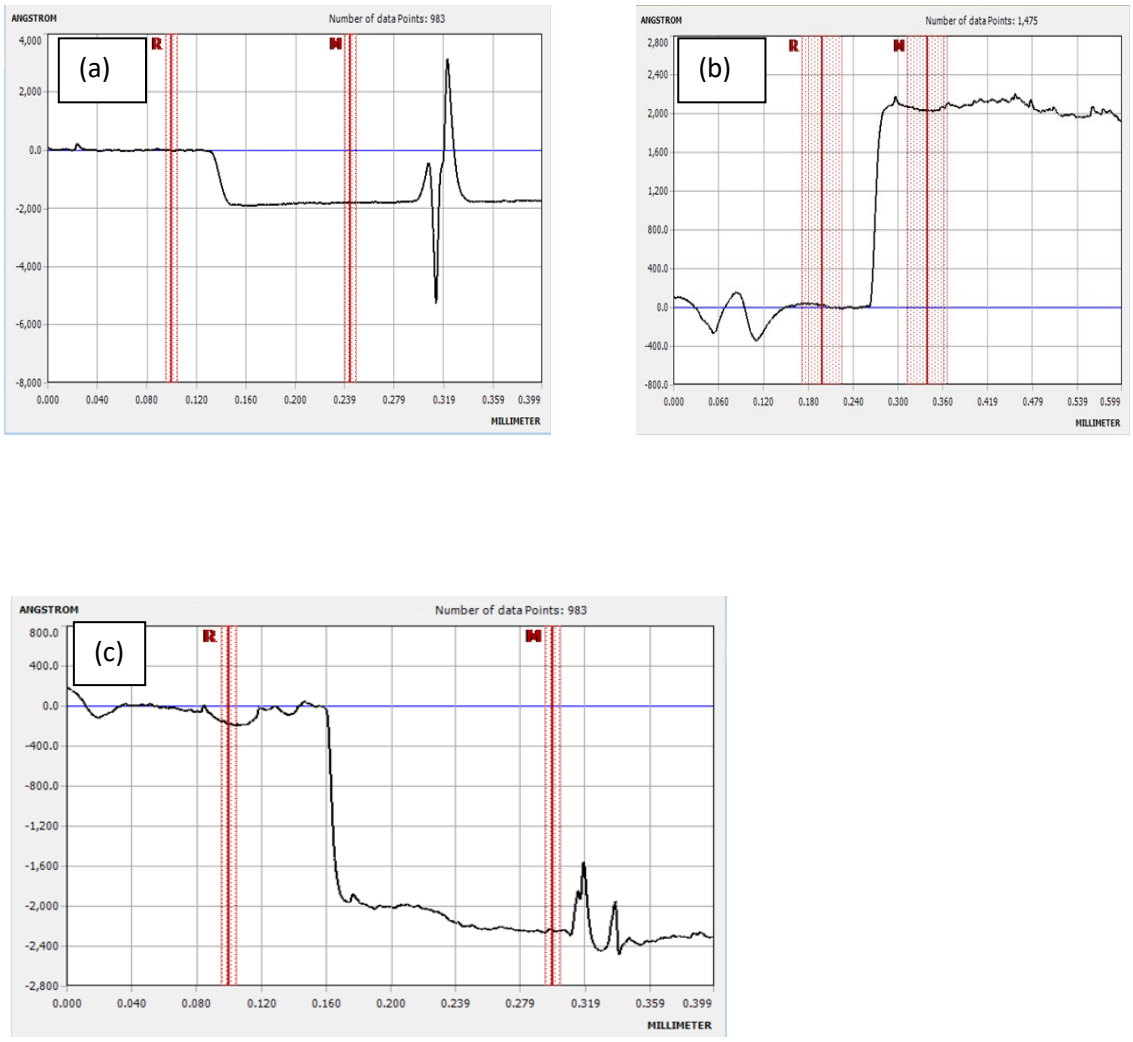

Fig 6.7: Dektak surface profiler CdS step-height (film thickness) measurement (a) 1 Å/s deposition rate (b) 5 Å/s deposition rate (c) 10 Å/s deposition rate

6.3.5 Optical properties analysis

Fig. 6.8 shows the transmission and absorption spectra for thermally deposited CdS films at different deposition rates in wavelength limit 200-850 nm. As seen from Fig. 6.8 (a) all the films show high transmittances (~80%) in visible region of solar spectrum.

From Fig. 6.8 (b) a decrease in absorbance is indicated in 350-550 nm, which is generally accepted for CdS thin films. The CdS thin films empower more than 50 % of the light above 400 nm to pass through. Thus , utilization of CdS thin films as a window layer in photovoltaic devices or solar cell

could raise its performance; the absorber layer will be light up with more photon that have energies greater than its band gap, which in the case of CdTe and CIGS is around 1.3 eV.

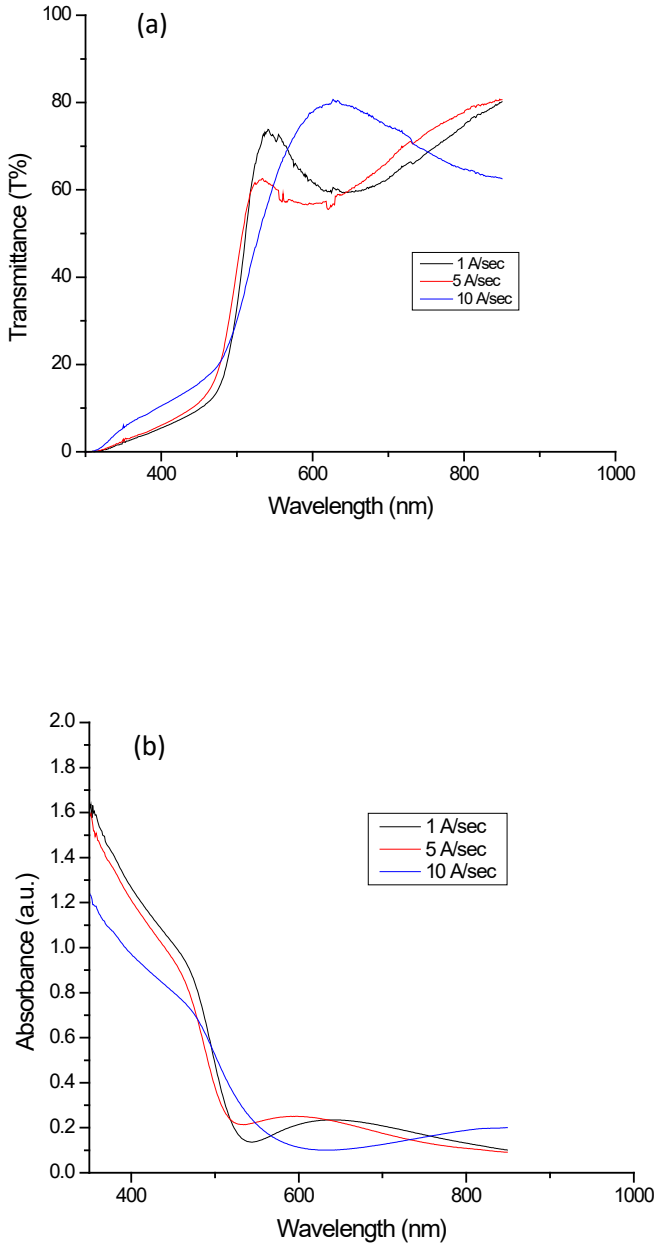

Figure 6.8: CdS thin films on glass for 1, 5 and 10 Å/s deposition rates (a) Transmittance vs wavelength (b) Absorbance vs wavelength

To determine the band gap for each CdS thin film on glass substrate, we have to obtain its absoroption coefficient α, which rely on the incident photon energy hν as [341]:

$$\alpha = A\,(h\nu - E_g)^{n/2} \qquad (6.11)$$

where A is an energy-independent constant, E_g is the optical band, and n is equal to 1 for direct band gap materials such as CdS. The absorption coefficient α is related to the transmittance T by the equation [339]:

$$\alpha = -\frac{1}{t}\ln\frac{1}{T} \qquad (6.12)$$

where t is the thickness of the film . Fig 6.9 shows the plots of $(\alpha h\nu)^2$ versus photon energy, hν of CdS thin films at 1,5 and 10 Å/s deposition rates. The band gap values of the CdS thin films are 2.37, 2.41 and 2.43 of 1, 5 and 10 Å/s deposition rates, respectively. The determined band gap values were comparable with the reported results [321,341,343]. It can be analyzed that decreasing particle size (crystallite size) as determined from XRD, causes increase in band gap [342].The optical band gap energy is lower for lower deposition rate (1 Å/s deposition rate), which can be due to improvement in morphology and crystallinity of CdS thin film as revealed by XRD results[342]. Also, the analysis of the optical absorption indicate that the E_g values of the films increases with increasing deposition rates, which can be due to structural changes of CdS [343].

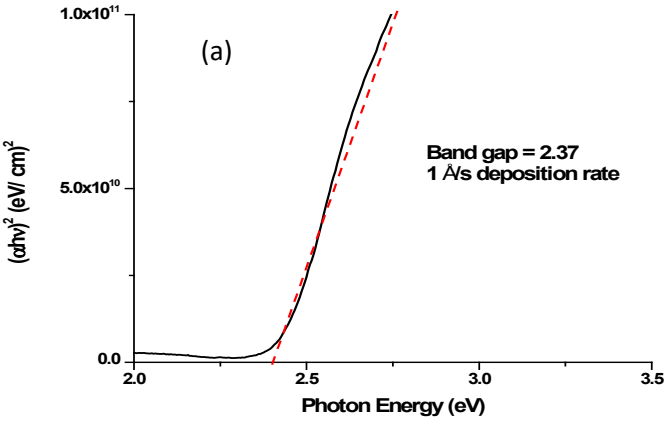

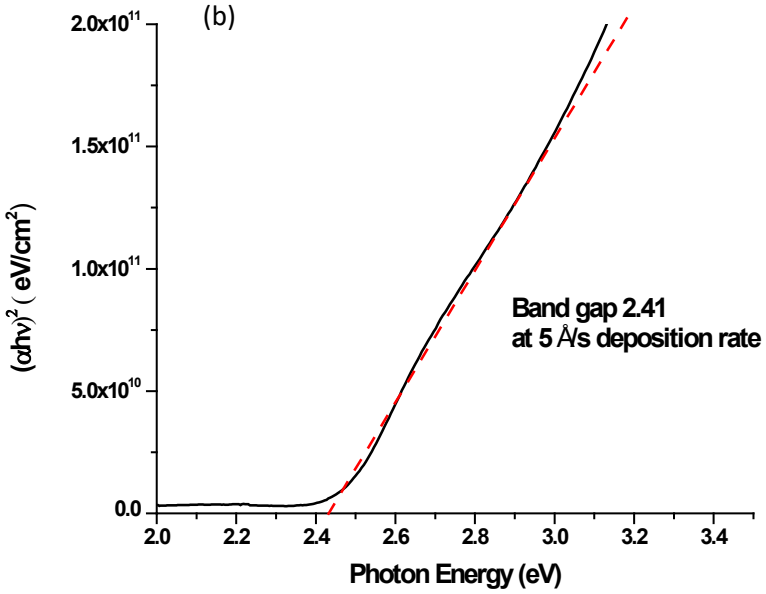

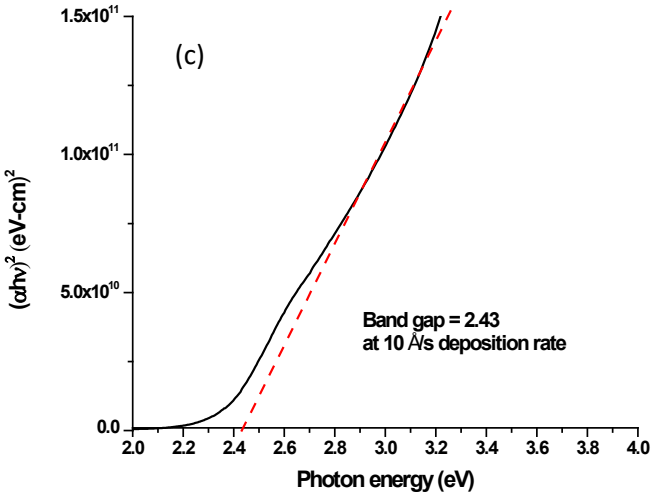

Figure 6.9: $(\alpha h\nu)^2$ versus hν graphs of CdS thin film (a) 1 Å/s deposition rate (b) 5 Å/s deposition rate (c) 10 Å/s deposition rate

6.3.6 Nanomechanical properties analysis

CdS thin films on glass substrate were subjected to nanoindentation tests using a Berkovich tip at deposition rates of 1, 5 and 10 Å/s. The following Eqn. (6.13) can be used to determine the CdS thin film's hardness [329,343]

$$H = \frac{P_{max}}{A_c} \qquad (6.13)$$

where P_{max} is the maximum load, and A_c is the contact projected area. Eq. 6.14 can be used to determine Young's modulus E [328,342]

$$E_r = \frac{S}{2\beta}\frac{\sqrt{\pi}}{\sqrt{A_c}} \quad (6.14)$$

$$\frac{1}{E_r} = \left[\frac{(1-\nu\ )}{E} + \frac{(1-\nu_i)}{E_i}\right] \quad (6.15)$$

where E_r is the reduced Young's modulus, which exemplify for the both interaction of the intender and the film material. The S is the contact stiffness obtained from the unloading curve of load-indentation depth curve and is the coefficient of indenter correction. The E and E_i are the analogous elastic moduli, and ν and ν_i are the film's and indenter's respective Poission's ratios.

The change from purely elastic to elastic/plastic contact is typically responsible for the increase in nanohardness at modest penetration depths, and the mean contact pressure is not a reliable indicator of nanohardness at this point. The mean contact pressure only represents nanohardness when the plastic zone is fully established. The mean contact pressure is lower than the nominal hardness when the plastic zone is absent or just partially developed [241,364]. Explaining the change from simply elastic to plastic contact with the Berkovich indenter is crucial. Plastic deformation at the contact point is facilitated by the geometry of the indenter once the indentation depth exceeds the tip radius. Hold times are frequently used at maximum load to reduce creep before the indenter is unloaded. The movement of material inside a specimen under high pressure in the contact zone causes time-dependent plastic deformation known as creep [346]. Numerous factors, including the plastic deformation properties of the material, diffusion constants, the normal-acting load of the indenter, and the indentation duration, affect the indentation hardness-creep. In other words, the pile-ups of grain boundary dislocations brought on by mobile dislocations released from grain borders that travel through entire grains regulate the creep mechanics [347-348].

According to the nanoindentation 10 % rule, the nanoindentation should not exceed 10% of the total film thickness to avoid the influence of the glass substrate [327]. Accordingly, the maximum load applied was 70 μN with a maximum depth penetration of 19 nm in the nanoindentation experiment.

The hardness and Young's modulus for the CdS films on glass were determined at maximum load of 20, 30,40 and 50 μN at 1,5 and 10 Å/s as shown in Fig 6.10(a), 6.12 (a) and 6.13(a), respectively[342-343]. CdS thin film creep at 1,5 and 10 Å/s deposition rates is shown in Fig. 6.10(b), 6.12(b) and 6.13(b), respectively with maximum load of 30 and 40 μN with a hold period of 5 s. CdS thin film's strain rates with maximum load of 70 μN for loading and unloading times of 0 s and 20 s are shown in Fig. 6.10(c), 6.12(c) and 6.13(c). In Fig. 6.11 (a) & 6.11(b) Scanning probe microscopy (SPM) indentation 2-dimensional and 3-dimensional images of 70 μN maximum load at 1 Å/s deposition rate are shown. CdS thin film nanohardness values rise with

rising applied indentation load at all deposition rates. This type of effect is called reverse indentation size effect (RISE) [343]. It is clearly indicated that nanohardness is a straight function of low peak indentation applied loads, where there is no fixed value for the nanohardness which is load dependent. Creep graphs analysis indicated that there was a small variation in the displacement during the holding times at a load of 30 μN compared to 40 μN. The strain rate graphs analysis indicated that a very little quantity of displacement from a loading and unloading time of 0 s and 20 s.

Three phenomena have been identified as the main causes of the pop-in shown in nanoindentation load-displacement characteristics under loading: (a) The beginning of elasto-plastic transition, (b) Phase Transition, and (c) Fracture propagation. After closely examining the materials using scanning probe microscopy (SPM), no cracks were found near the indentation marks [332-334, 349-352]. Pop-in effects from the sudden displacement of material as a result of accumulation and slip of dislocations, leading to a strain hardening effect, were observed during loading. This was due to increased resistance to deformation as a result of a greater density of dislocations, restricting the creation and movement of new dislocations. Pop-in effects were observed during increasing loads and hold periods due to the accumulation of dislocations from previous loads and the formation of new dislocations. The pop-out feature is assigned to poor densification of the film on substrate, phase transformation, and residual deformation [353]. In CdS thin film this feature may be due to the formation of a chain-like island texture in the indented microstructure.

Grain boundary diffusive creep (cobble) dominates indentation creep in materials with tiny grain sizes. This type of creep is caused by atoms being added or removed from the boundary between two grains. The higher displacements seen for creep and strain rate data are thought to be caused by this diffusional creep [344-345,354-356]. Creep and strain rate measurements for the thin film revealed longer loading-unloading durations and displacements of a few nanometers during the hold period. This is thought to be caused by diffusion creep related to translation of grain boundaries.

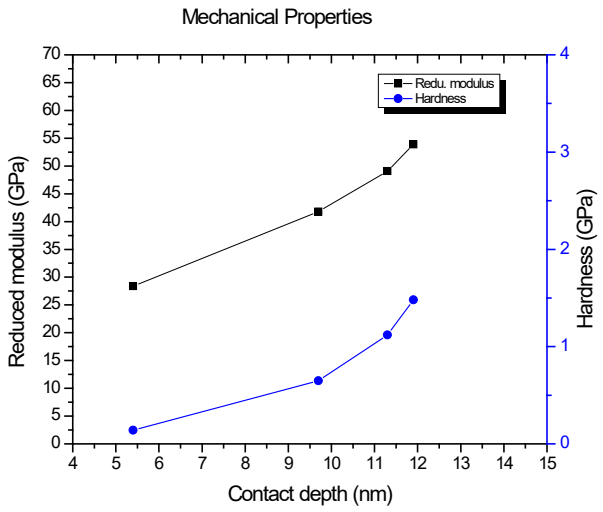

Figure 6.10 (a): Mechanical properties of CdS film at 20, 30, 40 and 50 µN loads for 1 Å/s deposition rate

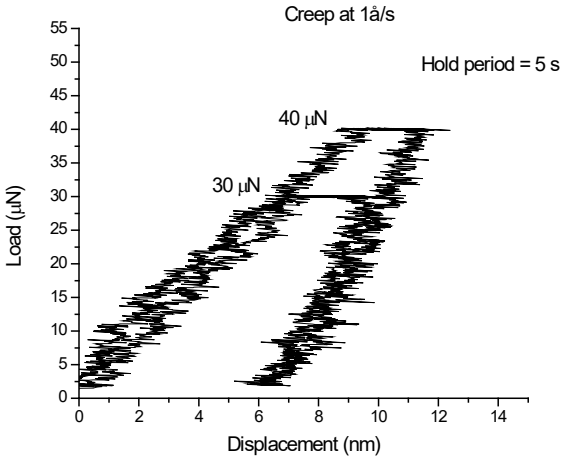

Figure 6.10 (b): Creep of CdS thin on glass at 1 Å/s deposition rate at 30 and 40 µN loads

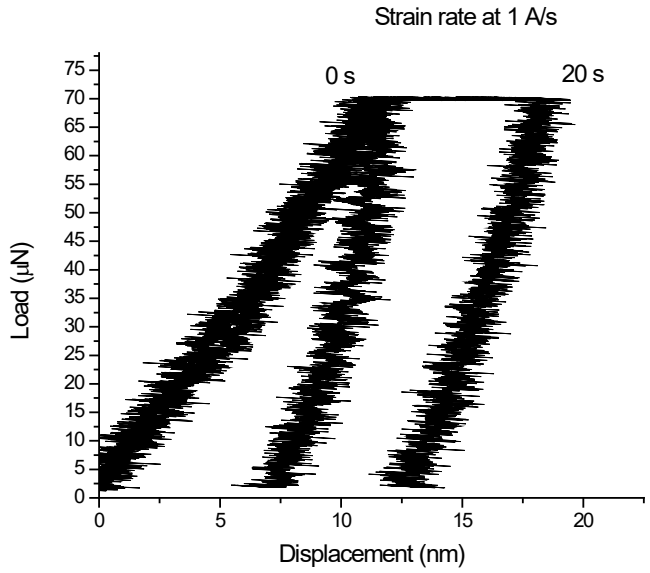

Figure 6.10(c) : Strain rate of CdS film at 1 Å/s deposition rate

The Fig. 6.10(b) shows creep for typical load-displacement curves with maximum loads of 30 and 40 μN with a hold period of 5 s at 1 Å/s deposition rate. The loading and unloading curves are almost overlapping with negligible displacement. Fig.6.12 (b) creep-curve at 5 Å /s deposition rate reveals that there is a gap between loading curves and curves are not smooth. Fig. 6.13(b) shows the creep at 10 Å /s deposition rate, the loading curves are overlapping but there is small displacement between unloading curves. Thus, overall creep behavior is good at 1 Å /s deposition rate as revealed by creep experiments.

Fig.6.10 (c), 6.12 (c) and 6.13 (c) show indentation-displacement curves for different strain rates with a maximum load of 70 μN for loading and unloading time of 0 and 20 s. The creep and strain rate data gives an indication of whether the experiments are sensitive to hold times and loading and unloading rates. For creep data there is very little difference in the displacement during the holding times at a load of 30 μN compared to 40 μN. The strain rate data also shows a small amount of displacement from a loading and unloading time of 0-20 s and smooth loading and unloading curves at 1 Å/s deposition rate as shown in Fig. 6.12. The strain rate data for same loading and unloading time shows also small displacement but the loading curves are not overlapping at 5 Å/s deposition rate as shown in Fig. 6.16. At 10 Å/s deposition rate the loading curves are overlapping with very small displacement but the unloading curves are not smooth rather pop out event occur. Thus, overall picture of strain rate experiments revealed that at 1 Å/s deposition rate the creep behavior of the CdS film is good.

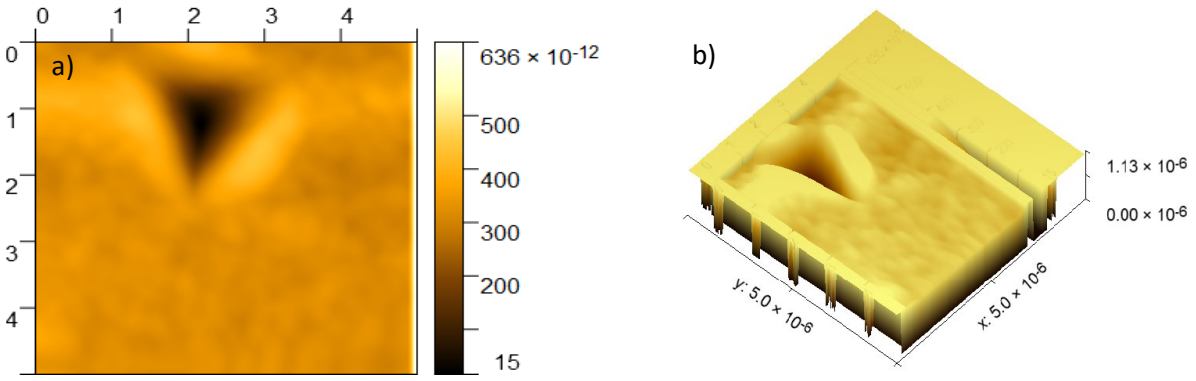

Figure 6.11: 70 µN indentation load impression image of CdS film at 1 Å/s (a) 2-dimensional image (b) 3-dimensional image

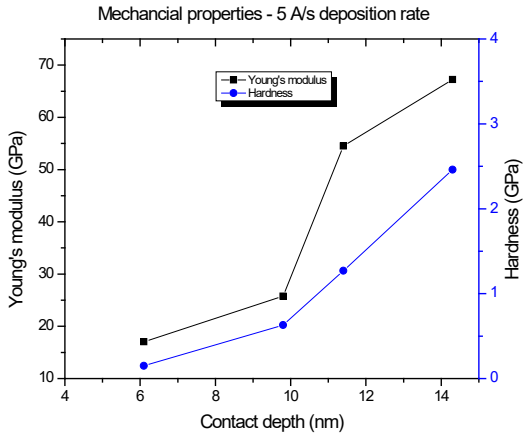

Figure 6.12 (a): Mechanical properties of CdS film at 20, 30, 40 and 50 µN loads for 5 Å/s deposition rate

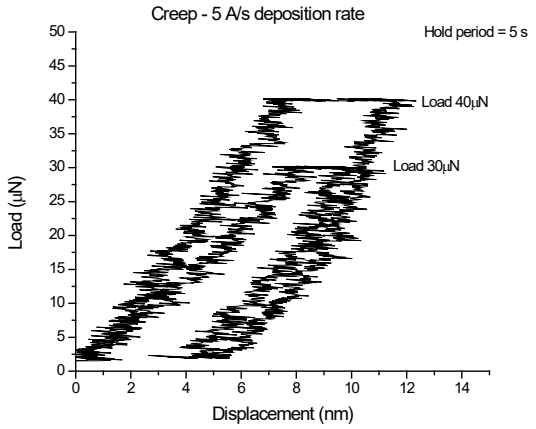

Figure 6.12 (b) : Creep of CdS thin on glass at 5 Å/s deposition rate at 30 and 40 μN loads

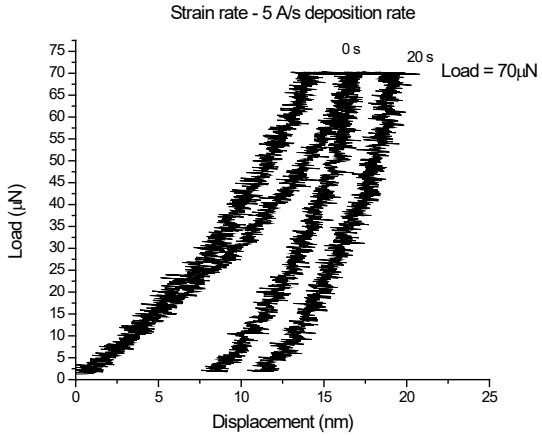

Figure 6.12 (c): Strain rate of CdS film at 5 Å/s deposition rate

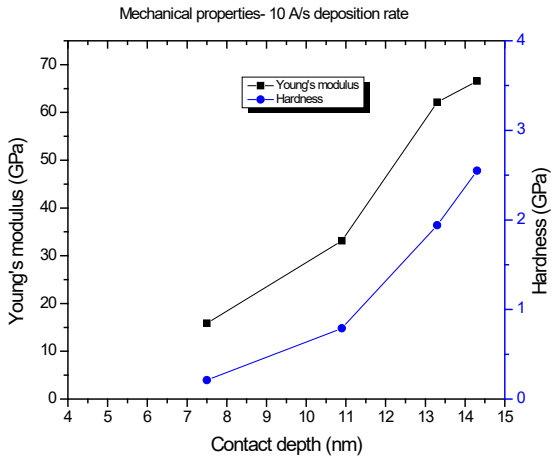

Figure 6.13 (a): Mechanical properties of CdS film at 20, 30, 40 and 50 µN load for 10 Å/s deposition rate

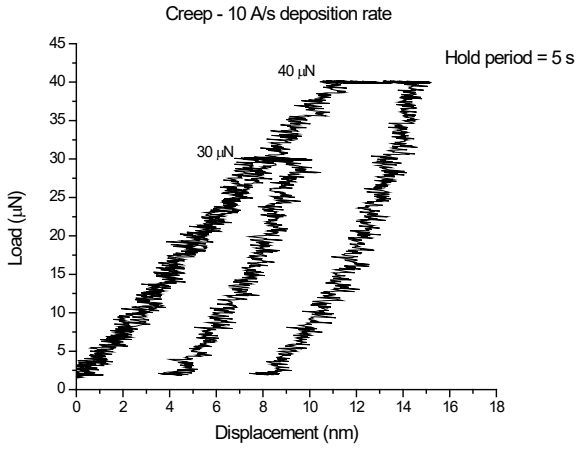

Figure 6.13 (b) : Creep of CdS film at 10 Å/s deposition rate at 30 and 40 µN loads

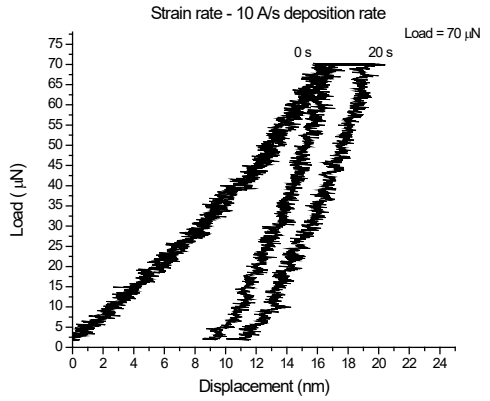

Figure 6.13 (c): Strain rate of CdS film at 10 Å/s deposition rate

The comparison of hardness and Young's modulus for different deposition rates of CdS thin film on glass deposition is shown in Fig. 6.14. CdS thin film hardness increases with increasing the rate of deposition due to decreased crystallite size for higher deposition rate (10 Å/s) as examined from XRD results. These results agreed well with the Hall-Petch effect [345]. Another reason for high hardness of CdS film at 10 Å/s deposition rate is due to higher defect density. A material's elastic modulus is its susceptibility to undergo elastic deformation in response to applied force. Stated differently, the elastic modulus was directly correlated with the strength of the bonds between the atoms or molecules in the material; a larger bond results in a higher elastic modulus [343]. Young's modulus decreases sharply from 1 to 5 Å/s deposition rate but from 5 to 10 Å/s it decreases very slowly (almost constant). Localized deformations can be studied through indentation experiments using a sharp three-sided pyramidal Berkovich tip owing to the depth-sensing nanoindenter. For polycrystalline material, strain gradient in nanoindentation at low penetration depths can be accommodated by geometrically necessary dislocations (GNDs) created to accommodate grain boundaries and interiors, or by multiplying pre-existing dislocations during loading. The dislocation density mechanism explained that as there are more dislocations per unit area, or density (ρ), when the grain size decreases because there is a higher total grain border area within the same volume on the nanoscale compared to the macroscale. The development, mobility, and multiplication of existing dislocations which are required to tolerate strain gradient and subsequent deformation are hampered by this dislocation entanglement. This leads to elevated yield stress and improved resistance to deformation [332, 340-341, 357-359].

In the pile-up mechanism, dislocations are formed along slip lines and finally pile up against the grain boundary for a certain applied stress (τ) on the grains. The pile up stress is the name given to the stress at the grain barrier. Larger grains have more dislocations in the pile up than smaller grains do, which increases the pile up stress (τ_p). In order for a slide to happen over the grain boundary, τ_p needs to be higher than τ_c, the critical stress. Therefore, in order to allow slip to occur and plastic deformation to precede, a greater initial stress (τ) is needed on small grain before the critical stress is reached [335-339,360-363]. This results in a larger yield stress than on large grain.

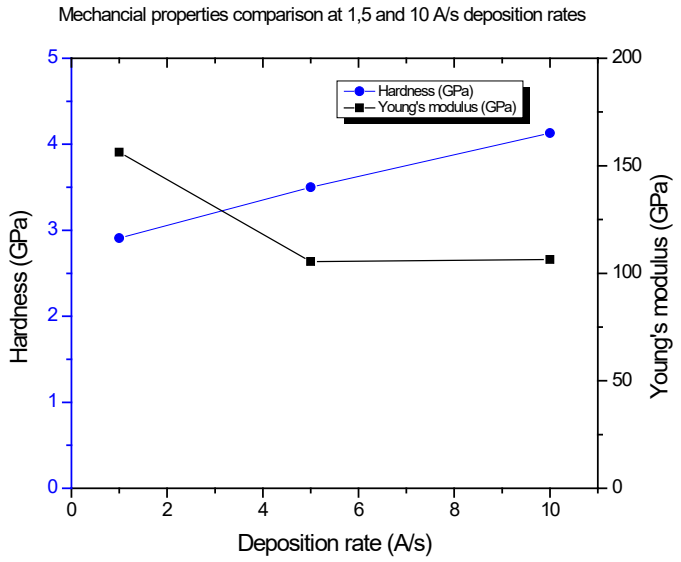

Figure 6.14: Comparison of mechanical properties of CdS films at 1, 5 and 10 Å/s deposition rates

6.4. Conclusions

In this study, thermal evaporation method was used to deposit CdS thin films of 200 nm thicknesses on glass substrates at 1, 5 and 10 Å/s deposition rates. The CdS thin film thickness of 200 nm verified by dektak surface profilometer. XRD examination indicated that the CdS thin films were of hexagonal structure with preferential orientation towards (002) plane for all deposition rates. The crystallite size was decreasing but microstrain and dislocation density were increasing with increasing deposition rates. The film surface roughness increases with deposition rates. The AFM 2-dimensional and 3-dimensional images revealed that the CdS film surface roughness value was lowest at 1 Å/s deposition rate. The SEM micrographs indicated that the films were not discontinuous and uniform coverage over the entire surface without any pin holes or cracks. The EDX elemental analysis showed that the film at 1 Å/s deposition rate was more stoichiometric than the other deposition rates. CdS thin films revealed higher transmittance (~80 %) in visible region and E_g value increase with deposition rate. From nanoindentation tests hardness, Young's modulus, creep and strain rates were determined at different deposition rates. The hardness of the CdS film rises with increasing deposition rate. The Young's modulus of the CdS film decreases with increasing rate of deposition and becomes almost constant 5-10 Å/s deposition rate. Force displacement curves reveal reverse indentation size effect for CdS thin films. The overall creep and strain rate behavior of CdS film is better at 1 Å/s deposition rate. Thus, overall experimental results of structural, morphological, optical and mechanical characteristics recommend CdS thin film at 1 Å/s deposition rate was having great potential in light emitting diodes, photon devices applications and a window layer for solar cells.

In future film properties can be studied for less than 1 Å/s and more than 10 Å/s deposition rates. The electrical properties as well as ellipsometry study can be added. In future statistical data analysis will be done for deeper understanding of the data after conducting more number of experiments.

CHAPTER 7

COMPARISON OF TIN AND INDIUM THIN FILM'S STRUCTURAL, MORPHOLOGICAL, ADHESION AND ELECTRICAL PROPERTIES FOR OHMIC CONTACT IN HgCdTe-BASED IR DETECTORS

7.1. Introduction

Infrared detector arrays, particularly those utilized for imaging infrared systems for vital military purposes, are made using tiny-gap $Hg_{1-x}Cd_xTe$. Mercury cadmium telluride (HgCdTe) is an excellent substance to use in the development of infrared detectors because of its optical and electrical characteristics. Technology for forming contacts with low as well as homogeneous contact resistance in HgCdTe detector elements is required for avalanche photodiode detector arrays, high operating temperature performance, reproducibility, and long-term stability. The metal/HgCdTe ohmic contact and low specific contact resistance are two of the key elements influencing the efficiency and dependability of an HgCdTe infrared detector [17,365-368]. In order to ensure the linearity of current-voltage (I-V) characteristics, a contact is considered "ohmic" if the voltage drop across it is significantly less than the voltage drop across the device. The repeatability and dependability of Ohmic connections are additional crucial characteristics [369-370]. During device fabrication, $Hg_{1-x}Cd_xTe$ alloys are more prone to damage than elemental semiconductors. On HgCdTe, the formation of metallic contacts at room temperature breaks the lattice and results in mixing of the alloy's constituent elements with the contact metal [371-372] Contact degradation brought on by this reaction may eventually lead to surface dissociation and heat instability during packing and field use.

When the interfacial barrier's height and width are at their minimum, an effective ohmic contact forms, allowing the current transport to be dominated by a massive tunneling component. On elemental semiconductors, forming an ohmic metallic contact is simple. However, in compound semiconductors, it has turn out to be extra tricky because pinning the Fermi level in the mid-gap section causes the creation of a high interfacial barrier width [57,373-374].

To create an ohmic electrical metal contact on HgCdTe-based IR photodetectors or devices, a variety of metal schemes, including single, double, and triple metal layers, have been presented. These schemes include Cr, In, Al, Au, Ti, Ni, etc [375-378]. A.R. Momen-Baghdadabad *et al.* [379] examined the iron thin film characteristics such as magnetization, hardness, friction coefficient, charge transfer resistance, and elemental composition.

***Portion of this work has been published in Materials Engineering and Performance 34, 18502–18515 (2025).**

Authors have studied the chrage transfer phenomena in film with XPS and anticipated the improvement in corrosion resistance. They have also evaluated the material hardness and scratch resistance using nanoindentation and nanoscratch tests. The vibrating sample magnetometer (VSM) study indicates that multi-phase steel films exhibit paramagnetic behavior, indicating the possibility of a retained austenite percentage dominating the films. The TLM method can be used to evaluate the electrical characteristic of the prepare Sn/n-$Hg_{o.4}Cd_{o.6}Te$ junctions. The creation of a surface region that is more strongly doped with n-type than the bulk and the inward diffusion of Sn. At temperatures of up to 300 °C, Sn was identified as an electrically active donor atom. Hg is ejected and replaced by Sn in the uppermost monolayer of the $Hg_{0.78}Cd_{0.22}Te$ lattice at the interface Sn/HgCdTe. An epitaxial layer of SnTe with inclusions of CdTe was shown to increase with additional Sn deposition (and Hg loss) [94,377,381-382].

According to a report [382], indium (In100 nm) can be used to furnish the indium/n-zinc selenide interaction with adequate Ohmic connection. Indium/n-MCT, mercury telluride/indium/gold/MCT, titanium/platinum/gold/MCT as well as organic organic (3,4-polyethylene-dioxythiophene) poly (styrene sulfonate) (PEDOT: PSS) /MCT are the other documented ohmic contact-schemes [57,91,94,377,383]. With the exception of the PEDOT: PSS /n-type MCT integration, that includes demonstrated a modest enhancing behavior, all interfaces had ohmic I-V characteristics [383]. The n type-In (1.4 μm) metal layer was used in the fabrication of the HgCdTe based injection laser, which is a light-emitting device with well-behaved electrical properties. On InGaN light-emitting diodes (LEDs), similar indium /indium tin oxide centered metallic design emerged into practice to achieve high-quality ohmic connections. The interface based on In and In (200 nm)/ITO (200 nm) was reported to have specific contact resistances of 2.2 × 10^{-5} Ωcm^2 and 1.8 × 10^{-3} Ωcm^2, respectively [384-386]. A flat contour of its outer layer on behalf of the In/I_2O_3/zinc oxide connectin has been achieved by Palimar *et al.* [387]. According to the literature [389], molybdenum/gold as well as molybdenum/indium connection be used to fabricate various infrared detecting devices (molybdenum/gold interface: Ohmic connection for discrete sensors, molybdenum/indium connection: indium bumps for multi element focal plane array). According to a recent report [388], the thermally grown In (100 nm) film was used to fabricate the ultraclean ohmic van der Waals contacts on MoS_2. The specific contact resistance (ρ_c) of the In/MoS_2 interface was 5.0×10^{-6} - 5.0×10^{-7} Ω cm^2 with a uniform surface morphology of the In film. Consequently, it is widely known that indium (In) can create an ohmic contact on n-type HgCdTe. The substrate/metal interface, surface treatments (during processing), deposition circumstances, and other factors are related to the electrical characteristics of metallic contacts. Thus, it is possible to generate ohmic electric contacts to a HgCdTe-based photodetector while preserving elements such as low-temperature deposition, a highly adherent metallic layer, and low noise levels [388-389]. Thus, by creating linear current-voltage metallic connection upon MCT surface as well as compact connectivity indium film (MCT-sensor alongwith silicon-readout integrated circuit), it be possible to create IR detectors with high reliability and performance. The In/HgCdTe pattern, encompassing the entire of its crystallograhic, surface countour as well as electrical features, has not been studied thoroughly earlier.

The physical-chemical phenomenon accountable for the joining of two surfaces when they come into contact is called adhesion. Adhesion force (pull-off force) in nano or micro system is controlled by topography of thin film and tip and chemical composition. Corina Birleanu *et al.* [390] determined the tribo-mechanical features of 100-500 nm thickness Cr-Au films. They determined the frictional force, work of adhesion, and adhesion force (pull-off force). The Cr-Au pull-off force measured 87–190 nN, the work of adhesion was 1-2.5 J/m^2 , and the coefficient of friction was 0.015. Due to their low specific contact resistance and low surface stickiness (adhesion), thin layer gold and silver were utilized in MEMS appliances, particularly in microgrippers [391-392].
The aim of the present work [393] is to study the structural, morphological and electrical properties both In and Sn film on n type $Hg_{.71}Cd0_{.29}Te$ material to understand their role for making good ohmic contact on n region of HgCdTe detector. In and Sn material are chosen for the present study as these two materials form a good ohmic contact on n HgCdTe among all other regularly used metals as reported by P. Leach *et al.*[377]. This work is specifically done for MWIR HgCdTe detector array for which x value is 0.29. Specific contact resistance is also estimated experimentally for both films to choose the best material between them for MWIR HgCdTe detector array. In addition to that surface adhesion force and adhesion work for both film on HgCdTe are estimated which is a novel work as it is not reported in literature for HgCdTe material. This is useful for determining the reliability of film.

The characteristics of thermally produced tin and indium films were assessed using a variety of characterization methods such as AFM, EDS, SEM, and XRD. The results show that the grown indium films, which were used to fabricate indium film (in the configuration of In/n-HgCdTe) for transmission line model (in the arrangement of indium/n/p-MCT), are optimal. SEM analysis was used to assess the microstructural characteristics of the (Sn/HgCdTe and In/HgCdTe) interface. I-V/resistance measurements have been used to analyze the formed TLM structures. The resulting In/HgCdTe interface electrical properties exhibit minimal contact resistance and ohmic behavior. In light of this, we may conclude that the indium is best suited material for forming n-type ohmic contact on HgCdTe based IR photodetector using thermal evaporation method.

7.2. Materials and methods

Using the TLM, test structures were created to gauge the Sn-HgCdTe and In-HgCdTe system's contact resistance. The investigation of thin films was conducted using the n-type $Hg_{1-x}Cd_xTe$ epilayers, and a homegrown technique known as vertical dipping liquid phase epitaxy (VD-LPE) was used to create the epilayers on cadmium zinc telluride (111) base. To carry out the proposed investigation work, epilayers with the following parameters were used: dimensions: 30×30 mm^2, thickness: 10 μm, composition: x = 0.29, concentration: 1×10^{16} cm^3, mobility: 416 cm^2 V^{-1} s^{-1}. These were refined utilizing bromine in methanol etching solution in chemo-mechanical and chemical etching procedures. After polishing, ellipsometric parameters were tested to guarantee a

defect-free and contamination-free surface. ZnS-capped thermally evaporated CdTe was an easy way to passivate recently polished and etched surfaces. ZnS/CdTe films were etched subsequent to the PLG contact pattern generation. Using a regulated junction depth (1.0–1.4 μm), boron charges are gradually dispersed inside the MCT substrate to form native defects accountable for kind transformation, resulting in a n/p area on the sample. At room temperature, the implantation process is usually carried out with the following parameters: incidence angle: 7 degree, implantation dose: 5×10^{14} atom/cm^2, and ion energy: 50–140 kilo electron volt. The epilayer was then descummed using oxygen plasma for 30 seconds (vacuum: 10^{-1} - 10^{-2} Torr, power: 100 watt, oxygen rate of flow: 200 milli litre/minute), and then transferred into the coating unit's vacuum chamber. Following the achievement of the maximum chamber vacuum, which was 4.0×10^{-7} Torr, the tin and indium thin film (5 μm) were deposited on the HgCdTe by vacuum evaporation process. A quartz crystal was employed to determine the film thickness and film deposition rate. The 99.999 % pure tin and indium small shots were placed in molybdenum boat for actual evaporation. After completing a photolithography lift-off procedure (in CH_3COCH_3) of the deposited specimen, the final TLM structure was obtained.

The structural properties of thermally evaporated films were evaluated using a high-resolution XRD system (Model: PAN Analytical B.V.-X'Pert PRO MRD), with a CuKα radiation source (wavelength = 1.542 angstrom) and Xe-proportional counter. Using the AFM (Model-5600LS, Agilent Technologies) instrument, the morphological data of small layers were obtained at the constraints (grazing angle = 3 degree as well as 2-theta = 20-85 degree). The microstructural and compositional characteristics of tin and indium films grown on HgCdTe were determined using a FESEM (Model: Carl Zeiss SUPRA55VP) assisted by an Oxford Instrument X-MAX EDX Spectrometer (voltage for functioning: 5–20 kilo volt). The surface quality of the film was measured by LSE MS STOKES Ellipsometer Model - 7109-C370 M from GAERTNER. Monochromatic helium-neon laser beam was used at examining angle of 70 degree and wavelength used 6328 Å. The thicknesses of films were determined by KLA alpha step D500 surface profiler. The Sn/HgCdTe and In/HgCdTe based TLM structure's current–voltage (I–V) and resistance measurements were carried out using a cryoprober (Model: Keithley Parametric analyzer, Model-4200, with integrated 4200–CUV card). At 80 K, the I-V properties of the TLM structure based on HgCdTe were observed.

7.3. Results and discussion

7.3.1 Crystalinity measurement

Tin (Sn) as well as indium (In) diffraction pattern of both Sn and In indicated good agreement with typical Bragg's peak of Sn and In with a tetragonal bcc phase as shown in Fig. 7.1 (a) & 7.1 (b), respectively. The good crystalline properties of the Sn and In films were interpreted by the fine intensity and close line-broadness of the analyzed XRD peaks. The XRD intensive peaks obtained related to tetragonal bcc phase (200) preferential plane at $2\theta = 30.66°$ and (101) preferential plane

at 32.94° of β-Sn and In films, respectively.The β-Sn film's other peaks obtained were at 2θ = 43.85°, 44.95° , 55.39°, 63.84°, 64.62°, 72.45°, 73.17°, and 79.55° of (220), (211), (301), (400), (321), (420), (411), and (312) planes , respectively (JCPDS no. 89-7898)[364-365]. The indium film's low intense peaks were at 2θ = 36.30°, 39.16°, 54.47°, 56.58°, 63.20° , 67.05°, 69.12°, and 77.15° of (002), (110),(112), (200), (103) , (211), (202), and (004) planes , respectively (JCPDS no. 85-1409)[366-401,403].The average crystallite size (D) of Sn as well as In films were calculated using the Debye Scherrer's equation,(D= $(0.94\lambda)/(\beta Cos\theta)$)[402-403,409], where θ is the angle of diffraction and β is full-width half maximum (FWHM). The lattice misfit due to film deposition conditions generates the strain in the film. The strain (ε) in the Sn and In were calculated by using the equation (ε = β/4Tanθ) [409 ~~49~~]. The dislocation density (δ) of the Sn and In were determined by employing the equation ($\delta=1/D^2$)

Table 7.1 Crystalline structural parameters of Sn and In for (200) and (101) preferred orientation planes

	Sn	**In**
Crystalline structural parameters	Calculated values	Calculated values
Lattice plane	(200)	(101)
2θ (degree)	30.66	32.94
FWHM β (radian)	0.004502	0.004537
Average crystallite size D ,nm	33.14	33.27
Strain ε (x 10^{-3})	4.10	3.83
Dislocation density δ (x 10^{10} lines/cm^2)	9.10	9.03

The β-Sn and In film's crystalline structural parameter for (200) and (101) plane calculated from X-ray diffraction results were given in Table 6.1. From Table 7.1, the obtained values of crystallite size, micro strain and dislocation density were comparable with the earlier reported results [366,368,400-408]. The X-ray results revealed that the grain sizes 33.14 nm and 33.27 nm of Sn and In films, respectively. The microstrain and dislocation density of In film were lower than the Sn film which indicated that In film was good crystalline structure.

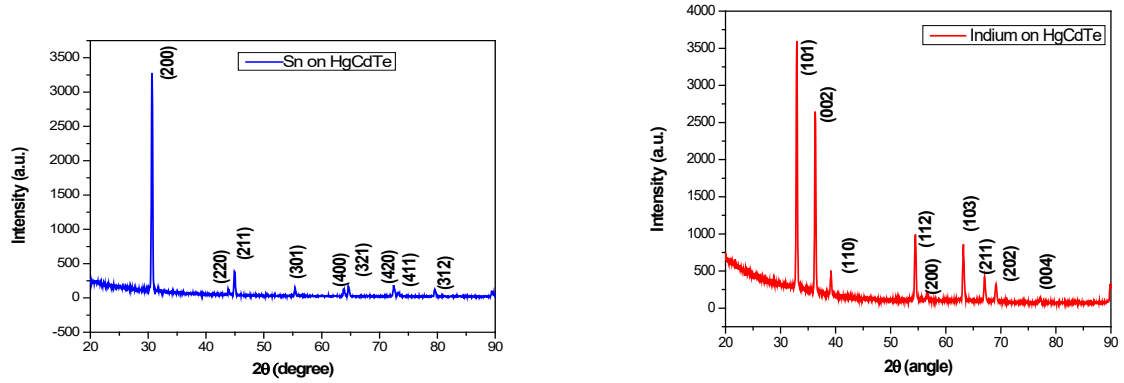

Fig. 7.1 XRD pattern (a) tin film (b) indium film

7.3.2 Surface morphology and compositional analysis

The SEM micrographs of the Sn as well as In were shown in Fig. 7.2 (a) (b) & 7.3 (a) (b), respectively. Visually both Sn and In films were having white shiny surface with no pin holes or cracks. The SEM images of Sn film indicated the rough film with cloudy surfaces. The Sn films showed non-uniform particle sizes ranging from few nanometers to micron size distributed all over the entire film [410]. The SEM images of In film indicated the continuous and uniform film with some uneven particle sizes of 1-2 µm [401,411].

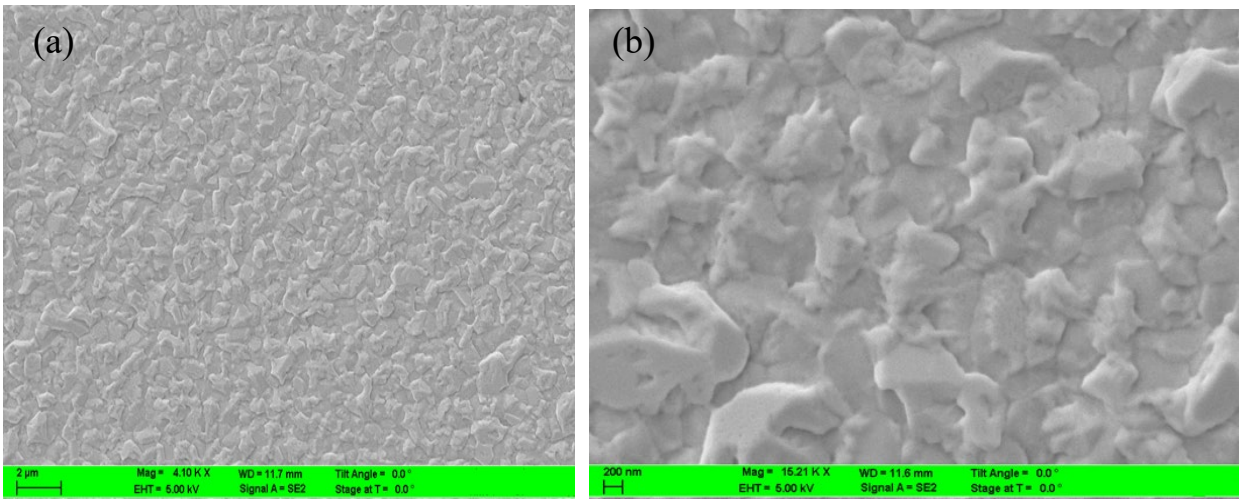

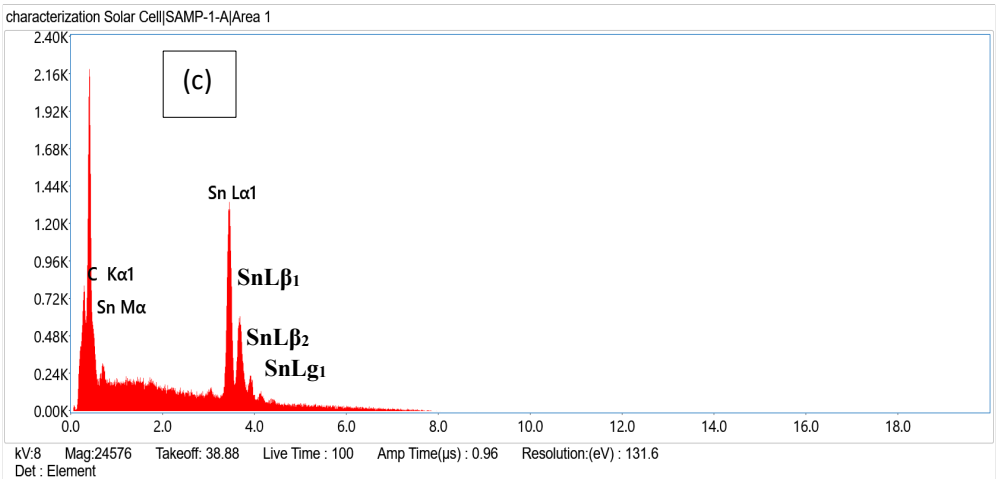

Figure 7.2 SEM images of tin (a) SEM image at 4 KX magnification (b) Close view at 15KX magnification (c) EDS spectrum graph of tin

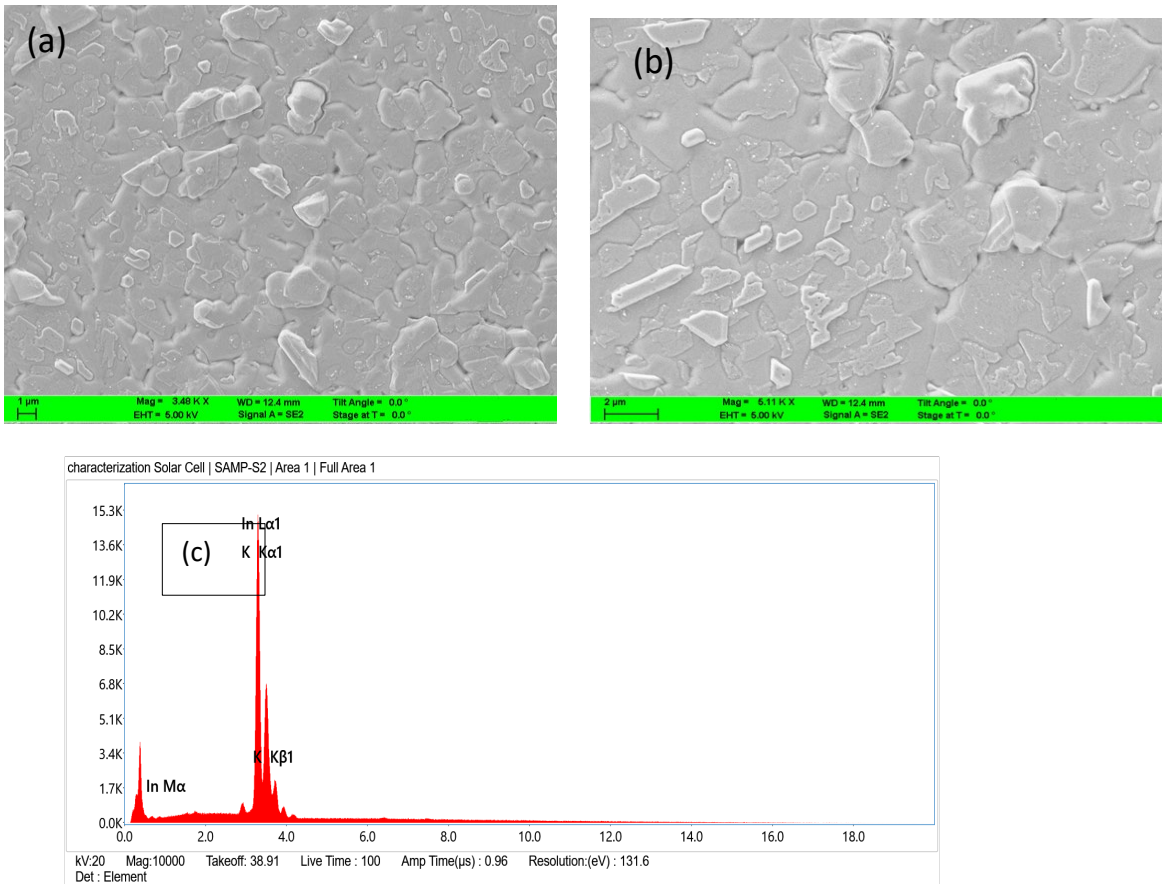

Figure 7.3 SEM images of indium (a) SEM image at 3.48 KX magnification (b) SEM image at 5.11 KX magnification (c) EDS spectrum graph of indium

The EDS analysis was done to verify the wholesomeness of tin and indium in the layers. The EDS spectrum of Sn and In films were shown in Fig. 7.2 (c) & 7.3 (c), respectively. The obtained experimental values indicated that the atomic % 51.50 and 94.80 of tin and indium elements, respectively [401,412]. The little quantity of carbon element was present in Sn film may due to HgCdTe film exposed to atmosphere during mounting on the sample holder or during the handling of HgCdTe sample. The small amount of K was present in In film may be because of contagionity of substrate at the time of handling of HgCdTe. Broad region around the dominate peaks in EDS spectrum are due to background, surface plasmon and interband transition. Interband transition plasmon, and electrons that are scattered are a result of interactions that cause the sample material's electrons to oscillate plasmonically or to transition between distinct energy levels. Due to its plasmon resonance, gold nanorods in particular and gold nanostructures in general have been used in numerous applications, including biosensors. There are two surface plasmon resonance bands in gold nanorods and one surface plasmon resonance band in gold nanoparticles. The plasmon oscillations on the (PVA / NiPc) sample surface are the reason why the crystallites are not spherical in shape [413-414]. Vamsi Borra *et al.* [412] grown rough Sn film at 0.05 nm/s -1.6 nm/s deposition rates and challenging smooth Sn film 2.6 nm/s - 2.8 nm/s deposition rate on Si and soda lime glass by thermal evaporation process. They done the EDS analysis of the smooth Sn film and found that the film was pure Sn only or no other elements was present which very well agreed with our study .

7.3.3 Surface topography analysis

The Sn and In film's topography were analyzed with silicon tip in tapping mode. Fig. 7.4 (a), (c), (e) and Fig. 7.4 (b), (d), (f) showed the AFM images of Sn and In films, respectively. The scan size was 5 μm x 5 μm for Sn and In films. The root mean square (rms) roughness, average roughness and other roughness values for both the films were given in Table 7.2.The AFM images indicated that r.m.s. roughness value were 44 nm and 20 nm of Sn and In, respectively. The Sn and In films roughness values were comparable with the previous study [403,415-416] but the Sn film surface roughness was double than the In film surface roughness.

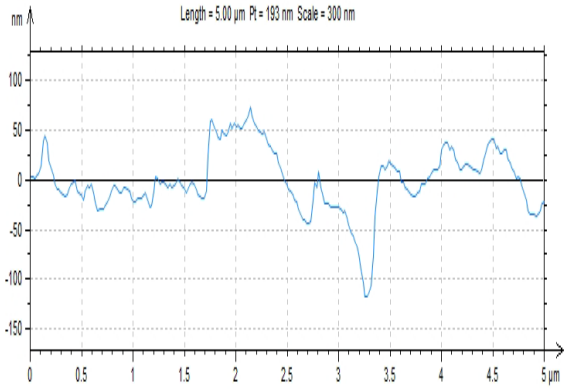

(a)Sn film line diagram

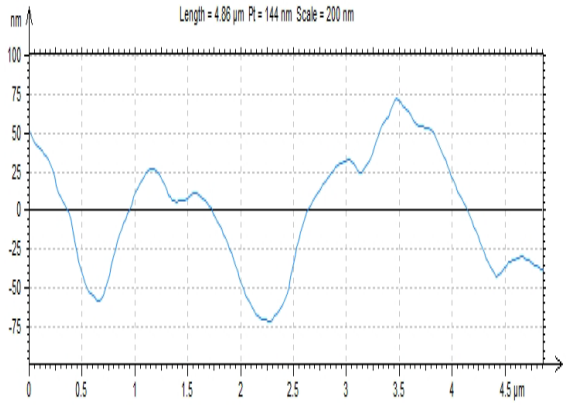

(b) In film line diagram

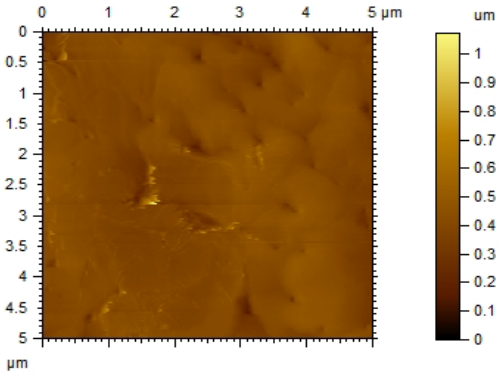

(c) Sn film 2-Dimensional image

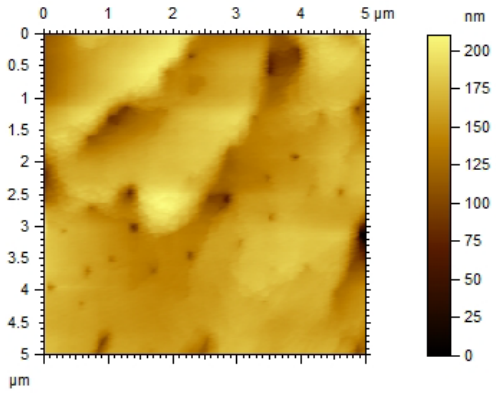

(d) In film 2-Dimensional image

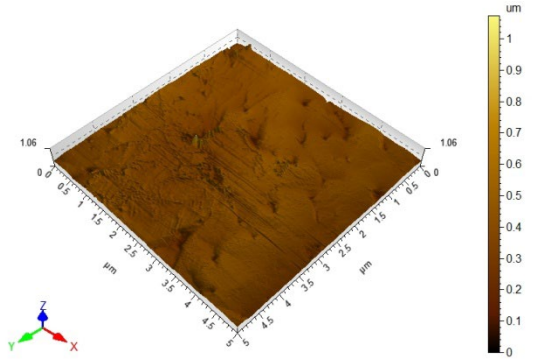

(e) Sn film 3-Dimensional image

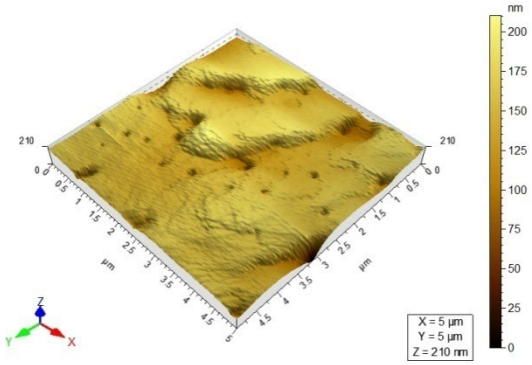

(f) In film 3-Dimensional image

Figure 7.4 AFM topography images of Sn and In film

The AFM line diagrams of Sn and In films scanned surface were shown in Fig. 7.4 (a) & (b), respectively. The line profile of the films given information about the increase of the grain size

and roughness of the film surfaces**.** R_z is the difference between the tallest peak and the deepest valley in the surface. R_{sk} is used to find the asymmetry of the roughness profile about the mean line. R_{ku} (roughness kurtosis) is used to find the peakedness of the profile about the mean line.

Table 7.2 Roughness Table of Sn and In films

Film	R_a (nm)	R_q (nm)	R_z (nm)	R_{sk}	R_{ku}
Sn	32	44	1060	0.19	10.62
In	15.2	20	210	0.94	5.78

7.3.4 Calculation of adhesion properties

The AFM force microscopy in contact mode was utilized to determine the adhesion-force (pull-off force) and adhesion-work of tin as well as indium films. From force-distance curve (f-d curve), obtained from AFM force spectroscopy the adhesion force is determined from adhesion force among film and AFM tip. The f-d curves of Sn and In film on n-HgCdTe substrate were shown in Fig. 7.5 & 7.6, respectively. DMT and JKR theories are used to calculate the thermodynamic work of adhesion assuming that the forces of affinity at the adjoin region are similar to those outside region. Corina Birleanu *et al.* [390] determined the pull-off force and work of adhesion of Au thin film of different thickness and found that the adhesion properties vary with film thickness. For adhesion properties measurement in contact mode, the tip used was Si with Au reflective side, tip curvature radius 10 nm, tip height 14-16 μm, resonant frequency 4-17 kHz. The maximum force, adhesion force and work of adhesion of Sn and In films were given in Table 6.3.The Eqns. (7.1) & (7.2) were used to determine the adhesion force and thermodynamic work of adhesion of Sn and In thin films;

$$F_{DMT=} -2\pi\gamma R \qquad (7.1)$$

$$F_{JKR=} \frac{-3}{2} \pi\gamma R \qquad (7.2)$$

where R was tip radius in nm and γ was the adhesion-work in J/m^2

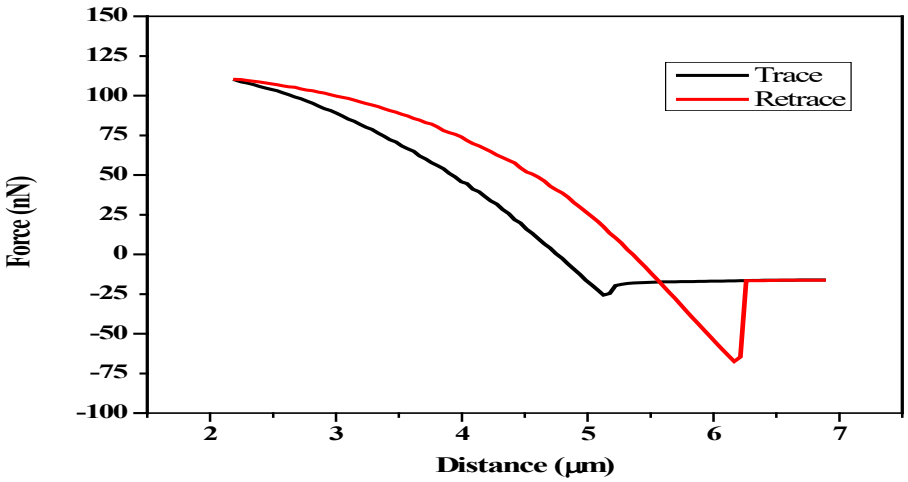

Figure 7.5 AFM f-d curve of Sn on HgCdTe substrate

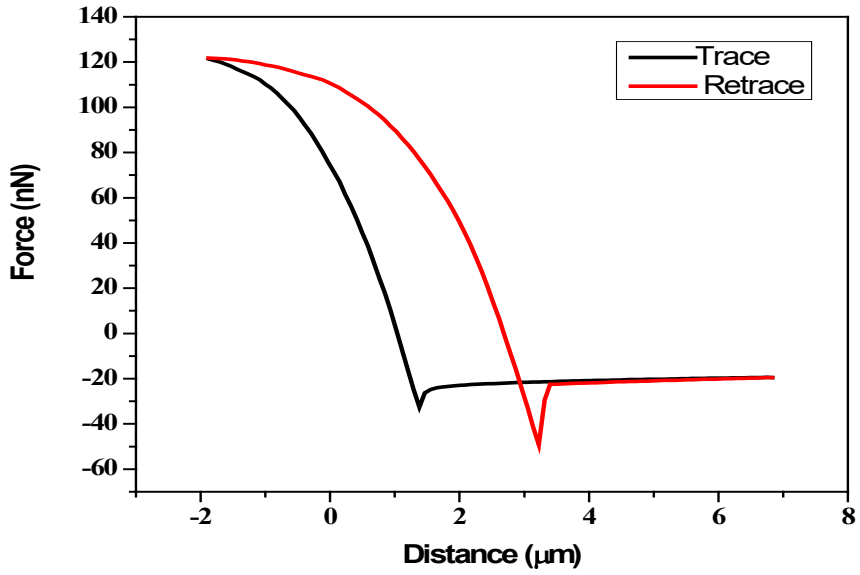

Figure 7.6 AFM f-d curve of In on HgCdTe substrate

Table. 7.3 Maximum force, pull-off force, and thermodynamic adhesion-work based on DMT and JKR theories

Film	Maximum force (nN)	Pull-off force (nN)	Adhesion-work (J/m^2)	
			ω_{DMT}	ω_{JKR}
In	121.73	26.95	0.42	0.57
Sn	110.25	50.73	0.80	1.07

From Table 7.3, we observed that the pull-off force and adhesion-work of Sn film were almost double the In film though the density (7.31 g/cm ^{3}) of bulk tin and indium were same. Thus, this difference was due to different metal particles arrangement on HgCdTe surface during film growth leading to different compact or denser films. The indium film's adhesion properties were studied and found comparable with our study [420]. The adhesion force and adhesion-work obtained by Corina Birleanu *et al.* [390]of Au films were different from our results due to different metal films physical properties as our metals (Sn and In) are soft with low density and low melting point compared to Au.

7.3.5 Ellipsometry analysis

The ellipsometry analysis is identified by two factors psi (ψ) and delta (Δ). It measures the complex reflection ratio ρ:

$$\rho = \frac{r_p}{r_s} = \text{Tan}\psi \, . \, e^{i\theta} \qquad (7.3)$$

where rp and r_s are Fresnel reflection coefficients. Tanψ is the amplitude ratio after reflection and Δ is the phase difference. The ellipsometric (laser ellipsometry) measurement of Sn and In films were done to find out the quality of surface and examination of distribution by using Eqn. 7.3. Ellipsometric parameters psi (ψ) and delta (Δ) of both films were given inTable 7.4. D.X. Zang *et al.* [421] studied the β-Sn film on Si by ellipsometry at different temperature. They studied the optical properties of melted and film and found that the dielectric parameter was different to two phases. J. Zang *et al.* [422] deposited In nanoparticle film on Si (100) and melting of nanoparticle was studied by ellipsometry. In particle of size larger than 44.9 nm, melting point was near to bulk In. For particle size less than 42.4 nm, no obvious melting point was found. Thus, our In film ellipsometry parameters were comparable with the above study.

Table 6.4 Ellipsometry parameters of Sn and In films

Film	Ψ (°)	Δ (°)
Sn	32.26	114.74
In	40.79	124.61

7.3.6 Tin and indium film's adhesion test

The Scotch tape test of Sn and In films confirmed the good strength of adhesion as no part of the film removed with scotch tape. The Sn and In films were suitable with the metal contact requirement for infrared detectors.

7.3.7 Surface profiler thickness measurement

A small portion on HgCdTe substrate covered such that no deposition takes place at that portion to make step-height. Thus, HgCdTe substrate has two regions one very small region with no deposition and large region with Sn and In films. Sn and In films thickness was confirmed by KLA Alpha step D500 surface profiler at several regions on the HgCdTe surface and found that average thickness was about 5 micrometers for both Sn and In as shown in Fig.7.7.

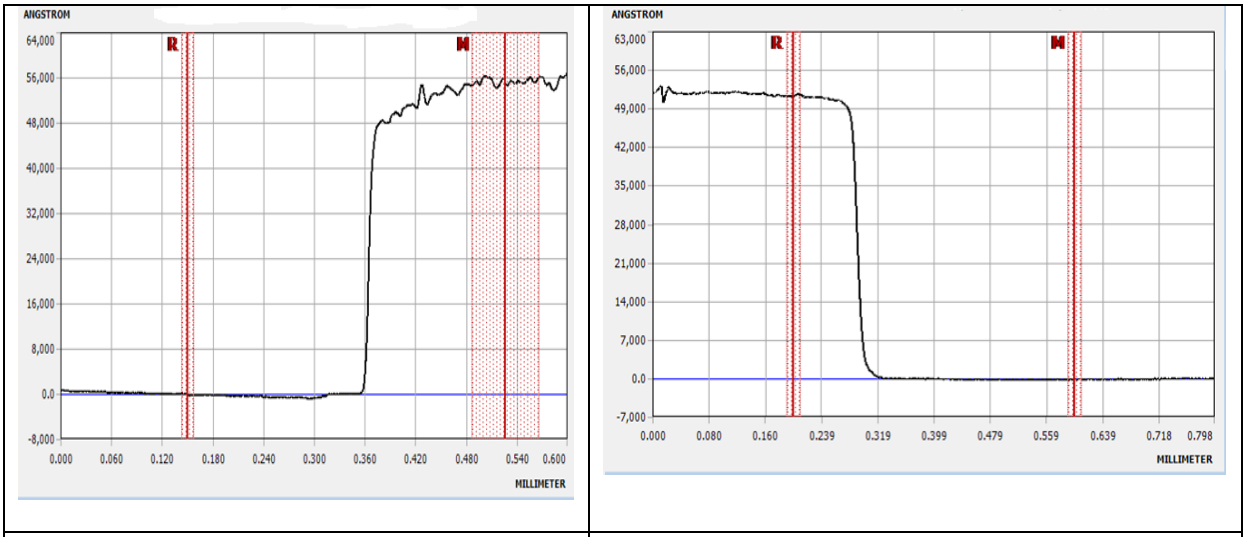

(a)Sn film thickness (step-height) | (b) In film thickness (step-height)

Figure 7.7 Surface profiler thickness measurement graphs

Thus measurement of tin and indium film thickness by this method reconfirmed the thickness monitored by quartz crystal during the thermal evaporation process.

7.3.8 Electrical properties of tin and indium films

The HgCdTe Sample-D1 & D2 were used to grow the tin and indium thin films at an optimal deposition rate in order to create the TLM structure and determine the electrical characteristics of the grown tin and indium thin films. Measurements of the Sn/n/p-HgCdTe & In/n/p-HgCdTe based TLM structure's I-V and resistances were then carried out. As illustrated in the schematic diagram (Fig. 7.8), the fabricated TLM structures have eight contact pads with the same area (100 × 200 μm^2; the contact pads' length, width, and length remain the same). The contact pads also have different interpad spacing, denoted as d1, d2, d3, d4, d5, d6, d7, and d8. d1-50 µm, d2-100 µm, d3-150 µm, d4-200 µm, d5-250 µm, d6-300 µm, d7-350 µm, and d8-400 µm are the values of the

interpad spacing between consecutive contact pads. All adjacent contact pad pairs in the TLM structure had their resistances measured.

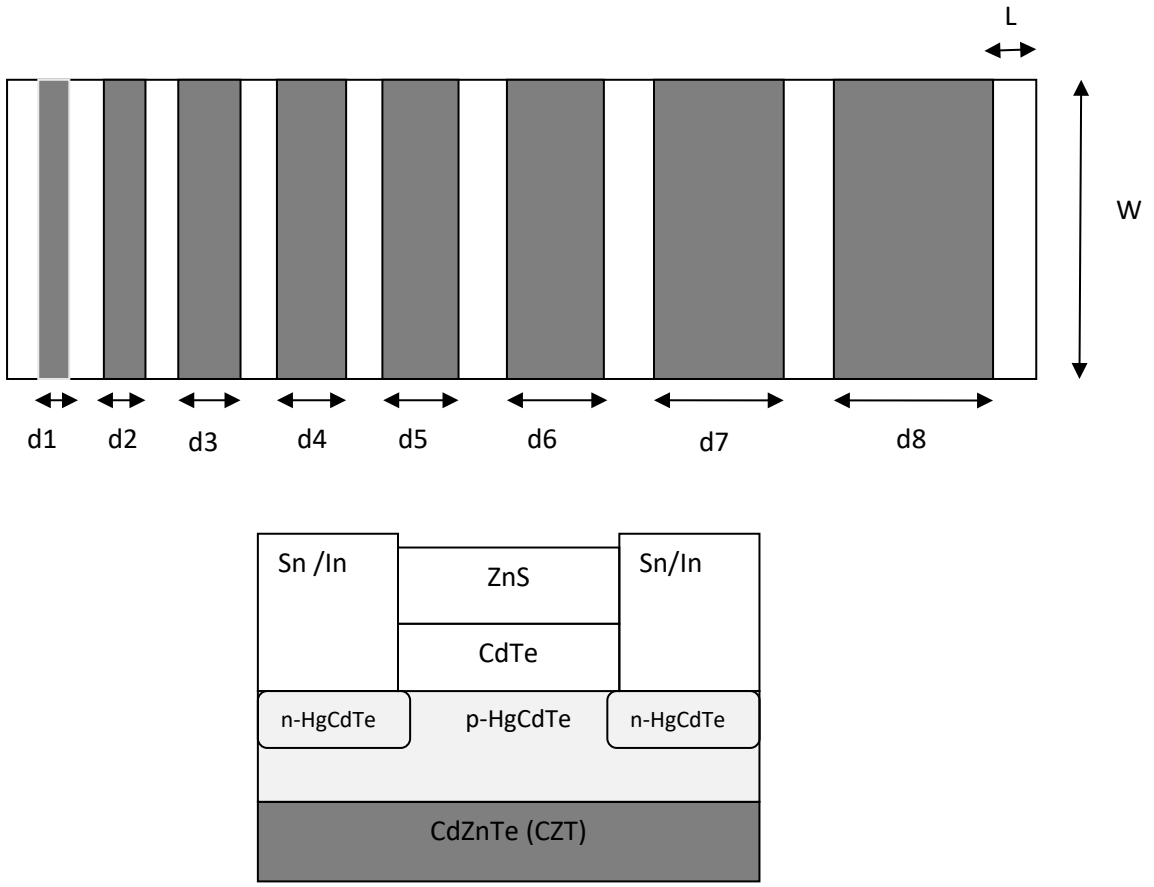

Figure 7.8 Schematic representation of HgCdTe based TLM test structure. (a) two TLM structures (Configuration: Sn/n/p-HgCdTe & In/n/p-HgCdTe) of same dimensions are fabricated with eight pads each and each pad has same width and same length. The interpad spacings are 50, 100, 150, 200, 250, 300, 350, and 400 μm. (b) the cross-section of a part of the test structure is revealed in this diagram**.**

7.3.8.1 Transfer Length Method calculation and analysis

For every pair of adjacent contact pads, the total resistances R_T of the HgCdTe sample-D1 & D2 based TLM structures (configuration: Sn/n/p-HgCdTe & In/n/p-HgCdTe) were measured at 80 K. Next, as seen in Fig. 7.9 (a) and (b), a graph of total resistance (R_T) against interspacing (d) was created of tin and indium, respectively. The electrical parameters (R_c, L_T, R_{sh}, and ρ_c) were estimated using Eqns. (9)– (14), and Table 6.5 lists the evaluated values of the electrical parameters of tin and indium. From Table 7.7, we found that the value of ρ_c for the tin-based TLM structure (Sample-D1) and indium-based TLM structure (Sample-D2) were 2.0×10^{-2} Ω•cm^2 and 3.0×10^{-4} Ω•cm^2, respectively. Thus, the indium-based TLM structure consisted much lower specific contact resistance than the tin, which was favourable and comparable to the early reported values of low specific contact resistance of indium films ($10^{-3} - 10^{-5}$ Ω•cm^2), where these low contact resistances were achieved for Hg_{1-x} Cd_x Te (where x = 0.28 and 0.30) substrate using different combinations of metals, for instance indium/n-MCT, indium/mercury telluride/n-mercury cadmium telluride, molybdenum/indium/n-mercury cadmium telluride, titanium/mercury telluride/n-mercury cadmium telluride, titanium/gold/PEDOT:PSS/n-mercury cadmium telluride, gold/mercury telluride/n-mercury cadmium telluride, and titanium/platinum/gold/n-mercury cadmium telluride [57,94,373,376-378,380-381,422]. The specific contact resistance (ρ_c) of indium layer has besides demonstrated a strong correlation with the ρ_c of indium-metallic connections, which are employed in the progress of high-performance optoelectronic devices based on MoS_2 and CdTe-based IR detectors [93,425].

The deposited film's surface roughness could be the cause of the low specific contact resistance observed at the In/n-HgCdTe interface as the roughness of indium film was lower than the tin film as investigated in AFM (Sn: R_q 44 nm and In: R_q 20 nm)

The more interior dispersion of indium than tin across the MCT in proximity to the upper layer, that increases therefore the additional reason for lower contact resistivity could be the MCT-doping aggregation (the dispersion of the charged ions donors promotes the doping density to become substantially larger than the bare MCT, which minimizes the span of a potential restriction) [57,373,424]. This process is also responsible for the creation of metal contacts with low specific contact resistance. The presence of characteristics in the grown-in films, such as contaminants, non-uniform thickness, and impurities, which might make it difficult to generate the necessary electrical characteristics, may be the third element responsible for high contact resistance.

The characteristics of the films that were obtained from energy dispersive x-ray, atomic force microscope, and scanning electron microscope examination reveal that the layers be consistent, unadulterated, and impenetrable. The indium film has little roughness as well as the appropriate small crystallite dimension as well as grain size. As a result, there won't be as many obstacles in the way of the charges as they pass over the In/n-HgCdTe interface, resulting in a low grown-in contact specific contact resistance [57,373,389].

To understand the behaviour of the tin and indium metals contact as well as the current-transportation phenomenon of the Sn/n-HgCdTe and In/n-HgCdTe interface, I-V measurements

were carried out. The current-voltage features of the constructed TLM structures (Sample-D-1 &D2), calculated at 80 kelvin, were shown in Fig. 7.10 (a) & (b) and indicated that the grown indium contacts on n-type HgCdTe exhibit ohmic behaviour but the tin contacts on n-type HgCdTe exhibit nearly ohmic behaviour. Hence, the linear I-V characteristics and ohmic behaviour of IR photodetectors utilizing metals/n-HgCdTe interfaces are comparable to the dependable I-V features of thermally produced indium films [57,373,94,380-381].

The thermionic field emission of HgCdTe (x = 0.30) substrate at 77 kelvin temperature recognizes the passage of current into indium/n-mercury cadmium telluride connection due to two types of current-transport phenomenon that operate simultaneously: quantum field emission tunnelling as well as thermionic emission. This occurs for doping concentrations ranging from 3.5×10^{16} to 1.6×10^{18} cm^{-3} [57]. Within the two aforementioned regimes, the specific contact resistance (R_c) has a clearly defined dependence. In the thermionic emission regime, the R_c is independent of the doping density (concentration). It is determined by the quantum field tunnelling's reciprocal exponential carrier concentration root. To enable the e^- to overcome the potential barrier with a high tunnelling probability, a small depletion layer (thin potential barrier) is created by high doping concentration. Given that the MCT-based TLM configuration's parameters (composition x = 0.29, doping concentration: 1×10^{16} cm^{-3}, and current-voltage evaluation temperature: 80 kelvin) match those of the structures that have been reported [91,378,380,426], it is likely that significant tunnelling and negligible thermionic emission are the main causes of the current passage in the made-up indium/n-mercury cadmium telluride interconnection. Therefore, the properties of thermally generated indium films were suitable for generating an Ohmic connection on the n-mercury cadmium telluride facade and may be utilized in the development of infrared photodetectors based on HgCdTe.

Table 7.5 The estimated values of electrical variables for the HgCdTe-based TLM structure made-up (sample D1 and D2; configuration : Sn/n-HgCdTe and In/n-HgCdTe interface)

Sample No.	R_c (Ω)	L_T (μm)	ρ_c (Ωcm^2)
D1	151	94	2×10^{-2}
D2	2.5	122	3×10^{-4}

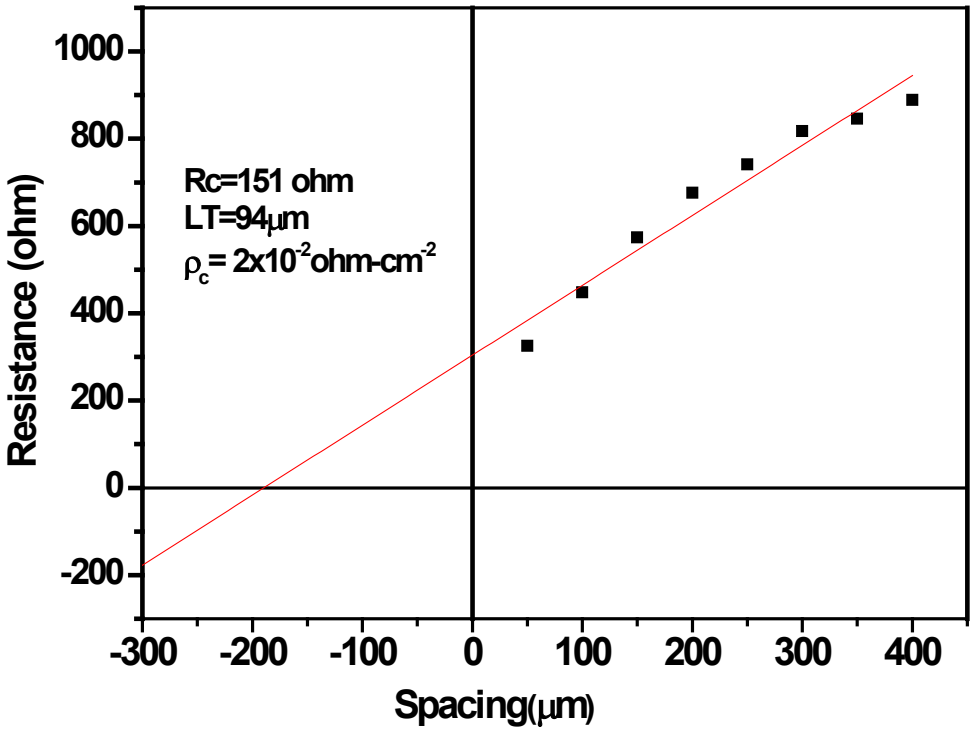

Figure 7.9 (a) Total resistance vs. interpad spacing curve of Tin-HgCdTe based on TLM pattern

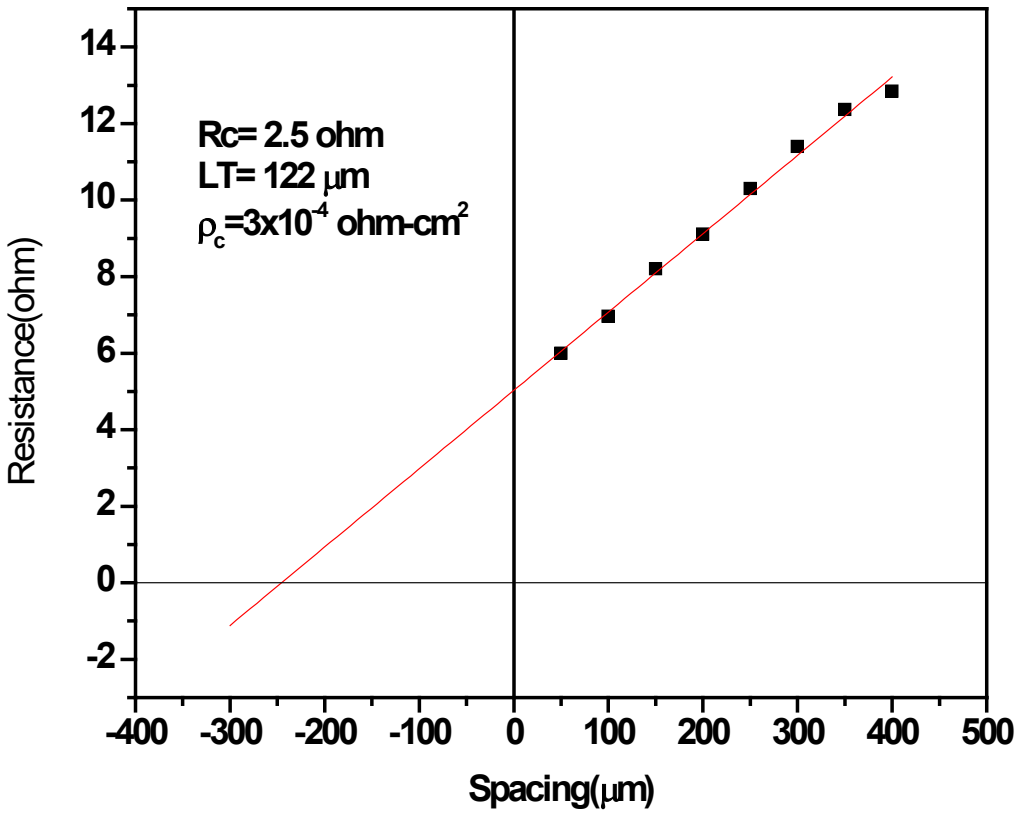

Figure 7.9 (b) The total resistance vs. interpad spacing curve of indium-HgCdTe based on TLM structure

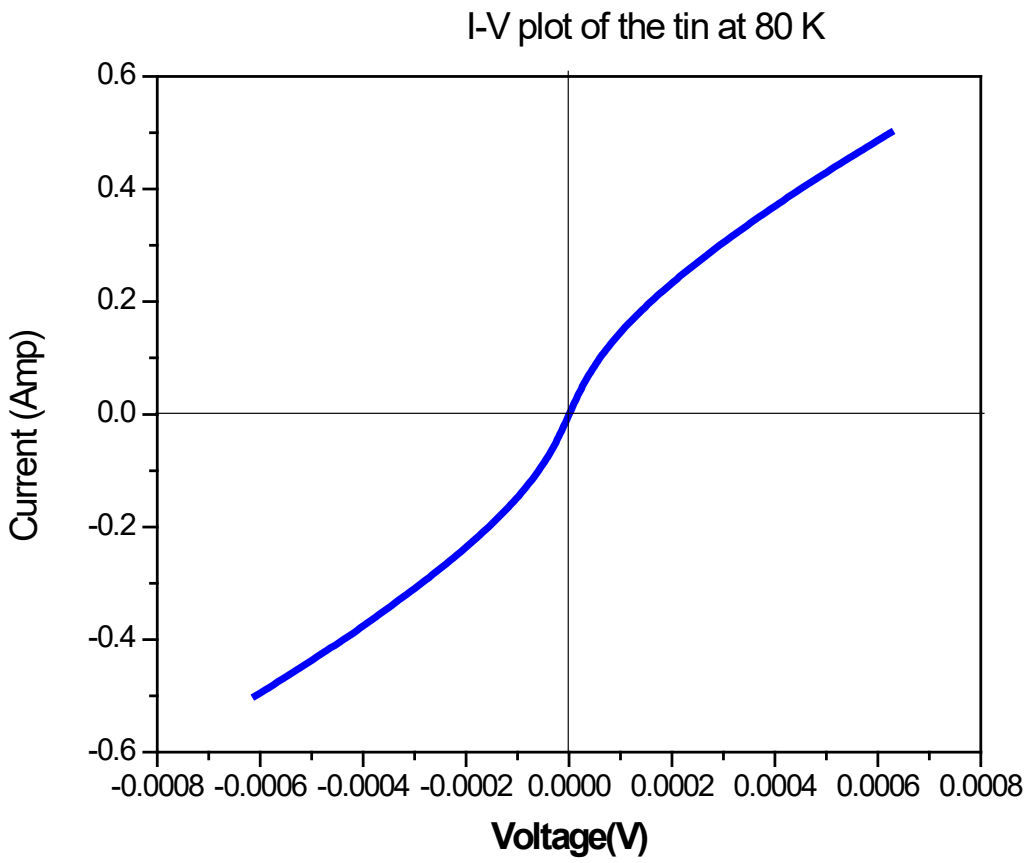

Figure 7.10 (a) I-V characteristics of tin TLM structure

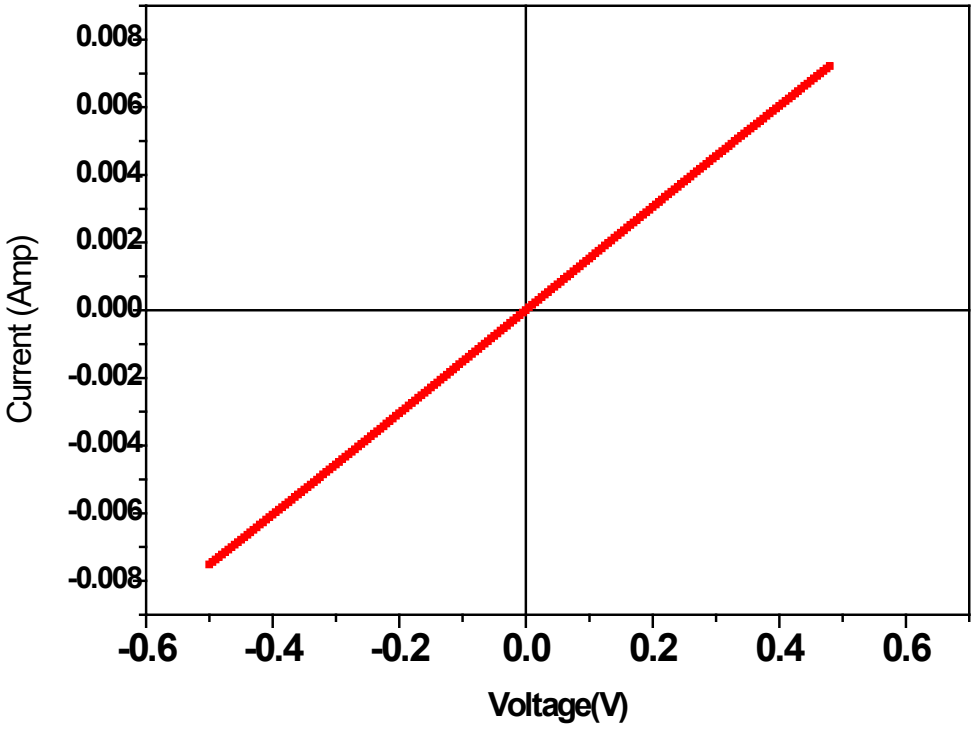

Figure 7.10 (b) I-V characteristics of indium TLM structure

7.4. Conclusions

Metals (tin and indium) films were deposited on the n-HgCdTe by the vacuum evaporation technique. A comparative study of tin(Sn) and indium(In) done based on their crystalline parameters, morphology, composition, topography, adhesion, surface quality and electrical characteristics. The XRD examination confirmed that the films were polycrystalline tetragonal bcc phase along (200) and (101) planes orientation of tin and indium, respectively. The XRD peak intensity of indium film was very large than the tin film's XRD peak intensity for the corresponding preferential planes which indicated that the In film's crytalinity was much better than the Sn. From XRD results, the calculated 33.14 nm crystallite size of β-Sn film was of slight small size than the 33.27 nm crystallite size of In film but the microstrain and dislocation density values of indium were lower than β-Sn film. Thus overall crystalline structure of indium film was better than the tin film. SEM images of β-Sn film shown crack free non-uniform particle size distribution while indium film SEM images indicated a continuous and uniform film over entire surface with a few large micron size particles. So, the morphology of the indium film was better than the tin film. EDS analysis revealed that deposited films were pure of tin and indium elements. AFM scanned images indicated that tin film was rougher than the indium film. The 44 nm rms

value and 32 nm average value were of β-Sn film while 20 nm rms value and 15.2 nm average value were of In film. This higher roughness of β-Sn film was be due to non-uniform cluster growth and non-uniform distribution of Sn clusters. Adhesion force and thermodynamic adhesion-work of tin film were nearly double than the indium film. The scotch tape test confirmed the good adhesion or bonding of Sn and In film molecules with HgCdTe surface. Surface profiler ensured the tin and indium 5 μm film thicknesses and validated the thickness monitored by the quartz crystal during evaporation process. Using TLM and I-V measurements for various contact geometries, the Sn/n-HgCdTe and In/n-HgCdTe interfaces were electrically examined. The In/n-HgCdTe interface indicated linear I-V characteristics (ohmic behavior) but the Sn/n-HgCdTe interface indicated non-linear I-V characteristics (nearly ohmic behavior). In this instance, the thermionic field emission mechanism controls current transport. The In/n-HgCdTe interface consisted low specific contact resistance, $\rho_c = 3 \times 10^{-4}$ Ωcm^2 than the Sn/n-HgCdTe interface specific contact resistance, ρ_c 2×10^{-2} Ωcm^2.

Compared to tin film, the indium film had lower specific contact resistance and surface adhesion force—two vital characteristics needed for metal contact in infrared device fabrication. Thus indium film's overall structural, morphological, compositional, topographical, adhesion, ellipsometric and electrical properties were better than tin. Indium was found to be suitable as a good ohmic n-contact in optoelectronic, micro-nano scale electronic devices and HgCdTe-based infrared detectors.

Appendix

(a) Adhesion characteristics

The potential or effort necessary to divide two superficial make contact with is called adhesion force (pull-off force). The interfacial forces and van der Waals force are the sources of adhesion force. Heinrich Hertz was an early researcher in the field of contact mechanics research. His estimates were based on a particular normal load for the radius of the circular contact region in macroscopic applications, where a flat surface and a sphere were crushed together. It was only used with homogeneous, isotropic, linear elastic materials that do not show adhesion or attraction. It was assumed that the identity could be roughly paraboloid because the contact radius was smaller than the sphere's radius. Johnson, Kendall, and Roberts (JKR) revealed a novel theory explaining adhesion between two elastic bodies [417]. Their motivation came from the finding of a tiny contact zone at zero utilized stress and from contact spaces observed in experiments that were higher than those predicted by the Hertz theory at low loads. They arrived at the following Eqn. (A1) to define the contact radius between a sphere and a plane when adhesion was in effect:

$$a = \left(\frac{R}{K} \left(P + 3\gamma \pi R + \sqrt{6\gamma\pi RP + (3\gamma\pi R)^2} \right) \right)^{1/3} \quad \text{(A1)}$$

where P denoted the applied load, γ the thermodynamic adhesion-work (or Dupré energy of adhesion), and K was a parameter that changed according on the Poisson's ratio and the elastic

modulus that matched each facade. It discovered that the measure of effort required to completely remove a unit region of the border was energy per unit area. Among the characteristics of this theory were a non-zero contact region with no load, an infinite tensile stress at the perimeter of the contact zone, and the lowest stable normal load that still revealed a non-zero contact area. The lowest load that was established by the following was the pull-off force, also referred to as the critical load:

$$F_{JKR} = \frac{-3}{2} \pi \gamma R \quad \text{(A2)}$$

A short time later, Derjaguin, Muller, and Toporov (DMT) added adhesion to an alternative expression [418]. They postulated that, in accordance with the Hertz hypothesis, adhesion would result in an overall increase in load while the deformed contact profile would remain unchanged. This resulted in attractive interactions between the sphere and the plane that acted as a dead weight at all distances, as shown below:

$$a = \left(\frac{R}{K} \right) (P + 2\pi \gamma R))^{1/3} \quad \text{(A3)}$$

and now the pull-off force or critical load was:

$$F_{DMT} = -2 \pi \gamma R \quad \text{(A4)}$$

where R was radius of tip in nm (12 nm) and γ was thermodynamic adhesion-work in J/m^2

In the Derjaguin-Müller-Toporov (DMT) theory, the contact area goes to zero at the pull-off force, and there was no singularity in the contact stresses. The theory assumed that the attraction forces at the interface region were equal to those outside of it in order to derive the thermodynamic adhesion-work or surface energy. David S. Grierson *et al.* [419] explained the theories about the adhesion and friction properties between contact surfaces. They explained about the Derjaguin, Muller, and Toporov (DMT) and Johnson, Kendall, and Roberts (JKR) theories in continuum contact mechanics to determine the adhesion and frictional characteristics.

(b) Electrical characteristics using transfer length method (TLM)

To determine the sheet resistance (R_{sh}) and transfer length (L_T), a resistance vs. interpad separation plot was created. The other factors, such as contact resistance (R_c) and specific contact resistance (ρ_c), were assessed using the resulting values of R_{sh} and L_T. current-voltage evaluations of TLM patterns were also carried out to look at the contacts' behaviour. The measured resistance (R_T) for a pair of TLM structure contact pads (length L, width W, and interpad spacing d) may be found using equation (A5) [91,92,94,376, 423].

$R_T = R_{semi} + 2R_c = R_{sh}(\frac{d}{W}) + 2(R_{sh} L_T)/W$ (A5)

Transfer length, sheet resistance, semiconductor resistivity, and contact resistance are represented, respectively, by the parameters L_T, R_{sh}, R_{semi}, and R_c. Eq. (A610) can be used to calculate the transfer length [91,92,94,376, 423].

$LT = \sqrt{(\dot{\rho}_c / R_{sh})}$ (A6)

Transfer length, sheet resistance, semiconductor resistivity, and contact resistance are represented, respectively, by the parameters L_T, R_{sh}, R_{semi}, and R_c. Eq. (A7) can be used to calculate the transfer length [91,92,94,376, 423].

$\rho_c = L_T R_{sh} \Rightarrow R_c = \rho_c /(L_T W) = (R_{sh} L_T) /W$ (A7)

Eqs. (A8), (A9) and (A10) were used to the ohmic planar contact in order to evaluate R_c and ρ_c [91,94,376,420-421]. Given that the definition of R_c for an ohmic planar contact is:

$R_c = ((R_{sh} L_T)/W) \coth(L/L_T) \approx (\rho_c /(L_T W)) \coth(L/L_T)$ (A8)

The quantity of R_c, which is expressed in the simpler version in this order, is altered by the limiting cases:

No considerable current penetration in the metal contact, or short contact limit ($L \ll L_T$) →

$\coth(L/L_T) \approx L/L_T$ then $R_c = \rho_c /(LW) \Rightarrow \rho_c = R_c LW$ (A9)

Long contact significant current transfer into the metal contact (limit $L \gg L_T$) →

$\coth(L/L_T) \approx 1$ then $R_c = \rho_c /(L_T W) \Rightarrow \rho_c = R_c L_T W$ (A10)

CHAPTER 8

STUDY OF THE NANOSCALE GOLD OHMIC CONTACT FOR PROSPECTIVE INFRARED DETECTORS ON A p-TYPE HgCdTe

8.1. Introduction

The semiconductor $Hg_{1-x}Cd_xTe$-based infrared detector (IR detector) has potential applications in defence, medical, and optical communications devices, including sensors, emitters, and field effect transistors in the near infrared spectral region (1-2.5 μm) [427-431]. To create these device architectures, low resistance ohmic connections must be formed with p-type $Hg_{1-x}Cd_xTe$). Because of its adjustable band gap, it can detect radiation in both the 3-4 and 8-12 μm air transmission ranges. Creating low resistance connections for p-MCT is challenging due to the material's high work function. For x-values less than 0.4, both native defect models and metal-induced gap states suggest that the Fermi-level is near to the conduction band minimum, regardless of contact material [94,369,432-433]. The quality of the metal/HgCdTe interfaces in infrared devices is largely determined by the interphasic reactions of HgCdTe with various metals or semiconductors across films. Four classifications apply to the over layer: unreactive (Au, Sb), reactive (aluminum, indium, chromium and silicon), intermediate (germanium, silver, copper, platinum, and palladium), and ultra-reactive (Ti, Yb, Sm, and Sn). Wet etching, surface preparation, sample history, and other parameters can all have an impact on how the over layer metals/HgCdTe interface behaves [92,424,434-440]. On HgCdTe, a variety of metals, including aluminum, silver, copper, titanium, palladium, platinum, germanium and mercury telluride are used to create contact. Ag, Cu, Pd, Pt, Sb, and Ge are examples of metals that exhibit rectifying behavior, while gold and aluminum have produced almost ohmic connections. Mercury telluride metal creates interaction with Ohmic nature, but growing this metal requires expensive and complex equipment (metal-organic chemical vapor deposition and molecular beam epitaxial processes). Furthermore, the HgCdTe substrate's characteristics can be changed by the high enough deposition temperature. In order to produce n and p-type Ohmic contacts on HgCdTe, titanium as well as the organic connections poly(3,4-polyethylenedioxythiophene) polystyrene sulfonate might furthermore be used [92,437,382,441-445]. Ion beam sputtering and deposition techniques were used to construct the connections of ohmic type on the MCT utilizing the Au/Sn, and Au/In [57,443-446].

Usually, gold is used to establish interface of Ohmic type in MCT of p-type, except this being a highly complex procedure. On MCT substrate of p-type the contact of Ohmic type could be achieved via vacuum evaporation, low substrate temperature, dominant stickiness, contact resistance of lower value, etc. [441,442,447].

*** Portion of this work has been published in Optics Communications, 604 (2026) 132846**

Research [91-93,447] has attempted to rectify shortcomings. Minimal resistance to contact at the HgCdTe (MCT)/gold connection along with Ohmic type contact studied where the gold pad made via vacuum evaporation as well as electroless procedure [93]. The HgCdTe photoconductive detector fabricated using a layered metal scheme (Ti/Pt/Au) [91]. At room temperature and below, the metal contacts (transmission line model structure) created by the DC sputtering deposition process have demonstrated an Ohmic behavior. According to a recent article [447], diverse kind of infrared sensors, for instance discrete sensors as well as multi element FPAs, can be made using molybdenum/gold and molybdenum/indium-based contacts of ohmic type. These detectors can be made using thermal evaporation and magnetron sputtering deposition processes to create the metals. A distinct report [92] asserted to address the problem of excessive contact resistance, which could compromise big format/fine pitch detector arrays' intended performance. It has been reported that the electroless Au/HgCdTe interface has a low contact resistance [92]. While studies [91,62,447] have addressed the electrical features of these contacts of Ohmic type in detail as well as demonstrated the use of gold Ohmic contacts in the construction of HgCdTe-based IR photodetectors. The other aspects, including as composition, morphology, structural characteristics, and so on, were not discussed because they are equally crucial to comprehending the electrical behavior of Au/HgCdTe contacts. All of these items have been used in several papers [448-450] to investigate the gold-titanium-aluminum-titanium/aluminum-gallium nitride/gallium nitride interface (HFET pattern), the tantalum/titanium/nickel/gold/n-type gallium nitride interface, as well as the platinum/rhenium/gold/p-type gallium nitride contact. The concerns with gold metal connections placed on substrates other than HgCdTe have been the only focus of the reports [448-450].

Nanoindentation is an attractive method to explore material deformation at the near-surface under various loads and constraints [451-452]. Depth-Sensing Nano Indentation (DSNI), also known as nanoindentation, is a popular approach for analyzing the mechanical properties of various materials, particularly for thin coatings and biomaterials [453-456]. Simon Roa et al. investigated that the elastic modulus and indentation hardness decreased significantly as film thickness and grain size increased. Annealing duration and temperature appear to alter the mechanical behavior of films by creating microstructural changes that are akin to those induced by size effects (film thickness) [457]. Edgar A. Villegas et al. studied the oxide films (SnO_2, TiO_2 and ZnO) deposited by spray pyrolysis and found that the hardness values were 6-11GPa. Titanium and tin dioxide films had better wear and mechanical properties than ZnO films [458].

The crystallographic, constituent, conformation, nanomechanical as well as electrical characteristics of the vacuum deposited gold layer on MCT substrate of p-type have all been attempted to be addressed in the current work. Because each of these characteristics is crucial to obtaining high-superiority contacts of Ohmic type (for gold/p-type HgCdTe (MCT) contact), which are required for the creation of larger configuration HgCdTe (MCT) infrared detectors with the best possible accomplishment. Several characterization methods, including atomic force microscopy, energy dispersive X-ray (EDX), and X-ray diffraction (XRD), scanning electron

microscopy (SEM), atomic force microscopy (AFM), nanoindentation etc. analysis, were used to appraise the deposited gold films. The contact resistivity of Au-metal contacts (thermally evaporated and e-beam evaporated) was then discovered by performing an I-V/resistance test on the constructed Transmission line model (TLM) structure in order to determine the electrical characteristics of the gold films. The electrical characteristics of the gold films were then ascertained by performing the voltage-current (V-I)/resistance evaluation for the constructed transmission line model pattern, which disclosed the particular contact resistance of Au-metal contacts. Therefore, a comparative analysis is done between the thermally evaporated and e-beam evaporated gold films to obtain a suitable and efficient Ohmic contact metal for the construction of HgCdTe IR photodetectors.

8.2. Materials and methods

The within the organization liquid phase epitaxy (LPE) growth method was used to create the p-$Hg_{1-x}Cd_xTe$ epitaxial layers on a substrate that matched the CdZnTe (111) lattice. A tube that was fixed in the furnace contained a tellurium excess emulsion with a predefined proportion (i.e., mercury: 0.70, cadmium: 0.30, and tellurium constituents, whose content x:0.30). To make this melt homogeneous, it was heated to 490° C, which is higher than the HgCdTe growth temperature of 475°C. The CdZnTe substrates were then added to the melt for 30 to 40 minutes after it had cooled to 475°C. Consequently, MCT epilayers with the necessary specifications (size: 30 millimeter × 30 millimeter, dimension: 18–20 micrometer thickness, composition x: 0.30, carrier-concentration: 1×10^{16} cm^3, mobility: 416 cm^{-2} $V^{-1}s^{-1}$) were produced. The gold films have been investigated using MCT epilayers with the previously mentioned dimensions (30 × 30 mm^2, thickness: 18–20 μm). These HgCdTe epilayers were mechanically polished using Al_2O_3 (alumina powder: 0.05 μm) to get the acceptable/desired dimension of 10 μm. In order to create a façade free from oxide composed of fine morphology, the epilayers were chemically as well as mechanically polished via a emulsion of (iodine: potassium iodide: $C_2H_6O_2$) :: (1gram: 4gram: 10 milliliter) as well as potassium hydroxide. After that, de-ionized (DI) water and extremely pure N_2 were used to wash and dry the epilayer, respectively. The obtained films were then examined using characterization methods like XRD, SEM, EDX, AFM, nanoindentation and non-contact sheet resistance testing. The surface of the epilayer was cleaned using a regular and typical cleaning process that involved heating the samples for five minutes in each of the following chemicals: trichloroethylene, acetone, and methanol. The samples were chemically etched for 20 seconds using a 0.1% bromine solution in methanol, and then they were successively washed with demonized water and dried with extremely pure nitrogen, respectively. Samples were also consecutively baked for five minutes at ninety-degree Celsius to eliminate any remaining H_2O constituent or ambient moistness from the specimen's facade. Prior to gold film deposition, microscopic and ellipsometry studies were used to guarantee a flawless and untainted surface for the HgCdTe samples. These samples were instantly moved into the vacuum chamber, and a molybdenum boat was also filled with the source material, gold (purity: 99.9%). Gold film (thickness: 220 nm) was evaporated on samples at a rate of 6 and 12 Å/s and an evaporation

current of 110–130 A after the vacuum chamber's pressure reached the necessary level of 7×10^{-7} mbar. The thickness of the layer and the pace of evaporation were observed via regulator of automatic type that was integrated to a piezoelectric sensor made of quartz. The entire gold thin-film growing procedure was conducted at ambient or 25°C. The electrical properties of the HgCdTe-based TLM structure were further investigated using the optimized gold-films. Beginning with the same processing procedures as the other samples (polishing via chemical-mechanical, extended rinsing, etching via chemical, and so on), the transmission line model was fabricated on the sample. Microscopic and ellipsometry observations were then made to verify the sample's defect-free and contamination-free surface. The intended transfer line model was created on sample using a photolithography procedure. Sample was next subjected to a descum-process, which involved bombarding it with oxygen plasma for about 30 seconds at pressures between 10^{-1} and 10^{-2} mbar, power of 100 watt, and oxygen rate of flow of 200 milliliter/minute. A photolithography liftoff procedure (using acetone) was then carried out to create the final TLM structure after a gold thin layer (thickness: 220 nm) was applied to the sample at a base vacuum of 2×10^{-7} mbar. The Fig. 8.1(a) (b) and (c) show the schematic diagram of the thermal evaporation, e-beam evaporation and stack layer of chromium (20 nm thickness)-gold (220 nm thickness) stack layer on HgCdTe and CdZnTe.

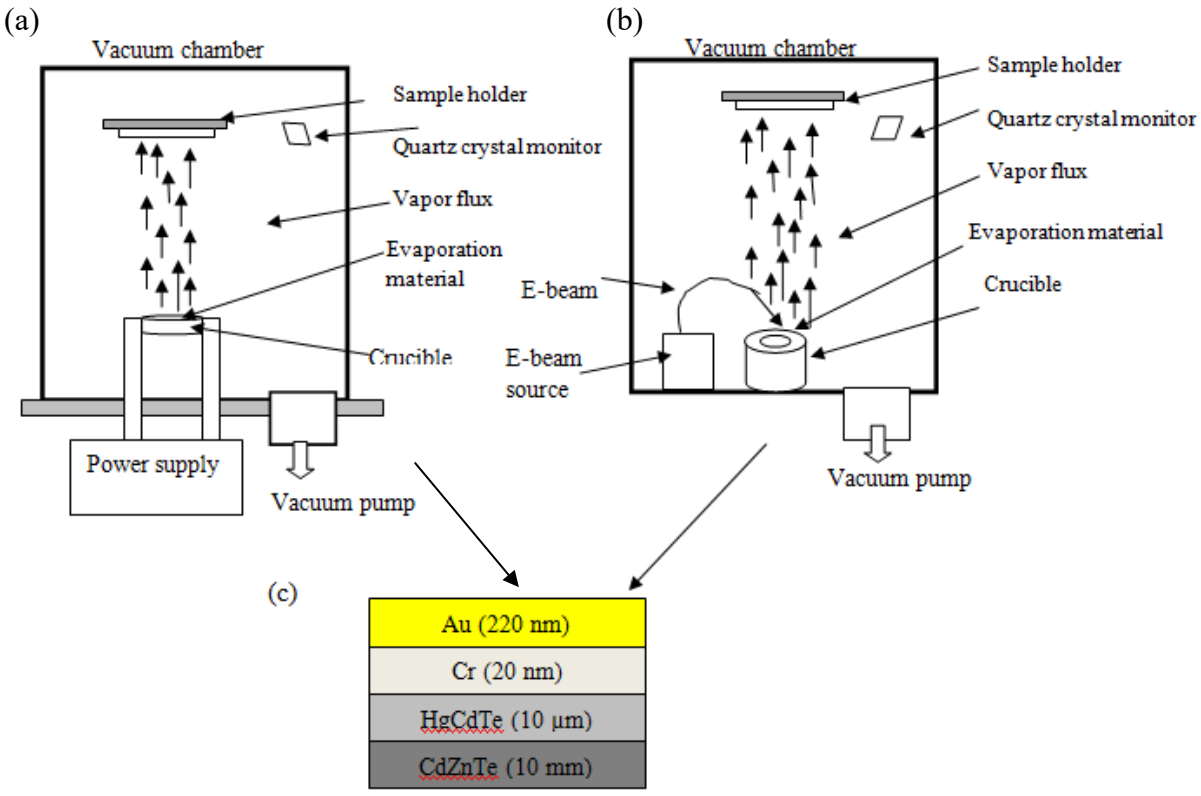

Figure 8.1 Schematic diagram (a) thermal evaporation (b) e-beam evaporation (c) the stack layer of chromium-gold film on HgCdTe, CdZnTe surface

To assess the structural characteristics of the generated gold films, an X-ray diffraction instrument-Analytical B.V.-X'Pert PRO MRD, was utilized. The morphological statistics of thermally produced gold films have been realized by the Agilent Technologies AFM (Model-5600LS) instrument. A FESEM (connected to an EDX Spectrometer, Make-Carl Zeiss SUPRA, functioning voltage: 5–20 kilo volt) was used to characterize the microarchitecture and elemental characteristics of gold layer. The industron Nanoguru NG50 nanoindenter with berkowitch tip was used to evaluate the nanomechanical properties. Voltage-current (V-I) as well as resistance readings of the Keithley Parametric Analyzer (Model: 4200 by way of incorporated 4200-CUV card) were performed using a cryo-prober. Constructed TLM structure (Au/p-HgCdTe pattern), and the test-structure's I–V parameters were recorded at 80 K.

8.3 Results and discussion

8.3.1. Crystal structure properties

XRD quantifications of the gold/p-mercury cadmium telluride specimens evaporated using thermal and e-beam deposition procedures (Sample-A1 & A2: 6 Å/s &12 Å/s (thermal), Sample-B1& B2: 6 Å/s &12 Å/s (e-beam)) were performed in order to determine the crystal structure characteristics of the gold-film. The outcome of the x-ray diffraction are revealed in Fig. 8.2(a, b, c and d). At 2θ values of 38.26 °, 44.45 °, 64.70 °, 77.71 °, and 81.84 °, Sample-A1 exhibited five diffraction peaks (Fig. 8.2a). The (111), (200), (220), (311), and (222) planes of an Au face centre cubic -pattern were represented by these numbers, correspondingly [459-463]. Similarly, sample A2 represented five peaks of diffraction at two-theta figures of 38.27 °, 44.48 °, 64.70 °, 77.70 °, as well as 81.87 °(Fig. 8.2b). Five diffraction peaks in Sample-B1 (Fig. 8.2c) are the same as those in Sample-A1 (Fig. 8.2a). The diffraction peaks of Sample-B1 are 38.29°, 44.49 °, 64.71 °, 77.72 °, and 81.88 ° along the 2θ axis, respectively. Fig. 8.2d showed the peaks of diffraction of Specimen-B2 at 2-theta values of 38.28°, 44.47 °, 64.69 °, 77.69 °, and 81.85 °.

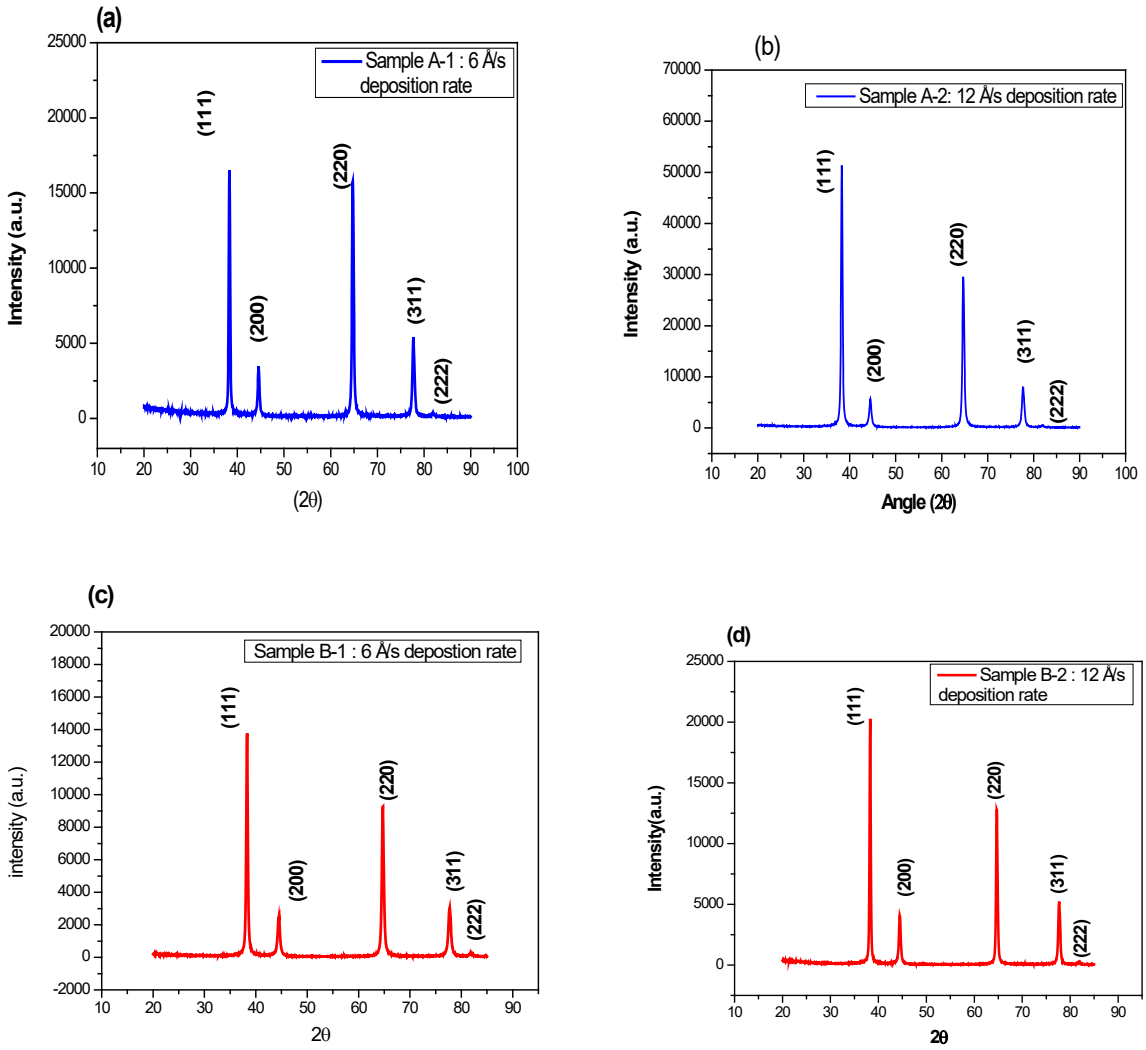

Figure 8.2 X-ray diffractogram of gold film (a) Sample A-1: 6 Å/s deposition rate by thermal (b) Sample A-2: 12 Å/s deposition rate by thermal (c) Sample B-1: 6 Å/s deposition rate by e-beam method (d) B-2: 12 Å/s deposition rate by e-beam method

These peaks match the crystal planes (111), (200), (220), (311), and (222) of a distinctive gold face centered cubic configuration (JCPDS no. 65–2870), according to reports in the literature [459-463]. As can be shown in Fig. 8.2 (a, b), the peak of diffraction gold (111) of Specimens (A1,A2) along with (B1,B2) is significantly stronger correlated to the remaining four peaks.

For the HgCdTe Samples (A1, A2, and B1, B2), the cubic as well as polycrystalline gold layers with the designated alignment gold (111) be verified. The obtained FWHM values for the prominent peak Au (111) show that Sample-B2 had the best crystallinity out of the four samples (A1, A2, B1, and B2) (Sample-A1: 0.0069 rad, Sample-A2: 0.0065 rad, Sample-B1: 0.0064 rad, and Sample-B2: 0.0054 rad). A XRD peak with a little full width at half maximum is considered to be extra crystallinity than one with a high FWHM because of the correlation between the films'

crystallinity and the diffraction peak's FWHM. Sample-B1 (e-beam evaporated) is marginally more crystalline than Sample-A2 (thermally evaporated) due to its lower FWHM value. The X-ray graphs (Samples A1 and B1) show that the peak intensity varies with variations in the evaporation technique. Two x-ray peaks of Sample-B2 (e-beam evaporated), Au (220) and Au (311), are comparatively more intense than the corresponding peaks of Sample-A1 (thermally evaporated). The increased peak intensity is also responsible for Sample-B2's (e-beam evaporated) higher crystallinity, which was generated using a significantly more e-beam deposition approach than Sample-A1 (thermal evaporation technique). The produced gold thin film of Sample-B2 (e-beam evaporated) and the previously reported thermally evaporated gold film [460] thus match well.

Table 8.1 Computed the gold film's structural properties for the dominating plane (111) using samples A1, A2, B1, and B2.

Structural parameters	**Computed values for thermally evaporated**		**Computed values for e-beam evaporated**	
	Sample- A1 (6 Å/s evaporation rate)	Sample- A2(12 Å/s evaporation rate)	Sample- B1 (6 Å/s evaporation rate)	Sample- B2 (12 Å/s evaporation rate)
2θ (degree)	38.26	38.27	38.29	38.28
Lattice plane (111)	(111)	(111)	(111)	(111)
FWHM, β (rad)	0.0069	0.0065	0.0064	0.0054
Lattice-constant, a (Å)	4.069	4.068	4.066	4.078
Average grain size, D (nm)	22.11	23.28	23.60	27.96
Defect density, δ(lines/cm^2)	2.04 x 10^{15}	1.84 x 10^{15}	1.79 x 10^{11}	1.27 x 10^{11}
Residual Stress,σ_s (GPa)	0.24	0.26	0.31	0.02
Strain, **ε (x 10^{-3})**	4.99	4.74	4.67	3.94

Table 8.1 lists the crystal structure characteristics of the evaporated gold films (FWHM, lattice-constant, Average crystallite size, and stresses) and the XRD parameters (diffraction angle, diffraction-peaks, and lattice plane) that were evaluated using the different formulas described below:

The interplanar distances (d) as well as the lattice constant (a) of gold were determined from Eqn. (8.1) and (8.2):

$$a = \frac{\lambda\sqrt{h^2+k^2+l^2}}{2sin\theta} \tag{8.1}$$

$$d = \frac{a}{\sqrt{(h^2+k^2+l^2)}} \tag{8.2}$$

where lambda (**λ**) was the falling X-ray wavelength, theta (θ) was the diffraction-angle and h, k, l represented the miller coordinates.
The average crystallite size (D) of the gold layer was determined by the Debye-Scherer formula, using Eqn. (8.3) [464-465].

$$D = \frac{0.94\lambda}{\beta Cos\theta} \tag{8.3}$$

where β was the full-width at half maximum of diffraction peaks, D was the average crystallite size of the thin layer, and θ was the angle of diffraction.
The length of dislocation lines per unit volume termed as dislocation (defect) density (δ), and it was determined with Eqn. (8.4) [93,448]

$$\delta = \frac{1}{D^2} \tag{8.4}$$

The stress of gold film was evaluated by Williamson-Hall expression with Eqn. (8.5) [449]

$$\sigma_s = \frac{Y(a - a_0)}{2a_0\gamma} \tag{8.5}$$

Strain (ε) of the evaporated film was named as the proportion of $(a - a_0)/ a_0$, where a and a_0 were the lattice constants of gold film as well as bulk gold material, respectively. The quantity of ε was evaluated with the subsequent Eqn. (8.6) [465-466]

$$\varepsilon = \frac{\beta}{4tan\theta} \tag{8.6}$$

where Y was the Young's modulus of gold in gigapascal, which was 79 gigapascal, a was the calculated quantity of lattice constant by X-ray diffraction examination, a_0 was the standard value of lattice constant (4.079 angstrom) for solid substance and γ represented the Poisson's ratio (0.4) for gold.

Consequently, the characteristics of gold film and standard/bulk gold material are identical. The structural characteristics such as microstrain and defect density (dislocation density) values of the gold film evaporated by thermal evaporation process at 12 Å/s evaporation rate (Sample-A2) is better than 6 Å/s (Sample-A1) evaporation rate as shown in table 1. Similarly, the gold film evaporated by e-beam process at 12 Å/s evaporation rate (Sample-B2) has lower values of microstain and defect density (dislocation density) than the gold film at 6 Å/s (Sample-B1) evaporation rate. Overall, the gold film evaporated at 12 Å/s (Sample-B2) by e-beam process has lowest mircrostrain and defect density values among all the evaporated gold films. The structural characteristics of the generated films (d, or average grain size, and ε, or strain) are good and comparable to those of the Au films that have been described [459-460]. It demonstrates that, in comparison to the conventional, thermal evaporation method, the e-beam technique may yield the necessary higher crystalline grade gold metal films.

8.3.2 Surface topography analysis

The AFM measurement was used to examine the topography of gold films that were evaporated using thermal and e-beam techniques. Fig. 8.3 (a, b, c, d, e, f, g, h, i, j, k and l) depicts the acquired AFM images (line diagram, 2D and 3D) as well as the linear image profile of Samples A1, A2 and B1, B 2 (gold film magnitude: 200 nm, detecting region: 2.0 μm × 2.0 μm). The density and homogeneity of the e-beam-evaporated gold films (Sample B-1: 6 Å/s evaporation rate, Sample B-2: 12 Å/s evaporation rate) thus seem to be higher than those of the thermally evaporated gold films (Sample A-1: 6 Å/s evaporation rate, Sample A-2: 12 Å/s evaporation rate). As illustrated in Fig. 8.3(k), (l), a number of extremely dense islands in the film are connected by tiny, paddy-like grains of the e-beam evaporated gold film Sample B-2(12 Å/s evaporation rate). From Table 8.2, we observed that the thermal and e-beam gold thin films have measured RMS (root-mean-square) surface roughness of Sample A-1: 5.00 nm, Sample A-2:.3.05 nm and Sample B-1: 2.84 nm, Sample B-2: 2.71 nm, respectively. The e-beam evaporated Sample B-2 film's average lateral diameter, grain (particle) heights and surface roughness are lowest than among all the samples (thermally evaporated gold film Samples A-1, A-2 and e-beam evaporated Sample B-1), according to the linear profiles (Fig. 8.3 (j), (k) and (l)).

According to XRD examination, the average crystallite size (D) and the lateral diameters (AFM) are similar. Consequently, the surface topological properties that were examined, it was discovered that the e-beam Au film's (lateral grain diameter, lateral height, and rms surface roughness) closely matched the gold films described in the literature [460,467-474].

The gold relying link/connection (gold/HgCdTe of p-type) with small contact resistivity can be created with the help of the e-beam evaporated gold film, which has a lower surface roughness than the thermally grown gold film and allows charges to move through interface with ease since their journey has the fewest restricting consequences. The electrical characteristics someplace the gold/p-mercury cadmium telluride interconnection of small contact resistivity be established have

confirmed this estimation. As a result, HgCdTe-based infrared detectors may benefit greatly from the uniform, densely packed, and low roughness topological properties of gold thin film.

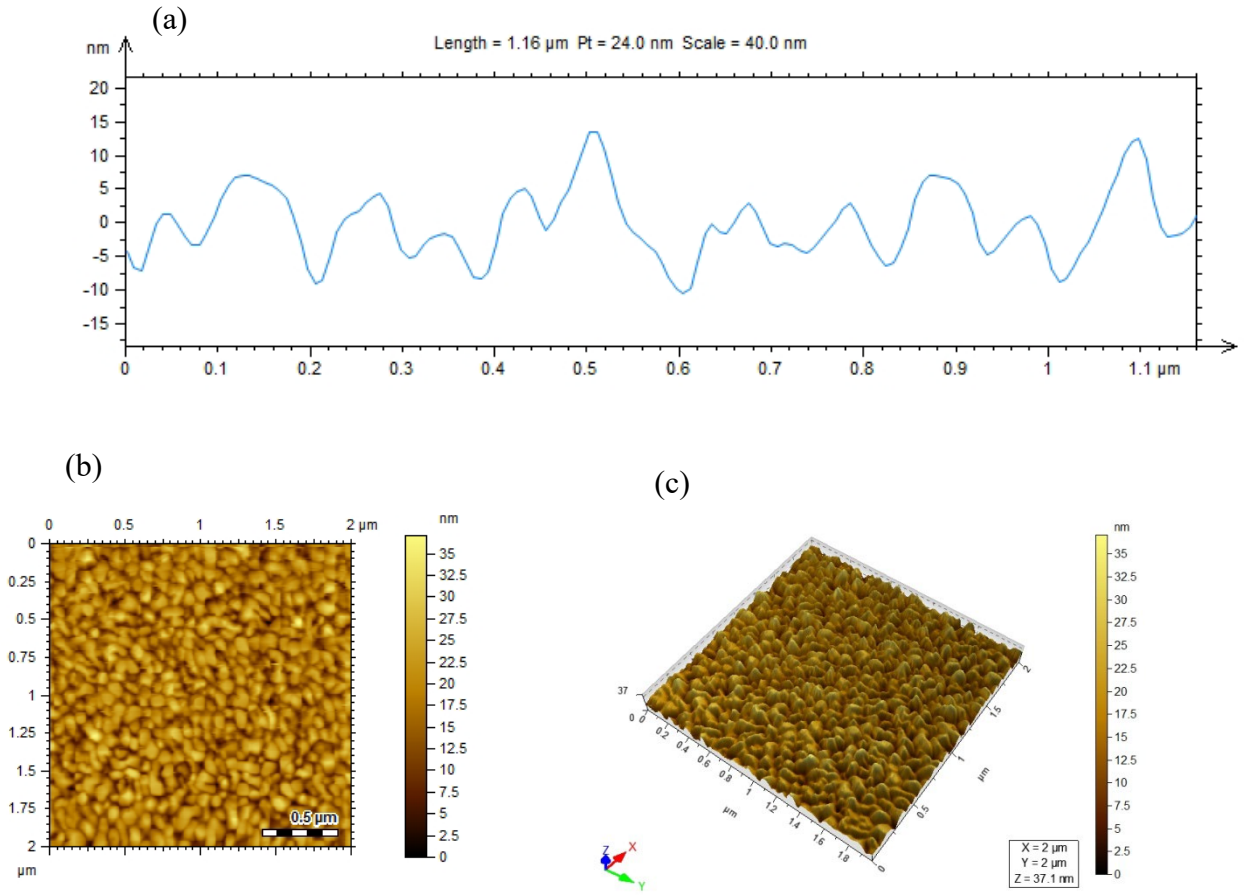

Figure 8.3 Surface roughness image of gold film (a) thermal evaporation process sample A-1line diagram (b) thermal evaporation process sample A-1 2D image (c) thermal evaporation process sample A-1 3D image

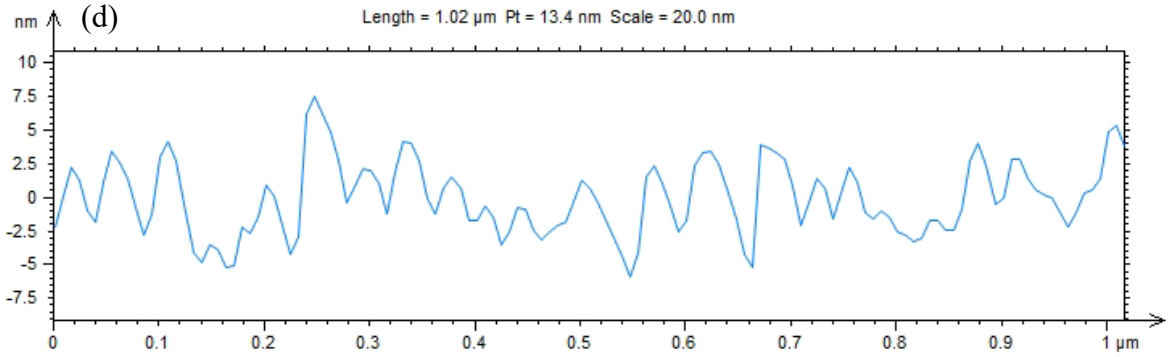

(e)

(f)

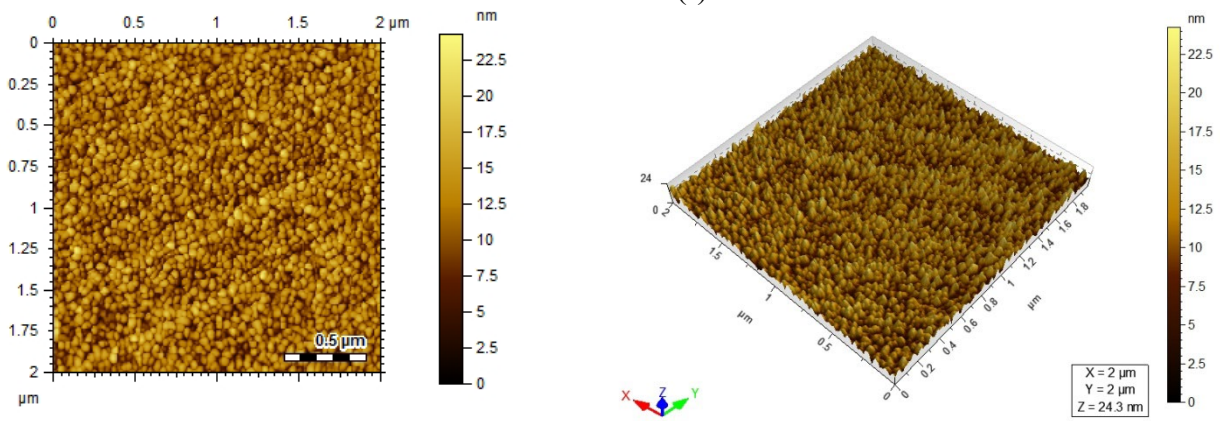

Figure 8.3 Surface roughness image of gold film (d) thermal evaporation process sample A-2line diagram (e) thermal evaporation process sample A-2 2D image (f) thermal evaporation process sample A-2 3D image

(g)

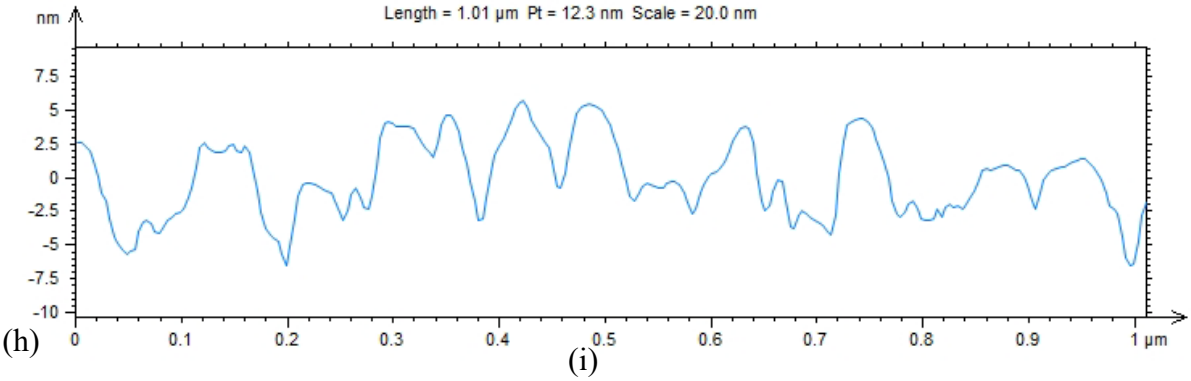

(h)

(i)

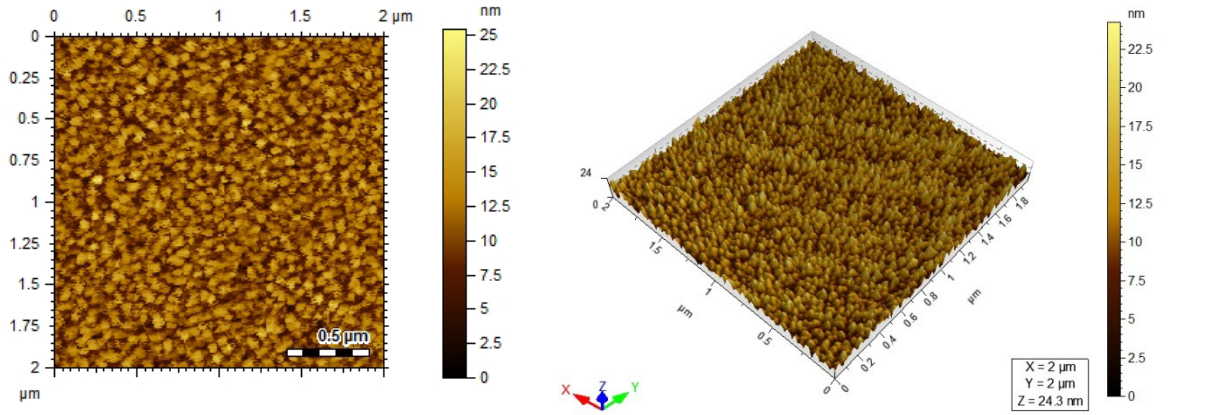

Figure 8.3 Surface roughness image of gold film (g) e-beam evaporation process sample B-1line diagram (h) e-beam evaporation process sample B-1 2D image (i) e-beam evaporation process sample B-1 3D image

(j)

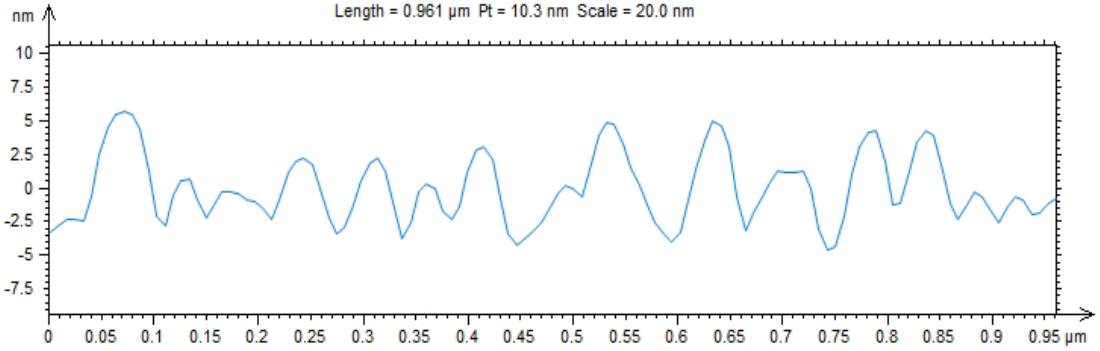

(k)

(l)

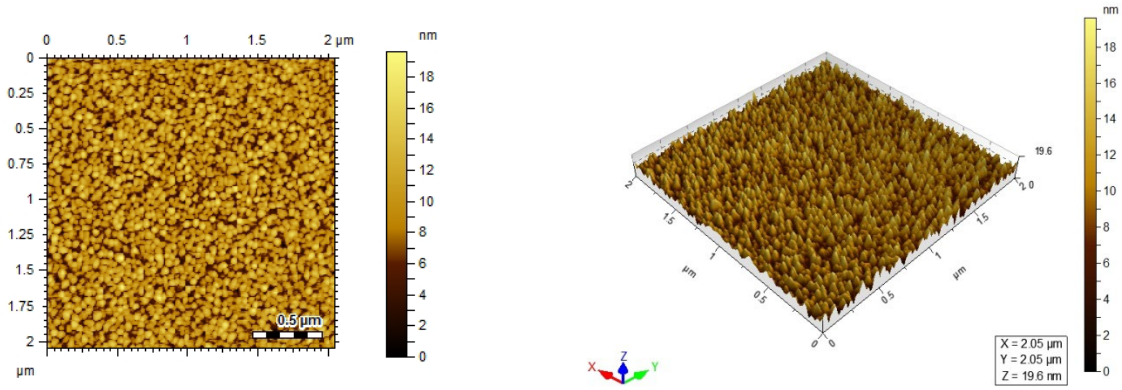

Figure 8.3 Surface roughness image of gold film (j) e-beam evaporation process sample B-1line diagram (k) e-beam evaporation process sample B-1 2D image (l) e-beam evaporation process sample B-1 3D image

Table 8.2 Surface roughness of gold films evaporated by thermal and e-beam process

Surface roughness value	Thermal gold film		E-beam gold film	
	Sample-A1: 6 Å/s evaporation rate	Sample-A2: 12 Å/s evaporation rate	Sample-B1: 6 Å/s evaporation rate	Sample-B2: 12 Å/s evaporation rate
Root mean square (S_q)	5.00 nm	3.05 nm	2.84 nm	2.71 nm
Max. roughness (S_z)	37.0 nm	24.2 nm	25.4 nm	19.6 nm

8.3.3 Morphology analysis

The performance of infrared devices in harsh environments is dependent on the durability of a thin metal film, which may be influenced by the characteristics of the grown film (metallic). Because their presence can impair the functionality of the manufactured device, it is crucial to reduce the undesired microstructural characteristics (such as fractures, voids, hollows, flaws, additional grain boundaries, etc.) of the evaporated metal layer. In order to create a very dense, conductive film with few flaws (cracks) and voids, the thickness of the gold film (220 nm) was tailored. The microstructural characteristics of the evaporated gold film on Samples A1, A2 and B1, B2 were examined using the scanning electron microscopy evaluation procedure, an efficient as well as widely applied scientific means for analyzing the semiconductor appliance facade, texture, collapse examination, and so on. Fig. 8.4(a, b, c, d, e, f, g, and h) displays the SEM images of measured Samples A1, A2 and B1, B2 at different scales and magnifications. With the exception of one place on the film's surface, the e-beam-evaporated Sample B-2 gold film seems more dense, continuous, and uniform, as shown in Fig.8.4 (f, h). Fig.8.4 (a), (b), (c) and (d) (Sample A-1 and Sample B-1 at 50 and 75 Kx magnifications) demonstrated that the e-beam gold film is primarily composed of spherically linked nanoparticles compared to thermal gold film. However, there are also some hexagonal nanoparticles in the thermal gold film. Similarly, from Fig. 8.4 (e), (f), (g) and (h) (Sample A-2 and Sample B-2 at 50, 75 and 100 Kx magnifications) revealed that the e-beam evaporated gold film’s grain size is smaller, dense and void-free compared to the thermally evaporated gold film. Consequently, the most recognizable and essential gold particle topographies were attained of Sample B-2 by e-beam technique. A typical nanoparticle is 22-30 nm in size (Fig.8.4 (f), (h)), and this size agrees rather well with the grain size determined by AFM. Therefore, there is great agreement between the microstructural findings of the gold thin film formed by e-beam and the best-reported results [467-481,475-477]. As a result, the SEM is a practical and efficient analytical tool for assessing the quality of generated metal films. E-beam evaporation is confirmed as an optimal evaporation approach by the SEM examination of the developed gold film, producing a gold thin film with the appropriate topography and flawless surface free of surface fractures. The reported gold metal films utilized for the manufacture of HgCdTe-based infrared detectors [446] are similar to the e-beam evaporated gold thin film in terms of narrower crystallographic boundaries of grains, longitudinal development, homogeneous step coverage, and negligible porosity. Thus, development of highly dependable HgCdTe (MCT) infrared detectors with high efficiency, high compactness, and small proportions may benefit from the use of gold film in the creation of ohmic connections with low contact resistance.

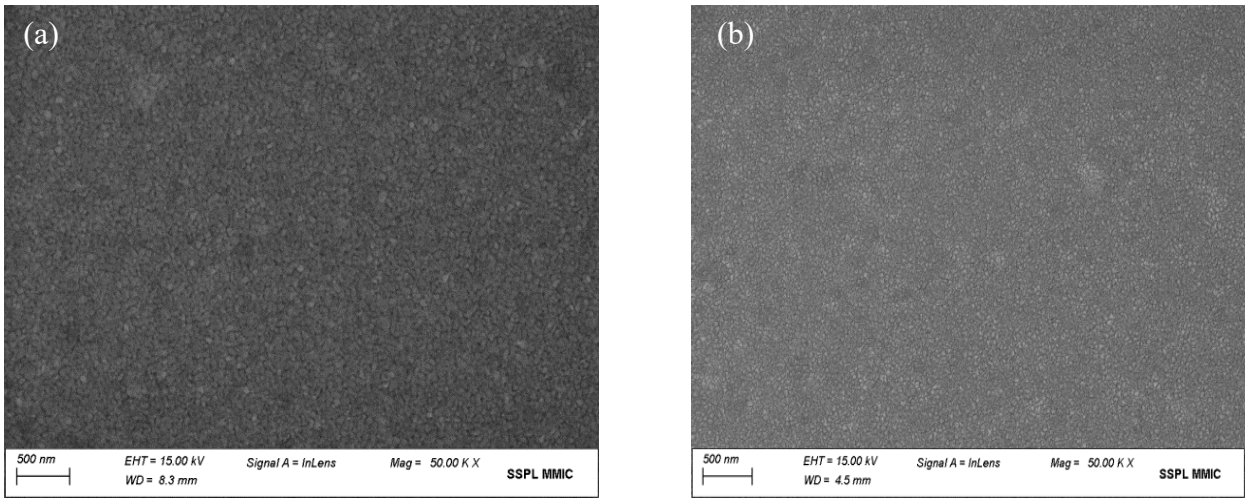

Figure 8.4 SEM micrograph of gold film (a) thermal evaporation Sample A-1 at 50 KX magnification (b) e-beam process Sample B-1 at 50 KX magnifications

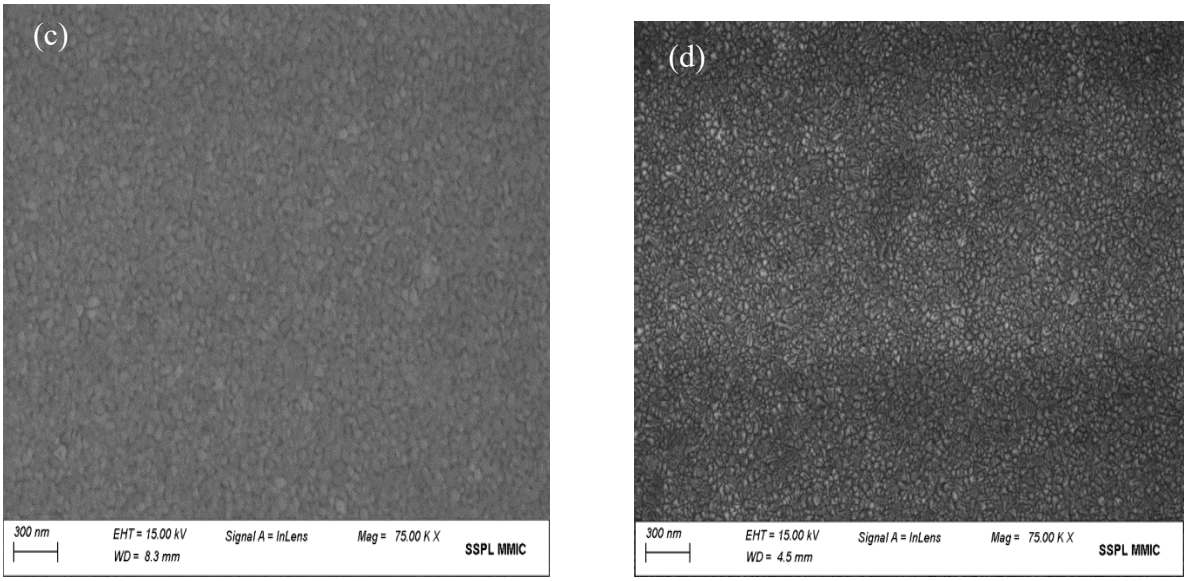

Figure 8.4 SEM micrograph of gold film (c) thermal evaporation Sample A-1 at 75 KX magnification (d) e-beam process Sample B-1 at 75 KX magnifications

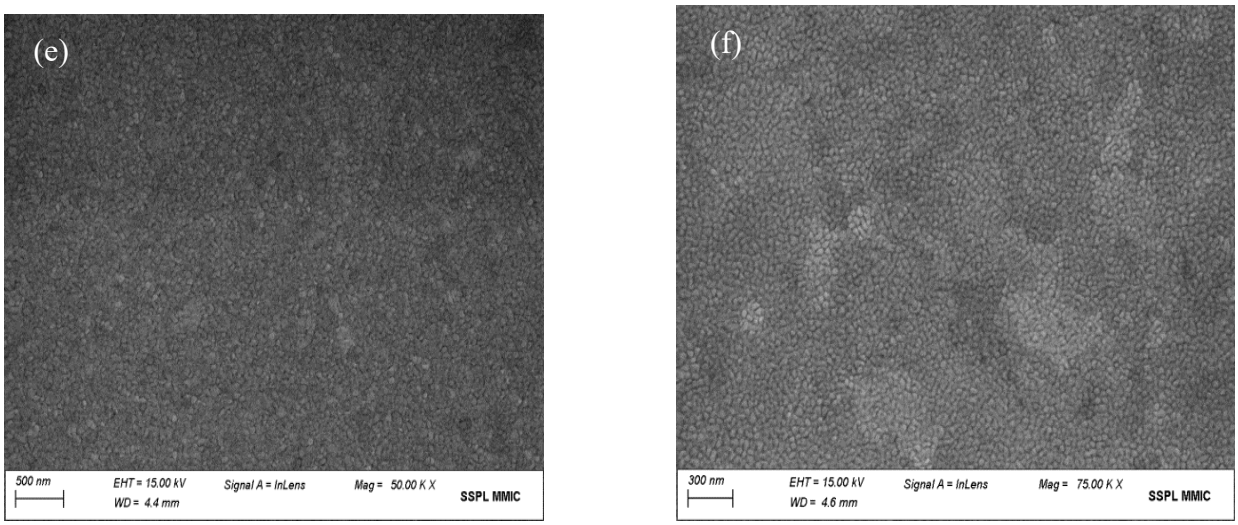

Figure 8.4 SEM micrograph of gold film (e) thermal evaporation Sample A-2 at 50 KX magnification (f) e-beam process Sample B-2 at 75 KX magnifications

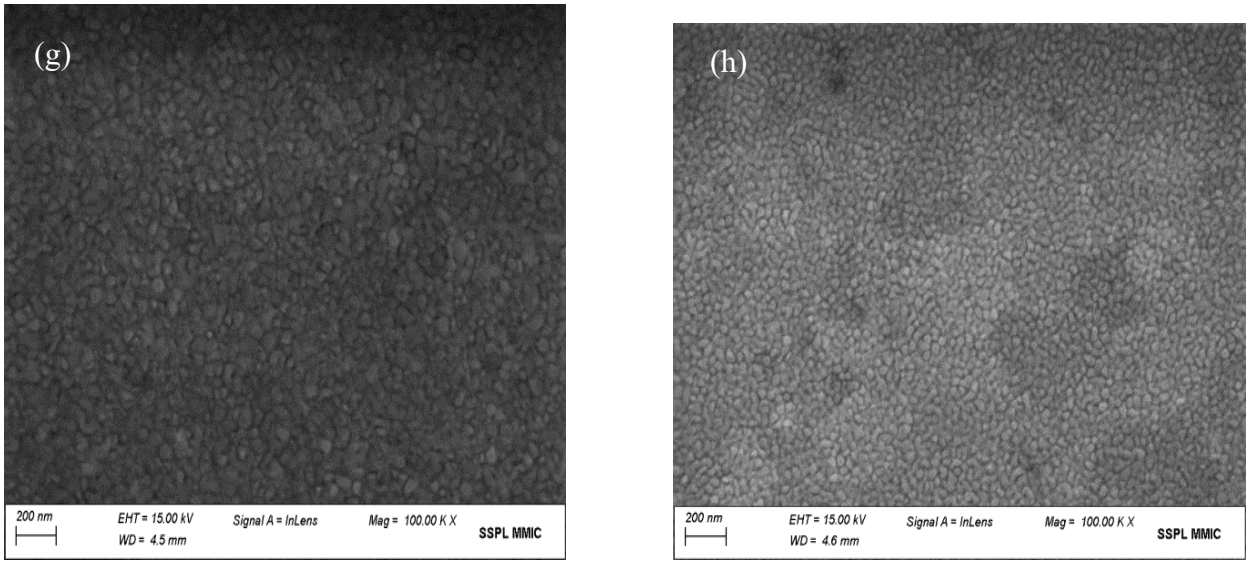

Figure 8.4 SEM micrograph of gold film (g) thermal evaporation Sample A-2 at 100 KX magnification (h) e-beam process Sample B-2 at 100 KX magnifications

8.3.4 Compositional examination

The energy dispersive x-ray identification procedure was utilized to undertake the compositional assessment of the thermally and e-beam evaporated gold films. Fig. 8.5 (a, b, c, and d) displays the resulting EDX spectra of gold samples made using various evaporation processes (Sample-A1:

6 Å/s, A-2: 12 Å/s evaporation rate (thermal); Sample-B1: 6 Å/s, B-2 : 12 Å/s evaporation rate (e-beam)). Fig. 8.4 (a) depicts the EDX spectrum of Sample-A1 (thermally), containing the peaks of chromium (Cr), and gold (Au) elements, respectively. Table 8.3 lists the energy dispersive x-ray outcome of gold film evaporated on HgCdTe samples using thermal and e-beam evaporation methods. The purity of the gold film may be influenced by Sample-B2's comparatively lower Cr and higher gold content than Sample-A2, however Sample-B2 has a higher proportion of Au element (weight: 99.30%, atomic: 97.20%) than Sample-A2 (weight: 97.40%, atomic: 90.80%). The EDX spectra of Samples A2 and B2 also show a few additional peaks of insignificant intensities, which could be the result of carbon adhesive and atmospheric water vapor residues from the EDX sample preparation process. Therefore, the elemental analysis of Samples A1, A2, B1 and B2 showed that e-beam evaporation process at 12 Å/s evaporation rate may be used to create a rather pure gold film. This EDX examination verified the high purity thin film that was produced by e-beam on the HgCdTe substrate with the necessary Au element, and it demonstrated excellent agreement with many gold film reports [448,475-477,482-484]. As a few contamination inside the gold contact can impair the functionality (in terms of tainted film eminence) of the infrared detector, this highly pure gold layer is particularly beneficial in creating a inteface of low contact resistivity on the MCT specimen.

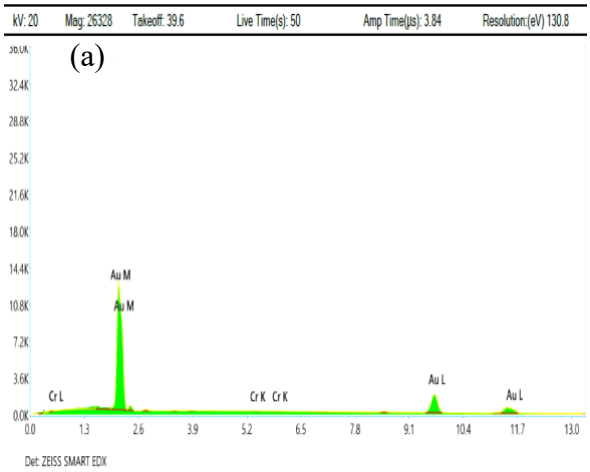

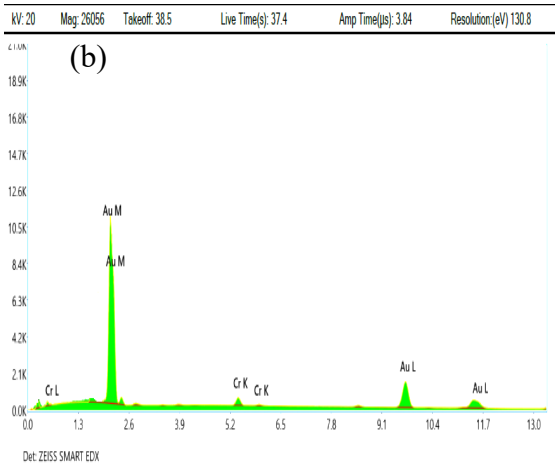

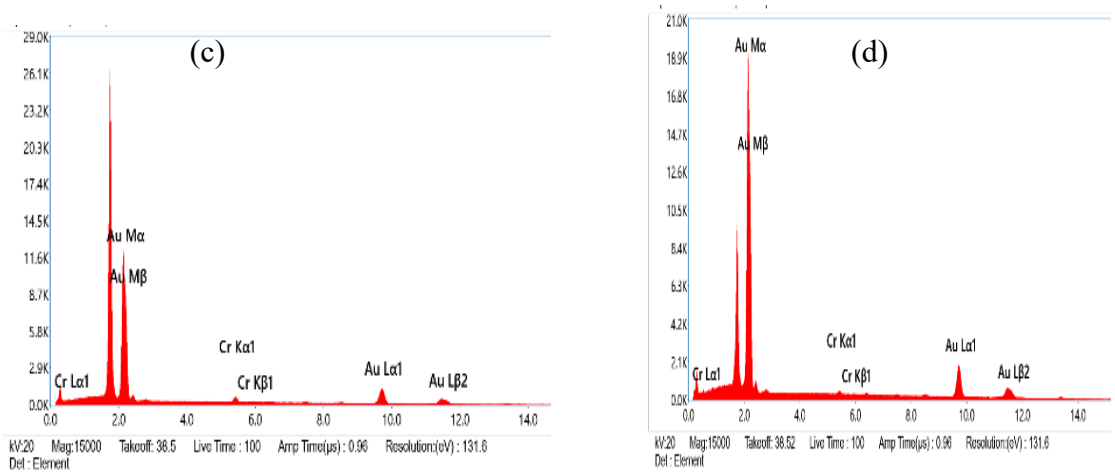

Figure 8.5 EDX spectrum graph of (a) thermally evaporated gold film Sample A-1 and (b) e-beam evaporated gold film Sample B-1 (c) thermally evaporated gold film Sample A-2 and (d) e-beam evaporated gold film Sample B-2

Table 8.3 Compositional analysis of thermal and e-beam evaporated gold films

	Thermally evaporated gold film				E-beam evaporated gold film			
Element	Sample A-1		Sample A-2		Sample B-1		Sample B-2	
	Atomic %	Weight %	Atomic %	Weight %	Atomic %	Weight %	Atomic %	Weight %
Cr	0.10	0.10	9.2	2.6	2.90	1.80	2.8	0.7
Au	27.80	72.90	90.8	97.4	33.30	77.20	97.2	99.3

8.3.5 Nanomechanical properties analysis

The cyclic nano-indentation studies were carried out utilizing a berkovitch indenter and an Industron Nanomechanical tester. The Oliver and Pharr approach [485] extracts stiffness from cyclic load-displacement curves by describing the beginning slope of the unloading curve. Hardness is the material's resistance to indentation, which can only be evaluated when the indenter stops penetrating at a specific load. Depth sensing nanoindenation experimental data (force (P)-displacement (h) curves) are often analyzed using the Oliver & Pharr (O&P) process, a widely used method in the contact mechanics research field. The following Eqn. 8.7 &8.8 [129,486] can be used to compute key mechanical properties of materials, such as hardness (H) and reduced elastic modulus (Er) [458,487].

$$H = P_m / A_c \quad (8.7)$$

$$E_r = (1 - \nu_i^2)/E_i + (1 - \nu_s^2)/E_s) - 1 \quad = \sqrt{\pi}\ 2\ S_m\ \sqrt{A_c} \tag{8.8}$$

The values P_m and S_m represent the maximum force applied during the indentation test and the maximum contact stiffness of the unloading curve. The parameters ν_i, and ν_s, represent the Poisson ratio of the indenter and sample, respectively isotropic elastic characteristics of the bodies participating in the contact process. The sub-indexes i and s identify the indenter and sample, respectively.

Grain dislocations in a polycrystalline film can come from the grain's interior and boundary, from a multiplication of preexisting dislocations during loading, or from geometrically necessary dislocations (GNDs) created to account for the strain gradient in nanoindentation at low penetration depths. Plastic deformation is made possible by the movement of dislocations caused by slip [488]. Following an initial slip, the yield stress or hardness increases as more dislocations are created and interact with one another or at the grain boundaries in polycrystalline materials. The "smaller is stronger" phenomenon, or the trend of improved mechanical properties with decreasing size, is caused by these interactions. They aid in the explanation of some observable effects, like the Hall Petch effect and the indentation size effect (ISE).

GNDs are created when materials with sharp tips are indented at shallow depths, causing significant strain gradients. This permits the material underneath the indenter to undergo plastic deformation. The formation and movement of new dislocations are impeded by the GNDs and statistically stored dislocations (SSD), which are dislocations that form in the absence of strain gradients. Larger strain gradients cause the density of dislocations to increase as indentation depths decrease. The observed increase in hardness at shallower indentation depths is explained by the resulting strengthening effect [487-491].

When Due to their physical dimensions, polycrystalline thin films and nano-objects will be made of materials with a nanocrystalline structure as the nanoscale approaches i.e. grains of nanometer size; in contrast to bulk materials with coarse grains, which can range in size from 10 to 300 μm [492]. When piling-up happens, which is frequently the case when testing metals by indentation, the material that has piled up bears the weight placed on the indenter, allowing the indenter to penetrate less deeply than it would in the absence of piling-up. The well-known 10% rule is very relevant to thin film testing. According to this rule, the indentation depth should not exceed 10% of the film thickness in order to reduce the impact of the substrate properties on the measurement of the film properties. Although elastic recovery can obviously greatly diminish the depth of penetration, the size of the residual impression is typically thought to be equal to the contact area at full load.

Gold film's mechanical characteristics and the creep and strain rate behavior were examined using indentation with a Berkovich tip, as seen in Fig. 8.6-8.8. For the thin gold films evaporated by thermal and e-beam processes (Sample A-2: 12 Å/s evaporation rate and Sample B-2: 12 Å/s evaporation rate), the hardness as well as Young's modulus were determined at utmost loads of

20, 30, 40 and 50 micro newton loads. As a function of the maximum load, the hardness and Young's modulus increase for the thin gold films evaporated by thermal and e-beam processes, as shown in Fig, 8.6(a) & (d). The nanoindentation indent images on e-beam gold film and thermal gold film at 40 µN load are shown in Fig 8.7 (b) & (c), respectively.

(a)

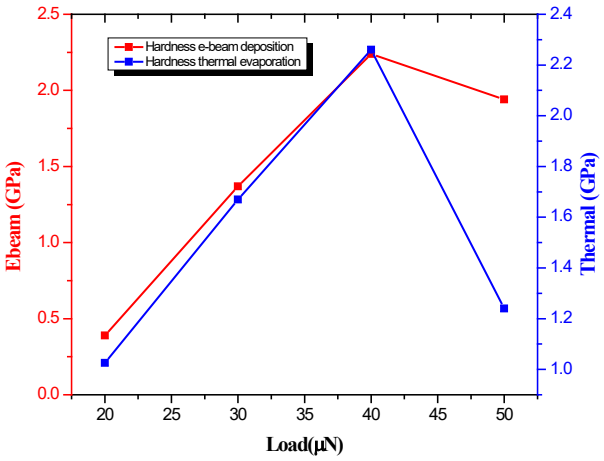

(b)

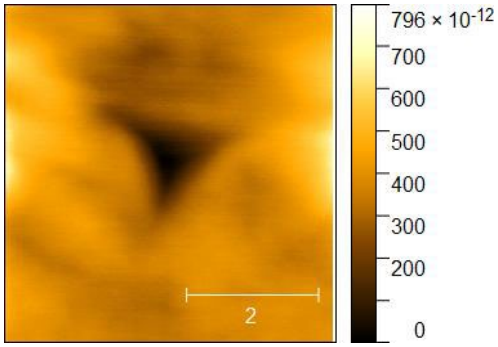

(c)

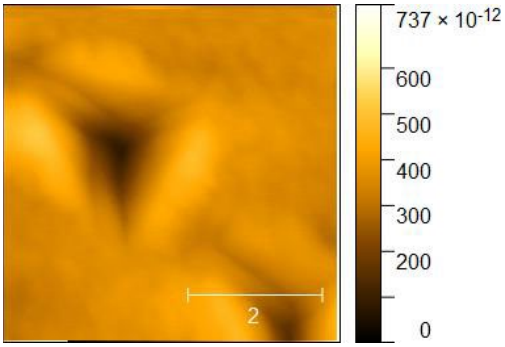

Figure 8.6 (a) Hardness plot of gold film e-beam evaporation and thermal evaporation (b) nanoindentation indent image of e-beam gold film at 40 µN load (c) nanoindentation indent image of thermal gold film at 40 µN load

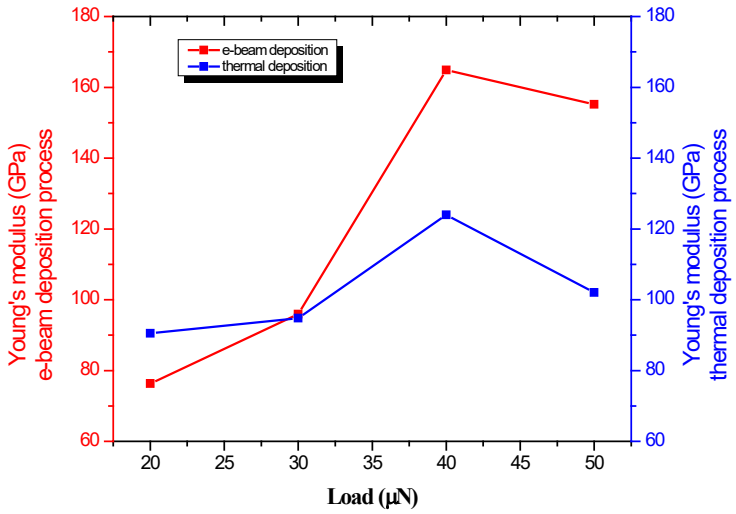

Figure 8.6(d) Young's modulus plot of gold film e-beam evaporation and thermal evaporation

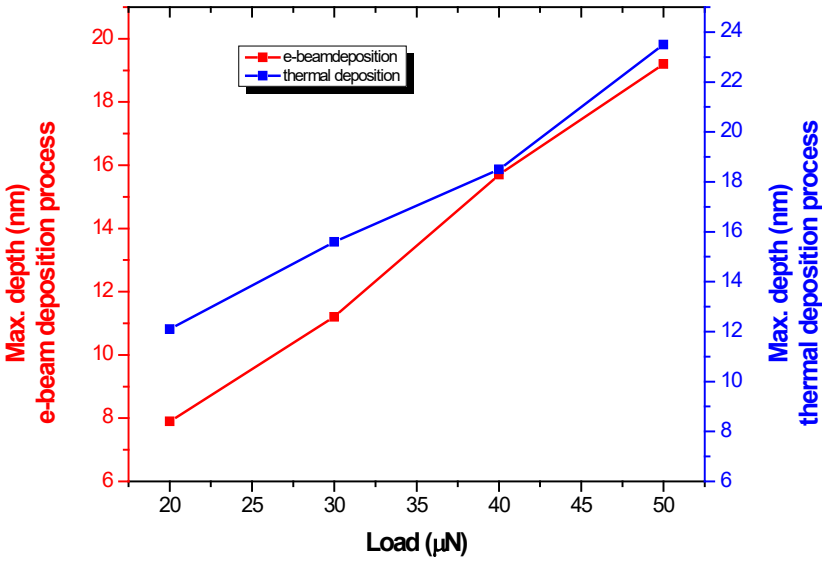

Figure 8.6(e) Maximum depth plot of gold films e-beam evaporation and thermal evaporation

Although the hardness and Young's modulus values were higher for gold film evaporated by e-beam process except Young's modulus at 20 μN load where it's lower for e-beam evaporated gold film. The obtained hardness and Young's modulus values of e-beam evaporated gold film is compatible with earlier reported results [493]. The maximum depth for the indented thermally evaporated gold film is higher than the e-beam evaporated gold film at 20-50 μN loads a shown in Fig. 8.6(e). As long as the depth of penetration is greater than 10 percent [494] and is not

exceeded, it is widely acknowledged that the substrate influences the hardness. According to the RISE (Reverse Indentation Size Effect) depicted in Fig. 8.6(a) and (c), the hardness increases with increasing penetration depth [495]. One factor contributing to the higher hardness of e-beam-evaporated gold film over thermally-evaporated gold film is the Hall-Petch effect [496-497]. The SEM micrographs in this instance demonstrate that the e-beam thin film's intrinsically smaller grain sizes than the thermal gold film result in a boost in yield stress or hardening incontrast to the grandscale. Both the dislocation-density and pile-up mechanisms can cause hardening. However, the number of dislocation pile-ups is limited by the nanosized grains because of the film's nanoscale thickness. The higher hardness is thought to be mostly caused by the dislocation density mechanism. For thermal and e-beam gold films, creep is depicted in Fig. 8.7(a) and (b) for typical load–displacement curves with maximum loads of 30, 40, and 50 μN and a hold period of 5 s. With a maximum load of 50 μN and loading and unloading times of 5 and 20 s for thermal and e-beam gold films, Fig. 8.8 (a) and (b) display indentation–displacement curves for various strain rates. An indication of how sensitive the experiments are to hold times and loading and unloading rates can be found in the creep and strain rate data. The displacement during the holding times at loads of 30, 40, and 50 μN varies very little according to the creep data. There is also a slight displacement from a loading and unloading time of 5–20 s in the strain rate data. From Fig. 7.7 and 7.8, it’s observed that the loading –unloading curves are not smooth for thermal gold film compared to e-beam gold film which is due to pop-in and pop-out events. Within the grain boundaries, pop-in events are associated with the creation of new dislocations and the multiplication of preexisting ones, increasing displacement at constant load. It is the dislocation density mechanism and possibly the pile-up mechanism that cause the final hardening. Grain boundary (cobble) diffusive creep, which is caused by the addition or removal of atoms from the boundary between two grains, predominates over indentation creep in materials with small grain sizes (less than 0.2–0.3 μm) [498-499]. Increased displacements seen in creep and strain rate data are thought to be caused by this diffusional creep. In tribological applications on the nanoscale, where there is a constant load or fluctuating loading rates, the low sensitivity of e-beam gold film to creep and strain rate in comparison to thermal gold film is advantageous. This stops the film from easily deforming.

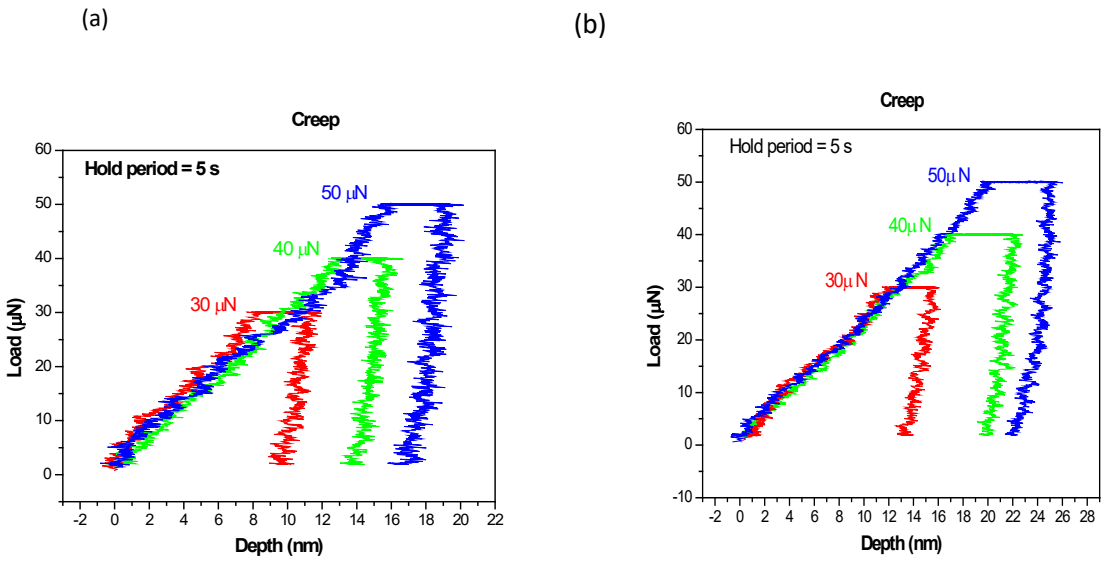

Figure 8.7 Creep at maximum loads of 30, 40 and 50 μN load (a) thermal evaporation process (b) E-beam evaporation process

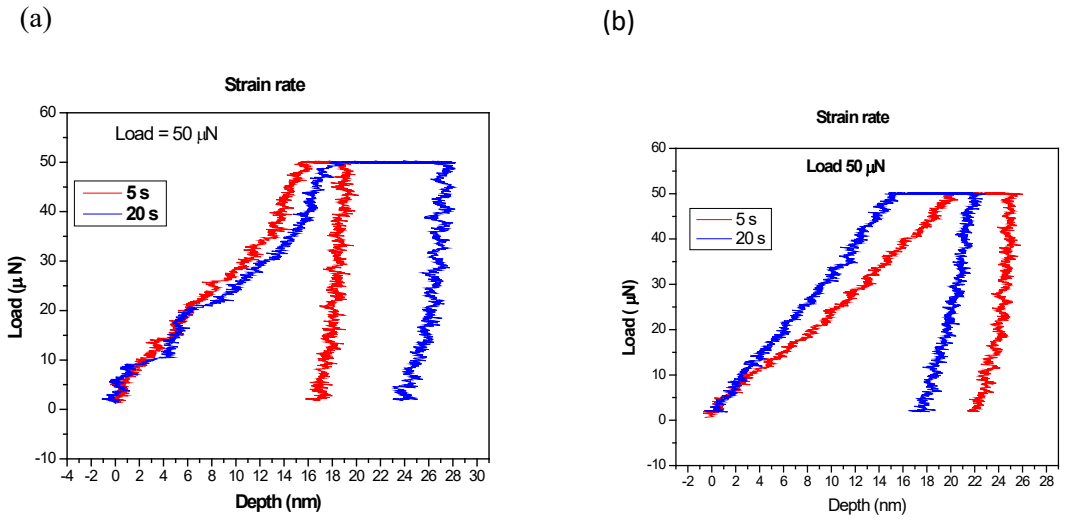

Figure 8.8 Effects of varying strain rate at a maximum load of 50 N for loading-unloading periods of 5 s and 20 s (a) thermal evaporation process (b) e-beam evaporation process

8.3.6 Electrical characteristics of gold film by TLM method

To determine the electrical characteristics of developed gold thin films evaporated by thermal and e-beam processes (Sample A-2: 12 Å/s evaporation rate and Sample B-2: 12 Å/s evaporation rate), contact resistivity estimation of HgCdTe sample based transmission line model pattern (TLM) (Au/p-HgCdTe) was carried out. The TLM pattern consists of alike eight pads with a contact area

of 100 x 200 μm^2 (L x W). The separation between two contact pads varies from 50, 100, 150, 200, 250, 300, 350, 400 μm as shown in fabricated TLM pattern Fig.8.9.

To assess sheet-resistance R_{sh} and transfer-length L_T, resistances between each neighboring contact pad were evaluated. A graph of resistance vs gap of intepads was then created. The other resistive characteristics, such as contact resistance (R_c) and contact resistivity(ρ_c), were then estimated using these subsequent values of R_{sh} and L_T. I-V measurement was also performed for the manufactured TLM structure (contact pads) in order to investigate the Au/p-HgCdTe interface's electrical behavior.

8.3.6.1. TLM structure measurement and analysis

The total resistances (RT) of all neighboring contact pads in the transfer length model were measured at a temperature of 80 K, as low-temperature evaluations are suitable for operational devices that have been fabricated. The graphs of total resistance (R_T) vs. gap of interpad (d) are shown in Fig. 8.10 (a) & (b). The electrical characteristics such as contact resistance, sheet resistance, transfer length and contact resistivity of the Au/p-HgCdTe-based TLM pattern was assessed using the equations [91,92,423,500]. The outcomes of the examinations are summarized in Table 8.2. The Au/p-HgCdTe TLM test pattern has evaluated specific contact resistances (ρ_c) of 1.1 × 10^{-3} Ω cm^2. The obtained ρ_c value is compatible to the documented outcomes of Au/p-HgCdTe interactions [92,382]. In order to provide an interface with low specific contact resistance, HgCdTe-based IR detectors can be made using thermally generated gold film [91-92,382,445]. The state (form) of sample surface and chemical treatments before evaporation are most likely the causes of the small contact resistivity for the gold/HgCdTe junction [91-93,482,501].

The resistance (R_T) between two consecutive contact pads of length L and width W separated by distance d is given by [428,446]:

$$R_T = \frac{d\,R_{sh}}{W} + 2R_c \tag{8.9}$$

where R_c is the contact resistance and R_{sh} is the sheet resistance of the material outside the contact region. Contact resistance and sheet resistance can be easily obtained from a graph of R_T against d for a transmission line model. The contact resistivity (ρ_c) is determined by the following relationship

$$L_T = \frac{\sqrt{\rho_c}}{\sqrt{R_{sh}}} \tag{8.10}$$

where L_T is transfer length

The contact front resistance or contact-resistance R_c for a planar ohmic contact is specified by [428,446]

$$Rc = \frac{R_{sh}L_T}{W}\ \coth\ \left(\frac{L}{L_T}\right) \approx \frac{\rho_c}{WL_T}\coth\left(\frac{L}{L_T}\right) \tag{8.11}$$

It is further made easier in the cases when (i) $L \ll L_T$ then (metal layer is not penetrated considerably by current)

$$R_c \approx \frac{\rho_c}{LW} \quad (8.12)$$

(ii) $L \gg L_T$ (current flow into the metal) then

$$Rc \approx \frac{\rho_c}{WL_T} \quad (8.13)$$

When a thin layer of material is absorbed during contact creation, the sheet resistance (R_{sk}) of the material beneath the contact region differs from R_{sh}. This results in a modification of the contact resistance [91-92,423]

$$R_c = \frac{\rho_c}{WL_{TK}} \coth\left(\frac{L}{L_{TK}}\right) \quad (8.14)$$

where

$$L_{TK} = \frac{\sqrt{\rho_c}}{\sqrt{R_{sk}}}$$

and total resistance for contacts with $L \geq 1.5L_T$ [91-92,423]

$$R_T = \frac{d\,R_{sh}}{W} + \frac{2\,R_{sk}}{W}\frac{L_{TK}}{} \quad (8.15)$$

R_T was evaluated among duo of the neighboring metal pads in transmission line model.

One possible explanation for the small resistance of contact of ohmic type is the presence of a skinny interstitial deposit of oxide—only a small number of angstroms thick—that acts as a barrier to gold diffusion into the HgCdTe during the gold metal evaporation process. This oxide layer forms when the HgCdTe surface is exposed to oxygen plasma for 30 seconds prior to gold deposition. Here are several junction states on the gold/p-HgCdTe junction as a result of an interaction between the HgCdTe sample and the evaporated gold metal. The high-value contact resistivity is achieved through rectifying contacts, which are influenced by Fermi-level pinning at the minima of the conduction band due to these junction states.

As a result, the thin interfacial oxide layer minimizes gold diffusion into HgCdTe, hence reducing the number of interface states. This results in a low contact resistivity, which is $2.73 \times$ x 10^{-3} Ωcm^2 for the e-beam evaporated gold/p-HgCdTe junction compared to thermally -evaporated Au/p-HgCdTe interface 1.1×10^{-2} Ω cm^2 (Fig. 8.10 a &b) [91-93,502]. The facade shapes as well as evaporated layer/HgCdTe facade conformations are linked to the second factor that causes low

specific contact resistance. Because the undesired characteristics of the film/substrate surface, such as pricks, impurity, flaws, score, variations in thickness, and a nonstoichiometric conformations could complicate reaching the intended electrical properties of the device. The sample of HgCdTe (transfer length model) was subjected to a number of efficient surface treatments, including chemical etching and chemo-mechanical polishing, which helped the sample to attain a defect and contamination-free surface. Furthermore, the created gold films are dense, pure, and homogeneous. The films also include the best particle size and the least amount of roughness. The features mentioned above are all covered in the study of EDX, AFM, and SEM. Because there are little obstacles in the way of charges moving through the Au/p-HgCdTe junction, these characteristics of the HgCdTe surface/Au film dictate how quickly they do so. This is all related to the second factor that causes the Au/p-HgCdTe interface's improved Ohmic nature and reduced specific contact resistance. In order to create high-quality infrared detectors with low specific contact resistance, the evaporated gold film possesses all the required morphological and compositional characteristics [93,482,501-502].

The performance of the gold metal contact as well as the phenomenon of current passage in the gold/p-mercury cadmium telluride junction is provided by the I-V characteristics. The Fig. 8.10 indicated the resulting I-V curves of the Au/p-HgCdTe interface (realized at 80 K).

Due to the fact that gold-contacts are not entirely Ohmic and since these contacts have certain rectifying characteristics, it was discovered that Au-contacts (TLM structure) exhibited almost Ohmic behavior. In order to create HgCdTe based infrared photodetectors with good Ohmic contacts, various metals such as gold, PEDOT: PSS, gold/platinum/titanium, electroless gold, and mercury telluride/titanium were employed. As a result, the I–V characteristics of the e-beam evaporated gold film are more consistent and comparable compared to thermally grown gold films as in earlier reported structures [91-92,382,424,445].

The number of junction states on the Au/p-HgCdTe junction has been comparatively reduced by the plasma descum procedure on the HgCdTe (MCT) facade before gold evaporation. The I–V graph of the evaporated gold contact (Fig. 8.11) is ohmic, with the exception of some partial rectifying nature. The Au/pHgCdTe interface of transfer line model with type of Ohmic (linear I–V graph) may be generated for these reasons. Fermi level pinning at the conduction-band minimum, which is caused by specific junction states formed at the Au/p-HgCdTe junction after the plasma descum process, at the gold/p-mercury cadmium telluride junction subsequent to the plasma descum process, explains the partially reforming I-V characteristic of the evaporated to some extent reforming current-voltage characteristic of the evaporated Au Ohmic contact (Fig. 8.11).

The plasma descum procedure applied to the HgCdTe surface before the evaporation of gold metal has effectively diminished the number of junction states at the gold/p-HgCdTe junction, resulting in the I-V graph of the evaporated gold contact (Fig. 8.11) exhibiting an ohmic characteristic, albeit with some partial reforming behavior. These factors likely contribute to the formation of the Au/p-

HgCdTe junction within transfer line model displaying an Ohmic character (indicated by a linear I-V graph). The partially reforming I-V characteristic of the evaporated gold Ohmic contact (Fig.8.11) arises from Fermi level pinning at the minimum of the conduction band, due to certain junction states present at the gold /p-HgCdTe junction following the plasma descum procedure. The second component accountable for the formation of an Ohmic contact is the gold contact's long-term durability, which is exaggerated by its cluster growth mechanism, elevated coefficient of diffusion, as well as weak adhesion. The grown metal/HgCdTe element in/out-diffusion processes happen during metal-evaporation/post-evaporation (which create junction states due to the imperfections) and can be reduced by low temperature evaporation and the thin interfacial oxide layer (made by the plasma descum process). The strong adherence of gold films to the HgCdTe surface/epilayer was demonstrated by a tape test, and it was also determined that these films could be used in the photolithography process to fabricate infrared detectors. After photolithography masking, the appropriate transfer length model patterns were interpreted on the MCT substrate by depositing gold films. In order to create the required motif of gold/p-HgCdTe-based transfer length model motif, photolithography lift-off procedures were carried out, and these procedures went off without a hitch. Because of its characteristics, which include high adhesion, low temperature evaporation, and few flaws (caused by a thin interfacial oxide layer), gold film favors stability and is crucial for the creation of infrared detectors with ohmic electrical connections [91-92,436,439,443,459]. The estimated values of transfer length, contact resistance, sheet resistance and contact resistivity of thermal and e-beam evaporated gold films are given in Table 8.4.

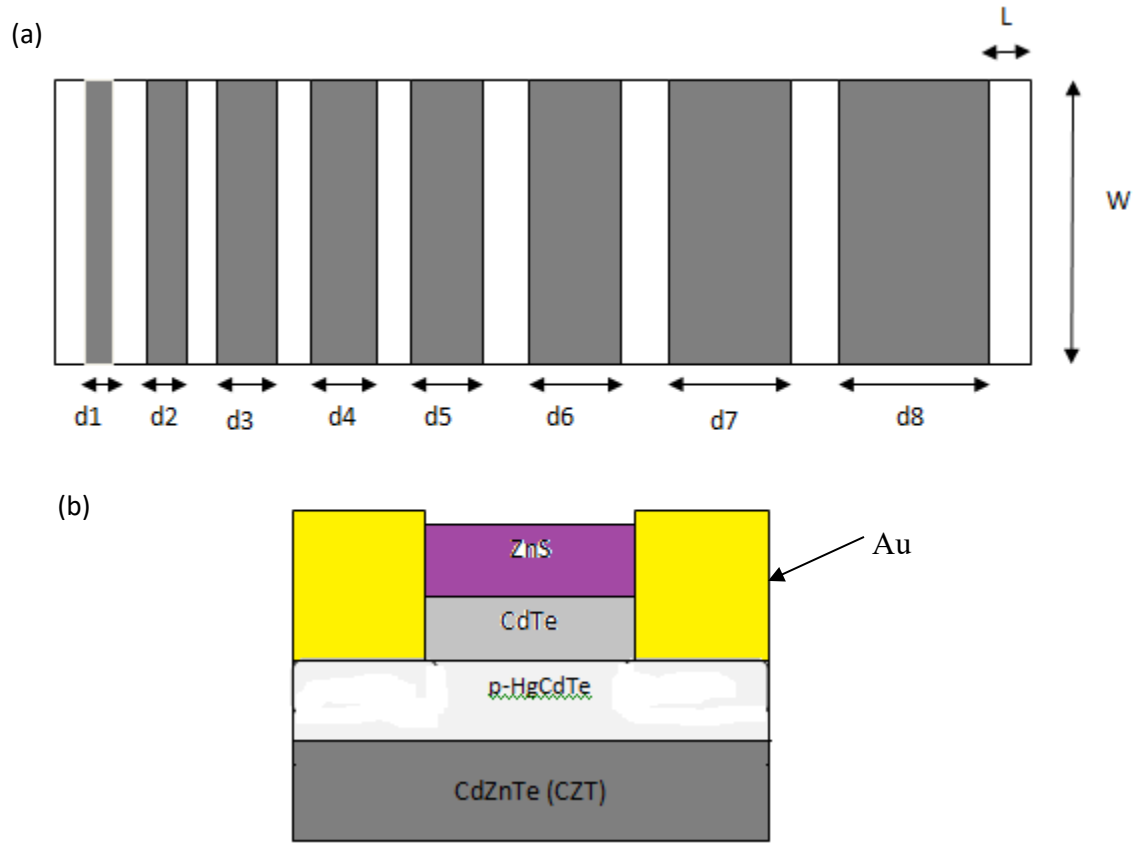

Figure 8.9 Layout of the transmission line model for the estimation of contact resistance.(a) Plan view: the structure has eight pads of same length and width. (b) Front view: the cross-section of one part of the test pattern is shown.

(a)

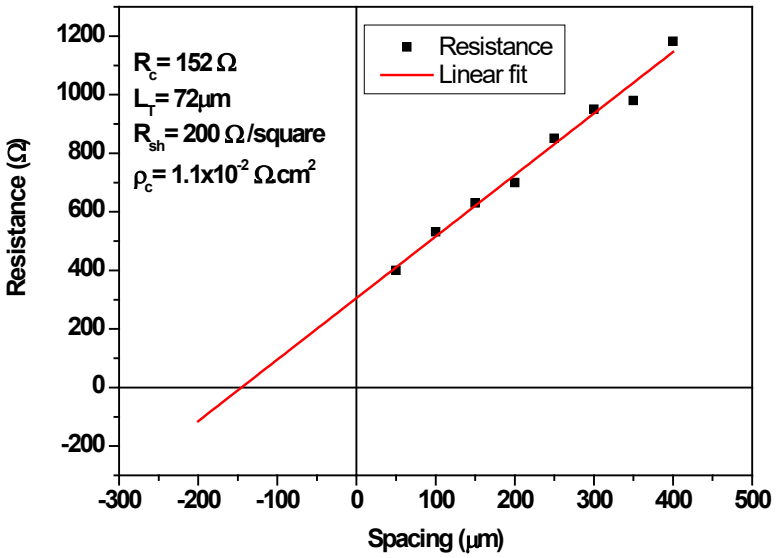

(b)

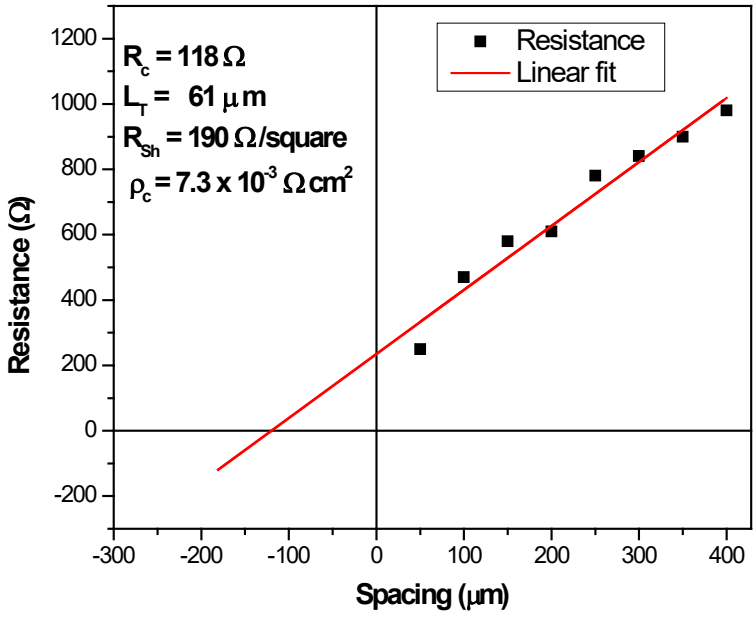

Figure 8.10 Total resistance vs spacing between pads graph for contact pads of gold film (transmission line model pattern: Au/p-HgCdTe) (a) thermally evaporated gold (b) e-beam evaporated gold. The graph was exploited to estimate the resistance of contact apart from electrical characteristics of evaporated gold contacts

Table 8.4 Electrical characteristics of the SampleA2 and Sample–B2 (transmission line model pattern: Au/p-HgCdTe) and gold layer amid enhanced rate of evaporation -12 Å/s) determined from its transfer line model calculation

Parameters	Transmission line model test structure	
	Sample-A2	Sample-B2
Transfer length, T_L (μm)	72	61
Sheet resistance, R_{sh} (Ω/square)	200	190
Contact resistance, R_c (Ω)	152	118
Contact resistivity, ρ_c ($\Omega.cm^2$)	1.1×10^{-2}	7.3×10^{-3}

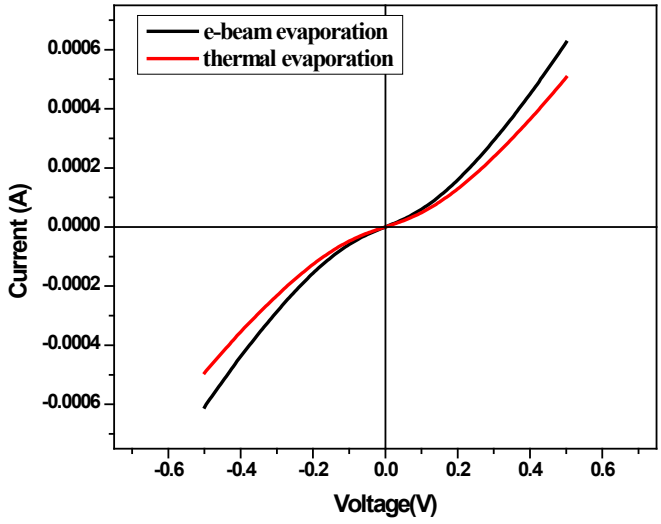

Figure 8.11 I-V assessment for the e-beam as well as thermally evaporated contacts of the gold-based transfer line model (pattern: Au/p-HgCdTe). The graph indicates the conduct of the Au/p-HgCdTe interface.

Consequently, a reliable ohmic contact (characterized by low contact resistivityand long-term stability) can be achieved using a gold film deposited by e-beam evaporation that possesses the appropriate properties, including the cubic structure with a preferred orientation of Au (111). This film should exhibit high purity, minimal roughness, small grain size, well-built adhesion, and adequate be in command of over the individual processing steps (such as surface preparation, surface treatment, and the evaporation state of HgCdTe).

8.4. Conclusions

The key characteristics of gold thin films fabricated thermally and by e-beam on a mercury cadmium telluride (HgCdTe) substrate were compared in this work. Structural study confirmed the favored orientation (111) of the cubic and polycrystalline gold films. The e-beam evaporated gold film at 12 Å/s had the lowest value of dislocation density, residual stress and microstrain indicating the best crystalline structure. In comparison to the thermal gold film (Sq = 5.0 (6 Å/s evaporation rate) and Sq = 3.0 nm (12 Å/s evaporation rate), respectively), the e-beam evaporated films at 6 and 12 Å/s evaporation rate are more pure, homogeneous, extremely dense, and have low surface roughness (Sq = 2.8 and 2.71 nm, respectively), according to the elemental and morphological properties. Thermal and e-beam gold films were found to have average grain sizes of 30.2 nm and 20.1 nm, respectively. Nanoindentation tests showed that hardness and Young's modulus rise with load up to a certain point before declining. At an indentation load of 20–50 μN, the e-beam gold film's hardness and Young's modulus were greater than those of the thermal gold film. The strain rate of the thermal and e-beam gold films were calculated and compared using a maximum load of 50 μN. The creep behavior was calculated for 5 seconds using loads of 20, 30, 40, and 50 μN. As evidenced by the absence of pop-in and pop-out during nanoindentation, the e-beam gold film's mechanical properties were improved over the thermal gold film due to the augmentation of structural features like grain boundaries, dislocation density, interstitial atoms, and surface roughness. To further investigate the beneficial properties of the optimized gold films in the manufacture of a HgCdTe-based infrared detector, the transmission line model pattern (Au/p-HgCdTe) was developed. The contact resistivity(ρ_c) for the thermally-evaporated and e-beam-evaporated Au/p-HgCdTe interfaces is 1.1×10^{-2} Ω cm^2 and 7.3×10^{-3} Ω cm^2, respectively, while the e-beam gold film showed superior Ohmic characteristics when compared to the thermally-evaporated Au/p-HgCdTe interfaces. As a result, the specific contact resistance of e-beam gold film is nearly one order of magnitude lower than that of thermal gold contact. The gold films evaporated by e-beam process at a 12 Å/s evaporation rate hold on well to the HgCdTe substrate and perform well with the photolithography method used for developing infrared detectors. Therefore, the best material to create a stable and repeatable p-Ohmic contact on MCT IR detectors could be e-beam evaporated gold film.

CHAPTER 9

CONCLUSIONS AND RECOMMENDATIONS

The current study used the vacuum evaporation approach to evaporate thin films of CdTe-ZnS (passivation), CdS (window layer), tin/Indium (as ohmic n-contact/detector-ROIC interconnector), and Cr-Au (ohmic p-contact). Therefore, the optimized films were evaporated (after evaluating their properties) using characterization techniques such as X-ray diffraction, atomic force microscopy (AFM), field emission scanning electron microscopy (FESEM), energy-dispersive spectroscopy analysis (EDS), nanoindentation, UV-vis spectrometer, surface profiler (Dektak), ellipsometry, multibeam optical stress sensor (MOSS), microscopy, and non-contact sheet resistance measurement. By establishing a variety of test structures and devices, including cadmium telluride and zinc sulfide films on silicon (configuration: ZnS/CdTe/Si), CdS film on glass, Sn/HgCdTe and In/HgCdTe structure, transfer length method (TLM) structure (configuration: Sn/n/p-HgCdTe and In/n/p-HgCdTe), TLM structure with Au/p-HgCdTe, and metal-insulator-metal (MIM) with the Au-Cr/ZnS/CdTe/Si configuration, the efficacy and usefulness of these optimized films were further investigated. Furthermore, the suitability of the fabricated structures/devices for IR detector, optoelectronic devices, and other semiconductor device fabrication-which may be the corresponding applications of these thin films-was confirmed using the characterization techniques of scanning electron microscopy (SEM), capacitance-voltage (C-V)/current-voltage (I-V) measurements, nanoindentation, and UV-vis spectrophotometer. The following conclusions were drawn:

(i) The combined thin films of CdTe and ZnS on Si substrate was found to be a good engineering approach suitable in photovoltaic and other optoelectronic devices meeting the required structural and mechanical properties. Lattice constant, crystallite size, dislocation density, intrinsic stress, strain and stacking faults of both the thin films were found from XRD data. The compositional analysis by EDX indicated that Te/Cd atomic ratio stoichiometric and S/Zn atomic ratio was less stoichiometric in the grown thin films. The strain rate of ZnS film was determined at a maximum load of 100 μN and creep was determined at loads of 50, 70, 100 μN loads for 20 s. Absence of distortion or cracks due to stress as a consequence of nano-indentation confirms the utilization of vacuum evaporated thins films of ZnS/CdTe for photovoltaic applications.

(ii) Using vacuum evaporation method, deposited the CdTe and ZnS thin films at 1,5, and 10 Ås^{-1} evaporation rates. Among the investigated deposition conditions, an evaporation rate of 1 Å s^{-1} developed the most favorable structural characteristics, as evidenced by improved crystallinity, reduced defect density, and lower microstrain. SEM images showed that CdTe films deposited at 1 Å s^{-1} were continuous, compact, and free from visible surface defects, whereas higher deposition rates of 5 and 10 Å s^{-1} resulted in comparatively less uniform morphologies. Energy-dispersive spectroscopy confirmed near-stoichiometric compositions, although slight Te enrichment was observed in CdTe films deposited at 1 and 10 Å s^{-1}, while ZnS films consistently exhibited a sulfur-

rich composition. MOSS measurements indicated comparatively low compressive residual stress under low-rate deposition, while nanoindentation revealed a decrease in hardness and Young's modulus with increasing deposition rate. No stress-induced cracking or plastic failure was observed under indentation hold loads of 80 μN for CdTe and 90 μN for ZnS, indicating good mechanical stability of the deposited layers. Electrical measurements of CdTe/ZnS MIM structures showed a pronounced reduction in leakage current and dielectric response upon cooling from 300 to 77 K. The corresponding static dielectric constants were 5.22 for CdTe and 7.36 for ZnS, with ZnS exhibiting a comparatively greater suppression of leakage current. Overall, the optimized deposition parameters yielded high-quality CdTe/ZnS thin films with structural, morphological, mechanical, optical, and electrical characteristics fully aligned with performance requirements for advanced photovoltaic and infrared optoelectronic devices.

(iii) Vacuum evaporation method was used to deposit CdS thin films of 200 nm thicknesses on glass substrates at 1, 5 and 10 Å/s deposition rates. XRD examination indicated that the CdS thin films were of hexagonal structure with preferential orientation towards (002) plane for all deposition rates. The crystallite size was decreasing but microstrain and dislocation density were increasing with increasing deposition rates. The SEM micrographs indicated that the films were not discontinuous and uniform coverage over the entire surface without any pin holes or cracks. The EDX elemental analysis showed that the film at 1 Å/s deposition rate was more stoichiometric than the other deposition rates. CdS thin films revealed higher transmittance (~80 %) in visible region and E_g value increase with deposition rate. The hardness of the CdS film rises with increasing deposition rate. The Young's modulus of the CdS film decreases with increasing rate of deposition and becomes almost constant 5-10 Å/s deposition rate. Force displacement curves reveal reverse indentation size effect for CdS thin films. The overall creep and strain rate behavior of CdS film is better at 1 Å/s deposition rate. Thus, overall experimental results of structural, morphological, optical and mechanical characteristics recommend CdS thin film at 1 Å/s deposition rate was having great potential in light emitting diodes, photon devices applications and a window layer for solar cells.

(iv) A comparative study of Sn and In on the n-HgCdTe done based on their crystalline parameters, morphology, composition, topography, adhesion, surface quality and electrical characteristics. The XRD examination confirmed that the films were polycrystalline tetragonal bcc phase along (200) and (101) planes orientation of Sn and In, respectively. From XRD results, the calculated 33.14 nm crystallite size of β-Sn film was of slight small size than the 33.27 nm crystallite size of In film but the microstrain and dislocation density values of indium were lower than β-Sn film. Thus, overall crystalline structure of indium film was better than the tin film. SEM images of β-Sn film shown crack free non-uniform particle size distribution while indium film SEM images indicated a continuous and uniform film over entire surface with a few large micron size particles. The 44 nm rms value and 32 nm average value were of β-Sn film while 20 nm rms value and 15.2 nm average value were of In film. This higher roughness of β-Sn film was be due to non-uniform cluster growth and non-uniform distribution of Sn clusters. Adhesion force and thermodynamic adhesion-work of tin film were nearly double than the indium film. Using TLM

and I-V measurements for various contact geometries, the Sn/n-HgCdTe and In/n-HgCdTe interfaces were electrically examined. The In/n-HgCdTe interface indicated linear I-V characteristics (ohmic behavior) but the Sn/n-HgCdTe interface indicated non-linear I-V characteristics (nearly ohmic behavior). In this instance, the thermionic field emission mechanism controls current transport. The In/n-HgCdTe interface consisted low specific contact resistance, ρ_c = 3 x 10^{-4} Ωcm^2 than the Sn/n-HgCdTe interface specific contact resistance, ρ_c 2 x 10^{-2} Ωcm^2. Compared to tin film, the indium film had lower specific contact resistance and surface adhesion force. Thus, indium film's overall structural, morphological, compositional, topographical, adhesion, ellipsometric and electrical properties were better than tin. Indium was found to be suitable as a good ohmic n-contact in optoelectronic, micro-nano scale electronic devices and HgCdTe-based infrared detectors.

(v) The e-beam evaporated gold film at 12 Å/s on a mercury cadmium telluride (HgCdTe) substrate had the lowest value of dislocation density, residual stress and microstrain indicating the best crystalline structure. In comparison to the thermal gold film (S_q = 5.0 (6 Å/s evaporation rate) and S_q = 3.0 nm (12 Å/s evaporation rate), respectively), the e-beam evaporated films at 6 and 12 Å/s evaporation rate are more pure, homogeneous, extremely dense, and have low surface roughness (S_q = 2.8 and 2.71 nm, respectively), according to the elemental and morphological properties. At an indentation load of 20–50 μN, the e-beam gold film's hardness and Young's modulus were greater than those of the thermal gold film. The strain rate of the thermal and e-beam gold films was calculated and compared using a maximum load of 50 μN. The creep behavior was calculated for 5 seconds using loads of 20, 30, 40, and 50 μN. As evidenced by the absence of pop-in and pop-out during nanoindentation, the e-beam gold film's mechanical properties were improved over the thermal gold film due to the augmentation of structural features like grain boundaries, dislocation density, interstitial atoms, and surface roughness. To further investigate the beneficial properties of the optimized gold films in the development of a HgCdTe-based infrared detector, the transmission line model pattern (Au/p-HgCdTe) was developed. The contact resistivity(ρ_c) for the thermally-evaporated and e-beam-evaporated Au/p-HgCdTe interfaces is 1.1× 10^{-2} Ω cm^2 and 7.3 × 10^{-3} Ω cm^2, respectively, while the e-beam gold film showed superior Ohmic characteristics when compared to the thermally-evaporated Au/p-HgCdTe interfaces. As a result, the specific contact resistance of e-beam gold film is nearly one order of magnitude lower than that of thermal gold contact. The gold films evaporated by e-beam process at a 12 Å/s evaporation rate hold on well to the HgCdTe substrate and perform well with the photolithography method used for developing infrared detectors. Therefore, the best material to create a stable and repeatable p-Ohmic contact on MCT IR detectors could be e-beam evaporated gold film.

Thus, these optimized thin films could be suitable for the development of electro-optic devices, HgCdTe-based IR detectors, and other photovoltaic equipment.

CHAPTER 10

SCOPE OF FUTURE RESEARCH WORK

The sections that follow are some possible directions of development that could be made in the future, taking into account the previously mentioned facts that the produced devices/structures (by using various optimal thin films) might be very useful in the manufacturing of optoelectronic devices, HgCdTe-based IR detectors, and other photovoltaic devices:

- In order to achieve an optimized passivation layer with the desired properties (i.e., a minimum value of surface leakage current/dark current: fixed charge density, oxide charges), a comparative study of CdTe/ZnS passivation layers with different/varying thicknesses can be conducted. Then, by fabricating an MIS structure or device using this passivation film, the effectiveness and usefulness of the optimized passivation layer in IR detector fabrication can be examined.
- One ZnS passivation layer can be grown over the HgCdTe substrate that has received $(NH_4)_2S$ treatment prior to deposition, and the other ZnS passivation layer can be grown over the HgCdTe substrate that has not received $(NH_4)_2S$ treatment. This is the effect of $(NH_4)_2S$ treatment on the characteristics of the ZnS passivation layer. In order to get an optimal passivation layer that would be appropriate in the construction of an HgCdTe-based infrared detector, different characterization techniques can be utilized to assess the properties of both passivation layers.
- To fabricate an In/n-HgCdTe interface (TLM structure) that is ohmic and has a comparatively low specific contact resistance in order to create high-performance infrared detectors (high photocurrent and easy current transmission).
- Examining In-bumps of different thicknesses to determine how thickness affects their characteristics (uniformity, grain size, stress, mismatch of thermal expansion coefficient, flaws, etc.) and how it relates to the performance of IR detectors and other semiconductor devices can be accomplished.
- Examine the characteristics of Cr- Au films with varying thicknesses and annealing to choose the best one to use in the development of an infrared detector, optoelectronic device, and other semiconductor devices.
- High-performance infrared detectors may benefit from the development of an ohmic Au/p-HgCdTe interface with a comparatively low specific contact resistance.
- The formation of high-performance ARC film stacks with dual-band (MWIR and LWIR spectral areas) and multi-band (SWIR, MWIR, and LWIR spectral regions) capabilities.
- The aforementioned thin films can be grown using alternative deposition methods, such as e-beam evaporation, sputtering, and atomic layer deposition to deposit thin films with comparatively good features that could be used to fabricate optoelectronic device, HgCdTe-based infrared detectors, and other semiconductor devices.

REFERENCES

[1] A. Rogalski, HgCdTe infrared detector material: history, status and outlook, Rep. Prog. Phys. 68 (2005) 2267-2336.
[2] C. L. Tan, H. Mohseni, Emerging technologies for high-performance infrared detectors Nanophotonics 7 (2018) 169-197.
[3] A. Rogalski, New material system for third generation infrared photodetectors, Opto-Electron. Rev. 16 (2008) 458-482.
[4] R. K. Bhan, V. Dhar, Recent infrared detector technologies, applications, trends and development of HgCdTe based cooled infrared focal plane arrays and their characterization, Opto-Electron. Rev. 27 (2019) 174-193.
[5] W. Lei, J. Antoszewski, L. Faraone, Progress, challenges, and opportunities for HgCdTe infrared materials and detectors, Appl. Phys. Rev. 2 (2015) 041303.
[6] C. Downs and T. E. Vandervelde, Progress in Infrared photodetectors since 2000, Sensors 13 (2013) 5054-5098.
[7] S. Bianconi and H. Mohseni, Recent advances in infrared imagers: toward thermodynamic and quantum limits of photon sensitivity, Rep. Prog. Phys. 83 (2020) 044101.
[8] B. Chen, Y. Chen and Z. Den, Recent Advances in high speed photodetectors for eSWIR/MWIR/LWIR applications, Photonics 8 (2021) 14.
[9] A. Rogalski, P. Martyniuk, M. Kopytko, W. Hu, Trends in performance limits of the HOT infrared photodetectors. Appl. Sci. 11 (2021) 501.
[10] A. Rogalski, Assessment of HgCdTe photodiodes and quantum well Infrared photoconductors for long wavelength focal plane arrays, Infrared Phys. Technol. 40 (1999) 279-294.
[11] J. Philips, Evaluation of the fundamental properties of quantum dot infrared detectors, J. Appl. Phys. 91 (2002) 4590.
[12] S. B. Hafiz, M. Scimeca, A. Sahu, D. K. Ko, Colloidal quantum dots for thermal infrared sensing and imaging, Nano Converg. 6 (2019) 7.
[13] A. Rogalski, J. Antoszewski, and L. Faraone, Third-generation infrared photodetector arrays, J. Appl. Phys. 105 (2009) 091101.
[14] M. Vaghayenegar, Characterization of HgCdTe and related materials for third generation infrared detectors, PhD thesis, Arizona State University, 2017.
[15]A. Rogalski, Toward third generation HgCdTe infrared detectors, J. Alloys Compd. 371 (2004) 53-57.
[16] M. Kimata, Development of infrared focal plane arrays, Sens. Mater. 30 (2018) 1221-1230.
[17] A. Rogalski, Recent progress in infrared detector technologies, Infrared Phys. Technol. 54 (2011) 136-154.
[18] J. Kenion White, Mid-wave infrared HgCdTe photodiode technology based on plasma induced p-to-n type conversion, PhD thesis, The University of Western Australia, 2005.
[19] A. Singh, V. Srivastav, R. Pal, HgCdTe avalanche photodiodes: A review, Opt. Laser Technol. 43 (2011) 1358-1370.
[20] R. K. Bhan, V. Srivastava, R. S. Saxena, L. Sareen, R. Pal, R. K. Sharma, Improved high resistivity ZnS films on HgCdTe for passivation of infrared devices, Infrared Phys. Technol. 53 (2010) 404-409.
[21]Xiaojie Xu, Siyuan Li, Jiaxin Chen, Sa Cai, Zhenghao Long, Xiaosheng Fang, Design Principles and Material Engineering of ZnS for Optoelectronic Devices and Catalysis, Advanced Functional Materials ,Volume28, Issue36, 2018, 1802029

[22] H A Mohamed, A S Mohamed and H M Ali, Mater. Res. Express, 5, 2018, 056411
[23] Shailendra Kumar Gaur, R. S. Mishra, Thermal Evaporation and microstructure study of CdTe, International Journal of Advance Research and Innovation, Volume 3, Issue 2 (2015) 440-445
[24] Shailendra Kumar Gaur, Ajay Kumar Saini, Vijay Singh Meena, B. L. Sharma, Modeling & Simulation of Thermal Evaporated CdTe Thin Film, The Physics of Semiconductor Devices, Springer Proceedings in Physics 215,
[25] S.I. Asiya, Kaushik Pal, Gharieb S. El-Sayyad, M. Abd Elkodous,Catherine Demetriades , Samo Kralj, Sabu Thomas, Reliable optoelectronic switchable device implementation by CdS nanowires conjugated bent-core liquid crystal matrix, Organic Electronics, Volume 82, 2020, 105592
[26] Dharmadasa, I.M., Ojo, A.A. Unravelling complex nature of CdS/CdTe based thin film solar cells. J Mater Sci: Mater Electron 28, 16598–16617 (2017).

[27] Westwood, William D. "Sputter Deposition", AVS Education Committee Book Series, AVS Vol. 2 (2003).
[28] Markus Back, Investigation of the properties of thin films grown via sputtering and resistive thermal evaporation, Uppsala University, [2015]
[29] M. Lorenz, R. MSR. 25 years of pulsed laser deposition. J. Phys. D. Appl. Phys.; 47:030301–030303, 2014.
[30] D. Lowndes, D. Geoghegan, P.AA Rouleau CM. Synthesis of novel thin film materials by pulsed laser deposition. Science; 273(5277):898–903, 1996
[31] Olayinka Oluwatosin Abegunde, Esther Titilayo Akinlabi, Oluseyi Philip Oladijo, Stephen Akinlabi, Albert Uchenna Ude. Overview of thin film deposition techniques, AIMS Materials Science, 2019, 6(2): 174-199.
[32] P. A. Savale, Physical Vapor Deposition (PVD) Methods for Synthesis of Thin Films: A Comparative Study, Archives of Applied Science Research, 8 (5):1-8, 2016
[33] Flow of a Viscous Liquid on a Rotating Disk, E. G. Alfred et al., J. Appl. Phys. (29), 858–862 (1958).
[34] Characteristics of resist films produced by spinning, D. Meyerhofer, J. Appl. Phys. (49), 3993–3997 (1978).
[35] Graniel O, Weber M, Balme S, et al. (2018) Atomic layer deposition for biosensing applications. Biosens Bioelectron 122: 147–159.
[36] Suntola T, Antson J (1977) Method for producing compound thin films. U.S. Patent 4,058,430.
[37] Guo HC, Ye E, Li Z, et al. (2017) Recent progress of atomic layer deposition on polymeric materials. Mat Sci Eng C-Mater 70: 1182–1191.
[38] Yagi, K. Kakizawa, K. Murakami and S. Kaneko, J. Ceram. Soc. Jap., 102 (1994)
[39] A. I. Y. Tok , F.Y. C. Boey, X. L Zhao, Journal of Materials Processing Technology 178, 270, 2006.
[40] Brinker CJ, Scherer GW. Sol-Gel Science. San Diego: Academic Press; 1990.
[41] C. L. Tan, H. Mohseni, Emerging technologies for high performance infrared detectors Nanophotonics 7 (2018) 169-197.
[42] W. Lei, J. Antoszewski, L. Faraone, Progress, challenges, and opportunities for HgCdTe infrared materials and detectors, Appl. Phys. Rev. 2 (2015) 041303.
[43] C. Downs and T. E. Vandervelde, Progress in Infrared photodetectors since 2000, Sensors 13 (2013) 5054-5098.
[44] J. Kenion White, Mid-wave infrared HgCdTe photodiode technology based on plasma induced p-to-n type conversion, PhD thesis, The University of Western Australia, 2005.

[45]Xiaojie Xu, Siyuan Li, Jiaxin Chen, Sa Cai, Zhenghao Long, Xiaosheng Fang, Design Principles and Material Engineering of ZnS for Optoelectronic Devices and Catalysis, Advanced Functional Materials ,Volume 28, Issue36, 2018, 1802029
[46] H A Mohamed, A S Mohamed and H M Ali, Mater. Res. Express, 5, 2018, 056411
[47] S.I. Asiya, Kaushik Pal, Gharieb S. El-Sayyad, M. Abd Elkodous,Catherine Demetriades , Samo Kralj, Sabu Thomas, Reliable optoelectronic switchable device implementation by CdS nanowires conjugated bent-core liquid crystal matrix, Organic Electronics, Volume 82, 2020, 105592
[48] Dharmadasa, I.M., Ojo, A.A. Unravelling complex nature of CdS/CdTe based thin film solar cells. J Mater Sci: Mater Electron 28, 16598–16617 (2017).
[49] S. Yan, Z. Xiao, Toward the Development of CdS Nanowires Synthesis and Application, Nanoscience & Nanotechnology-Asia, 1 (2011) 171-176.
[50**]** Shailendra Kumar Gaur, Qasim Murtaza, R.S. Mishra, Study of CdS Thin Film's Structural, Morphological, and Mechanical Properties, Recent advances in mechanical engineering, proc. ICMET 2023, Springer
[51]Nafiseh Memarian, Seyeed Mohammad Rozati ,Isabella Concina andAlberto Vomiero, Deposition of Nanostructured CdS Thin Films by Thermal Evaporation Method: Effect of Substrate Temperature, Materials 2017, 10(7), 773
[52] Laura Aislinn Carrasco-Chavez , José F. Rubio-Valle, Abimael Jiménez-Pérez, José E. Martín-Alfonso, andAmanda Carrillo-Castillo, Study of CdS/CdS Nanoparticles Thin Films Deposited by Soft Chemistry for Optoelectronic Applications, Micromachines 2023, 14(6), 1168
[53] Jaber AY, Alamri SN, Aida MS. CdS thin films growth by ammonia free chemical bath deposition technique. Thin Solid Films 2012;520:3485–9
[54] Salah Abdul-Jabbar Jassim, Abubaker A. Rashid Ali Zumaila, Gassan Abdella Ali Al Waly, Influence of substrate temperature on the structural, optical and electrical properties of CdS thin films deposited by thermal evaporation, Results in Physics,Volume 3, 2013, 173-178
[55] A. Rogalski, Infrared detectors: status and trends, Prog. Quantum Electron. 27 (2003) 59-210.
[56] J. A. Montoya, Z. B. Tian, S. Krishna, and W. J. Padilla, Ultra-thin infrared metamaterial detector for multicolor imaging applications, Opt. Express 25 (2017) 23345-23355.
[57] P. W. Leech, G. K. Reeves, Specific contact resistance of indium ohmic contacts to n-type $Hg_{1-x}Cd_xTe$, J. Vac. Sci. Technol. A 10 (1992) 105.
[58] J. Jiang, S. Tsao, T. O"Sullivan, M. Razeghi, G. J. Brown, Fabrication of indium bumps for hybrid infrared focal plane array applications, Infrared Phys. Technol. 45 (2004) 143-151.
[59] T. V. Blank and Y. A. Goldberg, Mechanisms of current flow in metal-semiconductor Ohmic Contacts, Semiconductors 41 (2007) 1263-1292.
[60] Shailendra Kumar Gaur, Qasim Murtaza, R.S. Mishra. Experimental Investigation of Thermally Grown Indium Film's Structural and Tribological Properties. Journal of Polymer & Composites. 2023; 11(Special Issue 12):S58–S66.
[61] Shailendra Kumar Gaur, R. S. Mishra, Thermal Evaporation- Modeling and Microstructure Studies of Indium and Tin Deposition, International Journal of Advance Research and Innovation, Volume 3, Issue 1 (2015) 207-215
[62] W. A. Beck, G. D. Davis, and A. C. Goldberg, Resistance and 1/f noise of Au, Al, and Ge contacts to (HgCd)Te, J. Appl. Phys. 67 (1990) 6340.
[63] Titu-Marius I. Băjenescu, Infrared detectors, J. Eng. Sci. XXV (3), (2018) 29-40.

[64] R. S. Mishra , Shailendra Kumar Gaur, Modeling &Simulation of Nano film thickness of Gold deposited by Thermal Evaporation Process (TEP), International Journal of Advance Research and Innovation, Volume 2 (2014) 505-510
[65] Suha. A. Fadaam, M.H.Mustafa, Ali Hussien,A. Alrazak, Aliyah A.. Shihab, "Enhanced efficiency of CdTe Photovoltaic by thermal evaporation Vacuum, Energy Procedia 157 (2019) 635–643
[66] Iman H. Khudayer, Bushra H. Hussein, Mohammed Hamid," Depending the Structure and Optical Properties of Cadmium Telluride Films on Doping Process, Al-Mustansiriyah Journal of Science, Volume 29, Issue 1, 2018
[67] Manal A. Mahdy , E.A. Mahmoud , Iman A. Mahdy," Linear and nonlinear optical response dependency on the crystallite size of CdTe and its structural properties, Surfaces and Interfaces 23 (2021) 100974
[68] Fatemeh Hosseini Siyanaki, Hamid Rezagholipour Dizaji, Mohammad Hosein Ehsani, Shiva Khorramabadi, The Effect of Changing the Vapor Flux on Physical Properties of Nanocrystaline CdTe Thin Film, Prepared by Thermal Evaporation Method, Advanced Materials Research Vol. 829 (2014) pp 492-496
[69] Melissa Mathews, Liping Guo, Xiao Han, Swapnil Saurav, Guozhong Xing, Lin Li, and Feng Yan, Local mechanical and electrical behavior in CdTe thin film solar cells revealed by scanning probe microscopy, AIP Advances 9, 085108 (2019
[70] G. Purceka, E. Bacaksızb, IMiskiogluc Karadeniz, Structure and nanomechanical properties of CdTe thin films, journal of materials processing technology 198 (2008) 202–206
[71] Felicia S. Manciu, Jessica G. Salazar, Aryzbe Diaz, Stella A. Quinones, Spectroscopic, microscopic, and internal stress analysis in cadmium telluride grown by close-space sublimation, Thin Solid Films 589 (2015) 298–302
[72] F. Sizov, M. Vuichyk, K. Svezhentsova , Z. Tsybrii, S. Stariy, M. Smolii, CdTe thin films as protective surface passivation to HgCdTe layers for the IR and THz detectors, Materials Science in Semiconductor Processing 124 (2021) 105577
[73] J. K. White, C. A. Musca, H. C. Lee, L. Faraone, Hydrogenation of ZnS passivation on narrow-band gap HgCdTe, Appl. Phys. Lett. 76 (2000) 2448-2450.
[74] I. Madni, Characterization of MBE-grown HgCdTe and related II-VI materials for next generation infrared detectors, PhD thesis, The University of Western Australia, 2017.
[75] J. K. White, J. Antoszewski, R. Pal, C. A. Musca, J. M. Dell, L. Faraone, and J. Piotrowski, Passivation effects on reactive-ion-etch-formed n-on-p junctions in HgCdTe, J. Electron. Mater. 31 (2002) 743-748.
[76] Q. Lu, X. Wang, S. Zhou, R. Ding, L. He and C. Lin, Effects of different passivation layers on RV characteristics of long-wave HgCdTe gate controlled diodes, Semicond. Sci. Technol. 35 (2020) 095003.
[77] F. S. Juang, Y. K. Su, S. J. Chang, S. M. Chang, F. S. Shu, C. D. Chiang, Y. T. Cherng, and T. P. Sun, Dark Currents in HgCdTe Photodiodes Passivated with ZnS/CdS, J. Electrochem. Soc. 146 (1999) 1540-1545.
[78] Xiaodong Li, Xinnan Wang, Qihua Xiong, and Peter C. Eklund, Mechanical Properties of ZnS Nanobelts, Nano Lett., Vol. 5, No. 10, 2005
[79] Iqbal S.Naji, Iman H.Khdyaer, Hanaa I. Mohammed, "The Effect of Annealing Temperature on the Optical Properties of CdS and CdS:Al Thin Films, International Journal of Application or Innovation in Engineering & Management, Volume 2, Issue 6, June 2013

[80] M. S. Kale, Y. R. Toda, M. P. Bhole and D. S. Bhavsar, “Structural, Optical and Thermo Electrical Properties of Nanostructured Vacuum Evaporated CdS Thin Films”, Electron. Mater. Lett., Vol. 10, No. 1 (2014), pp. 21-25
[81 Shafi Ullah , Amal Bouich , Hanif Ullah , Bernab´e Mari, Miguel Mollar, “Comparative study of binary cadmium sulfide (CdS) and tin disulfide (SnS_2) thin buffer layers, Solar Energy 208 (2020) 637–642
[82] Binbin Weng, Jijun Qiu, Lihua Zhao, Caleb Chang, and Zhisheng Shi, “CdS/PbSe heterojunction for high temperature mid-infrared photovoltaic detector applications, Applied Physics Letters 104, 121111 (2014)
[83] Obi Kingsley Echendu, Francis Birhanu Dejene,1 Imyhamy Mudiy Dharmadasa and Francis Chukwuemeka Eze, “Characteristics of Nanocrystallite-CdS Produced by Low-Cost Electrochemical Technique for Thin Film Photovoltaic Application: The Influence of Deposition Voltage, Hindawi International Journal of Photoenergy, Volume 2017, Article ID 3989432, 13 pages
[84] Vamsi Borra, Daniel Georgiev, Coery R. Grice, ‘Fabrication of Optically Smooth Sn Thin Films, Thin Solid Flms 616(2016) 311-315
[85] T. Rerek, L. Skowronski, R. Szczesny, M.K. Naparty, B. Derkowska-Zielinsk, ‘The effect of the deposition rate on microstructural and opto-electronic properties of β-Sn layers”, Thin Solid Films 670 (2019) 86–92
[86] Patrick W. Leech, The specific contact resistance of Ohmic contacts to HgTe/$Hg_{1-x}Cd_xTe$ heterostructures, Journal of Applied Physics 68, 907 (1990)
[87] P. Kozłowski, K. Czuba , K. Chmielewski , J. Ratajczak, J. Branas, A. Korczyc, K. Regi´nski and A. Jasik, Indium-based micro-bump array fabrication technology with added pre-reflow wet etching and annealing, Materials 14 (2021) 6269.
[88] Q. Huang, G. Xu, Y. Yuan, X. Cheng and L. Luo, Development of indium bumping technology through AZ9260 resist electroplating, J. Micromech. Microeng. 20 (2010) 055035.
[89] S. Nozaki and A. G. Milnes, Specific contact resistivity of indium contacts to n - type CdTe, J. Electron. Mater. 14 (1985) 137-155.
[90] Z. Tsybrii, Y. Bezsmolnyy, K. Svezhentsova, M. Vuichyk, I. Lysiuk, M. Apatska, M. Smolii, N. Dmytruk, S. Bunchuk, K. Andreeva, F. Sizov, HgCdTe/CdZnTe LPE epitaxial layers: from material growth to applications in devices, J. Cryst. Growth 529 (2020) 125295.
[91] V. Srivastav, R. Pal, B. L. Sharma, V. Mittal, V. Gopal, and H. P. Vyas, Electrical properties of titanium-HgCdTe contacts, J. Electron. Mater. 34 (2005) 225-231.
[92] A. Singh, A. K. Shukla, S. Jain, B. S. Yadav, R. Pal, Electrical characteristics of electroless gold contacts on p-type $Hg_{1-x}Cd_xTe$, Mater. Sci. Semicond. Process. 26 (2014) 294-300.
[93] V. Krishnamurthy, A. Simmons, C. R. Helms, Oxide interfacial layers in Au ohmic contacts to p-type $Hg_{1-x}Cd_x$ Te, Appl. Phys. Lett. 56 (1990) 925.
[94] F. Sizov, Z. Tsybrii, M. Apats'ka, N. Dmytruk, V. Slipokurov, S. Bunchuk, Yu Bezsmolnyy, V. Popovych, M. Wiertel and N. Mikhailov, Ohmic metal/$Hg_{1-x}Cd_xTe$ ($x \approx 0.3$) contacts, Semicond. Sci. Technol. 35 (2020) 125030

[95] R. Nokhwal, V. Srivastav, A. Goyal, B. L. Sharma, S. A. Hashmi, and R. K. Sharma, Surface Studies on HgCdTe Using Non-aqueous Iodine-Based Polishing Solution, J. Electron. Mater. 46 (2017) 6795-6803.

[96] Yong-Chul Jung, Seok-Jin Yoon, Sang-Hee Suh, Jin-Sang Kim, The effect of ammonium sulfide treatment on interfacial properties in ZnS/HgCdTe heterostructure, J. Electroceram. 17(2006) 1041-1045.

[97] Comparison of Tin and Indium Thin Film's Structural, Morphological, Adhesion, and Electrical Properties for Ohmic Contact in HgCdTe-Based Infrared Detectors, Shailendra Kumar Gaur, Qasim Murtaza, R.S. Mishra, Journal of Materials Engineering and Performance 34 (2025) 18502–18515.

[98] J. Sun, L. Fu, Z. Nie, Y. Shi, L. Yapeng, The effect of chemical polishing on the interface structure and electrical property of Au/$Cd_{0.9}$ $Zn_{0.1}$Te contact, Appl. Phys. A 115 (2013) 1309-1316.

[99] Analysis of structural, morphological and nano-mechanical properties of vacuum evaporated nanoscale CdTe and ZnS films, Shailendra Kumar Gaur, Qasim Murtaza, R.S. Mishra, Optical Materials 154 (2024) 115764

[100] Comparative analysis of thermally evaporated nanoscale CdS thin film's structural, morphological, optical and nanomechanical properties, Shailendra Kumar Gaur, Ashwani Chaudhary, Qasim Murtaza, R.S. Mishra, Journal of Molecular Structure 154 (2024) 115764

[101] K. Priya, V.K. Ashith, G.K. Rao, G. Sanjeev, A comparative study of structural, optical and electrical properties of ZnS thin films obtained by thermal evaporation and SILAR techniques, Ceram. Int. 43 (2017) 10487–10493.

[102] C.H. Sun, P. Zhang, T.N. Zhang, X. Chen, Y.Y. Chen, Z.H. Ye, ZnS thin films grown by atomic layer deposition on GaAs and HgCdTe substrates at very low temperature, Infrared Phys. Technol. 85 (2017) 280–286.

[103] N. Bouguila, D. Bchiri, M. Kraini, A. Timoumi, I. Halidou, K. Khirouni, S. Alaya, Structural, morphological and optical properties of annealed ZnS thin films deposited by spray technique, J. Mater. Sci. Mater. Electron. 26 (2015) 9845–9852.

[104] J. Jiang, S. Tsao, T. O"Sullivan, M. Razeghi, G. J. Brown, Fabrication of indium bumps for hybrid infrared focal plane array applications, Infrared Phys.Technol.45 (2004) 143–151.

[105] Q. Huang, G. Xu, Y. Yuan, X. Cheng and L. Luo, Development of indium bumping technology through AZ9260 resist electroplating, J. Micromech. Microeng. 20 (2010) 055035.

[106] B.K. Kim, T.H. Kim, D.H. Choi, H. Kim, K. Watanabe, T. Taniguchi, H. Rho, J.J. Kim, Y.H. Kim and M.H. Bae, Origins of genuine Ohmic van der Waals contact between indium and MoS_2, NPJ 2D Mater. Appl. 5 (2021) 9.

[107] Y. Tang, Jia Jia, H. Qiao, Y. Zhang, X. Li, Application of Au/Sn in the formation of p-HgCdTe photoconductive detectors electrodes, 6th International Symposium on Advanced Optical Manufacturing and Testing Technologies: Optoelectronic Materials and Devices for Sensing, Imaging, and Solar Energy, Proc. of SPIE, 8419 (2012) 84190Z.

[108] Z. Tsybrii, Y. Bezsmolnyy, K. Svezhentsova, M. Vuichyk, I. Lysiuk, M. Apatska, M. Smolii, N. Dmytruk, S. Bunchuk, K. Andreeva, F. Sizov, HgCdTe/CdZnTe LPE epitaxial layers: from material growth to applications in devices, J. Cryst. Growth 529 (2019) 125295.

[109] G. Bahir, R. Adar, and R. Fastow, The electrical properties of metal contact Au and Ti on p type HgCdTe, J. Vac. Sci. Technol. B 9 (1991) 266.

[110] Y. Matsuoka, S. Mathonneire, S. Peters, and W. T. Masselink, Broadband multilayer anti-reflection coating for mid-infrared range from 7 μm to 12 μm, Appl. Opt. 57 (2018) 1645-1649.

[111] M. Gholampour, A. Miri, S. I. Karanian and A. Mohammadi, Design and fabrication of multi-layers infrared anti-reflection nanostructure on ZnS substrate, Acta Phys. Pol. A 136 (2019) 527-530.

[112] M. B. Kala, P. K. Bandyopadhyay, B. B. Nautiyal, Thorium free anti-reflection coating in MWIR region on silicon optics, Infrared Phys. Technol. 55 (2012) 409-411.

[113] A. Behranvand, M. D. Darareh, M. Jannesari, M. Mahdavi, Design and fabrication of PbTe/BaF2 hydrophobic high-efficiency broad-band anti-reflection coating on Ge substrate in long-wave infrared region, Infrared Phys. Technol. 92 (2018) 163-165.

[114] F. Lemarquis, G. Marchand, and C. Amra, Design and manufacture of low-absorption ZnS–YF3 anti-reflection coatings in the 3.5-16 μm spectral range, Appl. Opt. 37 (1998) 4239-4244.

[115] D. Suthar, S. Chuhadiya, R. Sharma, Himanshu and M. S. Dhaka, An overview on the role of ZnTe as an efficient interface in CdTe thin film solar cells: a review, Mater. Adv. 3 (2022) 8081.

[116] P. Rahi, Challenges in PVD technique (Thin film formation by thermal evaporation), Int. J. Adv. Res. Dev. 2 (2017) 30-37.

[117] J. T. Gudmundsson, A. Anders, and A. von Keudell, Foundations of physical vapor deposition with plasma assistance, Plasma Sources Sci. Technol. 31 (2022) 083001.

[118] O. O. Abegunde, E. T. Akinlabi, O. P. Oladijo, S. A. and A. U. Ude, Overview of thin film deposition techniques, AIMS Mater. Sci. 6 (2019) 174–199.

[119] P. A. Savale, Physical Vapor Deposition (PVD) Methods for Synthesis of Thin Films: A Comparative Study, Arch. Appl. Sci. Res. 8 (2016) 1-8.

[120] A.V. Rajgure, Synthesis and characterization of nanocrystalline ZnO gas sensor, PhD thesis, Solapur University, India, 2014.

[121] A. A. Bunaciu, E. G. Udristioiu, and H.Y. Aboul-Enein, X-Ray diffraction: Instrumentation and applications, Crit. Rev. Anal. Chem. 45 (2015) 289–299.

[122] D. G. Diso, Research and development of CdTe based thin film PV solar cells, PhD thesis, Sheffield Hallam University, 2011.

[123] A. K. Ghatage, S. G. Kanitkar, Characterization of materials by X-Ray diffraction, Int. J. Eng. Res. Technol. 8 (2019).

[124]Binnig, G.; Quate, C. F.; Gerber, Ch. (1986). "Atomic Force Microscope". Physical Review Letters. 56 (9): 930–933.

[125] J. A. Last, P. Russell, P. F. Nealey, and C. J. Murphy, The Applications of atomic force microscopy to vision science, Invest. Ophthalmol. Vis. Sci. 51 (2010) 6083–6094.

[126] K. W. Shinato, F. H. and Y. Jin, Principle and application of atomic force microscopy (AFM) for nanoscale investigation of metal corrosion, Corros. Rev.38 (2020) 423–432.

[127] M. Joshi, A. Bhattacharyya, S.W. Ali, Characterization techniques for nanotechnology applications in textiles, Indian J. Fibre Text. Res. 33(2008) 304-317.

[128] G.M. Pharr, Measurement of mechanical properties by ultra-low load indentation, Materials Science and Engineering: A, Volume 253, Issues 1–2, 1998, 151-159

[129] W.C. Oliver, G.M. Pharr, J. Mat. Res. 7, 1992, 154-1583

[130] William D. Nix, Elastic and plastic properties of thin films on substrates: nanoindentation techniques, Materials Science and Engineering A234-236 (1997) 37744

[131] Oliver, W. C., and Pharr, G. M., J. Mater. Res. (2004) 19, 3-20

[132]Bhushan, B., In Handbook of Micro/Nano Tribology, Bhushan, B., (ed.) CRC Press, Boca Raton, Florida (1999), 433

[133] Fischer-Cripps, A. C., Mater. Sci. Eng. A (2004) 385, 74

[134] Johnson, K. L., Contact Mechanics, Cambridge University Press, UK (1985)

[135]Anthony C. Fischer-Cripps, Nanoindentation, Third Edition, Springer

[136] J. Zhang, A Fundamental study of interface effects in HgCdTe materials and devices, PhD thesis, The University of Western Australia, 2015.

[137] A. K. Saini, V. Srivastav, S. Gupta, B. L. Sharma, M. Asthania, N. Singh, S. K. Gaur, V. S. Meena, R. Thakur, Chanchal, V. Sharma, R. K. Sharma, Improvement of electrical properties of ZnS/CdTe-HgCdTe interface by $(NH_4)_2S$ treatment, Infrared Phys. Technol. 102 (2019) 102988.

[138] Cole, Kenneth; Levine, Barry S. (2020), Levine, Barry S.; Kerrigan, Sarah (eds.), "Ultraviolet–Visible Spectrophotometry", Principles of Forensic Toxicology, Cham: Springer International Publishing, pp. 127–134,

[139] Vitha, Mark F. (2018). "Chapter 2". Spectroscopy: principles and instrumentation. Hoboken, NJ: John Wiley & Sons. I

[140] John C.; Tranter, George E.; Koppenaal, David W. (eds.), Encyclopedia of Spectroscopy and Spectrometry (Third Edition), Oxford: Academic Press,(2017) pp. 511–519,

[141] R. S. Drago (1992). Physical Methods for Chemists, 2nd Edition. W. B. Saunders. ISBN 0-03-075176-4.

[142] Skoog, Douglas A.; Holler, F. James; Crouch, Stanley R. (2007). Principles of Instrumental Analysis (6th ed.). Belmont, CA: Thomson Brooks/Cole. pp. 169–173. ISBN 978-0-495-01201-6.

[143] L. Z. Maulana, K. Megasari, E. Suharyadi, R. Anugraha, K. Abraha and I. Santoso, Inexpensive home-made single wavelength ellipsometer (□ = 633 nm) for measuring the optical constant of nanostructured materials, IOP Conf. Ser.: Mater. Sci. Eng. 202 (2017) 012031.

[144] Ronald R. Willey, Practical Production of Optical Thin Films, 5th edition, Willey optical, consultants 2016

[145] J. A. Floro, E. Chason and S. R. Lee, “Real Time Measurement of Epilayer Strain Using a Simplified Wafer Curvature Technique,” Materials Research Society Symposium Proceedings Vol. 406, 1996, pp. 491-496

[146] G. G. Stoney. "The Tension of Metallic Films Deposited by Electrolysis." P. Roy. Soc. Lond. A-Conta. 82 (553): 172-175, (1909)

[147] Yinghong Zhou1, Zhiliang Wu1, Nian Cai1, Daohua Zhan, Shaoqiu Xu, Meiyun Chen, Guang Zhou, Han Wang, A High-Precision Multi-Beam Optical Measurement Method for Cylindrical Surface Profile, Micromachines 2023, 14(8), 1555

[148] A. Piegari and E. Masetti, Thin film thickness measurement: A comparison of various techniques, Thin Solid Films 124 (1985) 249-257.

[149] B. J. Mrstik, P. J. McMarr, J. R. Blanco, J. M. Bennett, Measurement of the thickness and optical properties of thermal oxides of Si using spectroscopic ellipsometry and stylus profilometry, J. Electrochem. Soc. 138 (1991) 1770-1778.

[150] I. Madni, Characterization of MBE-grown HgCdTe and related II-VI materials for next generation infrared detectors, PhD thesis, The University of Western Australia, 2017.

[151] M. B. Dowell, C. A. Hultman, and G. M. Rosenblatt, Determination of slopes of microscopic surface features by Nomarski polarization interferometry, Rev. Sci. Instrum. 48 (1977) 1491.

[152] W. Wejgaard and V. S. Tomar, Contactless measurement of electrical resistivity by eddy current methods: discussion and a new technique, J. Phys. E: Sci. Instrum.7 (1974) 395.

[153] J. García-Martín, J. Gómez-Gil and E. Vázquez-Sánchez, Non-destructive techniques based on eddy current testing, Sensors 11(2011) 2525-2565

[154] K. Mahmood, Jolly Jacob, R. Zahra, A. Ail, U. Rehman, A. Ashfaq, W. Ahmed , N. Amin, M.I. Arshad, Kashif Javaid, S. Ikram, M. Ajaz un Nabi, S. Hussain, Yuyi Feng, Thermoelectric properties of Zn_2 GeO_4 nano-crystals grown on ITO and Au coated Si substrates by thermal evaporation, Ceramics International 45 (2019) 18333–18337

[155] Jolly Jacob , Hafiz T. Ali, A. Ali, Khurram Mehboob , Arslan Ashfaq , Salma Ikram,U. Rehman, K. Mahmood, Nasir Amin, Improvement of thermoelectric properties of sol gel grown $Cu_2Zn_{1-x}SnS_4$ thin films with the incorporation of Cd atoms, Materials Science in Semiconductor Processing 123 (2021) 105587

[156] Sofia Tahir, Arslan Ashfaq, Shammas Mushtaq, Muhammad Haneef, Rania Saleh Alqurashi, Elsammani Ali Shokralla, Michael M. Sabugaa, Rasmiah S. Almufarij, Ubaid ur Rehman, Ruy Sebastian Bonilla, Performance Optimization of Inorganic Cs_2TiBr_6 Based Perovskite Solar Cell via Numerical Simulation, Energy Technology, 11 (2023), 8, 2300359

[157] Ubaid ur Rehman, Khalid Mahmood, Arslan Ashfaq a, Adnan Ali a, Sofia Tahir, Salma Ikram, Abdul Rehman a, Kashaf ul Sahar b, Waqas Ahmad a, Nasir Amin, Enhanced thermoelectric performance of

hydrothermally synthesized $CuFeS_2$ nanostructures by controlling the Cu/Fe ratio, Materials Chemistry and Physics 279 (2022) 125765
[158] Sofia Tahir, Rabia Saeed, Arslan Ashfaq, Adnan Ali, Khalid Mehmood, Nouf Almousa, Elsammani Ali Shokralla, Romulo R. Macadangdang Jr., Anastasia H. Soeriyadi, Ruy Sebastian Bonilla, Optical modeling and characterization of bifacial SiN_x /AlO_x dielectric layers for surface passivation and antireflection in PERC, Prog Photovolt Res Appl. 32 (2024) 63–72
[159] Syed Asfar Ahmad Jafri, Rasmiah S. Almufarij, Arslan Ashfaq, Rania Saleh Alqurashi, Lamiaa G. Alharbe, A.R. Abd-Elwahed, O.A. Albeydani, Emaan Alsubhe, S.M. Alghamdi, Salhah Hamed Alrefaee, Ahmed H. Ragab, Abeer A. Hassan, Enhancing photovoltaic efficiency: Integrating graphene and advanced interface layers to reduce the recombination losses in lead-free $MASnI_3$ perovskite solar cells, Solar Energy 270 (2024) 112391
[160] Shammas Mushtaq, Sofia Akbar Tahir, Arslan Ashfaq, Waqas Ahmad, Adnan Baig, Ubaidur Rehman, Rabis Saeed, M. Haneef, Kainat Shabbir and Khushi Muhammad Khan, 'Effect of ammonia on the structural, morphological and optical properties of nanocrystalline ZnS thin film' , Optik, vol. 261 (2022) 169088
[161] Iosif-Daniel Simandan, Florinel Sava, Angel-Theodor Buruiana, Ion Burducea, Nicu Becherescu, Claudia Mihai, Alin Velea and Aurelian-Catalin Galca ,' The Effect of the Deposition Method on the Structural and Optical Properties of ZnS Thin Films ' , Coatings (2021) 11, 1064
[162] C.Doroody, K.S. Rahman, H.N. Rosly, M.N. Harif, K.Sopian, S.F. Abdullah, N. Amin, A comprehensive comparative study of CdTe thin films grown on ultrathin glass substrates by close-spaced sublimation and RF magnetron sputtering, Materials Letters 293(2021) 129655
[163] Melissa Mathews, Liping Guo, Xiao Han, Swapnil Saurav, Guozhong Xing, Lin Li and Feng Yan, Local mechanical and electrical behavior in CdTe thin film solar cells revealed by scanning probe microscopy, AIP Advances 9, 085108 (2019)
[164] Tomota Nagaura, Hoang-Phung Phan, Victor Malgras, Tuan-Anh Pham, Hyunsoo Lim, Aditya Ashok, Jeonghun Kim, Jungmok You, Nam-Trung Nguyen, Jongbeom Na and Yuskuke Yamauchi, ' Universal Electrochemical Synthesis of Mesoporous Chalcogenide Semiconductors : Mesoporous CdSe and CdTe Thin films for Optoelectronic Applications ' , Angew. Chem. Int. Ed. 10.1002/anie.202013541
[165] Felicia S. Manciu, Jessica G. Salazar, Aryzbe Diaz and Stella A. Quinones, 'Spectroscopic, microscopic, and internal stress analysis in cadmium telluride grown by close-space sublimation ', Thin Solid Films 589 (2015) 298-302
[166] K.A.M.H. Siddiquee, M.A.K. Pathan, S. Alam, O. Islam and M.R. Qadir, ' Investigation of CdS and CdTe thin films and influence of $CdCl_2$ on CdTe/CdS ' , Optik 124 (2013) 4383-4388
[167] G. Purcek, E. Bacaksiz and I. Miskioglu, 'Structure and nanomechanical properties of CdTe thin films', Journal of Materials Processing Technology, 198 (2008) 202-206
[168] Suha A. Fadaam , Mohamed Hamid Mustafa , Ali Hussein , Abd. Alrazak and Aliyah A. Sahihab,' Enhanced efficiency of CdTe Photovoltaic by thermal evaporation vacuum ', Energy Procedia, 157 (2019) 635-643
[169] Manal A. Mahdy, E.A. Mahmoud, Iman A. Mahdy, ' Linear and nonlinear optical response dependency on the crystallite size of CdTe and its strucutural properties', Surfaces and Interfaces 23 (2021) 100974
[170] Fatemeh Hosseini siyanaki, Hamid Rezaghoipour Dizaji, Mohammad Hosein Ehsani and Shiva Khorrambadi,'The Effect of Changing the Vapor Flux on Physical Properties of Nanocrystaline CdTe Thin Film, Prepared by Thermal Evaporation Method',Advanced Materials Research Vol. 829 (2014) 42-496

[171] Zinoviia Tsybrii, Mykola Vuichyk, Kateryna Svezhetsova, Mariia smolii, Yuri Gomeniuk, Alexei Nazarov and Fedir Sizov, ‘ Low-temperature growth of CdTe thin films as passivation layers for IR and THz functional elements ‘ , Materials Chemistry and Physics, vol. 278 (2022) 125581
[172] Xiutao Yang, Chuiyu Li, Jiayi Wang, Biao Zhou, Sen Lin, Shenghui Xie, Bing Li, Jinguan Zhang, Lili Wu, Wei Li, Dewei Zhao, Lianghuan Feng, Guanggen Zeng, Xia Hao and Smagul Karazhanov,‘Investigation of the surface and Interfacial Properties of Polycrystalline CdTe/Monocrystalline Si Structure ‘ , Journal of Electronic Materials, vol. 51 (2022) 4378-4387
[173] V.K. Ashith, K. Priya and Gowrish K. Rao,’ The electrical properties of n-CdS/p-CdTe and n-ZnS/p-CdTe heterojunctions fabricated by a combination of SILAR and vacuum deposition techniques ‘ , Physica B : Physics of Condensed Matter , vol. 614 (2021) 413025
[174] O.Tomaa, L. Lona, S. Lftimiea, V.A. Antohea, A.Radua, A.M. Radutaa, D. Manicaa and S.Antohe,’ Physical properties of fr-sputtered ZnS and ZnSe thin films used for double heterojunction ZnS/ZnSe/CdTe photovoltaic structures’ , Journal of Applied Surface Science 478 (2019) 831839
[175] Gitashri Arandhara, Jyotimoni Bora, P.K. Saikia, Effect of pH on the crystallite size, elastic properties and morphology of nanostructured ZnS thin films prepared by chemical bath deposition technique, Journal of Materials Chemistry and Physics http://doi.org/10.1016/j.matchemphys.2019.12227722
[176] Yue Wu, Haofei Wu, Yue Zhao, Guangyu Jiang, Jiangtao Shi, Chunjiang Guo, Pan Liu, Zhijian Jin, Metastable structures with composition fluctuation in cuprate superconducting films grown by transient liquid-phase assisted ultra-fast heteroepitaxy, Materials Today Nano 24 (2023) 100429
[177] Chang-Heng Li, Zhengyong Huang, Junping Lin, Tingting Hou, Yunlong Zi, Jian Li, Excellent-Moisture-Resistance Fluorinated Polyimide Composite Film and Self-Powered Acoustic Sensing, ACS Appl. Mater. Interfaces 2023, 15, 29, 35459–35468
[178] Junhua Xu, Hiroyuki Umehara, Isao Kojima, Effect of deposition parameters on composition, structures, density and topography of CrN films deposited by r.f. magnetron sputtering, Applied Surface Science 201 (2002) 208–218
[179] Guangchun Zhang, Jianhua Zhao, Martin A. Green, The effect of substrate heating on the adhesion and humidity resistance of evaporated MgF_2/ZnS antireflection coatings and on the performance of high-efficiency silicon solar cells, Solar Energy Materials and Solar Cells 51 (1998) 393-400
[180] Yan He, Zikai Gao, Meiling Tang, Xingjun Gao, Lin Fan, Jingting Sun, Study on the atomic removal behavior and damage formation mechanism of nano cutting copper–nickel alloy with diamond tool, Modeling and Simulation in Material Science and Engineering 32 (2024) 035011
[181] Manimozhi Thangaraju, Archana Jayaram, Ramamurthi Kandasamy, Structural, morphological, optical and electrical properties of e-beam deposited nanocrystalline CdTe:Cu alloy thin films from mechanical alloyed samples, Applied Surface Science 449 (2018) 2-9
[182] Weipeng Chen, Hua Hou, Yuntao Zhang, Wei Liu, Yuhong Zhao, Thermal and solute diffusion in a-Mg dendrite growth of Mg-5wt.%Zn alloy: A phase-field study, Journal of Materials Research and Technology, 24 (2023) 8401-8412
[183] Wangwang Kuang, Haifeng Wang, Xin Li, Jianbao Zhang, Qing Zhou, Yuhong Zhao, Application of the thermodynamic extremal principle to diffusion-controlled phase transformations in Fe-C-X alloys: Modeling and applications, Acta Materialia 159 (2018) 16-30
[184] V.D. Vankar, D.K. Pandya, K.L. Chopra, Structural and optical properties of ZnS-MgF_2 alloy films, Thin Solid Film, 59 (1) (1979) 43-49
[185] X.J. Jiang, S.J. Bao, L.W. Zhang, X.Y. Zhang, L.S. Jiao, H.B. Qi, F. Wang, Effect of Zr on microstructure and properties of TC4 alloy fabricated by laser additive manufacturing, Journal of Materials Research and Technology, 24 (2023) 8782- 8792
[186] Jun Wang, Zengxi Pan, Yangfan Wang, Long Wang, Lihong Su, Dominic Cuiuri, Yuhong Zhao, Huijun Li, Evolution of crystallographic orientation, precipitation, phase transformation and mechanical

properties realized by enhancing deposition current for dual-wire arc additive manufactured Ni-rich NiTi alloy, Additive Manufacturing 34 (2020) 101240
[187] J Li, Y F Zheng, J B Xu, K Dai, Te-doped cadmium telluride films fabricated by close spaced sublimation, Semicond. Sci. Technol. 18 (2003) 611–614
[188] Li Jin, Yang Linyu, Jian Jikang, Zou Hua, Sun Yanfei, Effects of Sn-doping on morphology and optical properties of CdTe polycrystalline films, *Journal of Semiconductors* 30 (2009) 112003
[189] Md. Anisuzzaman Shakil, Sangita Das, Md. Ashiqur Rahman, Umma Salma Akther, Md. Kamrul Hassan Majumdar, Md. Khalilur Rahman, A Review on Zinc Sulphide Thin FilmFabrication for Various Applications Based on Doping Elements, Materials Sciences and Applications, 9 (2018) 751-778
[190] Md Abu Sayeed, Hasan Khaled Rouf, Kazi Md Amjad Hussain, Doping and annealing effects on structural, optical and electrical characteristics of Sn-doped ZnS thin film, Mater. Res. Express 8 (2021) 086401
[191] A. Sundhar, Development of ZnS thin film with Co, Cu and Ag doping using SILAR method, Materials Today: Proceedings, https://doi.org/10.1016/j.matpr.2020.09.550
[192] Chen Zhang, Amnaya P. Awasthi, Jeauk Sung, Philippe H. Geubelle, Nancy R. Sottos, Multi-scale model of effects of roughness on the cohesive strength of self-assembled monolayers, International Journal of Fracture 208 (2017) 131–143
[193] Ziyi Shen, Ruipeng Dong, Jiao Li, Yutai Su, Xu Long, Determination of gradient residual stress for elastoplastic materials by nanoindentation, Journal of Manufacturing Processes 109 (2024) 359–366
[194] F. Spaepen, Interfaces and Stresses in Thin Films, Acta Materialia. 48 (2000) 31-42
[195] Giedrius Laukaitis, Seppo Lindroos, Sigitas TamulevicÏius, Markku LeskelaÈ, Stress and morphological development of CdS and ZnS thin film during the SILAR growth on (100) GaAs, Applied Surface Science 185 (2001) 134-139
[196] D. M. Mattox, J. E. Mcdonald, Interface Formation during Thin Film Deposition, Journal of Applied Physics 34, (1963) 2493
[197] G.A. Webster, A.N. Ezeilo, Residual stress distributions and their influence on fatigue lifetimes, International Journal of Fatigue, Volume 23, Supplement 1, 2001, Pages 375-383
[198] Qimeng Zhu, Jia Chen, Guoqing Gou, Hui Chen, Peng Li, Ameliorated longitudinal critically refracted—Attenuation velocity method for welding residual stress measurement, Journal of Materials Processing Technology 246 (2017) 267–275
[199] Chen Zhang, Amnaya P. Awasthi, Philippe H. Geubelle, Martha E. Grady, Nancy R. Sottos, Effects of interface roughness on cohesive strength of self-assembled monolayers, Applied Surface Science 397 (2017) 192-198
[200] A.J.Ghazai, O.M. Abdulmunem, K.Y. Qader, S.S. Chiad and N.F. Habubi,' Investigation of Some Physical Properties of Mn Dopsed ZnS Nano Thin Films, 'AIP Conference Proceedings 2213 , 020101 (2020)
[201] Saha and Nix, 'Effect of the substrate on the determination of thin films mechanical properties by nanoindentation ', Acta 2002, 50, 23
[202] S.U. Jen and T.C. Wu,' Young's modulus and hardness of Pd thin films ', Thin solid Films (2005) 492, 166
[203]A. Portinha, V. Teixeira, J. Carneiro, J. Martins, M.F. Costa, R. Vassen and D.Stoever,' Characterization of thermal barrier coatings with a gradient in porosity ', Surface and Coatings Technology, vod. 195 (2005) 245-251
[204] Sheikh Rashel Al Ahmed, Jannatul Ferdous, Md Suruz Mian, Development of a novel CdTe/ZnS/ZnTe heterojunction thin-film solar cells: a numerical approach, IOP SciNotes 1 (2020) 024802
[205] S.R. Jian, H.G. Chen, G.J. Chen, J.S.C. Jang and J.Y.Juang, 'Structural and nanomechanical properties of a-plane ZnO thin films deposited under different oxygen partial pressures', Curr.Appl. Phys. 12(2012) 849-853

[206] S.K. Wang, T.C. Lin, S.R. Jian, J.Y. Juang, J.S.C. Jang and J.Y. Tseng ,' Effects of post annealing on the structural and nanomechanical properties of Ga-doped ZnO thin films deposited on glass substrate by rf-magnetron sputtering ', Applied Surface Science 258 (2011) 1261-1266
[207] Shailendra Kumar Gaur, Qasim Murtaza, R.S. Mishra, Analysis of structural, morphological and nano-mechanical properties of vacuum evaporated nanoscale CdTe and ZnS films, Optical Materials 154 (2024) 115764
[208] Arslan Ashfaq, A. Ali, K. Mahmood, Ubaid ur Rehman, S. Tahir, N. Amin, W. Ahmad, Rana Naveed Aslam, Murtza Arshad, Kamran Rasheed, Al doping induced high thermoelectric performance in Cu_2ZnSnS_4 nanoparticles synthesized by the hydrothermal method, Ceramics International 47 (2021) 35356–35360
[209] Arslan Ashfaq, Rasmiah S. Almufarij, M. Yasir Ali, Adnan Ali, Sofia Tahir, Michael M. Sabugaa, Mohamed Abdelsabour Fahmy, Elsammani Ali Shokralla, Ahmed H. Ragab, D.E. El-Refaey, Khalid Mehmood, High thermoelectric power factor of n-type $Bi_2(Se,S)_3$ via synergetic influence on the charge carrier concentration and energy filtering effect, International Communications in Heat and Mass Transfer 146 (2023) 106870
[210] Arslan Ashfaq, Jolly Jacob, Mongi Amami, F.F. Al-Harbi, A. Ali, K. Mahmood, U. Rehman, N. Amin, S. Ikram, S. Tahir Akbar, S. Hussain, Effect of Al-doping on the thermoelectric properties of CZTS thin film grown by sol-gel method, Solid State Communications 345 (2022) 114701
[211] Ubaid ur Rehman, Khalid Mahmood, Muhammad Arshad Kamran, Rawaa M. Mohammed, H.H. Somaily, Arslan Ashfaq, Qeemat Gul, Adnan Ali, Muhammad Faisal Iqbal, Kashaf ul Sahar, Enhanced thermoelectric power generation performance of mixed-phase FeS/FeS_2 nanostructures by controlling the reaction time duration, Ceramics International 49 (2023) 512–517
[212] Iman H. Khundayer, Bushra H. Hussein, Mohammed Hamid, 'Depending the structure and Optical Properties of Cadmium Telluride Films on Doping Process, Al-Mustansiriyah Journal of Science, Vo. 2 Issue 1, 2018
[213] S.G.Deshmkh, Akshay Jariwala, Anubha Agarwal, Chetna Patel, A.K. Panchal and Vipul Kheraj ,ZnS Nanostructured Thin-Films Deposited by Successive Ionic Layer Adsorption and Reaction, AIP Conference Proceedings 1724, 020033 (2016)
[214] H. Eilers,' Synthesis and characterization of CO_2-laser-evaporated ZnS: Mn thin films, Materials letters, vol. 62, issue 6-7(2008) 967-969
[215] Y.P.V. Subbaiah, P.Prathap, KTR Reddy, ' Structural ,electrical and optical properties of ZnS films deposited by close-spaced evaporation ', Applied Surface Science , Vol 253, issue5 (2006) 2409-2415
[216] Hasan Ghasemi, Mohammad Hazir Mozaffari and Rostam Moradian, 'Effects of deposition time on structural and optical properties of ZnS and ZnS/Au thin films grown by thermal evaporation' , Physica B : Physics of Condensed Matter, 627 (2022) 413616
[217] Rashmitha Keshav and Mahesha MG, 'Photoluminescence and Raman spectroscopic analysis of PV deposited ZnS thin films ', Materials Research Bulletin 105 (2018) 360-367
[218] Ke Yang, Bing Li and Guanggen Zeng, 'Effects of temperature on properties of ZnS thin films deposited by pulse laser deposition ', Journal of Superlattices and Microstructures 130 (2019) 409-415
[219] N. Bouguila, D.Bchiri,M. Kraini, A. Timoumi, I. Halidou, K. Khirouni and S. Alaya, ' Structure, morphological and optical properties of annealed ZnS thin films deposited by spray technique' , J. Mater Sci : Mater Electron (2015) 26 , 9845-9852

[220] Abdessamad Najim, Bouchaib Hartiti, Hicham Labrim, Salah Fadili, Mehmet Ertugrul and Philippe Thevenin, ‘ Synthesis of ZnS thin films using the spray pyrolysis Technique’, Journal of Materials Science in Electronics : June 2022
[221] Idris Akyuz and Irem Yeni,‘ Effect of Heat Treatment in Different Atmospheres on Thermally Evaporated ZnS films ‘, Optical Materials 119 (2021) 111381
[222] J. Kennedy, P.P. Murumu, P.S. Gupta, D.A. Carder, S.V. Chong, J.Leveneur and S. Rubanov, ‘ Effects of annealing on the structural and optical properties of zinc sulfide thin films deposited by ion beam sputtering ‘ , Journal of Materials in Semiconductor Processing 23 (2014) 561-655
[223] Nafiseh Memarian, Seyeed Mohammad Rozati, Isabella Concina, Alberto Vomiero, Deposition of Nanostructured CdS Thin Films by Thermal Evaporation Method : Effect of substrate Temperature, MDPI, Materials , 2017
[224] Hasan Ghasemi, Mohammad Hazir Mozaffari and Rostam Moradian, ‘ Effects of deposition time on structural and optical properties of ZnS and ZnS/Au thin films grown by thermal evaporation ‘, Physica B : Physics of Condensed Mattter , 627 (2022)413616
[225] Arun Kumar, Samrat Mukherjee, Sanjay Sahare and Ravi Kant Choubey , ‘ Influence of deposition time on the properties of ZnS/P-Si heterostructures’ , Journal of Material Science in Semiconductor Processing, vol. 122 (2021) 10547
[226] http://cp.literature.agilent.com/litweb/pdf/5990-5700EN.pdf; Indentation rules of thumb-Applications and Limits
[227] http://wwe.nanomechnic.sinc.com/index.php/Service-Lab/sample-preparation.html
[228] H.M.M.N. Hennayaka and Ho Seong Lee, ‘Structural and optical properties of ZnS thin film grown by pulsed electrodeposition ‘, Thin Solid Films 548 (2013) 86-90
[229] Nowshad Amin, Mohammad Rezaul Karim and Zeid Abdullah Alothman, ‘ An in-Depth Analysis of CdTe Thin-Film Deposition on Ultra-Thin Glass Substrate via Close-Spaced Sublimation (CSS)’ , Coatings 12 (2022) 589
[230] Te-Hua Fang and Win-Jin Chang, Nanomechancial properties of copper thin films on different substrates using the nanoindentation technique, Journal of Microelectronic Engineering vol. 65 (2003) 231-238
[231] Zong Hu, Chapter 6-Characterization of Materials, Nanomaterials, and Thin Films by Nanoindentation, Mircoscopy Methods in Nanomaterials Characterization, Micro and Nano Technologies, 2017, 165-239
[232] Corina Birleanu, Marius Pustan, Florina Serdean and Violeta Merie, ‘AFM Nanotribomechancial Characterization of Thin Films for MEMS Applications, Micromachines (2022), 13, 23.
[233] N. Mukherjee, A. Sinha, G.G. Khan, D. Chandra, A. Bhaumik, A. Mondal, A study on the structural and mechanical properties of nanocrystalline CuS thin films grown by chemical bath deposition technique, Mater. Res. Bull. 46(2011) 6-11
[234] S. Simunkova, O. Blahova and I. Stepanek, Mechanical properties of thin film-substrate systems, Journal of Materials Processing Technology, 133 (2003), 189-194
[235] W.D. Nix and H.Gao, Indentation size effects in crystalline materials: a law for strain gradient plasticity, J. Mech. Phys. Solids 46 (1998) 411-425
[236] K. Durst, M. Goken, G.M.Pharr, Indentation size effect in spherical and pyramidal indentations, Journal of Physics D : Applied Physics 41, 0741005 (2008)

[237] M.S.R.N. Kiran, S. Kshirsagar, M.G. Krishana and Surya P. Tewari, Structural, optical and nanomechancial properties of (111) oriented nanocrystalline ZnTe thin films, European Physical Journal of Applied Physics, 51 ,10502 (2010)
[238] Bharat Bhushan, Ashok V. Kulkarni, Wayne Bonin and Jerzy T. Wyrobek, ' Nanoindentation and picoindentation measurements using a capacitive transducer system in atomic force micrscopy' , Philosophical Magazine A, Vol. 74 , (1996) issue 5
[239] M. F. Ashby, 'The Deformation of Plastically Non-homogeneous Materials ', Philosophical Magazine, 1970, 21, 399-424
[240] N.A. Fleck, J.W. Hutchinson, ' A phenomenological theory for strain gradient effects in plasticity' , Journal of the Mechanics and Physics of Solids, vol 41, issue 12 (1993) 1825-1857
[241] Nanoindentation, in: A.C. Fischer-Cripps (Ed.), Mechanical Engineering Seried, 3rd ed., Springer, New York, NY, USA , 2011.
[242] W.B. Li, J.L. Henshall, R.M. Hooper and K.E. Easterling,The mechanism of indentation creep , Acta Metallurgica et Materialia, vol. 39, (1991) 3099-3110
[243] R.N. Stevens, 'Grain-boundary sliding and diffusion creep in polycrystalline solids, The Philosophical Magazine: A journal of Theoretical Experimental and Applied Physics, Vol. 8, (1971) issue 182
[244] S. Del Sordo, L. Abbene, E. Caroli, A.M. Mancini, A. Zappettini, P. Ubertini, Sensors 9, 3491 (2009).
[245] S. Tewari, A. Bhattacharjee, and P.P. Sahay, J. Mater. Sci. 44, 534 (2009).
[246] X. Mathew, Semicond. Sci. Technol. 18, 1 (2003).
[247] G.G. Rusu, J. Optoelectron. Adv. Mater. 8, 931 (2006).
[248] G. Sarusi, G. Cinader, A. Zemel, and D. Eger, Application of CdTe epitaxial layers for passivation of $Hg_{0.77}Cd_{0.33}Te$, J. Appl. Phys. 71 (IO), 15 May 1992 0021-8979/92/ 105070-07$04.00 0 1992 American Institute of Physics
[249] Y. Nemirovsky, L. Bumtein, I. Kidron, J. Appl. Phys. 58, 366 (1985).
[250] John G. Simmons, Transition from electrode-limited to bulk-limited conduction processes in Metal-Insulator-Metal system, Physical Review, Vol. 166, No.3, 1968
[251] Sanjeev K. Gupta, A Azam and J Akhtar, Experimental analysis of current conduction through thermally grown SiO2 on thick epitaxial 4H-SiC employing Poole-Frenkel mechanism, Pramana, Vol. 74, No. 2,2010 physics pp. 325-330
[252] R. W. Hoffman, (1976). Mechanical Properties of Non-Metallic Thin Films. In: Dupuy, C.H.S., Cachard, A. (eds) Physics of Nonmetallic Thin Films. NATO Advanced Study Institutes Series, vol 14. Springer, Boston, MA
[253] R. F. Bunshah (Ed), Handbook of Deposition Technologies for Films and Coatings, Noyes Publications, 1994
[254] D.A. Glecker, S.I. Shahd (Eds.) Handbook of Thin film Process Technology, IOP, Bristol, 1995
[255]G.Laukaitis, S.Lindroos , S.Tamulevicˇius, M.Leskela, M.Racˇkaitis, Stress and surface studies of SILAR grown ZnS thin films on (100)GaAs substrates, Materials Science and Engineering A288 (2000) 223–230
[256] A.C. Fischer-Cripps, Nanoindentation, (Springer, New York,2004)
[257]S.J. Bull, J. Phys. D Appl. Phys. 38(25), R393 (2005)
[258] S.Y. Chang, Y.C. Huang, Microelectron. Eng. 84, 319 (2007)
[259] J. Malzbender, J.M.J. den Toonder, A.R. Balkenende, Sci. Eng. R36, 47–103 (2002)
[260] S.Y.Chang, H.L.Chang,Y.C. Lu, S.M. Jang, S.J. Lin, M.S.Liang, Thin Solid Films 460,164–167 (2004)
[261] R.Saha, W.D. Nix, 2002. Acta Mater. 50, 23.
[262] Simunkova, S., Blahova, O., Stepanek, I., 2003. J. Mater. Process. Technol. 133, 189.

[263] G. Purc , E. Bacaksız , I. Miskioglu, Structure and nanomechanical properties of CdTe thin films, journal of materials processing technology 198 (2008) 202–206
[264]Taraknath Mandal, Prabal K. Maiti, and Chandan Dasgupta, Mechanical properties of ZnS nanowires and thin films: Microscopic origin of the dependence on size and growth direction, Physical Review B 86, 024101 (2012)
[265]Shailendra Kumar Gaur, Qasim Murtaza, R.S. Mishra, Analysis of structural, morphological and nano-mechanical properties of vacuum evaporated nanoscale CdTe and ZnS films, Optical Materials 154 (2024) 115764
[266] Ireneusz Strzalkowski, Sharad Joshi, and C. R. Crowel, Dielectric constant and its temperature dependence for GaAs, CdTe, and ZnSe, Applied Physics Letters, Vol. 28, No.6, 15 March 1976
[267] S. Tewari, A. Bhattacharjee, P. P. Sahay , Structural, dielectric, and electrical studies on thermally evaporated CdTe thin films , J Mater Sci (2009) 44:534–540
[268] A. Goswami, Amit P. Goswami, Dielectric and optical properties of ZnS films, Thin Solid Films, 16 (1973) 175-185
[269] Annealing temperature effect on the structural, optical and electrical properties of ZnS thin films, Physica B 406 (2011) 1653–1659
[270] K.A.M.H. Siddiquee, M.A.K. Pathan, S. Alam, O. Islam and M.R. Qadir, ‘ Investigation of CdS and CdTe thin films and influence of $CdCl_2$ on CdTe/CdS ‘ , Optik 124 (2013) 4383-4388
[271] I. M. Dharmadasa and A. E. Alam, How to Achieve Efficiencies beyond 22.1% for CdTe-Based Thin-Film Solar Cells, Energies 2022, 15, 9510
[272] Dong Hyun Hwang, Jung Hoon Ahn1, Kwun Nam Hui, Kwan San Hui and Young Guk Son, ‘Structural and optical properties of ZnS thin films deposited by RF magnetron sputtering, . Nanoscale Research Letters 2012, 7:26
[273]Rashmitha Keshav and Mahesha MG, ‘Photoluminescence and Raman spectroscopic analysis of PV deposited ZnS thin films ‘, Materials Research Bulletin 105 (2018) 360-367
[274] N. Bouguila, D.Bchiri,M. Kraini, A. Timoumi, I. Halidou, K. Khirouni and S. Alaya, ‘ Structure, morphological and optical properties of annealed ZnS thin films deposited by spray technique’ , J. Mater Sci : Mater Electron (2015) 26 , 9845-9852
[275] Arun Kumar, Samrat Mukherjee, Sanjay Sahare and Ravi Kant Choubey, ‘Influence of deposition time on the properties of ZnS/P-Si heterostructures’, Journal of Material Science in Semiconductor Processing, vol. 122 (2021) 10547
[276] D. H. Hwang, J.H. Ahn, K. N. Hui, Structural and optical properties of ZnS thin films deposited by RF magnetron sputtering, Nanoscale Research Letter, 7 (2012) 26
[277] H.M.M.N. Hennayaka and Ho Seong Lee, ‘Structural and optical properties of ZnS thin film grown by pulsed electrodeposition ‘, Thin Solid Films 548 (2013) 86-90
[278] Melih Manir, Gamze Genç, Vagif Nevruzoglu, Murat Tomakin, Mehmet Gokhan Sensoy , Fabrication and Characterization of CdTe Thin Films: Insights into Classical and Cryogenic Fabrication Techniques, ACS Omega 2025, 10, 6567−6577
[279] Xiaochun Wu, Fachun Lai , Limei Lin, Jing Lv, Binping Zhuang, Qu Yan, Zhigao Huang, Optical inhomogeneity of ZnS films deposited by thermal evaporation, Applied Surface Science 254 (2008) 6455–6460
[280]. K.L. Johnson, Contact Mechanics, Cambridge University Press, Cambridge, 1985.
[281] http://cp.literature.agilent.com/litweb/pdf/5990-5700EN.pdf;Indentation rules of thumb-Applications and Limits
[282] http://wwe.nanomechnic.sinc.com/index.php/Service-Lab/sample-preparation.html
[283] Jinbo Jiang, Bong Kee, On astigmatism of multi-beam optical stress sensor mounted at large incident angle, Optik 114, No. 9 (2003) 427–432
[284]G.G. Stoney, Proc. R. Soc. Lond. Ser. A Contain. Pap. Math. Phys. Character 82/553 (1909) 172.
[285] C. Lynch, R. Beresford, E. Chason, Real-time stress evolution during growth of $In_xAl_{1-x}A_s$/GaAs metamorphic buffer layers, Journal of Vacuum Science & Technology B 22, 1539 (2004)

[286] Akhilesh Pandey, Shankar Dutta, Ravi Prakash, Sandeep Dalal , R. Raman, Ashok Kumar Kapoor, Davinder Kaur, Growth and evolution of residual stress of AlN films on silicon (100) wafer, Materials Science in Semiconductor Processing, Vol 52, 2016, 16-23
[287] V.V. Patil, R.K. Puri, Vijaya Puri, Comparison of adhesion and intrinsic stress of chopped and non-chopped ZnS thin films, Materials Chemistry and Physics, 47 (1997) 156-159
[288] N. Mukherjee, A. Sinha, G.G. Khan, D. Chandra, A. Bhaumik, A. Mondal, A study on the structural and mechanical properties of nanocrystalline CuS thin films grown by chemical bath deposition technique, Mater. Res. Bull. 46(2011) 6-11
[289] S.Simunkova, O. Blahova and I. Stepanek, Mechanical properties of thin film-substrate systems, Journal of Materials Processing Technology, 133 (2003), 189-194
[290] W.D. Nix and H.Gao, Indentation size effects in crystalline materials: a law for strain gradient plasticity, J. Mech. Phys. Solids 46 (1998) 411-425
[291] K. Durst, M. Goken, G.M.Pharr, Indentation size effect in spherical and pyramidal indentations, Journal of Physics D : Applied Physics 41, 0741005 (2008)
[292] N.A. Fleck, J.W. Hutchinson, 'A phenomenological theory for strain gradient effects in plasticity', Journal of the Mechanics and Physics of Solids, vol 41, issue 12 (1993) 1825-1857
[293] Portinha, A., Teixeire, V., Carneiro, J.O., Dup, S.N., Shmegera, R., Tavares, C.J., 2005. Surf. Coat. Technol. 200, 765.
[294] Jen, S.U., Wu, T.C., 2005. Thin Solid Films 492, 166.
[295] Callister Jr., W.D., 1997. Materials Science and Engineering: An Introduction. John Wiley & Sons, Inc., New York.
[296] Thompson, C.V., Carel, R., 1996. J. Mech. Phys. Solids 44 (5), 657
[297] C. Caër, E. Patoor, S. Berbenni, J.-S. Lecomte, Stress induced pop-in and pop-out nanoindentation events in CuAlBe shape memory alloys, Materials Science and Engineering: A, Vol. 587, (2013), 304-312
[298] T.Y. Tsui, W.C. Oliver, and G.M. Pharr, "Influences of stress on the measurement of mechanical properties using nanoindentation. 1. Experimental studies in an aluminium alloy," J. Mater. Res. 11 3, 1996, pp. 752–759.
[299] V. Srivastav, R. Pal, N. Saini, R.S. Saxena, R.K. Bhan, L. Sareen, K.P. Singh, R.K. Sharma, and V. Venkatraman, The effect of Temperature Cycling on Conduction Mechanisms in CdTe Thin Films, Journal of Electronic Materials, Vol. 42, No. 3, 2013
[300] M. Rapos, M. Ruzinsky, S. Luby, J. Cervenak, Low Frequency Relaxation Phenomena in Thin Film MIM and MSM Dielectric Structurs, IEEE Explore, 1976
[301] R.K. Bhan , V. Srivastava, R.S. Saxena, L. Sareen, R. Pal, R.K. Sharma, Improved high resistivity ZnS films on HgCdTe for passivation of infrared devices, Infrared Physics & Technology 53 (2010) 404–409
[302] Marc Beale, Peter Mackay, The origins and characteristics of negative capacitance in metal-insulator-metal devices, Philosophical Magazine B, 1992, vol. 65, No. 1,47-64
[303] A.V. Sukach, V.V. Tetyorkin, N.M. Krolevec, Semicond. Phys. Quant. Electron. Optoelectron. 13, 221 (2010).
[304] G.G. Rusu, M. Rusu, E.K. Polychroniadis, C. Lioutas, J. Optoelectron. Adv. Mater. 7, 1957 (2005).
[305] Riyadh Sami, Alaa J. Ghazai, 'Synthesis and Characterization of Nanostructural CdS Thin Film using Spin Coating Technique for Photodetector Application ', J. Nanostuct 12 (2) 2022, 405-413
[306] Jumaa Mohammed, Jasmim M. Abbas, Mustafa Falah, ' Effect of Annealing Temperature on the Physical Properties of Cadmium Sulphide Thin Films Deposited by using Thermal Evaporation Technique ' , IOP Conf. series : Materials science and engineering, 757 (2020) 012077
[307] Shafi Ullah, Amal Bouich, Hanif Ullah, Bernabe Mari, Miguel Mollar, ' Comparative study of binary cadmium sulfide (CdS) and tin disulfide (SnS_2) thin film buffer layers ', Journal of Solar Energy 208 (2020) 637-642

[308] Nafiseh Memarian, Seyeed Mohammad Rozati, Isabella Concina, Alberto Vomiero, 'Deposition of Nanostructured CdS Thin Films by Thermal Evaporation Method: Effect of Substrate Temperature ', Materials (2017) 10, 773
[309] Binbin Weng, Jijun Qiu, Lihua Zhao, Caleb Chang, Zhisheng Shi, ' CdS/PbSe heterojunction for high temperature mid-infrared photovoltaic detector applications' , Applied Physics Letters 104 (2014) 121111
[310] V.D. Morenao-Regino, F.M. Castaneda-de-la-Hoya, C.G. Torres-Castanedo, J.Marquez-Marin, R. Castanedo-Perez, G.Torres-Delgado, O. Zelaya-Angel, ' Structural,optical,electrical and morphological properties of CdS films deposited by CBD varying the complexing agent concentration ' Results in Physics 13 (2019) 102238
[311] J.I. Contreras-Rascon, J.Diaz-Reyes, A. Flores-Pacheco, R. Lozada Morales, M.E. Alvarez-Ramos, J.A. Balderas-Lopez, 'Structural and optical modifications of CdS properties in CdS-Au thin films prepared by CBD ' , Results in Physics 22 (2021) 103914
[312] Duraisamy Sivagamai, Badhirappan Geetha Priyadarshini, 'Composition dependent structural, morphological, optical and electrical properties of CdS: Co window layer grown by chemical bath deposition ', Journal of Materials Science for Energy Technologies 3 (2020) 709-718
[313] Abdulwahab S.Z. Lahewil, Y. Al-Douri, U. Hashim, N.M. Ahmed, ' Structural analysis and optical studies of Cadmimum Sulfide Nanostructured ' , Procedia Engineering 53 (2013) 217-224
[314] Sung-Gi Hur, Eui-Tae Kim, Ji-Hong Lee, Geun-Hong Kim, Soon-Gil Yoon, ' Characterization of photoconductive CdS thin films prepared on glass substrates for photoconductive-sensor applications' , Journal of Vacuum Science Technology, B 26 (2008) 1334-1337
[315] M.G. Faraj, K. Ibrahim,'Comparison of cadmium sulfide thin films deposited on glass and polyethylene terephthalate substrates with thermal evaporation for solar cell applications ', Journal of Material Science : Mater Electron (2012) 23 : 1219-1223
[316] F.T.Z. Toma, K.M.A. Hussain, M.S. Rahman, Syed Ahmed, ' Preparation and characterization of CdS thin film using chemical bath deposition (CBD) technique for solar cell application' , World Journal of Advanced Research and Reviews, (2021), 12 (03)
[317] Iqbal S. Naji, Iman H. Khdayer, Hanna I. Mohammed, ' The effect of annealing temperature on the optical properties of CdS and CdS : Al thin films' , International Journal of Application or Innovation in Engineering & Management, vol. 2 (2013) 6
[318] K.M.A. Hussaini, M.S.S. Chowdhury, T. Faruqe, ' Study of CdS/AZO/FTO, CdS/FTO and CdS thin films deposited by modified double layer thermal evaporation ' , Journal of Nanoscience, Nanoengineering and Applications ' , (2019) 56-63
[319] M.S. Kale, Y.R.Toda, M.P.Bhole. D.S. Bhavsar, ' Structural, optical and thermo electrical properties of nanostructured vacuum evaporated CdS thin films', Electron. Mater. Letter , Vod. 10,1 (2014) 21-25
[320] A. Carrillo-Castillo, F.S. Aguirre-tistado, A. Salasvillasenor, I.Mejia, B.E. Gnade, M.Sotelo-Lerma, M.A. Quevedo-lopez, ' Effect of deposition rate on the morphology of CdS films deposited in an ammonia free solution' ,Chalcogenide letters, (2013) Vol. 10 ,2, 81-86
[321] Sarveswaran Thangarajan, Gopinathan Chellachamy, Saravanakumar Kulendran, Pandi Pitchai, Mahalakshmi Kandasamy , ' Synthesis and study of CdS thin films prepared with different $KMnO_4$ activation time ', Journal of Materials, 2016, article id 3439827
[322] M.A. Islam, M.S. Hossain, M.M. Aliyu, P.Chelvanathan, Q. Huda, M.R. Karim, K.Sopian, N.Amin, ' Comparison of structural and optical properties of CdS thin films grown by CSVT, CBD and sputtering techniques ' , Energy Procedia 33 (2013) 203-213

[323] Mark A.Buckingham, Kane Norton, Paul D.McNaughter, George Whitehead, Inigo Vitorica-Yrezabal, Firoz Alam, Kristine Laws, David J. Lewis, ‘ Investigating the effect of steric hindrance within CdS single-source precursors on the material properties of AACVD and spin-coat-deposited CdS thin films ‘ , Inorganic Chemistry 61 (2022) , 8206-8216
[324] F. Lisco, P.M.Kaminski, A.Abbas, K.Bass, J.W.Bowers, G.Claudio, M.Losurdo, J.M.Walls, ‘ The structural properties of CdS deposited by chemical bath deposition and pulsed direct current magnetron sputtering ‘, Thin Solid Films 582 (2015) 323-327
[325] J.J.Roa, G.Oncins, J.Diaz, X.G. Capdevila, F.Sanz, M.Segarra,’ Study of the friction, adhesion and mechanical properties of single crystals, ceramics and ceramic coatings by AFM’ ,Journal of the European Ceramic Society , 31 (2011), 429-449
[326] Yi Ma, Yuxuan Song, Xianwei Huang, Zhongli Chen, Taihua Zhang, ‘ Testing effects on shear transformation zone size of meatallic glassy films under nanoindentation ‘, Mircomachines , 9(2018) 636
[327] Anthony C. Fischer-Cripps, Mechanical engineering series, Nanoindentation 3rd edition , Springer
[328] A. R. Shugurov, A. V. Panin, K.V.Oskomov, ‘Specific features of the determination of the mechanical characteristics of thin films by the nanoindentation technique ‘, Physics of the Solid State, vol. 50 (2008),6,1050-1055
[329] T.Y. Tsui, G.M.Phrr, ‘Substrate effects on nanoindentation mechanical property measurement of soft films on hard substrates’ , Journal Mater. Res. Vol. 14 (1999) 1
[330] Xi Chen, Joost J. Vlassak, ‘Numerical study on the measurement of thin film mechanical properties by means of nanoindentation ‘ , Journal. Mater. Res. Vol 16 (2001), 10
[331] Yeon-Gil Jung, Brian R. Lawn, Mariusz Martyniuk, Han Huang, Xiao Zhi Hu, ‘Evaluation of elastic modulus and hardness of thin films by nanoindentation ‘, Journal of Mater. Res. vol. 19 (2004)10
[332] A.V.Panim, A.R.Shugurov, K.V.Oskomov, ‘ Mechancial properties of thin Ag films on a silicon substrate studied using the nanoindentation technique ‘, Physics of the Solid State, vol. (2005) 11, 2055-2059
[333] A.Ashok, G. Regmi, A. Romero-Nunez, M. Solis-Lopez. S.Velumani, H. Castaneds, ‘Comparative studies of CdS thin films by chemical bath deposition techniques as a buffer layer for solar cell applications’, J. Matter. Sci. Mater. Electron (2020) 1-20
[334] A. Cortes, H.Gomez, R. E. Marotti, G.Riveros, E.A. Dalchieie, ‘ Grain size dependence of the bandgap in chemical bath deposited CdS thin films’, Sol.Energy Mater. Sol. Cells 82 (1-2) (2004) 21-34
[335] I. Ramthinamala, N.Prithivikumaran, ‘ Sol-Gel Synthesis of CdS/Glass and CdS/Si Thin films for Optoelectronic Devices, Research square, 2021, http ://doi.org/10.21203/rs.3-688129/v1
[336] Obi Kingsley Echendu, Francis Birhanu Dejene, Imyhamy Mudiy Dharmadasa, Francis Chukwuemeka, ‘ Characteristics of nanocrystallinte-CdS produced by low-cost electrochemical technique for thin film photovoltaic application : The influence of deposition voltage ‘ ,International Journal of Photoenergy , 2017, article id 3989432
[337] A.A.Lakmal, R.K.K.G.R.G.Kumarasinghe, V.A.Seneviratne, Jiann-Yeu Chen, Jenn-Ming Song, B.S.Dassanayake, ‘ Thermally evaporated CdS thin films for CdS/CdTe solar cells : Effect of substrate temperature on CdS layer ‘, Materials Science and Engineering B 273 (2021) 115406
[338] V.H.Martinez-Landeros, N.Hernandez-Como, G. Gutierrez-Heredia, M.A. Quevedo-Lopez, F.S.Auguirre-Tostado , ‘ Structural, chemical and electrical properties of CdS thin films fabricated by pulsed laser deposition using varying background gas pressure ‘ ,Thin Solid Films 682 (2019) 24-28

[339] Sachin Rondiya, Avinash Rokade, Adinath Funde, Moses Kartha, Habib Pathan, Sandesh Jadkar, ' Synthesis of CdS thin films at room temperature by RF-magnetron sputtering and study of its structural, electrical,optical and morphology properties', Thin Solid Films 631 (2017) 41-49
[340] C.Doroody, K.S.Rahman, H.N. Rosly, M.N.Harif, M.Isah, Y.B.Kar,S.K.Tiong, ' A comparative study of CdS thin films grown on ultra-thin glass substrates by RF magnetron sputtering and chemical bath deposition ', Journal of Materials Science in Semiconductor Processing , 133 (2021) 105935
[341] M.Isik, H.H.Gullu, S.Delice, M.Parlak, N.M.Gasanly, ' Structural and temperature-dependent optical properties of thermally evaporated CdS thin films ', Journal of Materials Science in Semiconductor Processing 93 (2019) 148-152
[342] A. Fernanendez-Perez, C.Navarrete,P. Valenzuela, W.Gacitua, E.Mosquera, H.Fernandez,' Characterization of chemically-deposited aluminum-doped CdS thin films with post-deposition thermal annealing ', Thin Solid Films 623 (2017) 134
[343] Ersin Yucel, Osman Sahin, 'Effect of pH on the structural, optical and nanomechanical properties of CdS thin films grown by chemical bath deposition ', Ceramics International 42 (2016) 6399-6407
[344] Mahmood, Junaid Ali, Iqra Zahid, Andrew Thomas, Anwar ul Haq, 'Optical and electrical studies of CdS thin films with thickness variation ', Optik 158(2018) 1558-1566
[345] Alex A. Volinsky, Neville R.Moody, William W.Gerberich, ' Nanoindentation of Au and Pt/Cu thin films at elevated temperatures ', Journal of Mater. Res. vol. 19 (2004) 9
[346] Mateja Egart, Biljana Jankovic, Stane Srcic, Application of instrumented nanoindentation in preformulation studies of pharmaceutical active ingredients and excipients, Acta Pharm. 66 (2016) 303–330
[347] W. B. Lp, J. L. Henshall, R. M. Hooper, K. E. Easterling, The Mechanism of Indentation Creep, Acta metall. mater. Vol. 39, No. 12, pp. 3099-3110, 199
[348] Z.S. Ma, S.G. Long, Y.C. Zhou, Y. Pan, Indentation scale dependence of tip-in creep behavior in Ni thin films, Scripta Materialia 59 (2008) 195–198
[349] Schuh C A 2006 Nanoindentation studies of materials Mater. Today 9 32–40
[350] S. R. Jian, J. Y. Jung, 2013 Nanoindentation-induced pop-In effects in GaN thin filmsIEEE Trans. Nanotechnol. 12 304–8
[351] S. R. Jian, J. Y. Juang, N. C. Chen, S.C Jang, Huang J. C. Huang, Y. S. Lai, 2011 Nanoindentation-induced structural deformation in GaN/AlN multilayers Nanosci. Nanotechnol. Lett. 2 315–21
[352] Hemant Kumar Sharma, Rajesh Kumar Sharma, Raghvendra Sahai Saxena, Aditya Gokhale, Rajesh Prasad, Cyclic nanoindentation studies of HgCdTe epitaxial films, Materials Research Express 7 (2020) 016430

[353] X. J. Zheng, Y.C. Zhou, J. Y. Li, Nano-indentation fracture test of $Pb(Zr_{0.52}Ti_{0.48})O_3$ ferroelectric thin films, Acta. Mater. 51 (2003) 3985-3997
[354] W. B. Li, J. L. Henshall, R. M. Hooper, K. E. Easterling, The mechanism of indentation creep, Acta Metall. Mater. 39(1991), 3099–3110
[355] R. N. Stevens, Grain-boundary sliding and diffusion creep in polycrystalline solids, Philos. Mag.,23 (1971) 265–283
[356] J. Zhao, P. Huang, K.W. Xu, F. Wang, T.J. Lu, Indentation size and loading strain rate dependent creep deformation of nanocrystalline Mo, Thin Solid Film, 653 (2018) 365-370
[357] M. F. Ashby, The deformation of plastically non-homogeneous materials, Philosophical Magagize, 21(1970) 399–424.

[358] J. J. Gracio, The double effect of grain size on the work hardening behavior of polycrystalline copper, Scr. Metall. Mater. 31(1994) 487–489
[359] Hans Conrad, Kang Jung, Effect of grain size from millimeters to nanometers on the flow stress and deformation kinetics of Ag, Mater. Sci. Eng., A, 391(2005) 272–284.

[360] Hall, E. O. Hall, The Deformation and Ageing of Mild Steel: III Discussion of Results , Proc. Phys. Soc., London, Sect. B 64 (1951) 747.
[361] N. J. Petch, The Cleavage Strength of Polycrystals, Journal of the Iron and Steel Institute, 174 (1953) 25–28.
[362] James C. M. Li, Pile-up of Dissociated Dislocations and the Strength-Grain Size Relationship, Philosophical Magazine, 19 (1969) 189–198
[363] D. J. Abson and J. J. Jonas, The Hall-Petch Relation and High-Temperature Subgrains, Metal Science Journal, 4 (1970) 24-28
[364] W. C. Oliver, G.M. Pharr, An improved technique for determining hardness and elastic modulus using load and displacement sensing indentation experiments, J. Mater. Res. 7 (1992) 154-1583
[365] S.M. Sze, Physics of Semiconductor Devices (New York: Wiley, 1969)
[366] C.T. Tan, Hooman Mohsani, Emerging technologies for high performance infrared detectors, Nanophotonics, 7 (2018) 169-197
[367] P. Capper, J. Garland, Mercury Cadmium Telluride Growth, Properties and Application, John Wiley and Sons Ltd., U.K., 2011, 340–347
[368] Vanya Srivastav, R.Pal, V. Venkataraman, Modeling of room temperature current-voltage measurements on homojunction HgCdTe diodes exhibiting nonequilibrium effects, J. Appl. Phys. 111 (2012) 033112
[369] D.K. Schroder, Semiconductor Material and Device Characterization, John Wiley and Sons, New Jersey, 2006, 127–150.
[370] G. K. Reeves, H. B. Harrison, Obtaining the specific contact resistance from transmission line model measurements , IEEE Electron Device Letters, vol. edl-3, No, 5, May 1982
[371] G.D. Davis,W.A.Beck, M.K.Kelly, N.Tache, G.Margaritondo, Deposition of the unreactive metal Au onto sputtered and cleaved $Hg_{1-x}Cd_xTe$ surfaces, J. Appl. Phys.60 (9) (1986) 3157–3161.
[372] G.D. Davis, Overlayer interactions with (HgCd)Te, J.Vac.Sci.Technol.A6(3)(1988)1939–1945.
[373] W.E. Spicer, Metal contacts on $Hg_{1-x}Cd_xTe$, J. Vac. Sci. Technol. A 8 (2) (1990) 1174–1177.
[374] Arthur M. Turner, HgTe contacts to p-HgCdTe, Journal of Vacuum Science & Technology B 10, (1992) 1534
[375] A. Wall, A. Raisanen, S. Chang, P. Philip, A. Franciosi, D.J. Peterman, Local stoichiometry and atomic interdiffusion during reactive metal/mercury-cadmium-telluride junction formation, J. Vac. Sci. Technol. A5 (1987) 3193
[376] Dan Liu, Chun Lin, Songmin Zhou, Xiaoning Hu, Ohmic Contact of Au/Mo on $Hg_{1-x}Cd_xTe$, Journal of Electronic Materials, vol. 45, No. 6, 2016 ,86
[377] Patrick W. Leech, Martyn H. Kibel, Properties of Schottky diodes on n-type Hg_{1-x} Cd_xTe, J. Vac. Sci. Technol. B9, 1770 (1991)
[378] A. R. Momen-Baghdadabad, A. Bahari, F. M. Aghamir, Synthesis of multi-phase steel thin films by a low energy plasma focus device, Materials chemistry and physics, 319 (2024) 129324
[379] Leech, P.W., Reeves, G.K. & Kibel, M.H. Ohmic Contacts on N-Type $Hg_{0.4}Cd_{0.6}Te$.. MRS Online Proceedings Library 216, 155–160 (1990).

[380] H. Zimmermann, Robert C. Keller, P. Meisen, H. J. Richter, M. Seelamnn-Eggebert, Interface Formation Between Deposited Sn and $Hg_{0.8}Cd_{0.2}Te$, Journal of Electronic Materials, Vol. 25, No. 8, 1996
[381] Y.X. Wang, P.H. Holloway, Indium ohmic contacts to n-ZnSe, Vacuum 43 (11) (1992) 1149–1151
[382] P.Y. Emelie, E. Cagin, J. Siddiqui, J.D. Phillips, C. Fulk, J. Garland, S. Sivananthan, Electrical Characteristics of PEDOT: PSS Organic Contacts to HgCdTe, J. Electron. Mater. 36 (2007) 841–845
[383] M. Zandian, J.M. Arias, R. Zucca, R.V. Gil, S.H. Shin, HgCdTe double heterostructure injection laser grown by molecular beam epitaxy, Appl. Phys. Lett. 59 (9) (1991) 1022–1024.
[384 KiMan Kang, J.M. Jo, JoonSeop Kwak, H. Kim, Y.S. Kim, C. Sone, Y. Park, In/ITO Ohmic Contacts to Ga-face and N-face n-GaN for InGaN-based Light-emitting Diodes, J. Korean Phys. Soc. 55 (1) (2009) 318–321.
[385] S.Y. Moon, J.H. Son, K.J. Choi, J.L. Lee, H.W. Jang, Indium as an efficient ohmic contact to N-face n-GaN of GaN-based vertical light emitting diodes, Appl. Phys. Lett. 99 (2011), 202106.
[386] S. Palimar, K.V. Bangera, G.K. Shivakumar, Study of the doping of thermally evaporated zinc oxide thin films with indium and indium oxide, Appl. Nanosci. 3 (6) (2013) 549–553.
[387] B.K. Kim, T.H. Kim, D.H. Choi, H. Kim, K. Watanabe, T. Taniguchi, H. Rho, J. J. Kim, Y.H. Kim, M.H. Bae, Origins of genuine Ohmic van der Waals contact between indium and MoS_2, NPJ 2D Mater, Appl. 5 (2021) 9
[388] Z. Tsybrii, Y. Bezsmolnyy, K. Svezhentsova, M. Vuichyk, I. Lysiuk, M. Apatska, M. Smolii, N. Dmytruk, S. Bunchuk, K. Andreeva, F. Sizov, HgCdTe/CdZnTe LPE epitaxial layers: from material growth to applications in devices, J. Cryst. Growth 529 (2019), 125295
[389] C. Birleanu, M. Pustan, V. Meire , R. Muller, R. Voicu, A. Baracu, S. Craciun, Temperature effect on the mechanical properties of gold nano films with different thickness, IOP Conf. Series : Materials Science and Engineering 147, (2016) 012021
[390] Casa M, Sarno M, Liguori R, et al. Conductive Adhesive Based on Mussel-Inspired Graphene Decoration with Silver Nanoparticles, Journal of Nanoscience and Nanotechnology, 18(2) (2018)1176-1185.
[391] Kolahdoozan M, Hamedi M, Nikkhah-Bahrami M., A novel model for the effect of geometric properties of micro/nanoscale asperities on surface adhesion. International Journal of Adhesion and Adhesives, 48 (2014) 280-287
[392] Shailendra Kumar Gaur, Qasim Murtaza, R.S. Mishra, Comparison of Tin and Indium Thin Films Structural, Morphological, Adhesion, and Electrical Properties for Ohmic Contact in HgCdTe-Based Infrared Detectors, Journal of Materials Engineering and Performance 34, 18502–18515 (2025).
[393] Jatinder Kaur, Ravish K. Jain, Atul Khanna, Amit K. Chawla, Effect of thickness on the wettability and electrical properties of Sn thin films, Journal of Vacuum Science and Technology B, 39 (2021) 032205
[394] Shunichi Hishita, Zdenek Stryhal, Isao Sakaguchi, Naoki Ohashi, Noriko Saito, Hajime Hanoda, Sn film deposition on silica glass substrates, Thin Solid Films, 464-465 (2004) 146-149
[395] R.S. Parra, P.J. George, G.G. S´anchez, A.E. Jim´enez Gonz´alez, L. Ba˜nos, P.K. Nair, Optical and electrical properties of Pbs + In thin films subjected to thermal processing, J. Phys. Chem. Solids 61 (5) (2000) 659–668.
[396] P.N. Bartlett, D. Cook, C.H. Kees de Groot, A.L. Hector, R. Huang, A. Jolleys, G. P. Kissling, W. Levason, S.J. Pearce, G. Reid, Non-aqueous electrodeposition of p-block metals and metalloids from halometallate salts, RSC Adv. 3 (36) (2013) 15645.
[397] R. Das, R.K. Soni, Synthesis and surface-enhanced Raman scattering of indium nanotriangles and nanowires, RSC Adv. 7 (51) (2017) 32255–32263.

[398] S.R. Kumar, B. Prajapati, S.K. Tiwari, V.K. Tiwari, Growth and characterization of copper, indium and copper-indium alloy films non-aqueous method of electrodeposition, Indian J. Pure Appl. Phys. 46 (2008) 198–203.
[399] K. Ulutas¸, D. De˘ger, N. Kalkan, S. Yıldırım, Y.G. Çelebi, Y. Iskarlatos, M. L. ¨Oveço˘glu, A. Genç, Structural properties of In-In_2O_3 composite films, IOP Conf. Ser.: Mater. Sci. Eng. 15 (2010), 012095.
[400] P. Lobaccaro, A. Raygani, A. Oriani, N. Miani, A. Piotto, R. Kapadia, M. Zheng, Z. Yu, L. Magagnin, D.C. Chrzan, R. Maboudian, A. Javey, Electrodeposition of High-Purity Indium Thin Films and Its Application to Indium Phosphide Solar Cells, J. Electrochem. Soc. 161 (14) (2014) D794–D800.
[401] Prashant Kumar, M. Ghanashyam Krishna, A comparative study of laser- and electric-field-induced effects on the crystallinity, surface morphology and plasmon resonance of indium and gold thin films, Phys. Status Solidi A 207, No. 4, 947–954 (2010)
[402] Jatinder Kaur, Atul Khanna and Amit Kumar Chawla, Metallic to semiconducting transition and hydrophobicity properties of Indium films, Vacuum, 203 (2022)11281
[403] C.Y.Tsay, H.C. Cheng, Y.T. Tung, W.H. Tuan, C. K. Lin, Effect of Sn-doped on microstructural and optical properties of ZnO thin films deposited by sol-gel method, 517 (2008) 1032 - 1036
[404] Rupali Das, Rajesh Kumar, Preparation of nanocrystalline PbS thin films and effect of Sn doping and annealing on their structural and optical properties Materials Research Bulletin 47 (2012) 239- 246
[405] R.P. Reed, C.N. McCowan, R.P. Walsh, L.A. Delgado, J.D. McColskey, Tensile Strength and Ductility of Indium, Mater. Sci. Eng. A 102 (1988) 227–236.
[406] G. Lee, J.Y. Kim, A.S. Budiman, N. Tamura, M. Kunz, K. Chen, M.J. Burek, J. R. Greer, T.Y. Tsui, Fabrication, structure and mechanical properties of indium nanopillars, Acta Mater. 58 (4) (2010)1361–1368.
[407] S.E. Al Garni, A.F. Qasrawi, Effect of Indium nano-sandwiching on the structural and optical performance of ZnSe films, Results Phys. 7 (2017) 4168–4173.
[408] Soekhee L , Juyun P , Jin-W O and Yong-C K 2020 Effect of compositional ratio of Sn in SnZn thin films morphological and chemical properties Physica B : Physics of Condensed Matter 591 412257
[409] Aleksandra. F , Yue L, Iman G , Peter C C and Eric C 2017 Investigation of Tin (Sn) film using an aerosol jet additive manufacturing deposition process, Journal of Electronic Materials doi : 10.1007/s11664-017-5524-7
[410] J. Ivanco, T. Todar, A. Firsov, M. Brzhezinskaya, M. Sperling, W. Braun, D. R. T. Zahn, Indium on a copper phthalocyanine thin film: Not a reactive system, Physical Review B, 81 (2010) 115325
[411] V. Borra , D. G. Georgiev, C. R. Grice, Fabrication of optically smooth Sn thin films, Thin Solid Films, 616 (2016) 311 -315
[412] Daryush Shajari, Ali Bahari, Pooria Gill, Mojtaba Mohseni, Synthesis and tuning of gold nanorods with surface plasmon resonance, Optical Materials, 64 (2017) 376-383
[413] Zahraa Hadi Ali, Ali Bahari, Addnan H. Alarajiy, Investigation the effect of concentration(x) in polyvinyl alcohol (PVA)x/ nickel phthalocyanine (NiPc)(1-x) nano composites: Real & imaginary component of permeability and optical conductivity, Optical Materials, 148 (2024) 114862
[414] V. B. Neimash, P. Y. Shepelyavyi, A. S. Nekolenko, V.V. Strelchuk, I. V. Chegel, 2022 Micro and nanostructure of layer Si/Sn/Si films formed by vapor deposition, Journal of Nanomaterials, article Id : 7910708
[416] K. Santosh Kumar, C. Manoharan, S. Dhanapandian, A. Gowri Manohari, T. Mahalingam, Effect of indium incorporation on the properties of SnS thin films prepared by spary pyrolysis, Optik, vol.25, issue 15 (2014) 3996-4000
[417] K.L. Johnson, K. Kendall, A.D. Roberts, Surface energy and the contact of elastic solids, Proc. R. Soc. A., 324 (1971) 301-313
[418] K. L. Derijaguin, V. M. Muller,Y. P. Toporov, Effect of contact deformations on the adhesion of particles, J Colloid Interface Sci. , 53 (1975) 314-326

[419] S. G. David, W. C. Robert, E. Flater, 2005, Accounting for the JKR-DMT transition in adhesion and friction measurements with atomic force microscopy, Journal of Adh. Sci. Tech. 19 3-5 291-311
[420] Corina Birleanua , Marius Pustana , Raluca Müllerb , Cristian Dudescua , Violeta Meriea , Rodica Voicub , Angela Baracu, Experimental investigation by atomic force microscopy on mechanical and tribological properties of thin films, Int. J. Mater. Res., 107 (2016) 1–10
[421] D. X. Zang, B. Shen , Y. X. Zeng , S. Y. Wang , J. B. Jang , S. D. Yang , R. J. Zang , L.Y.Chen ,C.Z. Wan, K. M. Ho, Evolution of optical properties of tin film from solid to liquid studied by spectroscopic ellipsometry and ab inito calculation, Applied Physics Letter 104 (2014) 121907
[422] Jingo Z , Yuxiang Z , Dongdong Z , Shangdong Y , Liao Y, Zhunhua L, Rongjun Z , Songyou W, Dongxu Zang, Liangyao C, Ellipsometric study on size-dependent melting point of nanometer-sized indium particles, Journal of Physical Chemistry 120 (2016)10686-10690
[423] P. N. Vinod, Specific contact resistance measurements of the screen-printed Ag thick film contacts in the silicon solar cells by three-point probe methodology and TLM method, J Mater Sci: Mater Electron 22 (2011) 1248–1257
[424] W. A. Beck, G. D. Davis, A. C. Goldberg, Resistance and 1/f noise of Au, Al, and Ge contacts to (Hg,Cd)Te, J. Appl. Phys. 67 (1990) 6340
[425] S. Nozaki, A.G. Milnes, Specific contact resistivity of indium contacts to n - type CdTe, J. Electron. Mater. 14 (2) (1985) 137–155
[426] E.H. Rhoderick, Metal Semiconductor Contacts, Oxford, United Kingdom: Oxford University Press, (1978), pp. 77–115.
[427] Norton P 2002 HgCdTe infrared detectors Opto-Electronic Rev. 10 159–74
[428] Rogalski A 2005 HgCdTe infrared detector material: history, status and outlook Reports Prog. Phys. 68 2267–336
[429] Kinch M A 2015 The future of infrared; III–Vs or HgCdTe, J. Electron. Mater. 44 2969–76
[430] Lee D, Carmody M, Piquette E, Dreiske P, Chen A, Yulius A, Edwall D, Bhargava S, Zandian M and Tennant W E 2016 High-operating temperature HgCdTe: a vision for the near future J. Electron. Mater. 45 4587–95
[431] Bisotto S, Abergel J, Dupont B, Ferron A, Mailliart O, Nicolas J A and Santailler J L 2019 May 7.5 μm and 5μm pitch IRFPA developments in MWIR at CEA-LETI Infrared Technology and Applications XLV vol 11002 (International Society for Optics and Photonics) pp 110021C
[432] H. Zimmermann, Robert C. Keller, P. Meisen, H.J. Richter, M. Seelmann -Eggbert, Interface Formation Between Deposited Sn and $Hg_{0.8}Cd_{0.2}Te$, Journal of Electronic Materials, Vol. 25, No. 8, 1996
[433] Patrick W. Leech, Geoffrey K. Reeves, Martyn. Kibel, Ohmic Contacts on n-type $Hg_{0.4}Cd_{0.6}Te$, Mat. Res. Soc. Symp. Proc. Vol. 216. ,1991 Materials Research Society
[434]G.D. Davis, Overlayer interactions with (HgCd)Te, J. Vac. Sci. and Techn. A 6(3) June 1988
[435] Authur M. Turner, HgTe contacts to p-HgCdTe, Journal of Vacuum Science & Technology B 10, 1534 (1992)
[436] Kinch M A 2014 State-of-the-art infrared detector technology SPIE
[437] P. Capper, J. Garland, Mercury Cadmium Telluride Growth, Properties and Application: Structure and Electrical Characteristics of Metal/MCT Interfaces, first ed., John Wiley & Sons Ltd., U. K., 2011, pp. 340–356.
[438] G.D. Davis, W.A. Beck, Y.W. Mo, D. Kilday, G. Margaritondo, Interfacial interactions between (HgCd)Te and Ti, an ultrareactive metal, J. Appl. Phys. 61 (1987) 5191.
[439] Lei W, Antoszewski J and Faraone L 2015 Progress, challenges, and opportunities for HgCdTe infrared materials and detectors Appl. Phys. Rev. **2** 041303

[440] G.D. Davis, J.T. McKinley, D.G. Kilday, G. Margaritondo, Effects of Al and Ti interlayers on Sb/(HgCd)Te interface behaviour, J. Appl. Phys. 65 (1989) 3435.
[441] Liu D, Lin C, Zhou S and Hu X 2016 Ohmic contact of Au/Mo on HgCdTe J. Electron. Mater. 45 2802–7
[442] Spicer W E 1990 Metal contacts on Hg1− x Cd x Te J. Vac. Sci. Technol. A 8 1174–7
[443] Y. Tang, Jia Jia, H. Qiao, Y. Zhang, X. Li, Application of Au/Sn in the formation of p-HgCdTe photoconductive detectors electrodes, 6th international symposium on advanced optical manufacturing and testing technologies: optoelectronic materials and devices for sensing, imaging, and solar energy, Proc. SPIE 8419 (2012) 84190Z.
[444] Schilz J and Thompson J 1993 Ohmic contacts to p-type $Hg_{0.3}Cd_{0.7}Te$ by metalorganic chemical vapour deposition of HgTe J. Mater. Sci. 28 6462–5
[445] P.W. Leech, G.K. Reeves, Low resistance ohmic contacts to n-Hg_{1-x} Cd_x Te using a HgTe cap layer, Infrared Detectors–Materials, Processing, and Devices, Proc. of Mat. Res. Soc. Symp. 299 (1994) 978, 1-107-40952-1.
[446] D. Qian, J. Jia, Y. Tang, F. Liu, X. Ma, L. Zhang, F. Liu, B. Ye, H. Qiao, L. Zhu, X. Li, The evaluation of curved extended electrodes for off-area bonding of HgCdTe photoconductive detectors, international symposium on photoelectronic detection and imaging 2011: advances in infrared imaging and applications, Proc. SPIE 8193 (2011), 81932E.
[447] Z. Tsybrii, Y. Bezsmolnyy, K. Svezhentsova, M. Vuichyk, I. Lysiuk, M. Apatska, M. Smolii, N. Dmytruk, S. Bunchuk, K. Andreeva, F. Sizov, HgCdTe/CdZnTe LPE epitaxial layers: from material growth to applications in devices, J. Cryst. Growth 529 (2019), 125295
[448] M.W. Fay, G. Moldovan, P.D. Brown, I. Harrison, J.C. Birkbeck, B.T. Hughes, M. J. Uren, T. Martin, Structural and electrical characterization of AuTiAlTi/AlGaN/ GaN ohmic contacts, J. Appl. Phys. 92 (2002) 94.
[449] A. Motayed, K.A. Jones, M.A. Derenge, M.C. Wood, D.N. Zakharov, Z. Liliental- Weber, D.J. Smith, A.V. Davydov, W.T. Anderson, A.A. Iliadis, S.N. Mohammad, Electrical, microstructural, and thermal stability characteristics of Ta/Ti/Ni/Au contacts to n- GaN, J. Appl. Phys. 95 (2004) 1516.
[450] V.R. Reddy, Study of the electrical, structural and surface morphological characteristics of Pt/Re/Au ohmic contacts on p-type GaN, Mater. Chem. Phys. 93 (2005) 286–290.
[451] S.U. Jen, T.C. Wu, Young's modulus and hardness of Pd thin films, Thin Solid Films 492 (2005) 166 – 172
[452] Hemant Kumar Sharma, Rajesh Kumar Sharma, Raghvendra Sahai Saxena, Aditya Gokhale, Rajesh Prasad, Cyclic nanoindentation studies of HgCdTe epitaxial films, Mater. Res. Express 7 (2020) 016430
[453] Z. Shan, S. K. Sitaraman, Elastic–plastic characterization of thin films using nanoindentation technique, Thin Solid Films 437 (2003) 176-181
[454] Y.-G. Jung, B. R. Lawn, M. Martyniuk, H. Huang, X. Zhi Hu, Evaluation of elastic modulus and hardness of thin films by nanoindentation, Journal of Materials Research 19 (2004) 3076-3080,
[455] S. Min Han, R. Saha, W. D. Nix, Determining hardness of thin films in elastically mismatched film-on-substrate systems using nanoindentation, Acta Materialia 54 (2006) 1571-1581
[456] E. L.Kossovich, F. M. Borodich, S. J. Bull, S. A. Epshtein, Substrate effects and evaluation of elastic moduli of components of inhomogeneous films by nanoindentation, Thin Solid Films 619 (2016)
[457] Simon Roa, Martin Sirena, Thickness and microstructure influence on the nanocrystalline Cu thin films' mechanical properties. Journal of Materials Research 36, 938–948 (2021)

[458] Edgar A. Villegas, Rodrigo Parra1 · Leandro Ramajo, Integral nanoindentation evaluation of TiO2, SnO2, and ZnO thin films deposited via spray-pyrolysis on glass substrates, Journal of Materials Science: Materials in Electronics, 2018 ,https://doi.org/10.1007/s10854-018-0404-3

[459] I. Dutta, C.B. Munns, G. Dutta, An X-ray diffraction (XRD) study of vapor deposited gold thin films on aluminum nitride (A1N) substrates, Thin Solid Films 304 (1997) 229–238.

[460] N. Mahmoodi, A.I. Rushdi, J. Bowen, A. Sabouri, C.J. Anthony, P.M. Mendes, J. A. Preece, Room temperature thermally evaporated thin Au film on Si suitable for application of thiol self-assembled monolayers in micro/nano-electro-mechanical-systems sensors, J. Vac. Sci. Technol. A 35 (4) (2017), 041514.

[461] A. Dandapat, S. Pramanik, S. Bysakh, G. De, Boat-like Au nanoparticles embedded mesoporous c-Al_2O_3 films: an efficient SERS substrate, J. Nanoparticle Res. 15 (2013) 1804. [46] G. Geng, P. Chen, B. Guan, Y. Liu, C. Yang, N. Wang, M. Liu, Sheetlike gold nanostructures/graphene oxide composites via a one-pot green fabrication protocol and their interesting two-stage catalytic behaviors, RSC Adv. 7 (2017) 51838–51846.

[462]Yutaro Nakoshi, Ken Suzuki, and Hideo Miura, Effects of crystallinity on mechanical properties of electroplated gold thin films used for three-dimensional electronic packaging, Japanese Journal of Applied Physics 58, SBBC04 (2019)

[463] V. Karoutsos, M. Toudas, A. Delimitis, S. Grammatikopoulos, P. Poulopoulos, Microstructural evolution in nanostructured gold films, Thin Solid Films 520 (2012) 4074–4079

[464] B.D. Cullity S.R. Stock, Elements of X-Ray Diffraction, Third Edition, © Pearson Education Limited 2014

[465] Ana C. Murrieta, Danyel Cavazos-Cavazos , Pamela Santos-Aguilar, Jorge L. Cholula-Díaz , Flavio F. Contreras-Torres, Microstructure of polycrystalline gold nanoparticles and thin-films from a comparative X-ray line profile analysis, Materials Chemistry and Physics 258 (2021) 123976

[466] B. Chen, M. Mokume, C. Liu, K. Hayashi, Structure and localized surface plasmon tuning of sputtered Au nano-islands through thermal annealing, Vacuum 110 (2014) 94–101.

[467] T. Rerek, L. Skowronski, R. Szczesny, M.K. Naparty, B. Derkowska-Zielinska, The effect of the deposition rate on morphology, opto-electronic properties and formation intermetallic compounds of Au-Sn alloys, J. Alloys Compd. 849 (2020), 156041

[468] Y. Kalachyova, O. Lyutakov, A. Solovyev, P. Slepiˇcka, V. ˇSvorˇcík, Surface morphology and optical properties of porphyrin/Au and Au/porphyrin/Au systems, Nanoscale Res. Lett. 8 (2013) 1–10, 547.

[469] F. Ruffino, V. Torrisi, G. Marletta, M.G. Grimaldi, Atomic force microscopy investigation of the kinetic growth mechanisms of sputtered nanostructured Au film on mica: towards a nanoscale morphology control, Nanoscale Res. Lett. 6 (2011) 112.

[470] O. Akogwua, D. Kwabi, S. Midturi, M. Eleruja, B. Babatope, W.O. Soboyejo, Large strain deformation and cracking of nanoscale gold films on PDMS substrate, Mater. Sci. Eng., B 170 (2010) 32–40.

[471] A. Toma, B.ˇS. Batiˇc, D. Chiappe, C. Boragno, U. Valbusa, M. Godec, M. Jenko, F. B. Mongeot, Patterning polycrystalline thin films by defocused ion beam: the influence of initial morphology on the evolution of self-organized nanostructures, J. Appl. Phys. 104 (2008), 104313.

[472] Riley Shurvinton , Valentin Allard, Aude Lereu, Antonin Moreau, Fabien Lemarchand, and Julien Lumeau, Investigating ultra-thin Ag and Au layers using spectrophotometry and AFM imaging, J. Eur. Opt. Society-Rapid Publ. 20, 8 (2024)
[473] Teguh Handoyo , Jun Kondoh, 'Development of gold thin-film for optical-based biosensor, AIP Conf. Proc. 2230, 020008 (2020)
[474] T.S.T. Amran, M.R. Hashim, N.K.A. Al-Obaidi, H. Yazid, R. Adnan, Optical absorption and photoluminescence studies of gold nanoparticles deposited on porous silicon, Nanoscale Res. Lett. 8 (2013) 35.
[475] N. Azizah, U. Hashim, M.K.M. Arshad, S.C.B. Gopinath, S. Nadzirah, M. A. Farehanim, M.F. Fatin, A.K.M. Muaz, A.R. Ruslinda, R.M. Ayub, Analysis study of single gold nanoparticle system of interdigitated device electrodes (IDES) by using energy-dispersive X-ray (EDX), ARPN J. Eng. Appl. Sci. 11 (2016) 14.
[476] C. Benazzouz, N. Benouattas, S. Iaiche, A. Bouabellou, Study of diffusion at surface of multilayered Cu/Au films on monocrystalline silicon, Nucl. Instrum. Methods Phys. Res., Sect. B 213 (2004) 519–522.
[477] M. Walther, D.G. Cooke, C. Sherstan, M. Hajar, M.R. Freeman, F.A. Hegmann, Terahertz conductivity of thin gold films at the metal-insulator percolation transition, Phys. Rev. B 76 (2007), 125408.
[478] J. Siegel, O. Lyutakov, V. Rybka, Z. Kolsk´a, V. ˇSvorˇcík, Properties of gold nanostructures sputtered on glass, Nanoscale Res. Lett. 6 (2011) 96.
[479] J.E. Mogonye, N. Argibay, R.S. Goeke, P.G. Kotula, T.W. Scharf n, S.V. Prasad, Tribology and sliding electrical contact resistance of e-beam hard Au: Effects of annealing, Wear 376-377 (2017) 1662–1672
[480] X. D. Li, T. P. Chen, Y. Liu, K. C. Leong, Evolution of the localized surface plasmon resonance and electron confinement effect with the film thickness in ultrathin Au films, J Nanopart Res (2015) 17:67
[481] J. Sun, L. Fu, Z. Nie, Y. Shi, L. Yapeng, The effect of chemical polishing on the interface structure and electrical property of Au/Cd0.9 Zn0.1Te contact, Appl. Phys. A 115 (2013) 1309–1316.
[482] T.E. Novelo, G.M. Alonzo-Medina, P. Am´ezaga-Madrid, R.D. Maldonado, Surface morphology and electrical resistivity in polycrystalline Au/Cu/Si (100) system, J. Nanomater. 2079204 (2017) 1–8.
[483] M. Deura, H. Fukuyama, Formation of SiC layer by carbonization of Si surface using CO gas, J. Cryst. Growth 434 (2016) 77–80.
[484] Li X D and Bhushan B 2002 A Review of Nanoindentation Continuous Stiffness Measurement Technique and Its Applications Materials Characterization, 48, 11-36
[485] Greer, J. R.; Oliver, W. C.; Nix, W. D. Acta Mater. 2005, 53, 1821–1830.
[486] Simón Roa1, Martín Sirena, AFM imaging analysis of nanoindentation-induced plastic strain in indium surface for calibrating nanoindenters area profiles, Physica B: Physics of
Condensed Matter (2022), doi: https://doi.org/10.1016/j.physb.2022.413773
[487] Hull, D.; Bacon, D. J. Introduction to dislocations, 4th ed.;Butterworth-Heinemann: Woburn, Massachusetts, 2001.
[488] Ashby, M. F. Philos. Mag. 1970, 21, 399–424. doi:10.1080/14786437008238426
[489] Fleck, N. A.; Hutchinson, J. W. J. Mech. Phys. Solids 1993, 41, 1825–1857.
[490] Nix, W. D.; Gao, H. J. Mech. Phys. Solids 1998, 46, 411–425.
[491] W. C. Oliver, G.M. Pharr, An improved technique for determining hardness and elastic modulus using load and displacement sensing indentation experiments, J. Mater. Res. 7 (1992) 154-1583
[492] Meyers, M. A.; Mishra, A.; Benson, D. J. Prog. Mater. Sci. 2006, 51, 427–556.

[493]V. Mulloni, R. Bartali,S.Colpo, F. Giacomozzi, N. Laidani, B. Margesin, Electrical and mechanical properties of layered chromium –gold thin films for ohmic contacts in RF-MEMS switches , Materials Science and Engineering B,163 (2009)199-203
[494] Bhushan, B.; Li, X. Int. Mater. Rev. 2003, 48, 125–164. doi:10.1179/095066003225010227
[495]Ersin Yucel, Osman Sahin, 'Effect of pH on the structural, optical and nanomechanical properties of CdS thin films grown by chemical bath deposition ', Ceramics International 42 (2016) 6399-6407
[496] Hall, E. O. Proc. Phys. Soc., London, Sect. B 1951, 64, 747.
[497] Petch, N. J. J. Iron Steel Inst., London 1953, 174, 25–28.
[498] Li, W. B.; Henshall, J. L.; Hooper, R. M.; Easterling, K. E. Acta Metall. Mater. 1991, 39, 3099–3110. doi:10.1016/0956-7151(91)90043-Z
[499] Stevens, R. N. Philos. Mag. 1971, 23, 265–283.doi:10.1080/14786437108216383
[500] L. Basset, W. Favre, O. Bonino, J. Sudre, G. M'enard, J.-P. Vilcot, In depth analysis of transmission line model application on passivated contacts under illumination, Sol. Energy Mater. Sol. Cells 230 (2021), 111255.
[501] R. Nokhwal, V. Srivastav, A. Goyal, B.L. Sharma, S.A. Hashmi, R.K. Sharma, Surface studies on HgCdTe using non-aqueous iodine-based polishing solution, J. Electron. Mater. 46 (2017) 6795–6803.
[502] T.V. Blank, Y.A. Goldberg, Mechanisms of current flow in metal–semiconductor ohmic contacts, Semiconductors 41 (2007) 1263–1292.

LIST OF PUBLICATIONS

Papers published during PhD

1. Analysis of structural, morphological and nano-mechanical properties of vacuum evaporated nanoscale CdTe and ZnS films, Shailendra Kumar Gaur, Qasim Murtaza, R.S. Mishra, *Optical Materials* 154 (2024) 115764, https://doi.org/10.1016/j.optmat.2024.115764, **Elsevier (Impact factor 4.2)**

2. Comparison of Tin and Indium Thin Film's Structural, Morphological, Adhesion, and Electrical Properties for Ohmic Contact in HgCdTe-Based Infrared Detectors, Shailendra Kumar Gaur, Qasim Murtaza, R.S. Mishra, *Journal of Materials Engineering and Performance* 34(17), (2025) 18502, https://doi.org/10.1007/s11665-024-10551-1, **Springer (Impact factor 2.0)**

3. Comparative analysis of thermally evaporated nanoscale CdS thin film's structural, morphological, optical and nanomechanical properties, Shailendra Kumar Gaur, Ashwani Chaudhary, Qasim Murtaza, R.S. Mishra, *Journal of Molecular Structure* 1324 (2025) 140850, https://doi.org/10.1016/j.molstruc.2024.14085, **Elsevier (Impact factor 4.7)**

4. Analysis of the nanoscale gold Ohmic Contact's structural, compositional, morphological, nanomechanical, and electrical properties for prospective infrared detectors on a p-type HgCdTe, Shailendra Kumar Gaur, Qasim Murtaza, R.S. Mishra, *Journal of Optics communications,* 604 (2026) 132846, https://doi.org/10.1016/j.optcom.2025.132846*,* **Elsevier (Impact factor 2.5)**

Papers communicated in SCIE journals:

1. Investigation of evaporated CdTe and ZnS thin film's crystallographic, morphological, nanomechanical and electrical characteristics for optoelectronic devices, Shailendra Kumar Gaur, Qasim Murtaza, R.S. Mishra

Publications in International conference/workshop proceedings:

1. Experimental Investigation of Thermally Grown Indium Film's Structural and Tribological Properties, Shailendra Kumar Gaur, Qasim Murtaza, R.S. Mishra, *Journal of Polymer & Composites*, **(ICAMMIA-2023, Scopus Indexed, Meerut Institute of Engineering and Technology, Meerut, U.P.)**

2. Study of CdS Thin Film's Structural, Morphological, and Mechanical Properties, *Recent Advances in Mechanical Engineering*, Shailendra Kumar Gaur, Qasim Murtaza, R.S. Mishra **(Conference ICMET-2023, Galgotias College of Engineering & Technology, Scopus Indexed, Greater Noida, U.P.)**

BRIEF PROFILE

I (Shailendra Kumar Gaur) am a research scholar in the Mechanical Engineering Department and enrolled in PhD in the year 2021 (Roll No. 2K20/PHDME/507). I did B.Tech (Mechanical) from Delhi College of Engineering in 2005 and M.Tech (Thermal) from Delhi Technological University in 2015. My research work area is thin film deposition of metals such as Cr-Au, In, & Sn and passivation films of materials such as CdTe, ZnS, and CdS. I am working in the Solid State Physics Laboratory, Timarpur, Delhi. I have good experience in the operation and maintenance of thermal evaporation system and e- beam evaporation systems. My research work involves deposition of thin films at various deposition conditions (different deposition rates, single layer, multi-layer, etc.) under high vacuum conditions and characterization of thin films for structural, morphological, topographical, mechanical, optical, and electrical properties by X-ray diffraction, scanning electron microscopy, atomic force microscopy, dektak surface profiler, multibeam optical stress sensor, nanoindentation, UV-spectrometer, ellipsometry, 4-probe electrical measurements, etc. These optimized thin films are suitable for the fabrication of photovoltaic and optoelectronic devices.